PETROLEUM RESEARCH JOURNAL

VOLUME 25 - (2021/2022)

Acting Chairman

KAMAL AREF MUNTASER

Editor-in-Chief

MAHMOUD T. ELBAKAI

Co-ordinator

ABDULMAGID A. ELMRYED

FOREWORD

It is our pleasure to introduce the 25th issue (the sliver volume) of the Petroleum Research Journal, that is published by the Libyan Petroleum Institute (LPI). This journal includes papers that classified as some technical experiences of Libyan oil and gas and covers many interesting subjects.

I would like to thank the editorial committee of this issue and editorial committees of the previous issues for their efforts along the journey to reach this sliver issue in a successful manner.

I also would like to take this opportunity to invite the researchers to contribute in future issues to increase the scientific value of this journal.

Kamal Aref Muntaser
Acting Chairman of the Management Committee
Libyan Petroleum Institute

EDITORIAL

Petroleum Research Journal continued to publish papers on science, engineering and industrial technology related to petroleum discipline. The journal seeks to promote the application of such papers by the oil sector in the exploring and producing of oil and gas.

With the support of the management committee of the Libyan Petroleum Institute and assistance of many other staff members and colleagues, editors were able to fulfill their responsibility of editing this volume (the silver one) and they are very grateful.

We would like to express our thanks to all researchers who showed interest in the Petroleum Research Journal and for choosing the PRJ to publish their ideas.

We shall not forget to express our gratitude and high appreciation to the management of the National Oil Corporation (NOC) for giving permission to publish this volume.

The papers printed herein were edited but not reviewed and therefore, the ideas expressed by authors are of course their own.

The Editors

PETROLEUM RESEARCH
JOURNAL

Editorial Policies

The Petroleum Research Journal (Petroleum Res. J.) is a multi-disciplinary scientific technical journal published periodically by the Libyan Petroleum Institute. The aim of the journal is to publish articles classified as original papers, short communications and reviews of both practical and theoretical interests, which deal with scientific and technical advances in the fields of geology, geophysics, geochemistry, chemistry, petroleum and chemical engineering. Subject matter should be relevant to hydrocarbon exploration, evaluation and industry. The opinions and views expressed by the authors in their contributions are solely their responsibility.

- Ideas of the preliminary results of investigation, that have not advanced yet to the point at which they warrant publication as a full paper, may be submitted for publication as short communications. Other types of contributions such as discussions, book reviews and conference reports may also be submitted.

- Manuscripts may be submitted in Arabic or in English. Manuscripts in Arabic require English abstract.

- Manuscripts are accepted with the understanding that they have not been published elsewhere, and are not currently under consideration by another journal nor will be submitted to another journal. Manuscripts accepted for publication are the copy right of the journal.

- Manuscripts are processed by the Editor-in-Chief. Three copies of each submitted manuscript are sent to the appropriate Associate Editor for technical review. The Associated Editor will seek evaluation from three reviewers qualified to judge value of the paper, collect the reviews received, synthesize their contents and make a recommendation to the Editor-in-Chief concerning the acceptability of the manuscript. The final decision on a paper's disposition is then made by the Editorial Committee and communicated to the author(s) by the Editor-in-Chief.

- Twenty five free reprints of each published paper will be supplied to the author.

Instructions to Authors

Conformity to the following instructions is a prerequisite for consideration:

1. Manuscripts should be submitted with a letter stating (1) that the contents have not been published elsewhere; and (2) that the paper is not being submitted elsewhere.

2. Manuscripts should be submitted in electronic format in Microsoft Word (.doc) on CD-ROM, which must be checked with up-to-date virus scanner. Manuscripts may also be submitted via e-mail.

3. Alternatively, an original copy for each manuscript can be sent to the Editor-in-Chief of the Journal. However, the final revised version of the accepted manuscript must be submitted in electronic format as described above.

4. A title page should accompany the text, which includes: (a) paper title which should be informative and brief; (b) all authors' full names; (c) all affiliations clearly indicated; (d) key words (up to six) characterizing the subject material; and (e) the name, post and e-mail addresses, and telephone and FAX numbers of the corresponding author.

5. Computer illustration, including photographs (which must be kept to a minimum), charts and diagrams, must be submitted in high resolution format, and must be at least 300 dpi. Submit each illustration as separate file and indicate its location within the manuscript. Non-computer illustrations should be submitted in 21x28cm format. They should accompany the manuscript but should not be inserted in the text.

6. Illustrations are to be referred to as "Figures" and should be numbered consecutively in the order in which they are referred to in the text. They should be designed to go across a single or double column width of the journal page. Brief captions should be provided to make the figures as informative as possible.

7. All hand line drawings should be made with black drawing on white paper (preferably tracing paper). The authors' last name should be written in the margins (or on back) for identifications.

8. Non-computer photographs should be glossy prints. The authors last name and identification, as to which is the top of the photo, is to be written in pencil on the back.

9. A list of figures and table captions are to be typed on a separate page and attached to the end of the manuscript. List the figure number in the form "Fig. 1".

10. In the manuscript, principal headings should be typed at the centre of the page in capital letters. Headings of the text, first lower rank should be typed in small letters (first letters of the headings and proper nouns are to be capitalized). The following text should begin on the next line. For headings of second lower rank, underline and place a dash after the headings, and follow with text on the same line.

11. All references should be grouped at the end of the paper, under the heading REFERENCES, either alphabetically or numbered in the order they appear in the text. For a given author referred to more than once, use chronological listings with a suffix (a, b, etc.) to distinguish references of the same year. In the list of references, the following order and punctuation should be observed:

For references to a paper from journals:
- author(s) name (last name first, initials),
- year of publication,
- title (capitalize first word):
- journal name (abbreviate conforming to world list of scientific periodicals), volume number should be in bold; journal name and/or book title in italics.
- Page number (followed by beginning and ending page numbers).

Example:
Lagha, S. (1997). Petrography of the Triassic Phosphorites in the Gharyan Area, N.W. Libya. *Petroleum Res. J.*, **9**, 45-50.

For reference books:
- author(s) name (as above).
- year of publication
- title (capitalize all words of the title).
- publisher (firm name).

Example:
Tucker, M.E. (1981). *Sedimentary Petrology: An Introduction*. Blackwell Scientific, 251 p.

For references to a paper within a book:
- author(s) name
- Year of publication,
- Title of paper/(followed by)
- Editor(s) name(s)
- Title (of book):
- Page range,
- Publisher.

Example:
El-Bakai, M.T. (1996). Diagnesis and diagenetic History of the Lidam Formation, N.W. Sirt Basin In: M.J. Salem, A.S. El-Hawat and A.M. Sbeta (eds.) *The Geology of Sirt Basin*, **I**, 83-97. Elsevier, Amsterdam.

12. All correspondence should be addressed to:

Editor-in-Chief
Petroleum Journal
Libyan Petroleum Institute P.O. Box: 6431
Tripoli
State of Libya
Tel: 4830022/27 – 4836821/24
Fax: (21) 4830031
e-mail address: m.elbakai@lpilibya.com
Web-site: www.lpilibya.com

DIAGENESIS AND RESERVOIR QUALITY OF THE UPPER PALEOCENE SUCCESSION, WESTERN DAHRA PLATFORM, SIRT BASIN, LIBYA

Ibrahim E. Elkanouni[1] and Maurice E. Tucker[2]

Abstract: The Selandian/Thanetian succession in the western Sirt Basin, Libya, is mainly composed of carbonates with lesser amounts of shale. They were deposited on a platform-homoclinal ramp with inner, mid and outer ramp facies, each with distinctive microfacies, ranging from mud-supported to grain-dominated carbonates. Two phases of dissolution, near-surface and burial, affected the late Paleocene succession. Marine and meteoric cements are minor, but early dolomite is locally developed. Burial compaction is widespread, associated with calcite and dolomite cements. The average $\delta^{13}C$ values in the Dahra and Zelten/Harash formations are 2.3‰ and 3.2‰, respectively. Both show no significant change up through the section, which suggests a stable carbon isotope composition of seawater through Selandian/Thanetian time, with little latter diagenetic alteration through organic matter decomposition. On the other hand, the $\delta^{18}O$ data show more negative values than most signatures reported for the Paleocene; this is largely the result of meteoric water influx and/or burial cementation-neomorphism under increasing temperature; this is supported by fluid-inclusion results. The best porosity is recorded in grainstones of the Dahra Formation, whereas, the Zelten and Harash formations have much lower porosity. The highest porosity is developed in bioclastic foraminiferal grainstone, bioclastic foraminiferal packstone-packstone/grainstone facies and, less important, foraminiferal nummulitic packstone. The porosity evolution in the Selandian/Thanetian succession is controlled by original depositional texture and subsequent diagenesis.

INTRODUCTION

The Sirt Basin (Fig. 1) developed through inter- and intra-plate movements resulting from the relative motion of the American, African and Eurasian plates during the opening of the Atlantic Ocean and the development of the Mediterranean on the foreland of the African Plate (Anketell, 1996). The Paleocene succession in the Sirt Basin is dominated for the most part by shallow-water carbonates deposited in restricted shallow-platform to open-marine environments. The carbonate platforms usually have a clearly definable ramp margin with more argillaceous sediments occurring in the deeper-water areas.

Diagenesis of carbonate sediments includes obvious processes such as cementation to produce limestones and dissolution to form cave systems but it also includes more subtle processes such as the development of microporosity and changes in trace element and isotopic signatures. Diagenetic changes can begin on the seafloor, even as the grains are still being moved around, or little may happen until significant burial when overburden pressure has increased, or pore-fluid chemistry has changed, so that reactions are then induced within the sediments (Tucker and Wright, 1990; Flügel and Munnecke, 2010; James and Jones, 2015). Major controls on the diagenesis of carbonates are the composition and mineralogy of the sediment, the pore-fluid chemistry and flow rates, geological history of the sediment in terms of sea-level change and prevailing climate, and burial and uplift (see Tucker, 1993).

After deposition and during their burial history, the Selandian/Thanetian carbonate rocks in the western Sirt Basin were affected by a range of diagenetic processes. These led to the development of porosity at particular levels which has resulted in these rocks becoming important reservoirs for hydrocarbons.

The main objectives of this paper are to describe and interpret the post-depositional processes that have affected the Paleocene succession in the western

[1] Libyan Petroleum Institute, Km 7, Gergarish Road, P. O. Box 6431, Tripoli, Libya.
[2] School of Earth Sciences, University of Bristol, Bristol BS8 3RW, UK.
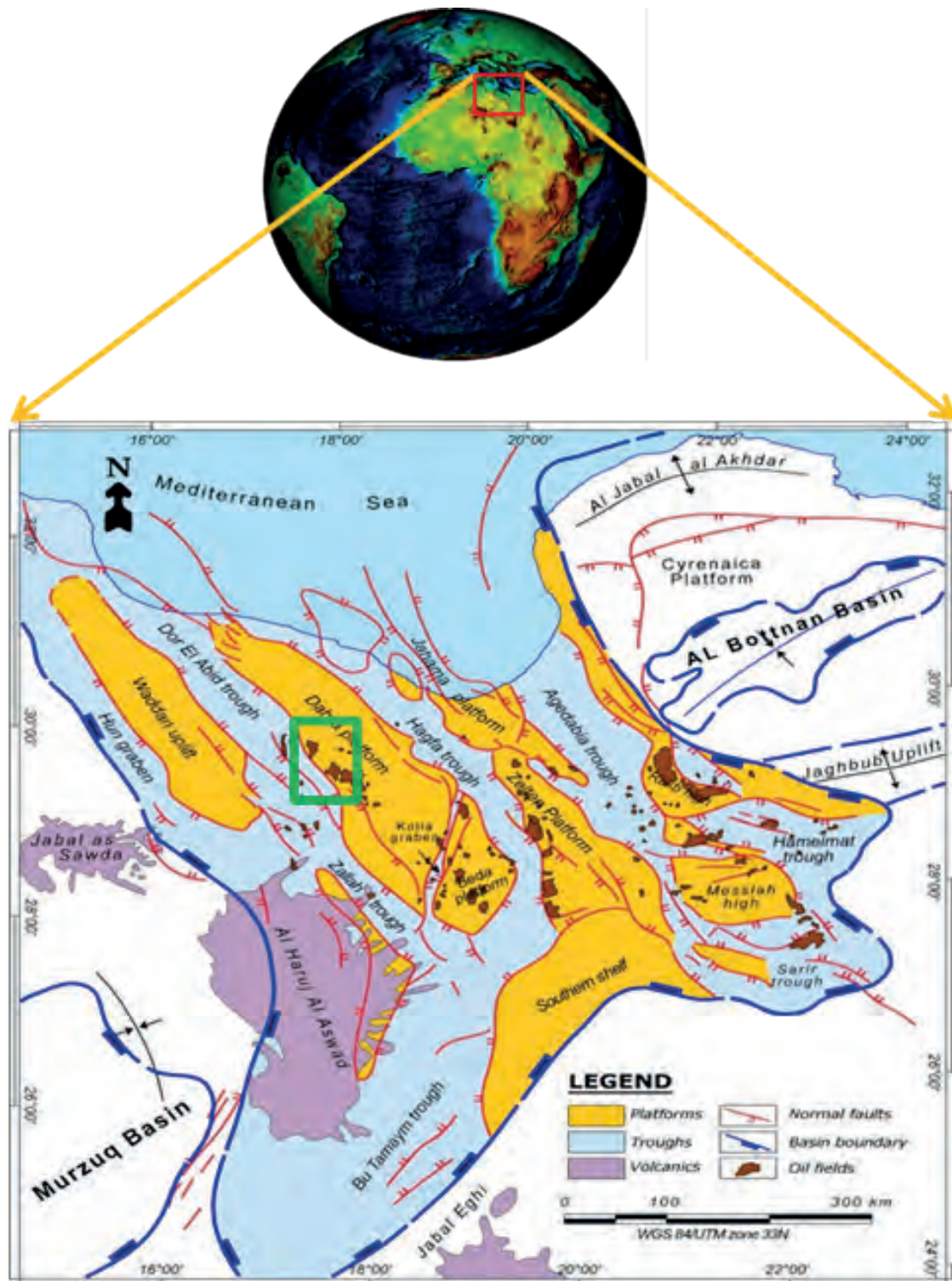
Fig. 1. Location map of the Sirt Basin and its structural elements. The study area in the western Sirt Basin are also shown (After Mouzoghi and Taleb, 1982, and Abadi, 2002).

Sirt Basin and to investigate the effect of these processes on the quality of the Selandian/Thanetian reservoirs. There are few studies of the diagenesis of lower Cenozoic carbonates in North Africa and these Paleocene limestones provide a useful case study of the paragenesis of lime-mud dominated carbonate

sediments to lithified limestones and dolomites and the wide range of textures developed.

MATERIALS AND METHODS

This study has been conducted through examination of Well-logs, core samples and thin-

sections (>170) from four wells in the Dahra Field on the Dahra Platform, western Sirt Basin (Fig. 1). The wells are a few kilometres apart and are located several kilometres back from the platform bounding fault. Around 900 feet (275m) of slabbed cores were logged. Thin-sections were stained or half-stained, using the method described by Adams *et al* (1984) adapted from Dickson (1965), and also examined with cathodoluminescence. Microfacies were classified according to Dunham (1962) and Embry and Klovan (1971).

Twenty samples were analysed using secondary electron mode and back-scattered mode of the SEM in the Department of Physics, Durham University and SEM Lab at the Libyan Petroleum Institute in Tripoli. Samples from two wells were analysed for carbon and oxygen stable isotope ratios at the University of Birmingham and fluid inclusions were examined by *Fluid Inclusion Technologies*, Oklahoma, USA. Porosity data were obtained from visual estimates of thin-sections.

GEOLOGICAL SETTING

A change from northward to westward motion of the African Plate in the Late Cretaceous promoted thinning of the cratonic lithosphere on its northern margin (Morgan, 1980, 1983). This was marked by major basin subsidence, reactivation of faults and crustal extension (Gumati and Nairn, 1991; Abdunaser and McCaffrey, 2014). On the northern foreland of the African Plate, subsidence and extensional fault reactivation continued intermittently into the Paleocene and Early Eocene, in response to the relative plate motions of the African, American and Eurasian plates during the opening of the central Atlantic and development of Tethys (Anketell, 1996; Abadi *et al*, 2008). Progressive erosion of younger sediments and subsequent episodes of block faulting resulted in placing the Palaeozoic and Mesozoic reservoirs in a high structural position with respect to thermally-mature Cretaceous source rocks that occupied the deeper portions of the Sirt Basin and its sub-basins.

The stratigraphic succession in the western Sirt Basin (Fig. 2) begins with the Hofra Sandstone of Cambro-Ordovician age overlain unconformably by Upper Cretaceous marine sediments, which, in turn, are succeeded by Cenozoic marine strata (Fig. 2). The Lower Cenozoic sediments are characterized by thick successions of shallow-marine carbonates and deeper-water shales. The latter were generally confined to low-energy zones in elongate basins (troughs) and they also blanketed platforms during phases of flooding and transgression. Carbonates were deposited across platforms and on ramp-type margins into the basins, with their facies controlled by water depth, topography and current-energy level (Gumati, 1982; Abdunaser, 2015).

The Paleocene strata in the Sirt Basin reach a thickness of 650m (~2000ft) on the platforms/horsts, where carbonates dominate, and up to 1000m (~3500ft) in the basinal areas, where the sediments are more muddy. The studied carbonate formations, according to Barr and Weegar (1972) are Dahra, Zelten and Harash. The Dahra, with a thickness of 140m (450ft), the Zelten, 65m (200ft) and the Harash, 45m (150ft). The Khalifa Shale, which separating the Dahra and Zelten formations on the platform is ~45m (150ft) thick.

RESULTS

Sedimentology
The Late Paleocene succession on the Dahra Platform is composed generally of limestone, dolomitic limestone, argillaceous limestone and shale (Fig. 2). There is no evidence from seismic for a shelf break nor from facies analysis for any slope resedimentation; thus, for the most part, the carbonates of the Dahra, Zelten and Harash formations were deposited on a broad flat platform passing to a homoclinal ramp dipping to the west, towards the basin. The platform bounding fault did not create any significant topography between platform and trough, but was responsible for differential subsidence. Macroscopic and microscopic investigations of this succession, which include details of grains, cements, microfabrics, micro-sedimentary structures and diagenetic features, have resulted in the recognition of five main facies and eleven microfacies within the Selandian/Thanetian carbonate succession (Table 1). The macrofacies are: 1) bioclastic foraminiferal packstone/grainstone, 2) foraminiferal bioclastic wackestone-wackestone/packstone, 3) dolomitic lime-mudstone, 4) bioclastic foraminiferal grainstone and 5) nummulitic foraminiferal packstone (Fig. 3). The first four facies have been recognised in the Dahra, Zelten and Harash Formations, whereas, the fifth one, nummulitic foraminiferal packstone only occurs within the Zelten and Harash formations.

The main carbonate grains within the Dahra Formation are rotaliids, miliolids, echinoderms,
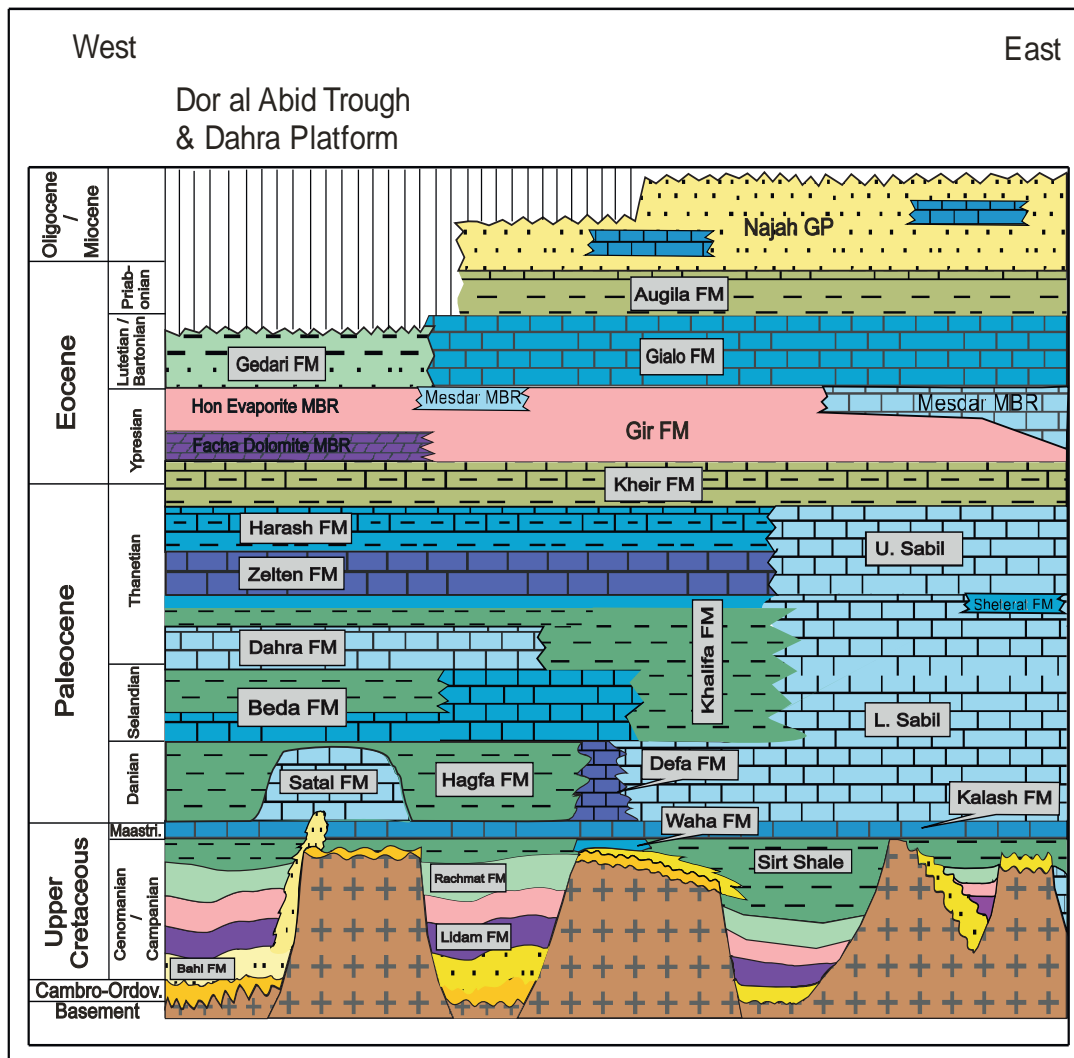
Fig. 2. Generalized stratigraphic and lithologic chart of the northern Sirt Basin. Compiled and modified by the author, 2012 (nomenclature after Barr and Weegar, 1972).

molluscs, ooids, peloids and green algae (Fig. 3A, D & E). Within the Dahra Formation carbonates, shallower to deeper-water facies and microfacies can be recognised, deposited in inner to outer parts of the homoclinal carbonate ramp. The core description, petrographic examination and geophysical logs indicate that there are no drastic changes in the facies and associated microfacies throughout the Dahra Formation; the main variation is in the amount of lime mud originally deposited. The Dahra was probably deposited under similar conditions throughout the east and west Dahra Field on the Dahra Platform, an area encompassing several 100 square kilometres.

The dominant bioclasts within the Zelten and Harash carbonates are benthic foraminifera, molluscan shells, nummulites, *Operculina,* bryozoans and echinoderm fragments (Fig. 3B & F).

A similar depositional setting to that of the Dahra Formation was probably re-established in the Zelten and Harash formations across the area, with local occurrences of nummulitic packstone instead of bioclastic grainstone as in the Dahra Formation, and the development of mainly wackestone-packstone.

Surprisingly, except for a generally regressive trend occurring in the late Thanetian, larger-scale transgressive-regressive (T-R) cycles cannot be detected within the Well-logs or cores examined. Thus, there is no correlation with the T-R patterns and eustatic sea-level changes which have been reported for this time-period elsewhere by Miller *et al* (2005) and Ruban *et al* (2010, 2012). The lack of T-R cycles could be a consequence of the data available (poor wireline-log response and/or key horizons missing in core) or a result of the longer-term relative sea-level changes not being recorded within the succession

Table.1. Facies and associated microfacies of the Dahra, Zelten and Harash Formations on the Dahra Platform.

Facies No.	Facies Name	Description	Microfacies	Depositional setting	Remarks
1	Bioclastic foraminiferal packstone-packstone/grainstone	Light yellowish grey to v. pale orange, locally mottled, m. sorted with abundant benthic forams and shell fragments of different bioclasts.	Bioclastic foraminiferal packstone/grainstone	Inner ramp (lagoon)	Similar to SMF 10 of Flügel (2004)
		Levels of echinoderms and/or molluscan shells in wells 7 & 8. Locally dolomitic and bioturbated. Slightly argillaceous with sporadic development of stylolites and PDS. Local concentration of iron minerals, particularly in wells 8&10. Overall porosity is fair to good.	Dolomitic bioturbated bioclastic packstone	Inner ramp (lagoon)	Similar to RMF 7 (SMF 10) of Flügel (2004)
2	Foraminiferal bioclastic wackestone/ packstone	Mainly light grey, locally light yellowish brown or mottled, m. sorted with rotaliids, miliolids, echinoderm fragments and peloids. Planktic forams, red algae, ostracoda and peloids are scattered throughout. Locally dolomitic, bioturbated and slightly argillaceous. Compaction features locally developed, particularly in wells 10 & 8. Iron minerals developed at few intervals in wells 9 & 8. Porosity is poor to fair.	Bioclastic wackestone/packstone	Inner ramp (lagoon)	Corresponds to RMF 20 or SMF 10 of Flügel (2004)
			Planktic foraminferal wackestone	Mid ramp	Corresponds to RMF 5or SMF 3 of Flügel (2004)
			Dolomitic bioturbated wackestone/packston	Inner ramp (lagoon)	Similar to SMF 10 of Flügel (2004)
3	Dolomitic mudstone	Dolomitic limestone, light yellowish grey to mottled, mod-well sorted with very scattered benthic forams, peloids and gastropod molds. Bored and/ or bioturbated. Locally chalky and/or argillaceous. Porosity is fair to good.	Dolo lime-mudstone	Inner ramp (lagoon)	Corresponds to RMF 19 of Flügel (2004)
4	Bioclastic grainstone	Light grey, light yellowish brown to v. pale orange, m. sorted. Benthic forams, green algae and echinoderms are common with scattered peloids, molluscan shells, intraclasts and bryozoans. Locally dolomitic, bioturbated, and slightly argillaceous. PDS and stylolites. Fe-minerals and syn-sedimentary compaction features in well 10. Porosity is good to very good.	Bioclastic foraminiferal grainstone	Inner to mid ramp. Possibly carbonate shoal/ lagoon with an open circulation (back bank)	Corresponds to SMF 10 or 11 of Flügel (2004)
5	Foraminiferal packstone	Light yellowish - light olive grey, hard, poorly-m. sorted, with common nummulites and common to scattered *Assilina*, operculina, bryozoans, echinoderms, molluscan shells and red algae. Slightly argillaceous and bioturbated. Porosity is generally good to v. good.	Nummulitic foraminiferal packstone	Middle ramp, probably foraminiferal bank	Similar to SMF 18 of Flügel (2004)

of the partly-restricted, quite lime-mud dominated, Sirt Basin during the Thanetian. On a global scale, the Late Selandian has been interpreted as a period of relative sea-level stability, and relatively stable climate and tectonics, conditions which persisted into the Early–Middle Thanetian (Ruban *et al*, 2010, 2012). However, higher-frequency metre-scale cycles (2-10 feet in thickness) can be recognised within the Dahra Formation from core, although some are quite subtle (Fig. 4).

Diagenesis Processes and products of the Selandian/Thanetian carbonates

After deposition, the Selandian/Thanetian carbonates in the western Sirt Basin were affected by various diagenetic processes during their burial history, which for the most part was one of continuous increasing overburden. The top of the Paleocene strata on the Dahra platform is currently at a depth of ~1000m and in the adjacent trough at ~1500m. These strata are overlain by the Eocene
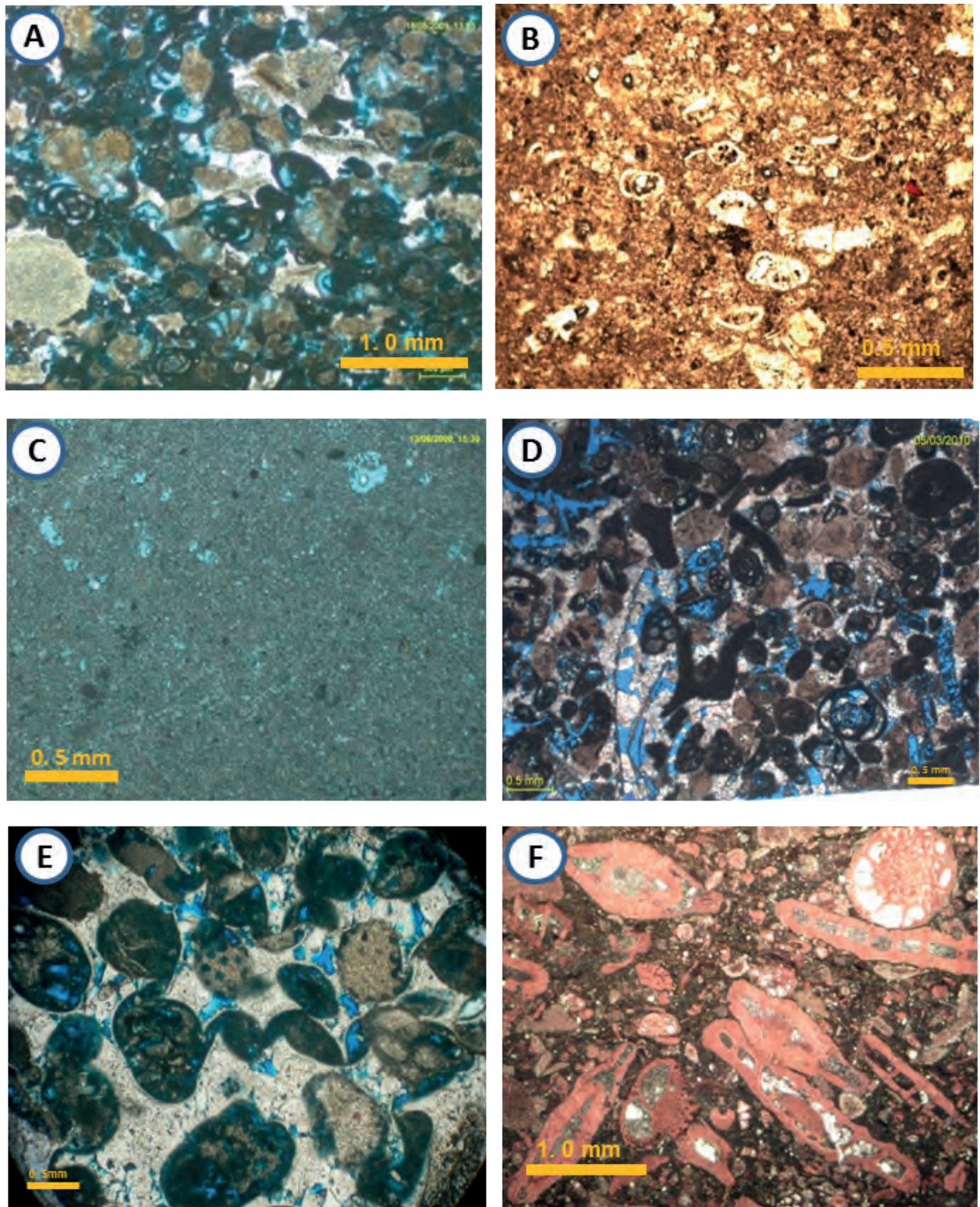
Fig. 3. Macrofacies of the Selandian/Thanetian carbonates in the Dahra Field. A) Bioclastic foraminiferal packstone/grainstone (Dahra Fm, Well no. 8); B) Foraminiferal bioclastic wackestone-wackestone/packstone (Harash Fm, Well no. 9); C) Dolomitic lime-mudstone (Dahra Fm, Well no. 8); D & E) Bioclastic foraminiferal grainstone (Dahra Fm, Well no. 9) and F) Nummulitic foraminiferal packstone (Harash Fm, Well no. 10).
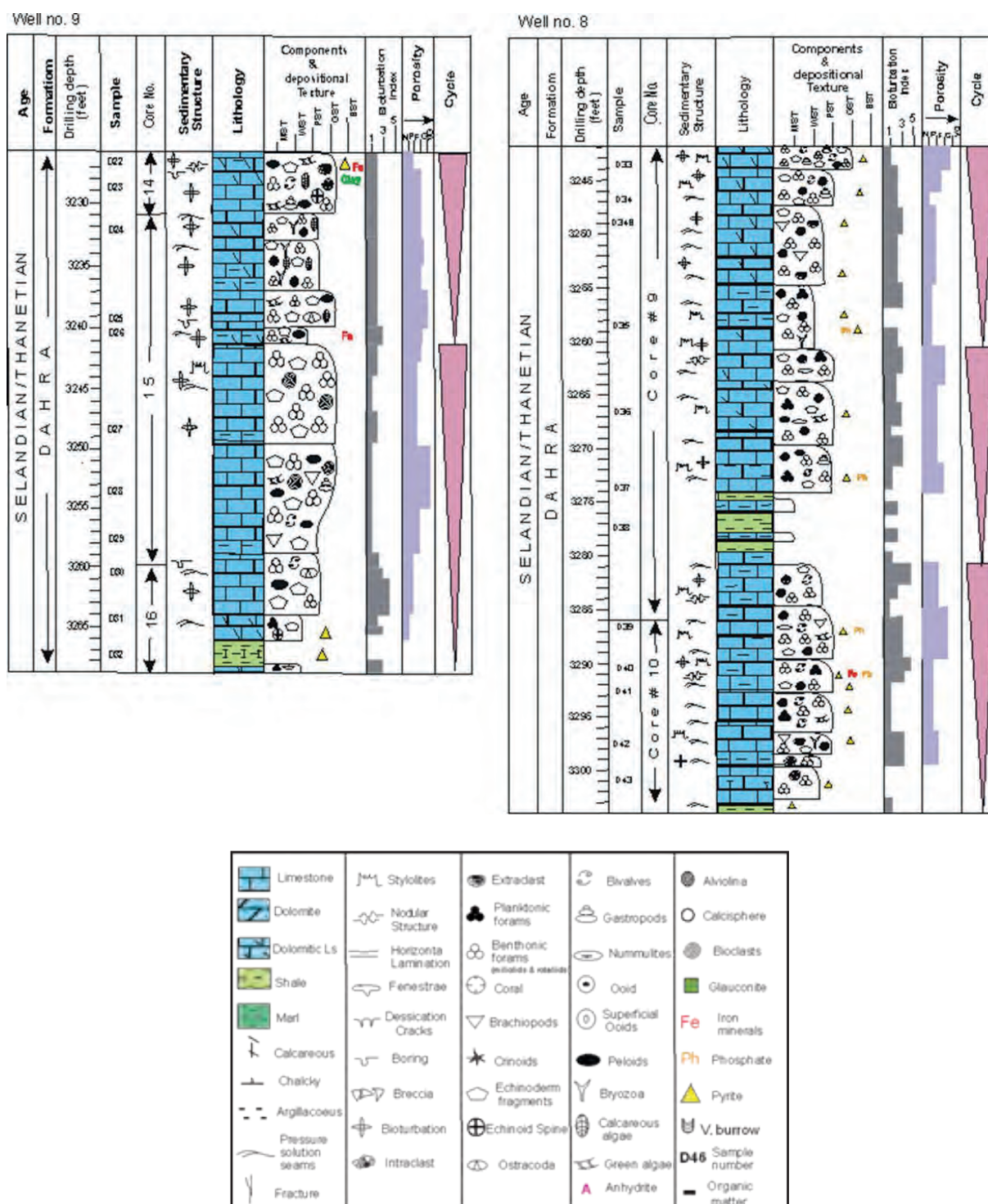
Fig. 4. Sedimentological core logs showing fairly Well-defined carbonate cycles within the Dahra Formation. Well no. 8 and Well no. 9.

Kheir and Gir formations to the present-day surface, although farther east Oligo-Miocene sediments are present too (Fig. 2). The muddy Kheir Formation is a seal to reservoirs in the Harash carbonates. Burial has been interpreted by Van der Meer and Cloetingh (1996) as near constant until the Late-Eocene, after

which there was some uplift and erosion. Abadi *et al* (2008) on the other hand, suggested significant uplift and erosion in the Late Eocene-Oligocene, followed by subsidence to the current depth. The geothermal gradient in the Sirt Basin, according to Hallett (2002), averages 25.5ºC/km, and the surface

temperature is about 30⁰C (Gumati and Schamel, 1988). Three diagenetic environments have been documented: marine, meteoric and burial; each has its own characteristic features and products.

Marine Diagenesis: Early marine diagenetic processes affecting the Selandian/Thanetian carbonates are represented by local marine cementation and lithification, boring and micritisation of bioclasts. Marine cements are recognised through their first generation occurrence as thin isopachous fringes around grains (Fig.5D). The crystals are acicular to fibrous and reach up to 50 microns in length. In some cases they have a slight pale brown colour relative to later, coarser clear calcite cement. Where there has been mechanical compaction of the limestones during shallow burial, the earlier precipitation of this cement-type is revealed (Fig. 3E). In more muddy facies, local evidence of early lithification is provided by borings which are recorded at several levels in cores of Dahra Platform sediments in the Dahra and Zelten formations. A hardground surface from Well 10 in the Dahra Formation, with borings up to 1mm in diameter, can be observed cutting both grains and substrate (Fig. 5A). The sediment here is a dolomitic packstone with a high concentration of pyrite, glauconite and phosphatic mineral grains.

Hardgrounds are typically developed in areas of slow sedimentation and high current activity at or just below the seafloor (Tucker and Wright, 1990; James and Jones, 2015). The borings are likely produced by polychaete annelids; they are too small to be formed by lithophagid-type bivalves, and they do not have the scalloped margin typical of clinoid borings.

Although micritisation has affected some grains in the Dahra, Zelten and Harash formations, overall it is a fairly rare feature. Repeated boring and filling of holes in a bioclast may result in the formation of a micrite envelope of irregular thickness, and eventually lead to totally micritised grains (peloids) that are smaller than associated skeletal grains. Micritised grains are characterized by an irregular shape, structureless nature, and they mostly range in size from 100 to 300μm (Figs 3D & 5B). Micritisation through microbial alteration is the origin of most peloids, but there are some of probable faecal origin, having a smoother spherical-ovoid shape and smaller size, occurring throughout the succession.

According to Volery *et al* (2009), marine microbial micritisation can be important in generating microporosity within grains. Micritic envelopes formed through endolithic cyanobacteria can be used as a depth criterion, indicating deposition within the photic zone, less than 100-200m (Zeef and Perkins, 1979). Micritisation is an early diagenetic event taking place within the marine phreatic environment, generally in more stagnant, low-energy areas, near or at the sediment/water interface (Longman, 1980). Flügel and Munnecke (2010) noted that microboring endolithic organisms are also found in deeper water. Micritisation is a common feature in Tertiary-Mesozoic shallow-water carbonates (e.g. Madden and Wilson, 2013; Elton *et al*, 2015).

Thus, overall, apart from micritisation, marine diagenetic processes of cementation and lithification are not extensive, occurring only at discrete horizons.

Meteoric Diagenesis: The effects of meteoric diagenesis, manifested in early calcite cementation and grain dissolution as a result of subaerial exposure, can be discerned at several levels within the Paleocene carbonates, but again, these early processes are not widespread.

Calcite cement of meteoric origin occurs in the form of localised to patchy calcite spar crystals to isopachous grain coatings, mainly in the bioclastic foraminiferal packstone-packstone/grainstone and bioclastic foraminiferal grainstone facies. In porous grainy facies, calcite crystals are irregularly distributed between grains and occur within molds resulting from dissolution of bioclasts (Fig. 3D). Rarely a meniscus arrangement of crystals can be discerned, as in occurrences of bioclastic foraminiferal grainstone of Well no. 7 in the Dahra Formation (Fig. 5E). Much porosity is still present (Fig. 3D). Isopachous coatings of bladed to stubby, clear calcite crystals oriented perpendicular to the substrate, mainly occur on the outer, rarely on the inner, walls of both non-skeletal and skeletal grains, particularly foraminifera. The features of this type of cement, notably the non-fibrous bladed fabric, indicate that it is low Mg-calcite of probable meteoric phreatic origin. Meteoric vadose cementation is indicated by meniscus texture, although it can also be formed through microbial activities in other environments (Hillgärtner *et al*, 2001).

Syntaxial overgrowth calcite cement has grown on echinoderm fragments mainly within the grain-dominated facies in the Dahra and Zelten, and less commonly, within the Harash Formation. It rarely occurs in wackestone-packstone facies as a result of the small amount of original pore-space. This cement is commonly a large single crystal developed
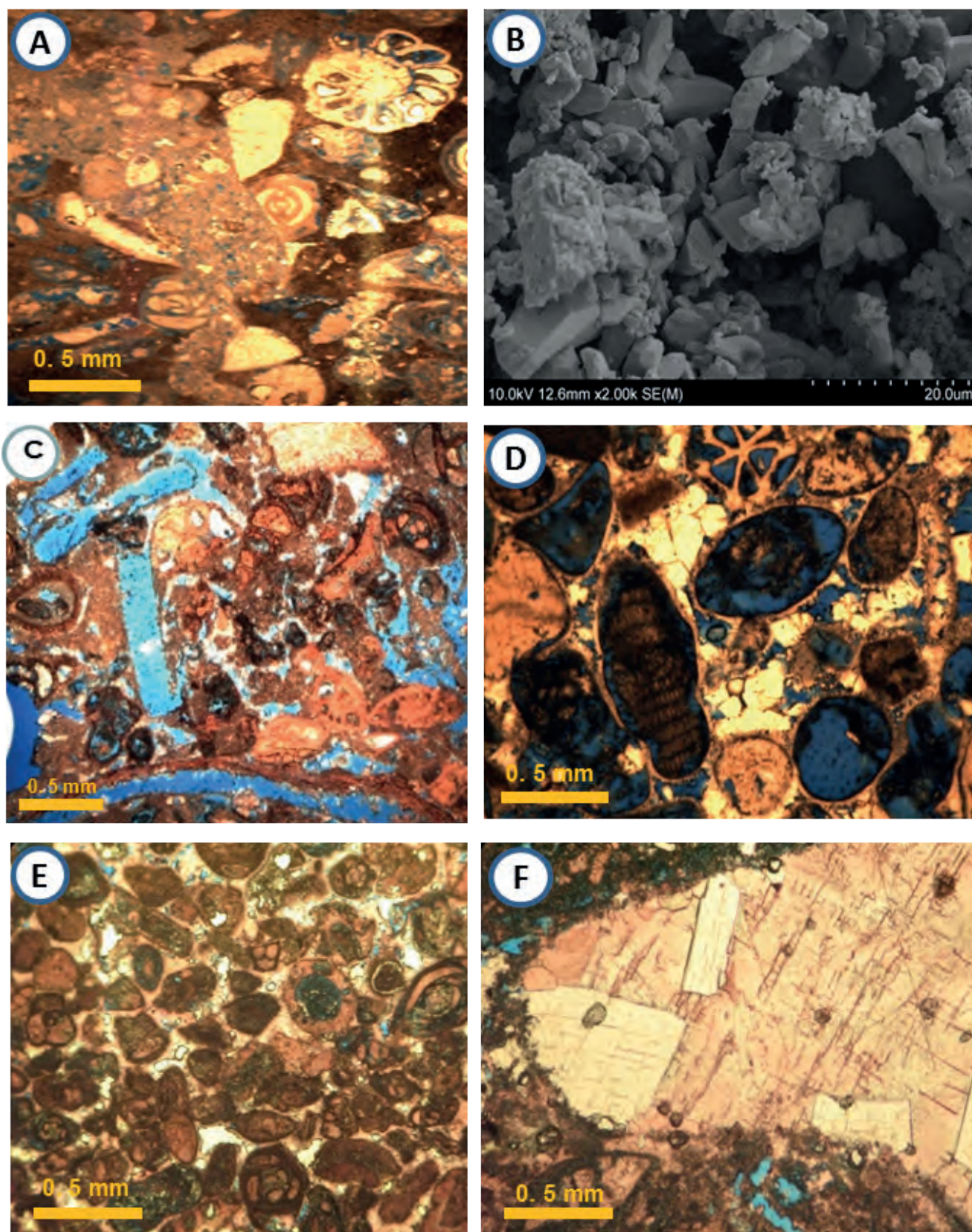
Fig. 5. A) Possible hardground surface, where boring has cut grains and the matrix in the Dahra Fm in Well no.10. B) SEM image of micritized grains in the Dahra Fm in Well no. 9. C) Dissolution (mainly molds) porosity in the Dahra Fm, Well no.10. D) Isopachous calcite cement around bioclasts, followed by equant sparry calcite. Dahra Fm, Well no.10. E) Meniscus vadose cement, Dahra Fm, Well no. 7. F) Very coarse Fe-free calcite cement occludes secondary porosity in bioclastic foraminiferal P-P/G. Zelten Fm, Well no. 7.
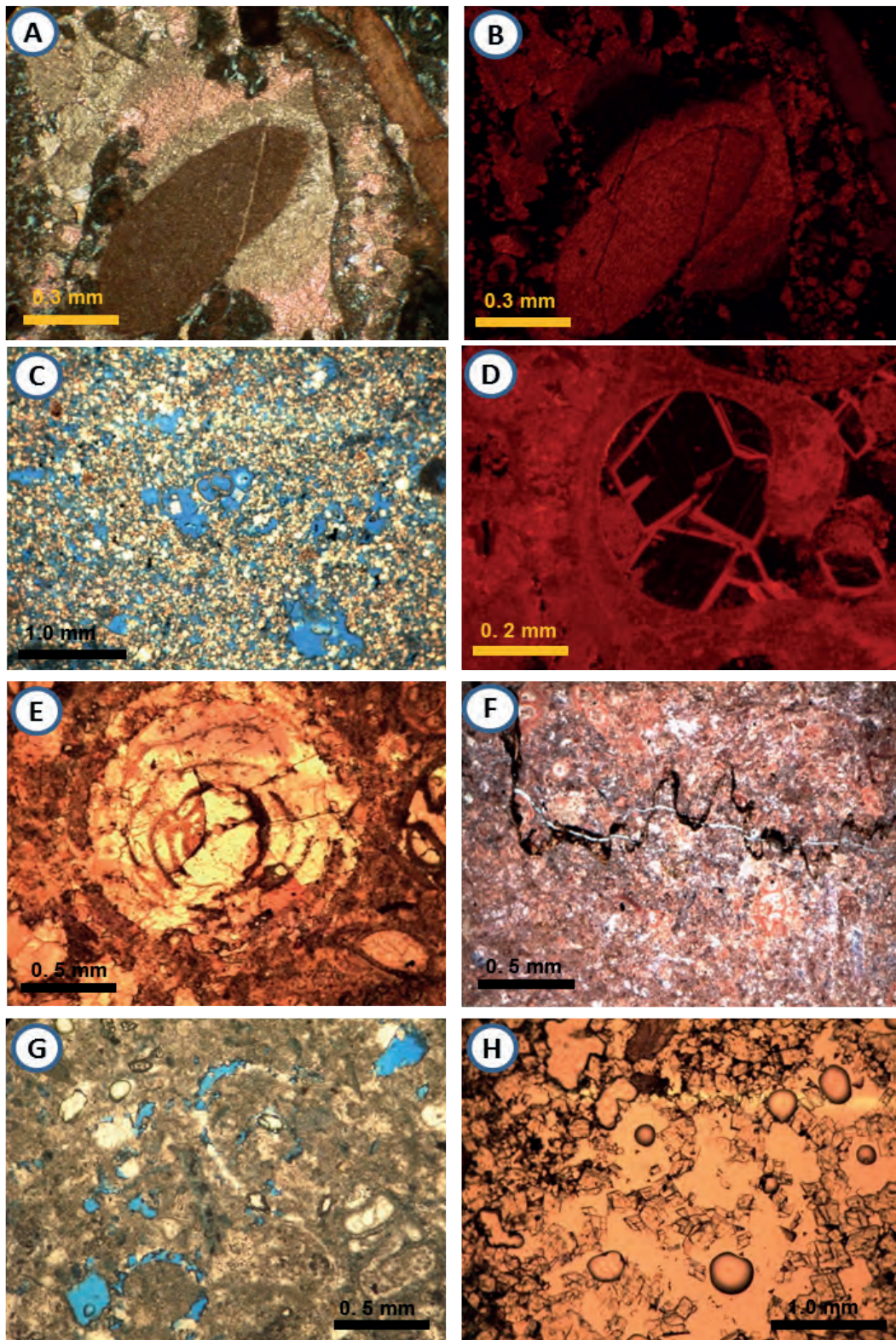
Fig. 6. A & B) Syntaxial rim cement around echinoderm followed by equant calcite cement (pinkish). The CL photo shows that both echinoderm and overgrowth have the same intensity, i.e. light brown to dull luminescence, whereas the equant calcite cement is non-luminescent. Dahra Fm, Well no. 8. C) Very fine-finely crystalline dolomite in dolomitic lime-mudstone facies. Note good intercrystalline and moldic porosity. Dahra Fm, Well no. 8. D) Medium crystalline dolomite filling intragranular porosity. Note the two luminescent characters of dolomite crystals. Dahra Fm, Well no. 9. E) Replacement of Alveolina foraminifera by dolomite and coarse calcite with a retentive fabric, Zelten Fm, Well no.9. F) Microstylolite cuts across matrix, grains and fracture. Dahra Fm, Well no.8. G) Rhomb-shaped pores in bioclastic packstone, Zelten Fm. Well no. 7. H) Extremely porous dolomite resulting from effects of burial dissolution of dolomite and relic limestone. Dahra Fm., Well no. 10.

on echinoid fragments in optical continuity with the grain. Of note is that the overgrowths commonly show two stages of growth, based on staining and cathodoluminescence. The calcite of the inner part of the overgrowth remains unstained whereas, the outer part is pink (Fig. 6A); with cathodoluminescence both echinoderm and the inner part of the growth have the same intensity, i.e. light brown to dull luminescence, whereas, the outer part has no luminescence (Fig. 6B). This pattern could indicate that the inner part has an elevated Mn^{2+} and low Fe^{2+} content, whereas, the outer part has lower Mn^{2+}. This could be the result of the early part being precipitated in a shallow-burial suboxic meteoric setting, and the later part being more of a burial precipitate (Tucker and Wright, 1990).

Post-Compaction Calcite Cementation: Equant sparry calcite cement occurs in most of the grainstone and packstone facies. It may occlude pore space as the second generation cement, following the early marine-meteoric cement, but in many cases there is still porosity present. This sparry calcite consists of clear, equant to elongate crystals, which are locally ferroan.

A drusy mosaic is common, where it occurs as a pore or biomold-filling cement (Fig. 3D). The crystals vary in size from commonly less than 50μm in diameter, locally reaching 200μm at the pore centre. Under cathodoluminescence, the cement crystals are largely non-luminescent to dull (weakly) luminescent, with very thin bright zones towards the outer part of some crystals. This could indicate Fe-rich fluids and the incorporation of Fe^{2+} during the early stage of crystal growth. A change in pore-fluid chemistry to suboxic with the incorporation of manganese into the crystal lattice has probably resulted in the precipitation of the bright outer zones. As stated by Have and Heijnen (1985), the zonation of the carbonate crystals is a reflection of fluctuations in the chemistry of the pore-fluids, but also of changes in the rate of crystal growth. The source of iron may have been clay minerals brought into the environment by continental run-off. A small percentage of terrestrial argillaceous material is finely distributed within the Paleocene carbonates and forms bed-partings and thin layers.

Coarse blocky calcite cement, typically ferroan, with crystals 250-600μm in diameter, in some cases over 1000μm, occurs in the grain-supported facies of the Dahra, Zelten and Harash formations. It usually fills vuggy, moldic, fracture and intergranular porosities and developed as clear, coarse subhedral to euhedral crystals with fairly straight crystal boundaries along with the local occurrence of fluid-inclusions (Figs. 5F & 6E).

Dolomitization: The replacement origin for much of the dolomite is indicated by the presence of ghosts of precursor grains and biomoldic pores, along with the occurrence of completely micritised grains which resisted, to some extent, the dolomitization.

Two types of dolomite are recognised in the Paleocene carbonates: 1) an early fine crystalline dolomite (crystals <20μm) which has mainly replaced the matrix in lime-mudstone microfacies of the Dahra Formation (Fig. 3C) ; 2) a medium to coarsely crystalline later dolomite (crystals 100-300μm) occurring as a pore-filling cement mainly in the Dahra Formation and less well developed in the Zelten and Harash formations.

The fine dolomite commonly has a loosely packed subhedral to anhedral crystal mosaic, with a sucrosic texture and good intercrystalline porosity (Fig. 6C). In the Dahra Formation, particularly in Well no. 9, the dolomite is mostly tightly packed and displays hypidiotopic (planar-s) to xenotopic (non-planar) mosaics. It commonly shows fairly good preservation of the original texture and poor intercrystalline porosity. In Wells no. 8 and 10, however, a better preservation of intercrystalline porosity is observed. In Zelten and Harash formations the very finely to medium crystalline dolomite occurs generally as isolated, scattered euhedral to subhedral crystals in the relatively fine-grained matrix of the wackestone/packstone facies.

The local association of this fine dolomite with peritidal features (fenestrae, desiccation cracks, rare evaporite molds, and rootlet structures), particularly in the dolomitic bioturbated wackestone/packstone microfacies, suggests an early diagenetic origin (i.e. eogenetic dolomite). The general lack of evidence for evaporites suggests dolomitization through circulating seawater rather than reflux of hypersaline brines.

Burrowed intervals have commonly been dolomitised preferentially and subjected to a higher intensity of compaction, which in several cases has resulted in the formation of a vaguely bedded fabric, making identification of the original depositional texture (wackestone versus packstone) difficult. Differential dolomitization of the burrowed intervals seems to be controlled by the grain-type (mineralogy) and grain-size of the burrow fill; i.e. many burrows

are completely dolomitised whereas, others are less dolomitic. The finer grain-size of burrow fills as compared with the micritic matrix may be one factor controlling the often observed selective dolomitization of burrow fills (Zenger, 1992). Bio-retexturing can control diagenetic processes because it can selectively increases individual bed permeability where coarse burrow back-filling is dominant. On the other hand, locally it can inhibit early sea-floor cementation by admixing micritic sediment into grain-support fabrics. Feeding, burrowing and irrigation increase solute transport and solid-phase reaction rates, thus leading to rapid carbonate dissolution-replacement (Green and Aller, 1992; Gingas *et al*, 2004; Rameil, 2008).

The medium to coarsely crystalline dolomite (100-300μm) usually occurs as a pore-lining and/or pore-filling cement and thus, contributes to reducing, and more commonly occluding, the intergranular, intragranular, moldic, vuggy and fracture porosities. It is characterised by single, usually non-ferroan, euhedral to subhedral crystals, locally with curved crystal faces; it may display some Cl-zonation (Fig. 6D).

In the Zelten/Harash formations coarse dolomite is commonly associated with the late, coarse, Fe-free calcite cement and together they plug remaining porosity (Fig. 5F). The dolomite rhombs are mostly weakly to non-luminescent, with a thin outer zone of bright orange colour (Fig. 6D). This pattern is probably reflecting a change in pore-water chemistry from iron-rich to iron-poor/Mn-rich, in response to a change of redox conditions (Tucker and Wright, 1990). It has been suggested that the amount of manganese necessary to induce bright luminescence in carbonates ranges from 80 to 100ppm (Machel and Burton, 1991). Some of these larger dolomites show undulose extinction, a strong, slightly curved cleavage and so are of the saddle/ baroque type.

Authigenic Clay Minerals: Apart from clay within more argillaceous limestone facies and thin clay layers and beds, clay minerals of probable authigenic origin have developed within the limestones, notably within wackestone-packstone intervals in the Dahra Formation. Minerals recognised on the basis of good-crystal form under SEM and EDS analysis include kaolinite, chlorite, illite and probably mixed-layer illite/smectite. They have been precipitated within intergranular cavities, and between calcite spar crystals (Fig. 7). In some cases the clay minerals have occluded the porosity.

Authigenic clay minerals are relatively rare in limestones compared to sandstones, although they do occur in fractures and vugs and along stylolites (e.g. El Hefnawi *et al*, 2010). As in sandstones, the clays can have a significant effect on porosity and permeability.

Compaction and Fracturing: Macroscopic and microscopic examination of the rocks under investigation revealed that they have been subjected locally to considerable compaction (physical and chemical) and to less significant fracturing.

The effects of mechanical compaction are found most commonly in grains that were affected by boring, leaching, or other grain-weakening processes during marine or meteoric diagenesis. Mechanical compaction in which some bioclasts, in particular foraminiferal tests, were crushed and/or flattened were observed in the Dahra, Zelten and Harash formations. Closer packing and deformation features are more common in the mud-supported facies. Fracturing of grains (mainly bivalve shells) and substrate is widely developed in the packstone/grainstone facies of the Dahra Formation. Many superficial ooids and coated grains show breakage and cracking along the lamellae and as a result the cortical layer or an early isopachous cement coating has spalled off, and intragranular secondary porosity has been produced (Fig. 5D). Mechanical compaction, which was probably accompanied by, or occurred just after, partial leaching of the grains, has produced deformed ooids. Some show the 'elephant-parade' (or 'trunk-to-tail') fabric of Folk and Lynch (2001), particularly in the middle interval of the Dahra Formation (Fig. 3E). Later equant calcite cement was precipitated within the cavities developed in the ooids and between compacted grains, although in many cases a fair amount of porosity has remained unfilled. Most of these mechanical compaction features would have occurred at shallow burial depths where the Upper Paleocene carbonates were semi-indurated by the early cement crusts of marine or meteoric origin. Indeed, the presence of the cement fringes around the grains, locally spalled off, alongside the patchy leaching of the grains themselves, suggests some mineralogical difference between the two (grains and cement), and leaching through meteoric water influx. The local patchy sparry calcite cement occurring within and between the ooids could be precipitated from meteoric water too, post-compaction, in the shallow-burial realm. Tucker (Pers. Commu.)
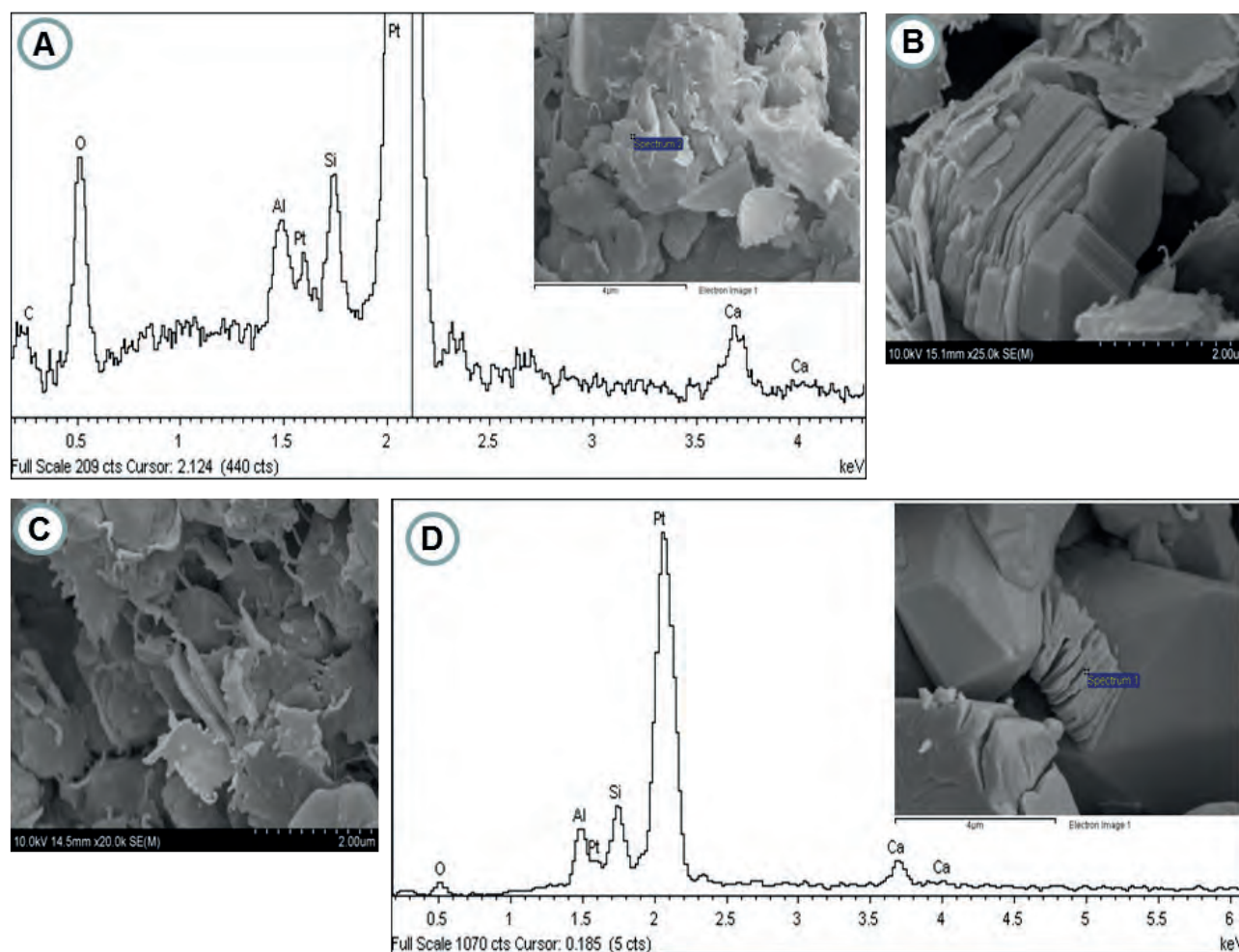
Fig. 7. SEM analysis of the clay minerals identified within the Paleocene succession. A: Smectite mineral between micrite crystals. The chemical composition of this smectite is shown in the EDS spectra. B: Kaolinite (book sheets) plugging intercrystalline porosity in bioclastic wackestone/packstone facies. (A&B) from the Dahra Fm, Well no. 9. C & D: Illite and kaolinite minerals from the Dahra Formation in Well no. 8 at depths of 3185 ft (970 m), and 3119 ft (950 m), respectively.

has noted mechanical compaction in Pleistocene aeolianites, which had less than 100m of overburden.

Networks of microfractures that interconnect different types of porosity have been observed in most of the Paleocene carbonate facies. They have been recorded chiefly in the Dahra and Harash formations, with fewer in the Zelten Formation. They are commonly open and in some cases crossed by stylolites (Fig. 6F). Stronger fractures and minor faults have been encountered in core, and a possible strike-slip fault with vague striations was observed in the lower interval of the Harash Formation in Well no. 9. Two intervals, ~ 1 metre thick, of fractured limestone were noted in the Dahra Formation at Wells no. 8 and 10.

Dissolution seams occur at many intervals in the studied rocks, particularly in the argillaceous limestone facies. They display fairly smooth, undulose seams of insoluble residue and usually pass between and around grains. Dissolution seams tend to be common in more argillaceous limestones, and develop preferentially along the clay layers or at the junctions of clay-rich and clay-poor limestones. Sutured contacts between carbonate grains have resulted in the formation of stylo-nodular structure or stylo-breccia fabric (cf. Logan and Semeniuk, 1976) at several intervals, especially in the Dahra Formation. In terms of petroleum reservoir quality, the pressure dissolution processes lead to a strong reduction in bulk rock-volume with a resultant loss in porosity caused by the occlusion of pores by late diagenetic cement (Wong and Oldershaw, 1981; Swati *et al*, 2014).

Stylolitization normally contributes to bulk volume reduction, resulting in a marked drop in the original thickness of carbonate units (Flügel and Munnecke, 2010). A variety of stylolite types is developed including large amplitude, small

amplitude and swarm types, and they usually cross-cut grains, matrix and cements. In some cases they are associated with fractures (Fig. 6F). They are commonly filled by insoluble residue (probably clay), which was derived from limestone dissolution, and pyrite. Locally, particularly in the Dahra, bitumen and finely crystalline dolomite are also present with the insoluble residue. Stylolites can be significant in the creation of permeability barriers within reservoir facies (e.g. Ebnor *et al*., 2010; Rustichelli *et al*, 2015).

In addition, there are other minor diagenetic events recognized in the Late Paleocene succession, which include precipitation of authigenic pyrite, glauconite, hematite, phosphate and anhydrite.

Burial Dissolution: Evidence of dissolution, both early and late, is widespread in the Paleocene carbonates, with at least two major phases of dissolution: one near-surface and the other later, during burial. The first phase caused the dissolution of the original aragonitic, and probably high Mg-calcite grains together with some matrix. This has resulted in the formation of moldic and vuggy secondary porosity which is present in most of the defined facies of the Dahra, Zelten and Harash formations, but to different degrees (Fig. 5C, D). Much of this porosity has subsequently been occluded, partly or completely, by equant non-ferroan, locally ferroan, calcite or dolomite cements.

The relatively early phase of dissolution probably occurred in the upper part of the meteoric phreatic environment, where the meteoric waters are strongly undersaturated with respect to the metastable carbonate species. Meteoric diagenesis starts with the loss of magnesium from high-Mg calcite followed by the gradual disappearance of aragonite and the replacement of aragonite by calcite (Flügel and Munnecke, 2010). Although dissolution is a major process in near-surface, meteoric, diagenetic environments, it can also take place on the sea-floor and during deep burial (Tucker and Wright, 1990).

The second phase of dissolution has caused the partial to total dissolution of the medium to coarsely crystalline void-filling dolomites. As a result, moldic porosity or dedolomite porosity has been developed, notably in the Dahra and Zelten formations (Fig. 6G, H). This type of porosity has probably been formed by leaching of dolomite crystals at intermediate to deep burial depths, probably through the presence of strong acidic formation waters, rather than early during subaerial exposure and dissolution by karst waters (Nader *et al*, 2008). The dissolution of

carbonates in a deep burial setting is attributed to the development of pore waters with high pCO_2 formed during the thermal decarboxylation of organic matter or to sulphate reduction (Mazzulo and Harris, 1992). However, there has been much discussion over the significance of burial dissolution in recent years, with the consensus being that it is a significant process and may lead to much porosity creation (see Ehrenberger *et al*, 2012; Wright and Harris 2013; Van Berk *et al*, 2015; Barnett et al. 2015; Chandra *et al*, 2015).

Isotope Geochemistry of the Selandian/Thanetian Carbonates

In general, the original carbon isotopic composition of a marine carbonate sediment is more resistant to diagenetic alteration (unless there is significant organic matter present undergoing decomposition), compared to its original oxygen isotopic signature. The latter is susceptible to change resulting from meteoric diagenesis and changes in pore-fluid isotopic composition, and increased temperature through burial, leading to cementation-neomorphism and generally more negative $\delta^{18}O$ values of carbonate. In view of the generally fine grain-size of the Paleocene carbonates, including the grainstones, whole rock samples were analysed although the least grainy samples were chosen where possible, since the objective was to determine the original variation, stratigraphy and the degree of diagenetic alteration.

Carbon Isotope Stratigraphy: The Dahra Formation shows a quite narrow range in $\delta^{13}C$ values, in Well no. 8, between +1.0‰ and +3.5‰ (except for one likely 'rogue' data point of -1.8‰) and an average value of +2.16‰. The $\delta^{13}C$ values in the Dahra in Well no. 9 range between +1.2‰ and +3.1‰, with an average of +2.44‰ (Figs. 8 &9).

Plotted stratigraphically, the carbon isotope values of the two Wells in the Dahra Formation show no significant change up through the section (apart from the 'rogue' point near the top of Well no. 8 (Fig. 8). This suggests that $\delta^{13}C$ seawater did not change significantly through the period of deposition, and that there was little diagenetic alteration of the $\delta^{13}C$ values, as through the effects of organic matter decomposition in a soil zone during subaerial exposure or during burial.

The carbon isotope values of the Zelten and Harash formations in the east and west Dahra fields are quite similar and confined to a narrow range between +2.22‰ to +3.89‰. The average $\delta^{13}C$ value
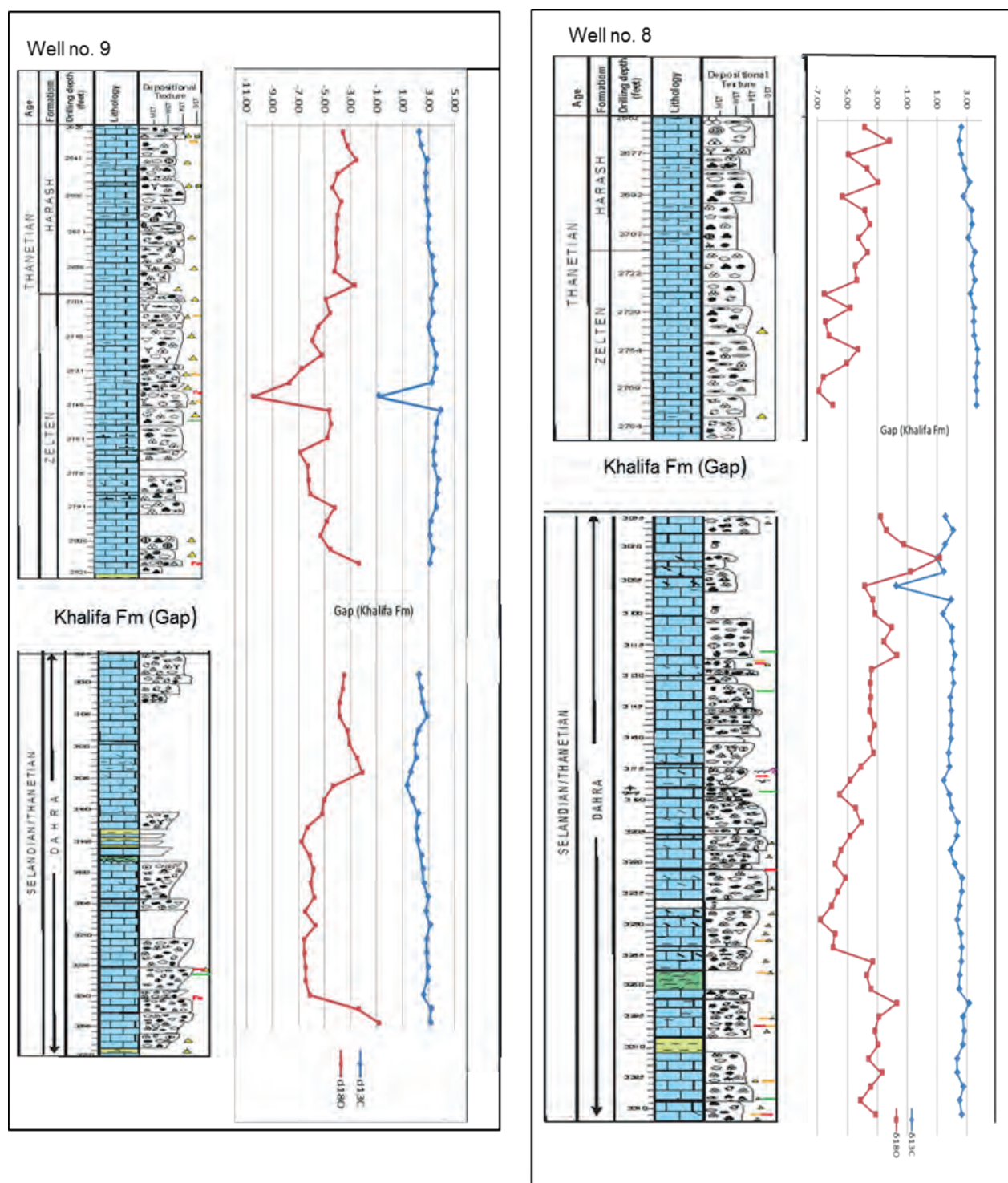
Fig. 8. Carbon versus oxygen isotopes of the studied Selandian/Thanetian succession (Dahra, Zelten and Harash Formations in Wells no. 8 & 9 on the Dahra Platform.

for Well no. 8 is 3.23‰ and for Well no. 9 is 3.17‰. Compared to the Dahra Formation, these averages are a little more positive. Plotted stratigraphically, the carbon isotope stratigraphy for the Zelten-Harash strata shows little change up-section, in both Wells 8 and 9, except for one likely rogue point of -1 ‰ in Well 9. Again this suggests a stable carbon isotope

composition of seawater, in this case through much of Thanetian time, with no significant diagenetic alteration.

During the Upper Paleocene the $\delta^{13}C$ signature of marine carbonate is generally between +1 and +2, before the sharp excursion to less positive values of +1 to 0 ‰ or low negative values at the Paleocene-

Eocene Thermal Maximum (PETM) (e.g. Koch *et al*, 2003; Zachos *et al*, 2006). There is also a sharp negative excursion in $\delta^{13}C$ within the late Selandian, which has been referred to as the Mid-Paleocene Biotic Event (MPBE, Pujalte *et al*, 2003; Bernaola *et al*, 2009). The carbon isotope stratigraphy for the Upper Paleocene on the Dahra Platform in the Sirt Basin presented here (Fig. 8) does not show any clear excursions. The two negative data-points, one in Well 9 and one in Well 8, are not present in both wells at the same horizon, hence they are interpreted as 'rogue' values with no stratigraphic significance. It would thus appear that the studied intervals of the Dahra and Harash are above the MPBE and below the PETM.

Oxygen Isotope Stratigraphy: The oxygen isotope data in the Dahra Formation, by way of contrast to $\delta^{13}C$, are much more scattered: between -6.8‰ and +1.1‰ in Well no. 8 (average -3.63‰), and between -6.7‰ and -0.8‰ in Well no. 9 (average -4.81‰) (Fig. 9). Plotted stratigraphically, the data show several pronounced shifts (Fig. 8). In Well no. 9 there is a trend from low negative (-0.8‰, depth 3268ft/995m) to more negative values (~-6.1‰, depth 3260ft/992m), and then a return to low negative values towards the top of the formation. In Well no. 8, there is a somewhat similar pattern, although with a longer section towards the base of low negative values (depths 3334-3259ft/1015-9933m). In the uppermost part of the Dahra Formation in Well no. 8, there is a positive excursion with $\delta^{18}O$ increasing from -3.79‰ to +1.15‰, and then reducing to -1‰. With the $\delta^{13}C$ in Well no. 8 at this level, apart from the one 'rogue' negative value, there is no significant change in this part of the section. This uppermost part of the Dahra is occupied by dolomitic, slightly bioturbated wackestone facies that is characterised by the development of desiccation cracks and fenestrae, indicating subaerial exposure. The positive $\delta^{18}O$ values coinciding with the occurrence of dolomite could indicate a near-surface precipitate from seawater (Tucker & Wright 1990). The negative values $\delta^{18}O$ values elsewhere in the core indicate meteoric or burial processes.

The oxygen isotope values in the Zelten and Harash formations range from -10.49‰ to -2.21‰, with an average of -4.60‰ in Well no. 8 and -4.77‰ in Well no. 9 (Figs. 8, 9). Plotted stratigraphically, the $\delta^{18}O$ data in Well no. 8 show a 'zig-zag' pattern but there is a long-term trend from more negative (-6‰) to less negative (-3 ‰) over the core thickness

of some 40 metres. In Well no. 9, there are again small-scale variations in $\delta^{18}O$, and one much more negative data-point (at -10.5‰ at 2742ft/835m), but overall there is a weak trend from low negative (-3‰) to more negative (-7‰) in the upper Zelten, and then back to less negative (-3‰) from the upper Zelten through to the top of the core in the Harash.

The $\delta^{18}O$ values of marine carbonate in the upper Paleocene are 0 to -2‰, depending on palaeolatitude and facies (Koch *et al*, 2003; Zachos *et al*, 2006). The $\delta^{18}O$ values shown by the Dahra, Zelten and Harash formations are mostly much more negative than these, averaging -4.3‰, apart from the upper part of the Dahra Formation in Well no. 8. The samples with $\delta^{18}O$ more negative than 3 are likely to have been altered by diagenetic processes. However, the data plotted stratigraphically are not completely random; there are long-term trends in the $\delta^{18}O$ data through the succession, which are interpreted here as reflecting original fluctuations in environmental conditions.

Following the MPBE and up to the PETM a long-term phase of warming has been recognised before the extreme thermal maximum of the PETM itself, which is represented by a sharp negative $\delta^{18}O$ excursion (Koch *et al*, 2003; Zachos *et al*, 2006). Climatic warming through the Selandian-Thanetian would be recorded in the $\delta^{18}O$ stratigraphic record as a long-term trend towards more negative values, from around 0 to -1 ‰ to closer to -2‰ or -3‰ as temperature increased. There is little indication of a long-term negative trend in the Libyan $\delta^{18}O$ data (Fig. 9); if anything the long-term trends are the other way, towards less negative values, as in the Harash Formation in both Wells no. 8 and 9, and in the Dahra in Well no. 8.

Overall then, it would, appear that the oxygen isotope data do not preserve the expected patterns reported from other Paleocene sections. The values themselves are more negative than most original values expected for the Paleocene; this would most likely be the result of diagenesis, through near-surface meteoric fluids with their typically more negative $\delta^{18}O$ composition compared to seawater and/or precipitation of cements during burial, with the higher temperatures there.

Fluid Inclusion Results

Several representative samples of coarse calcite crystals were examined for their fluid inclusions. The inclusions are generally absent to rare, but there are some crystals where they are relatively common.

Inclusions are normally 3-6µm in diameter and are filled with oil or water. The inclusions fluoresce with colours ranging from yellow to white, with some being blue (Figs. 10, 11). Sample no. 49, from the Dahra Formation at a depth of 3229ft (985m) in Well no. 8, shows several white fluorescent inclusions within coarse late calcite in a porous dolomitic grainstone (Fig. 10 and Table 2). Sample no. 46 from the Dahra Formation in Well no. 9 at a depth of 3216 ft (980m) contains several to many inclusions with a blue fluorescent colour in calcite cement within a porous bioturbated grainstone.

In the Zelten Formation, Well no. 8, sample no. 21 (depth 2788ft/850m), a high oil saturation is detected suggesting an oil column or palaeo-column. Calcite crystals contain a high visual abundance of yellow fluorescent inclusions in a non-porous wackestone/packstone (Fig. 11 and Table 2). In the Harash Formation in Well no. 9, sample no. 13 (2698 ft/825 m), on the other hand, rare to several white fluorescent inclusions in calcite occur in a non-porous packstone.

Measurements taken on inclusions containing hydrocarbon from the Dahra Formation show that the

Table 2. Fluid inclusion results of sample no. 49, the Dahra Fm, Well no.8 (A); Sample no. 46, the Dahra Fm, Well no. 9 (B); Sample no. 21, Zelten Fm, Well no.8 (C), and sample no. 13, the Harash Fm, Well no. 9 (D).

Well no. 8 – 2788 (Z)						
Population	Fluor Color	Th hc (°C)	API hc (°)	Th aq (°C)	Tm aq (°C)	Sal (wt%)
pr/sec; cc	wt	63 (1)				
pr/sec; cc	wt	60 (1)				

Well no.9 -3216 (D)						
Population	Fluor Color	Th hc (°C)	API hc (°)	Th aq (°C)	Tm aq (°C)	Sal (wt%)
pr/sec; cc	bl	59 (2)				
pr/sec; cc	bl	54 (1)				
pr/sec; cc	bl	67 (1)				

Well no. 8 – 2788 (Z)						
Population	Fluor Color	Th hc (°C)	API hc (°)	Th aq (°C)	Tm aq (°C)	Sal (wt%)
pr/sec; cc	wt	57 (1)				
pr?/sec; cc	wt	48 (1)				
pr?/sec?; cc				59 (1)	-10.5	14.5

Well no. 9 – 2698 (H)						
Population	Fluor Color	Th hc (°C)	API hc (°)	Th aq (°C)	Tm aq (°C)	Sal (wt%)
pr/sec; cc	wt	60 (1)		90 (1)	-4.1	6.6
pr/sec; cc				67 (1)	N/A	N/A
pr; cc				70 (1)	-21.2	23.1

Legend

Fluorescence Color: based on illumination with Nikon UV-2A filter
Th hc: homogenization temperature of petroleum inclusions
API hc: measured or estimated API gravity of petroleum inclusions

Th aq: homogenization temperature of aqueous inclusions
Tm aq: final melting temperature of aqueous inclusions
mixed: inclusion contains aqueous fluid and petroleum
metastable: final Tm above 0 C precludes accurate salinity

NOTE: data on same line indicate coexisting aq and pet

Sal (wt%): salinity computed from NaCl-H2O system
Capital Letter: population or area

Number in Parentheses: number of inclusions measured
N/A: could not be determined
S?: high Th from deformation of inclusion cavity
pr: primary
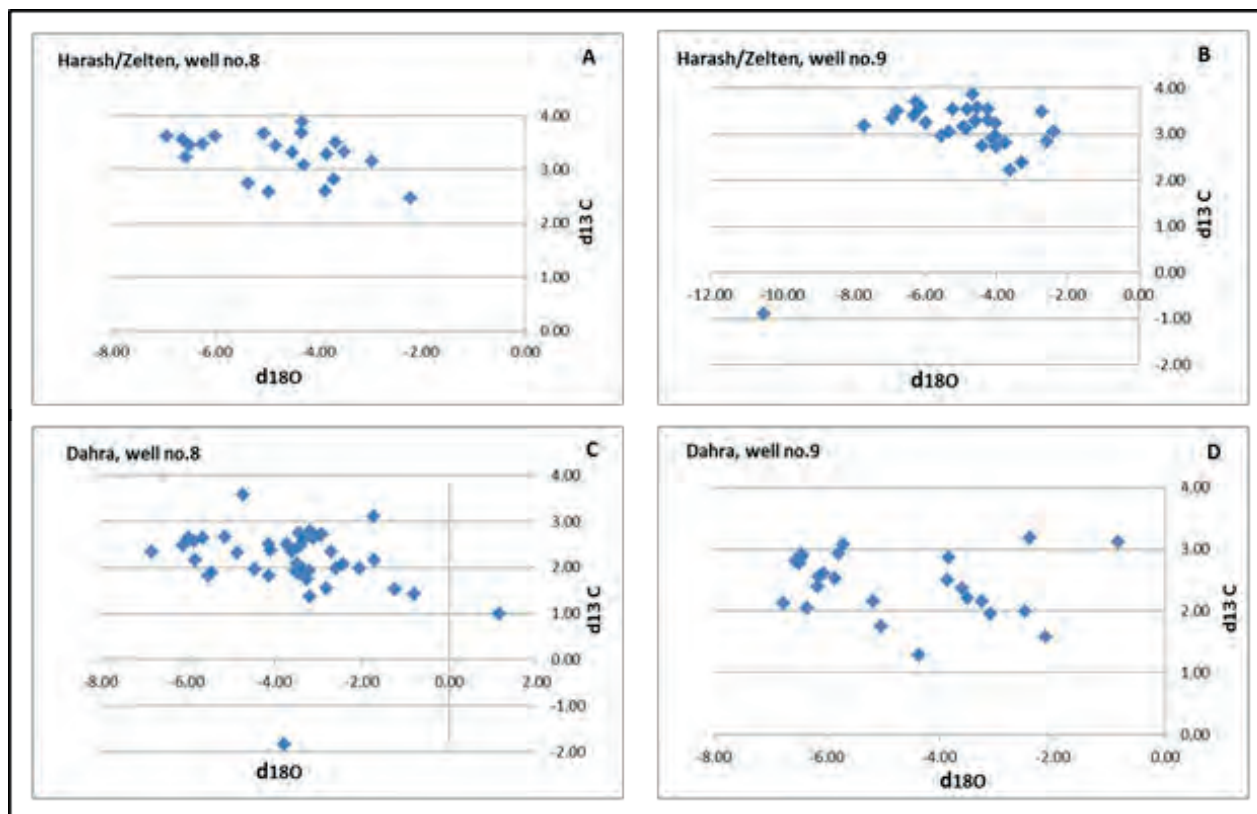sec: secondary
psec: pseudo-secondary

Fig. 9. Oxygen and carbon isotopes for the Zelten and Harash Formations (A & B) and Dahra Formation (C & D) in Well no. 8 and 9. Dahra Field on the Dahra Platform.

homogenisation temperature ranges between 48 and 67^0C. With aqueous inclusions, the homogenisation temperature varies from 59 to 90^0C (Table 2). The homogenisation temperature of both petroleum and aqueous inclusions against frequency is shown in (Fig. 12).

The homogenisation temperature from hydrocarbon inclusions in the Zelten Formation is between 48 and 57^0C, and in the Harash Formation it is 60^0C. The homogenisation temperature of aqueous inclusions in the Zelten Formation is 59^0C, and in the Harash Formation it ranges between 67 and 90^0C (Table 2). The homogenisation temperature of the aqueous inclusions is higher than that of the petroleum inclusions in the Zelten Formation, and is much higher in the Harash Formation. This could suggest two phases of calcite precipitation, an earlier, shallow burial one coinciding with some hydrocarbon generation, and another later, somewhat deeper phase of calcite precipitation.

The maximum temperatures of homogenisation, reaching 90ºC, indicate that burial depths of cementation were the order of 2000 metres (geothermal gradient 25º/km). With the Paleocene

carbonates at a depth of 700-1500m, this supports the interpretation of Abadi *et al* (2008) of significant uplift in the Oligo-Miocene.

DISCUSSION

Paragenesis

The relative timing of diagenetic features in the Selandian/Thanetian carbonates has been considered on the basis of petrographic observations and cross-cutting relationships between diagenetic fabrics. A paragenesis for these carbonates is presented in (Fig. 13).

Evidence of early marine diagenesis is recorded throughout all 3 formations and is represented by local acicular fibrous cement coatings of grains, lithified sediment forming hardgrounds penetrated by borings, microbial micritisation and formation of micritic envelopes. The early rim cement has preserved some primary intergranular porosity in certain levels of the Dahra Formation. On the whole, the degree of marine cementation is minor.

Dissolution of grains of metastable mineralogy, and precipitation of calcite cement with a meniscus
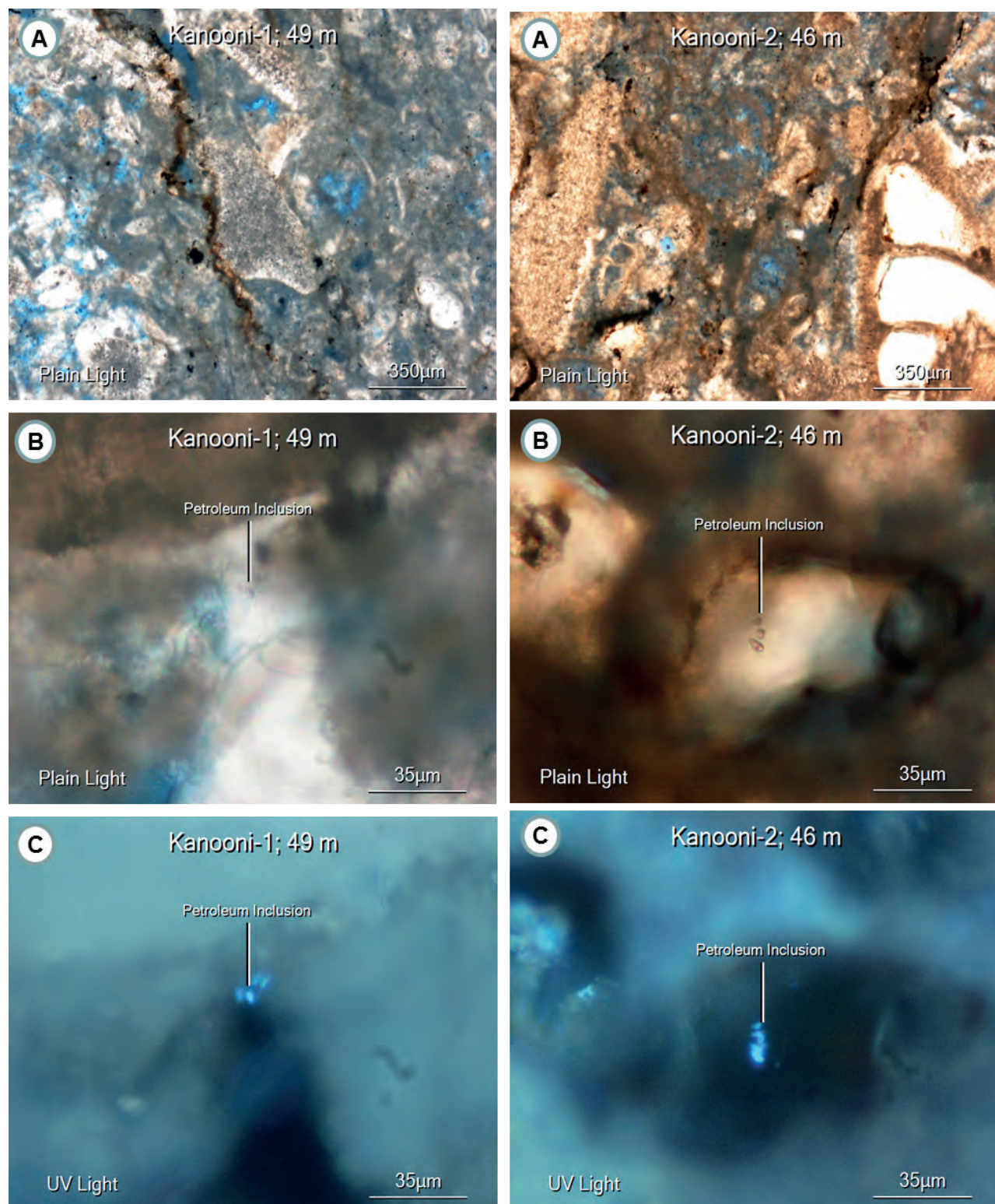
Fig. 10. A-C (left column) several white fluorescent, unknown gravity oil inclusions in bioclastic foraminiferal grainstone microfacies, Dahra Formation, Well no. 8 (3229 ft / 985 m); A-C (right column) several to common occurrences of blue fluorescent, unknown gravity petroleum inclusions in porous bioclastic foraminiferal grainstone microfacies, Dahra Formation, Well no.9 (3216 ft / 980 m).

mosaic took place in the near-surface meteoric zone from freshwater. Pre-compaction patchily-distributed equant sparry calcite and the early stage of syntaxial cement overgrowth around echinoderm grains were probably also precipitated in the meteoric zone, but in the phreatic part. Under cathodoluminescence, the meteoric cements are generally non-luminescent to dull (weakly)
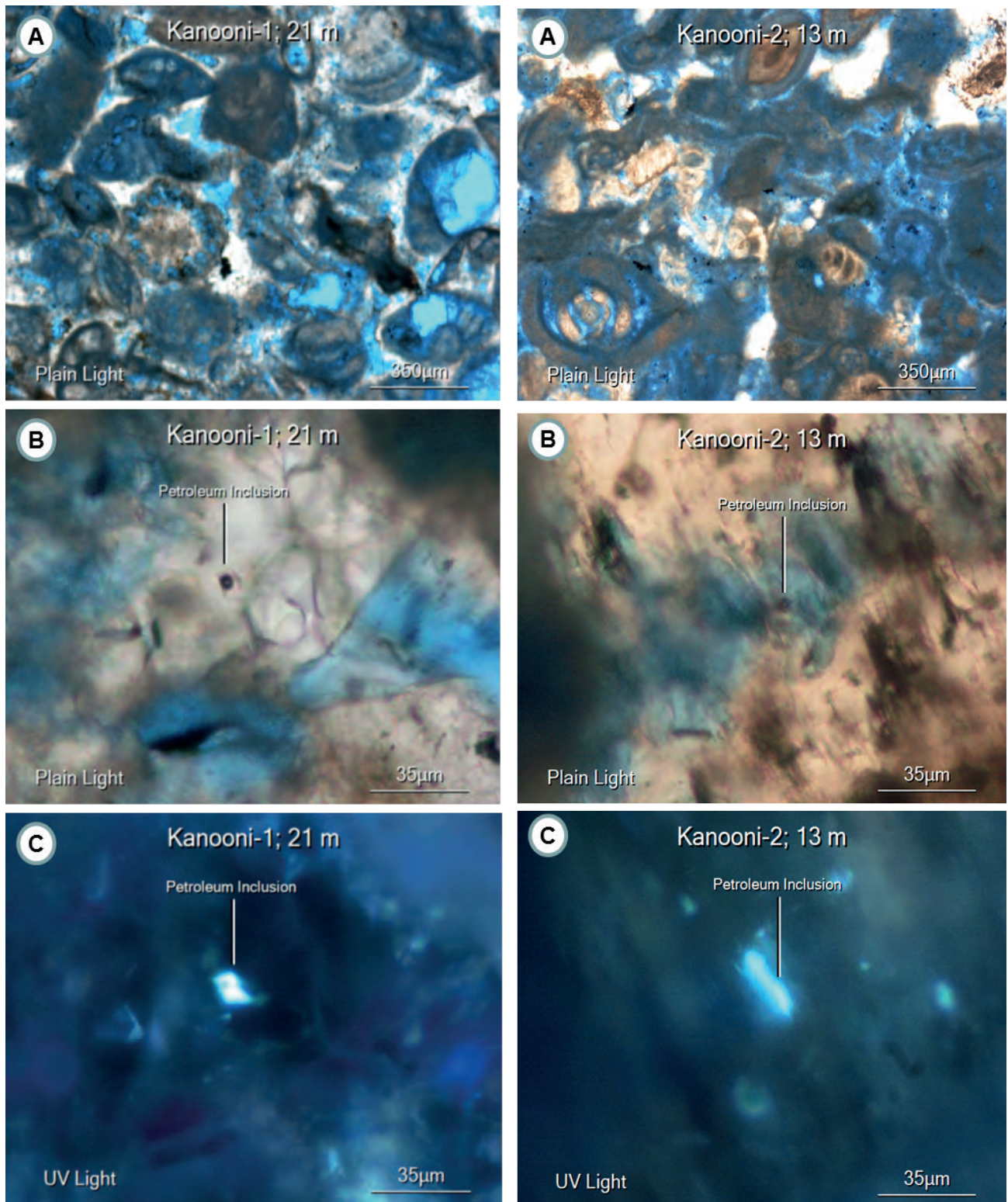
Fig. 11. A-C (left column) abundance of yellow fluorescent, unknown gravity oil inclusions in porous bioclastic wackestone/ packstone microfacies, Zelten Fm, Well no. 8 (2788 ft / 850 m); A-C (right column) rare to several white fluorescent, unknown gravity oil inclusions in dolomitic bioturbated bioclastic packstone microfacies, Harash Fm, Well no.9, (2698 ft / 820 m).

luminescent. There is some indication of subaerial exposure and pedogenesis in the form of desiccation cracks, fenestrae and rootlets in a dolomitic, brecciated and mottled fabric, in the Dahra Formation and lower part of the Zelten Formation.

In the deeper burial environment, the precipitation of coarse ferroan calcite and dolomite cements, fracturing, and formation of pressure
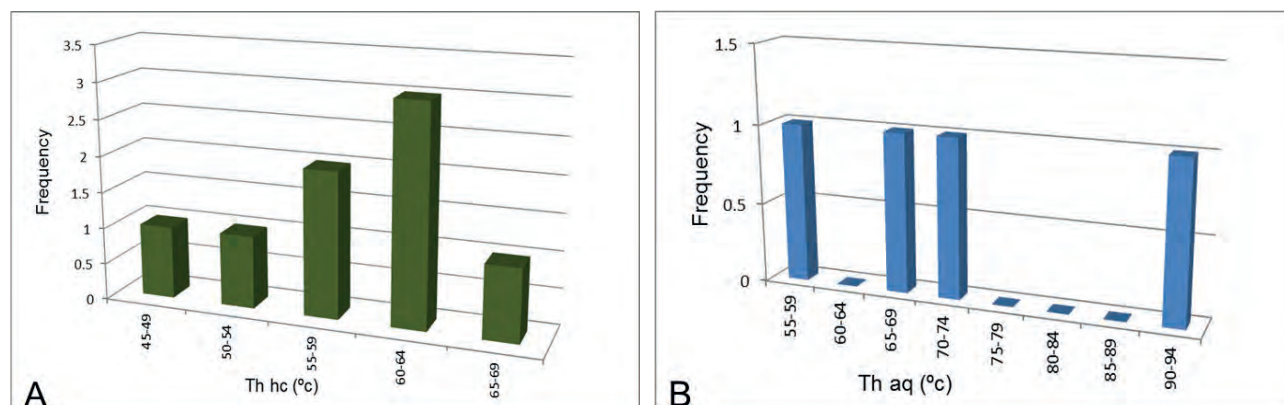
Fig. 12. Homogenization temperature of petroleum inclusions (A) and aqueous inclusions (B) against frequency in the Selandian / Thanetian succession (Harash, Zelten and Dahra Formations).

Fig. 13. Main diagenetic events and environments of the Selandian/Thanetian carbonates in the study area.

dissolution seams and stylolites were the main processes affecting the Selandian/Thanetian carbonates. The medium to coarsely crystalline dolomite has two luminescence characters; inner weakly to non-luminescent and thin outer slightly bright orange zones, indicating precipitation during a time of changing pore-fluid chemistry. The homogenisation temperatures of both petroleum inclusions and aqueous inclusions could indicate two phases of burial calcite precipitation. There is clear petrographic evidence for dissolution having

taken place in the burial environment, especially of coarse dolomite crystals and the muddy-matrix between grains. On the whole, burial diagenetic processes have affected these carbonates much more than near-surface, eogenetic processes.

Porosity and Permeability Distribution in the Selandian/Thanetian Carbonates

The two main reservoir parameters (porosity and permeability) of the Paleocene succession are discussed following core sample (hand specimen)
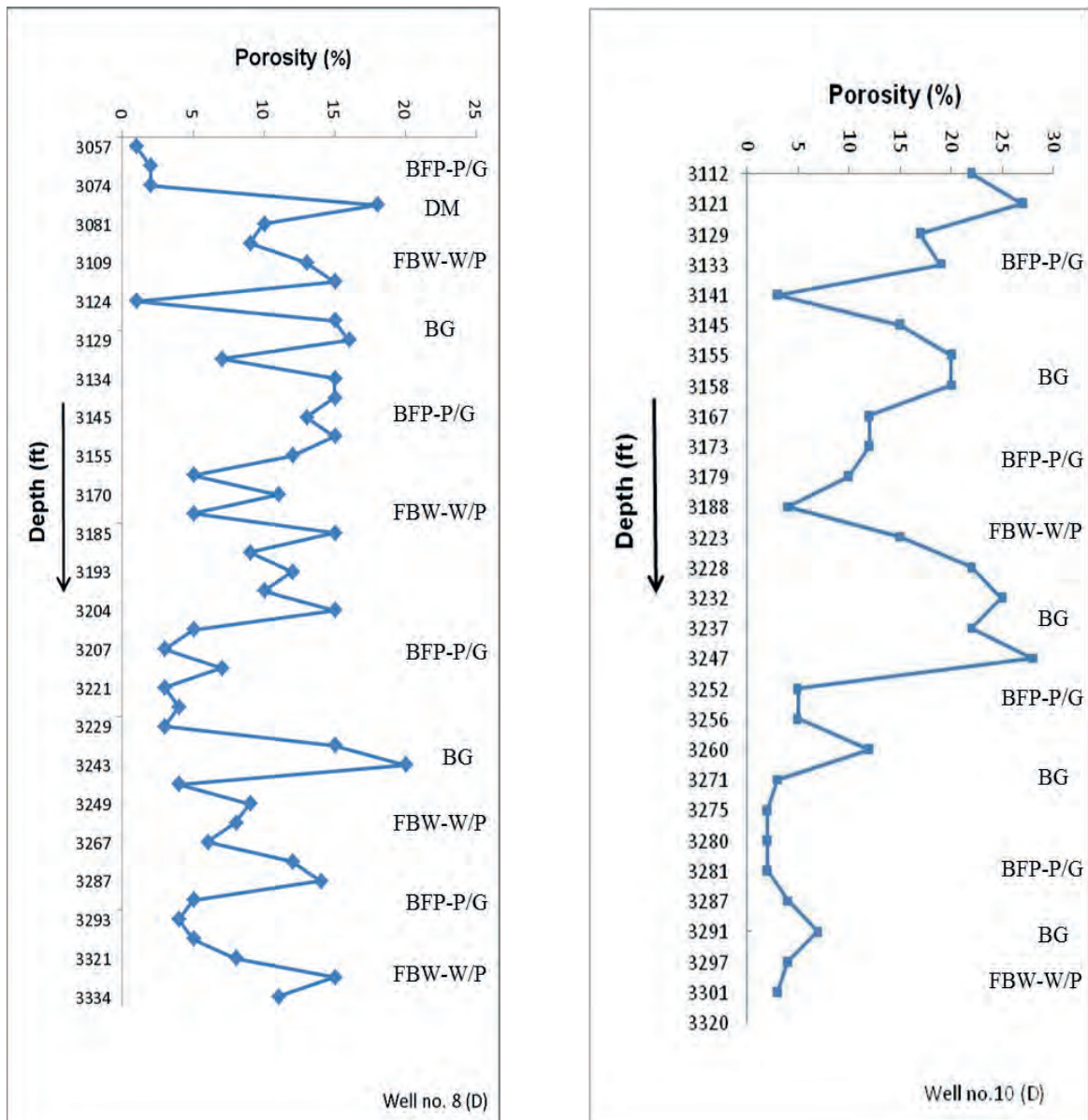
Fig. 14. Depth-porosity (observed) relationship for the cored section of the Dahra Formation in Well no. 8 (A) and Well no. 10 (B). The facies types are also shown.

inspection, thin-section observations, core analysis results, and scanning electron microscope examination.

The Dahra Formation: Macroscopic and microscopic investigations reveal that the porosity types developed in the Dahra platform carbonates are dominated by moldic, vuggy, intergranular and intragranular types, with less common fracture and intercrystalline porosity (Figs. 3, 5C & D, 6C). The porous layers are separated locally by thin beds of shale and marl/argillaceous limestone that

act as porosity and permeability barriers; these compartmentalise the formation into several major reservoir units.

The best primary porosity is developed in bioclastic grainstone and bioclastic foraminiferal packstone-packstone/grainstone facies, where it reaches up to 10%. The intragranular type of porosity is commonly developed within both the skeletal and non-skeletal carbonate grains, in particular foraminifera and coated grains. Intergranular porosity appears to have provided pathways for undersaturated fluids to pass through the sediment
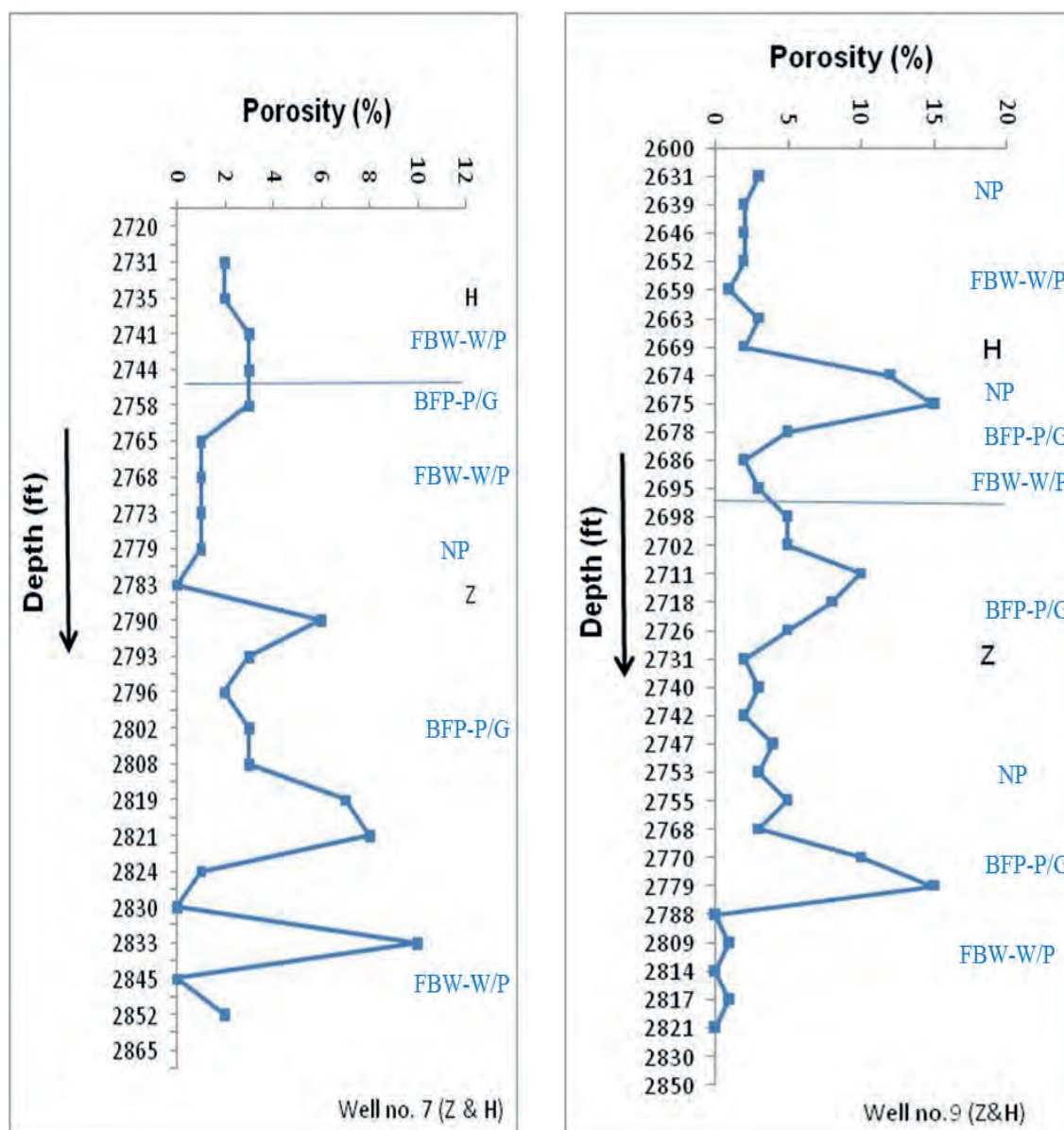
Fig. 15. Depth/porosity (observed) relationship of the cored section of Zelten (Z) / Harash (H) Formations in Well no.7 (A) and Well no. 9 (B).

and thus create secondary dissolution porosity (Figs. 5C & 6C). The low primary porosity of most facies is attributed mainly to the quite muddy (lime mud) nature of many units and the precipitation of equant calcite, Fe-rich calcite, dolomite and syntaxial rim cements in more grainy facies (Figs. 3E, 5F, 6A).

Intercrystalline porosity occurs wherever dolomite is present, in completely dolomitised facies and, less importantly, in partially dolomitic limestone facies. It is the main porosity type, along with moldic, in the dolomitic mudstone facies (Fig. 6C). Dolomite-dominated intervals are relatively

thin in relation to limestone-dominated units; they generally have fair to good porosity even in the mud-supported layers, reaching 20% in some cases. This is probably related to dolomitization leading to an increase in crystal size, an increase in pore volume due to a net addition of dolomite, the development of moldic pores and an increasing resistance to compaction (Lucia, 1999).

Dissolution porosity is widespread in the Dahra Formation and occurs in many facies in different proportions, and usually in association with primary inter- and intra-granular porosity. Its highest value

occurs in grain-supported facies, where it reaches 15%. Fracture porosity has developed locally within the Dahra Formation and is well developed in some wells. A network of open microfractures that were connected to each other developed notably within marl/argillaceous limestone intervals.

Microporosity is also present in the Dahra Formation, particularly in Wells no. 8 and 9, and occurs as intercrystalline micro-voids between subhedral to anhedral micrite, microsparite and/or dolomite crystals (Fig. 5B). It is usually moderately connected through relatively narrow pore-throats, but locally it is almost completely isolated. Thus, its contribution to reservoir quality is likely insignificant. The best observed porosity in the Dahra Formation is within the bioclastic foraminiferal packstone/grainstone facies in almost all of the examined wells. It is averaging 20-25% in Well no. 9, and 15-20% in Well no. 8. This is probably related to meteoric influence during minor sea-level fluctuations. Increased porosity near the top of the Dahra Formation may be related to uplift and meteoric exposure during the Mid Tertiary. There is no apparent relation between observed porosity and depth (Fig. 14), suggesting that porosity evolution was controlled by the original depositional texture and subsequent diagenetic alterations (Fig. 4).

The Zelten and Harash Formations: The thin-section porosity in the Zelten/Harash interval is generally low, particularly in the Harash Formation (Fig. 15). The Zelten Formation, however, has marginally better porosity, especially in the grain-dominated facies, where the best porosity is developed in the bioclastic foraminiferal packstone-packstone/grainstone and, less important, foraminiferal nummulitic packstone facies. Porosity reaches 20%, especially in Well no. 10. A notable feature is that the least estimated porosity in the grain-supported facies is mostly recorded where echinoderm fragments are relatively common. This is probably the result of overgrowth cements around echinoderms, which can grow faster than finer, polycrystalline cements.

There is no clear relationship between the observed porosity and depth within the Zelten/Harash succession (Fig. 15). The low reservoir quality is due to the presence of mud-supported facies throughout the cored interval, the occurrence of argillaceous material within the grain-supported facies, fairly extensive compaction, and less important calcite cementation.

CONCLUSIONS

The Dahra, Zelten and Harash formations in the western Sirt Basin, Libya, contain units which are significant hydrocarbon reservoirs. They are mainly composed of bioclastic, especially foraminiferal carbonates with minor amounts of shale. They were deposited on a platform with a marginal homoclinal ramp towards the basin in the west. Inner, mid and outer ramp facies are recognised, each with distinctive microfacies. After the Dahra Formation, a phase of terrigenous mud deposition across the basin (Khalifa Shale) was followed by the Zelten and Harash formations with local occurrences of nummulitic packstone, in a mainly wackestone-packstone succession.

Different types of calcite and dolomite cements occur within the Late Paleocene succession and dissolution took place at various stages in the sediment's history from near-surface to burial. For the most part the diagenesis of the ramp carbonates is dominated by burial compaction and cementation, with minor marine-meteoric effects. The low positive $\delta^{13}C$ trend varying little through the succession reflects near-constant seawater $\delta^{13}C$ and primary marine signatures in the carbonates, and thus, a lack of diagenetic alteration involving organic matter. The presence of positive $\delta^{18}O$ values within the upper Dahra Formation coinciding with finely crystalline dolomite, suggests early dolomitization through circulating seawater. This contrasts with zones of negative $\delta^{18}O$ and the variable values of the Zelten-Harash formations which reflect meteoric influences and/or the effect of increased temperature during burial and calcite cementation-neomorphism.

The porosity types developed in the Selandian/Thanetian succession are dominated by moldic, vuggy, intergranular and intragranular types, with less common fracture and intercrystalline porosity. Overall, the porosity evolution in the Selandian/Thanetian succession is controlled by original depositional texture and subsequent diagenesis.

REFERENCES

Abadi, A. M. (2002). Tectonics of the Sirte Basin. *Unpublished PhD Dissertation*, Vrije Universiteit, Amsterdam ITC. Enschede, 187p.

Abadi, A. M.; Van Wees, J-D.; Van Dijk, P. M., Cloetingh, S. A. P. L. (2008). Tectonics and Subsidence Evolution of the Sirt Basin, Libya. *AAPG Bulletin*, *92*: 993-1027.

Abdunaser, K. M. (2015). Review of the Petroleum Geology of the Western Part of the Sirt Basin, Libya**.** *Journal of African Earth Sciences, 111*: 76-91.

Abdunaser, K. M.; McCaffrey, K. J. W. (2014). Rift Architecture and Evolution: The Sirt Basin, Libya: The influence of Basement Fabrics and Oblique Tectonics. *Journal of African Earth Sciences 100*: 203–226.

Adams, A. E.; Mackenzie, W. S. and Guilford, C. (1984). Atlas of Sedimentary Rocks Under the Microscope. Longman, 104p.

Anketel, J. M. (1996). Structural History of the Sirt Basin and its Relationship to the Sabratah Basin and Cyrenaican Platform, Northern Libya. In: *The Geology of the Sirt Basin* (Edit. by: M. J. Salem; M. T. Busrewil; A. A. Isallati and M. A. Sola), Amsterdam, Elsevier *3*: 57–87.

Barnett, A. J.; Wright, V. P.; Chandra, V. S. and Jain, V. (2015). Distinguishing Between Eogenetic, Unconformity-Related and Mesogenetic Dissolution: a Case Study from the Panna and Mukta Fields, Offshore Mumbai, India. *Geological Society, London, Special Publication*: 435p.

Barr, F. T. and Weegar, A. A.(1972). Stratigraphic Nomenclature of The Sirte Basin, Libya. 179 p. *Petrol. Explor. Soc. Libya*, Tripoli.

Bernaola, G.; Martín-Rubio, M. and Baceta, J. I. (2009). New High Resolution Calcareous Nannofossil Analysis Across the Danian/Selandian Transition at the Zumaia Section: Comparison with South Tethys and Danish Sections. *Geologica Acta, 7*: 79-92.

Chandra, V.; Wright, P.; Barnett, A.; Steele, R.; Milroy, P.; Corbett, P.; Geiger, S. and Mangione, A. (2015). Evaluating the Impact of a Late-Burial Corrosion Model on Reservoir Permeability and Performance in a Mature Carbonate Field Using Near-Wellbore Upscaling. *Geological Society*, London, *Special Publication 406*: 427-445.

Dickson, J. A. D. (1965). A Modified Staining Technique for Carbonate in Thin Section. *Nature*, 205-587.

Dunham, R. J. (1962). Classification of Carbonate Rocks According to Depositional Texture. In: Classification of Carbonate Rocks (Edit. by: Ham, W. E.). *Am. Assoc. Petr. Geo.s Bulletin, Memoir 1*: 108-171.

Ebner, M.; Piazolo, S.; Renard, F. and Koehn, D. (2010). Stylolite Interfaces and Surrounding Matrix Material: Nature and Role of Heterogeneities in Roughness and Microstructural Development. *Jou. Structural Geo., 32*: 1070-1084.

Ehrenberg, S. N.; Walderhaug, O. and Bjorlykke, K. (2012). Carbonate Porosity Creation by Mesogenetic Dissolution: Reality or Illusion. *BAAPG, 96*: 217-233.

El Hefnawi, M. A.; Mashaly, A. O.; Shalaby, B. N.and Rashwan, L. A. (2010). Petrography and Geochemistry of Eocene Limestone from Khashm Al-Raqaba Area, El-Galala El-Qibliya, Egypt. *Carbonates & Evaporites, 25*: 193-202.

Elton , H.; Abdullatif, O.; Makkawi, M.; Al-Ramadan, K. and Abdulraziq, A. (2015). Porosity Evolution Within High-Resolution Sequence Stratigraphy and Diagenesis Framework: Outcrop Analog of the Upper Jurassic Arab-D Reservoir, Central Saudi Arabia. *Arabian Journal of Geosciences*, *8*: 1669-1690.

Embry, A. F. and Klovan, J. E. (1971). A Late Devonian Reef Tract on Northeastern Banks Island, Northwest Territories. *Bull. Can. Petrol. Geol., 19*: 730 - 781.

Flügel, E. and Munnecke, A. (2010). *Microfacies of Carbonate Rocks: Analysis, Interpretation and Application.* **2nd edn**. Springer-Verlag, Berlin, 984 p.

Folk, R. L. and Lynch, F. L. (2001). Organic Matter, Putative Nanobacteria and the Formation of Ooids and Hardgrounds. *Sedimentology, 48*: 215-229.

Gingras, M. K.; Pemberton, S. G.; Muelenbachs, K. and Machel, H. (2004). Conceptual Models for Burrow-Related, Selective Dolomitization with Textural and Isotopic Evidence from the Tyndall Stone, Canada. *Geobiology, 2*: 21–30.

Green M. A. and Aller, J. Y. (1992). Experimental Evaluation of the Influences of Biogenic Reworking on Carbonate Preservation in Nearshore Sediments. *Marine Geology, 107***:** 175–181.

Gumati, Y. D. (1982). Paleocene Facies of the Sirte Basin and Structural Evolution of the Basin During Paleocene Time: *Master's Thesis*, University of South Carolina, Columbia, South Carolina: 55p.

Gumati, Y. D. and Nairn, A. E. (1991). Tectonic Subsidence of the Sirt Basin, Libya. *Jour. Pet. Geol., 14*: 93–102.

Gumati, Y. D. and Schamel, S. (1988). Thermal Maturation History of the Sirte Basin, Libya: *Jour. Pet. Geol., 11*: 205–218.

Hallett, D. (2002). *Petroleum Geology of Libya.* Elsevier, Amsterdam. 503 p.

Have T. Ten, Heijnen W. (1985). Cathodoluminescence Activation and Zonation in Carbonate Rocks: An Experimental Approach. *Geol Mijnbouw, 64*: 297–310.

Hillgärtner, H.; Dupraz, C. and Hug, W. (2001). Microbially Induced Cementation of Carbonate Sands: are Micritic Meniscus Cements Good Indicators of Vadose Diagenesis? *Sedimentology, 48*: 117–131.

James, N. P. and Jones, B. (2015). Origin of Carbonate Sedimentary Rocks. American Geophysical Union & John Wiley, Chichester.

Koch, P. L.; Clyde, W. C.; Hepple, R. P.; Fogel, M. L.; Wing, S. L. and Zachos, J. C. (2003). Carbon and Oxygen Isotope Records from Paleosols Spanning the Paleocene-Eocene Boundary, Bighorn Basin, Wyoming. In: Causes and Consequences of Globally Warm Climates in the Early Paleogene.Geol (Edit. by: Wing, S. L., Gingerich, P. D., Schmitz, B. and Thomas, E.) *Soc*. Am. Spec. Publ., *369*: 49-64.

Logan, B. W. and Semniuk, V. (1976). Dynamic Metamorphism; Process and Products in Devonian Carbonate Rocks: Canning Basin, Eastern Australia. Western Australia. *Geol. Soc. Australia, Spec. Publ., 6*: 138-150.

Longman, M. W. (1980). Carbonate Diagenetic Textures from Near-Surface Diagenetic Environments. *Bull. Am. Ass. Petrol. Geol., 64*: 461-487.

Lucia, F. J. (1999). *Carbonate Reservoir Characterization*. Springer-Verlag Berlin Heidelberg, 226 p.

Machel, H. G. and Burton, E. A., (1991). Factors Governing Cathodoluminescence in Calcite and Dolomite. In: Luminescence Microscopy: Quantitative aspects (Edit. by: Barker, C. E and Kopp, D. C.). *Soc. Econ. Paleont. Miner, Short Course, 25*: 37-57.

Madden, R. H. C. and Wilson, M. E. J. (2013). Diagenesis of a SE Asian Cenozoic Carbonate Platform Margin and its Adjacent Basinal Deposits. *Sedimentary Geology, 286-287*: 20–38.

Mazzulo, S. and Harris, P. M. (1992). Mesogenetic Dissolution: its Role in Porosity Development in Carbonate Reservoirs. *BAAPG, 76*: 607-620.

Miller, K. G.; Kominz, M. A.; Browning, J. V.; Wright, J. D.; Mountain, G. S.; Katz, M. E.; Sugarman, P. J.; Cramer, B. S.; Christie-Blick, N. and Pekar, S. F., (2005). The Phanerozoic record of global sea-level change. *Science, 310*: 1293-1298.

Morgan, W. J. (1980). Hot-Spot Tracks and the Opening of the Atlantic and Indian Oceans. In: *The Sea* (Edit. by: C. Emiliani) Wiley, New York, *V. 7*: 443-467.

Morgan, W. J. (1983). Hot-Spot Tracks and the Early Rifting of the Atlantic. *Tectonophysics, 94*: 123-139.

Mouzughi, A. J. and Taleb, T. M. (1982). Tectonic elements of Libya (1:2 000 000). National Oil Corporation, Libya.

Nader, F. H.; Swennen, R. and Keppens, E. (2008). Calcitization/Dedolomitization of Jurassic Dolostones (Lebanon): Results from Petrographic and Sequential Geochemical Analyses. *Sedimentology, 55*: 1467-1485.

Pujalte, V.; Orue-Etxebarria, X.; Schmintz, B.; Tosquela, J.; Baceta, J. I.; Payros, A.; Bernaola, G.; Caballero, F. and Apelleniz, E. (2003). Basal Ilerdian (Earliest Eocene) Turnover of Larger Foraminifera: Age Constraints Based on Calcareous Plankton and 8I3C Isotopic Profiles from New Southern Pyrenean Sections (Spain). *Geol. Soc. America, Special Paper, 369*: 205-221.

Rameil, N. (2008). Early Diagenetic Dolomitization and Dedolomitization of Late Jurassic and Earliest Cretaceous Platform Carbonates: A Case Study from the Jura Mountains (NW Switzerland, E France). *Sedimentary Geology, 212*: 70-85.

Ruban, D. A.; Zorina, S. O. and Conrad, C. P. (2010). No Global-Scale Transgressive-Regressive Cycles in the Thanetian (Paleocene): Evidence from Interregional Correlation. *Palaeogeography, Palaeoclimatology, Palaeoecology, 295*: 226-235.

Ruban, D. A.; Zorina, S. O.; Conrad, C. P. and Afanasieva, N. I., (2012). In Quest of Paleocene Global-scale Transgressions and Regressions: Constraints from a Synthesis of Regional Trends. *Proceedings of the Geologist's Association, 123*: 7-18.

Rustichelli, A.; Tondi, E.; Korneva, I.; Baud, P.; Vinciguerra, S.; Agosta, F.; Reuschlé, T. and Janiseck, J. M. (2015). Bedding-Parallel Stylolites in Shallow-Water Limestone Successions of the Apulian Carbonate Platform (Central-Southern Italy). *Italian Journal of Geoscience, 135DOI*: 10.3301/IJG.2014.35.

Swati, M. A. F.; Haneef, M.; Ahmad, S.; Latif, K.; Naveed, Y.; Waseem Zeb, W.; Akhtar, N. and Owais, M. (2014). Diagenetic Analysis of the Early Eocene Margala Hill Limestone, Pakistan. *Journal of Himalayan Earth Sciences, 47*: 49-61.

Tucker, M. E. (1993). Carbonate Diagenesis and Sequence Stratigraphy. In: *Sedimentology Review* (Edit. by: V. P. Wright), *1*: 51-72. BlackWell Science, Oxford.

Tucker. M. E. and Wright, V. P. (1990). *Carbonate Sedimentology*. BlackWell Science, Oxford, 482p.

Van Berk, W.; Yunjiao Fu, Y. and Schulz, H. M. (2015). Creation of Pre-Oil-Charging Porosity by Migration of Source-Rock-Derived Corrosive Fluids Through Carbonate Reservoirs: One-Dimensional Reactive Mass Transport Modelling. *Petroleum Geoscience, 21*: 35-42.

Van der Meer, F. and Cloetingh, S. (1996). Intraplate Stresses and the Subsidence History of the Sirt Basin. In: *First Symposium on the Sedimentary Basins of Libya, Geology of the Sirt Basin* (Edit. by: M. J. Salem, M. T. Busrewil, A. A. Misallati, and M. J. Sola), Elsevier, *V. 3*: 211-230. Amsterdam

Volery, C.; Davaud, E.; Foubert, A. and Caline, B. (2009). Lacustrine Microporous Micrites of the Madrid Basin (Late Miocene, Spain) as Analogues for Shallow-Marine Carbonates of the Mishrif Reservoir Formation (Cenomanian to Early Turonian, Middle East): *Facies, 56*: 385-397.

Wong P. K. and Oldershaw, A. E. (1981). Causes of Cyclicity in Reef Interior Sediments, Kaybob Reef, Alberta. *Bull. Can. Petrol. Geol., 28*: 411-424.

Wright, V. P. and Harris, P. M. (2013). Carbonate Dissolution and Porosity Development in the Burial (Mesogenetic) Environment. *AAPG*, Search & Discovery article *# 50860*.

Zachos, J. C.; Schouten, S.; Bohaty, S.; Quattlebaum, T.; Sluijs, A.; Brinkhuis, H.; Gibbs, S. J. and Bralower. T. J. (2006). Extreme Warming of Mid-Latitude Coastal Ocean During the Paleocene-Eocene Thermal Maximum: Inferences from TEX86 and Isotope Data. *Geology, 34*: 737-740.

Zeff, M. L. and Perkins, R. D. (1979). Microbial Alteration of Bahamian Deep-Sea Carbonates. *Sedimentology, 26*: 175-201.

Zenger, D. H. (1992). Burrowing and Dolomitization Patterns in the Steamboat Point Member, Bighorn Dolomite (Upper Ordovician), Northeast Wyoming. *Contributions to Geology, 29*: 133-142.

ABOUT THE AUTHORS

Ibrahim Elkanouni is a senior geologist (Associate Researcher) in the Exploration Department at Libyan Petroleum Institute (LPI). He has got an MSc degree from University of Manchester and PhD from Durham University, UK.

He is specialist in carbonate sedimentology and sequence stratigraphy and has been involved in several studies concerning Libyan sedimentary basins and oil fields, in onshore and offshore regions, studied carbonates from Paleozoic, Mesozoic and Cenozoic successions. Has supervised the sedimentology research group at Libyan Petroleum Institute (2002-2009). He has been teaching at Geology Department, University of Tripoli since 2002.

Maurice Tucker is a visiting professor at the University of Bristol and emeritus professor at Durham University since 2011, after nearly 30 years at Durham, after positions at Newcastle, UC Berkeley, Cardiff and Sierra Leone. His interests are in limestones, their deposition, diagenesis, reservoir potential and he has studied carbonates from most geological periods from many parts of the world. He has published over 150 papers and written several books including Sedimentary Petrology (2000), Sedimentary Rocks in the Field (2011), Carbonate Sedimentology (with Paul Wright, 1990), and Petrologia Sedimentar Carbonatica (with Dimas Dias-Brito, 2017). His current interest is in viruses and their role in carbonate precipitation: viruses are the new role in Earth Science.

PETROGRAPHY AND DIAGENESIS OF THE HAWAZ SANDSTONE FORMATION, MURZUQ BASIN, SW LIBYA

Eman Abdel-Latif Taktek[1]

Abstract: Middle Ordovician Hawaz Formation represents the primary reservoir rocks in Murzuq Basin. In J Oil Field Hawaz Formation consists of a 550 feet thick succession made of fine-grained quartz-arenite displaying a variable degree of bioturbation. This J Oil Field study is an integration approach and it is based on 235 feet thick of slabbed cores photographs from well J4-NC186, with core samples, petrography, wireline log data, and conventional core analysis of the Hawaz siliciclastic sediments. The Hawaz Formation was deposited in wave-dominated shoreface and shelf environments. The stratigraphical and sedimentological characteristics of the Hawaz Formation in the study area in Murzuq Basin are attributed to shoreface and shelf facies associations within which some 9 facies have been distinguished. The lower part of the cored section of the Hawaz Formation is dominated by the outer and inner shelf facies associations. The outer shelf association is dominated by mudstone whereas, the inner shelf association is dominated by siltstone/sandstone.

Petrographic analysis provides a means of assessing the composition of the sandstone and relating this to their provenance, tectonic setting, diagenetic evaluation and economic potential (Pettijohn *et al*, 1987). Petrographic investigations show that Hawaz sediments can be divided into six categories: (a) rock fragments, (b) quartz, (c) feldspar, (d) micas and authigenic quartz, clay minerals and other constituents. Originated mainly from metamorphic rocks in humid climates.

Keywords: Hawaz Sandstone Formation, Murzuq Basin, Petrography, Diagenesis.

INTRODUCTION

General Overview of the Study Area

Murzuq Basin is located on the North African Platform, covers an area of some 350,000 km², extending southwards into Niger. Thomas (1995) mentioned that the present-day borders of the basin is defined by erosion resulting from multiphase tectonic uplifts (Fig. 1). It is not a sedimentary basin in the normally accepted sense and could more accurately be described as an erosional remnant of a much larger Palaeozoic and Mesozoic sedimentary basin which originally extended over much of North Africa.

The flanks comprise the Tihemboka High to the west, the Tibesti High to the southwest, and the Gargaf and Atshan highs to the north and north west. These uplifts were generated by various tectonic events ranging from middle Palaeozoic to Tertiary time, but the main periods of uplift took place during Middle Cretaceous to Early Tertiary

Alpine movements. The present-day Murzuq Basin contains a maximum sedimentary fill of about 4000m. Davidson, *et al* (2000) pointed out that, despite successive erosive episodes during several phases of uplift and erosion throughout the history of the basin, the maximum sedimentary thickness probably never exceeded 5000m at any single point in time. Murzuq Basin has different concessions containing some oil fields, one of them is J Oil Field in concession NC186 in.

The petroleum system is represented by structural Hawaz paleo-high created during the post Hawaz erosional event, the main regional seal is the Silurian Tanezzuft shale Formation, and the basal Tanezzuft hot shale member acts as the main source rock in study area. This formation is considered the main target. The strata are faulted and the faults are most frequently parallel to the axis. Tectonic movements affected the basin to a greater or lesser degree from middle Palaeozoic, Oligocene (Alpine) times, Bellini and Massa, (1980). Hawaz Formation rests conformably over the Ash Shabiyat Formation. Both formations are cut by an erosive surface recognizable in outcrop and subsurface. Hawaz Formation is typically

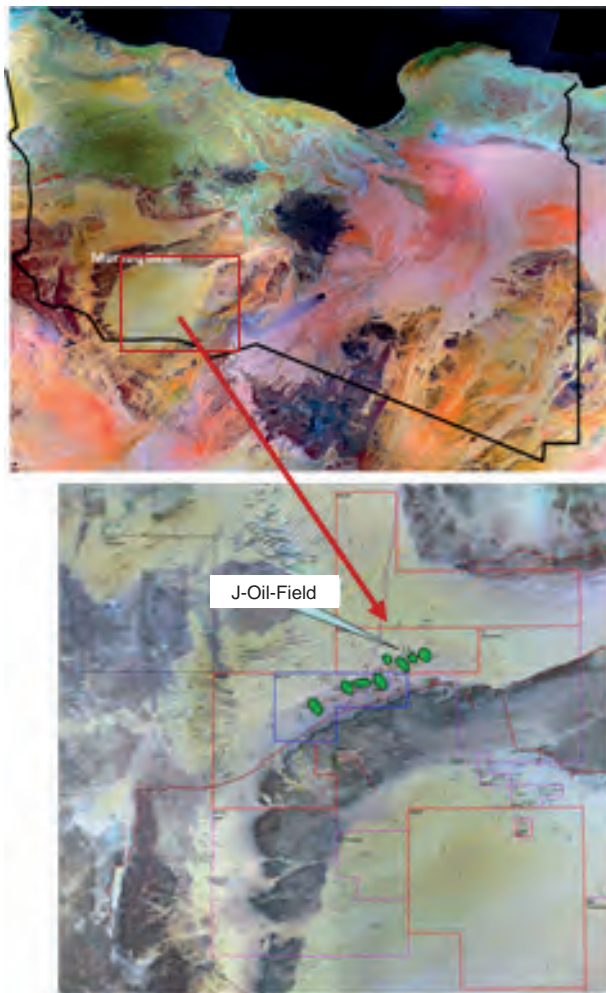[1] Email: eman_tek2012@yahoo.com, Waha Oil Company, Tripoli, Libya.

Fig. 1. Location map of J-Oil-Field in Concession 186, Murzuq Basin.

consisting of cross bedded, quartzitic sandstone with kaolinitic and thin shaley intercalations (Tigillites) bioturbated levels and ripple marks are conspicuous. The formation thickness ranges from 50 meters at Dor al-Qussah to 300 meters at Al-Qarqaf in outcrops, and 30 to 230 meters in the subsurface.

Location of the Study Area

Murzuq Basin is located at the southwestern part of Libya. Concession NC186 is in northwestern flank of the Murzuq Basin (Fig. 1).

Aims of the Study

To provide a detailed sedimentological description of the core from well J4-NC186. To integrate the sedimentological and thin section data in order to derive any variation of the mineralogical composition and diagenetic sequence which adequately account for the Hawaz

Formation in the study well. The main objective of this study to: a) assess the mineral composition. b) Classify the sandstones. c) Reconstruct their diagenetic history, and d) determine the source rock provenance and composition.

Structure of the Area (J Oil Field)

J Field-NC186 is located in Murzuq Basin, SW Libya; in the middle southern part of NC186 block between H and B fields. J Field NC186 is an elongated NW-SE of Hawaz Paleo-High and tilted to the SE, associated with a 4 way dip structural closure. Middle Ordovician Hawaz Formation is the main reservoir in J Oil Field, the formation comprises a distinctive suite of facies associations representing a broad range of environments from low energy shelf marine sediments deposited largely below storm wave base, through to sub-aerial delta plain channel environments.

METHODOLOGY

The petrograpic study was provided by Akakus Oil Operation. This study is based on a total of 30 thin-sections, from J4-NC186. However, thin sections have been impregnated with blue resin in order to facilitate the microscopic examination of texture and quantitative analysis of composition and porosity. Because the mineralogy of a sandstone, is primarily inherited from the source area, modified by sedimentary processes and diagenesis, mineralogical examination provides one of the most useful approaches to obtain information about the provenance. These informations including tectonics and climate, the effects of transportation, including distance and direction, and the addition of minerals during sedimentation and diagenesis (Pettijohn *et al*, 1987).

The thin sections were analyzed using a point counter to determine the percentage of quartz, feldspar, rock fragments, heavy minerals, mica, kaolinite, calcite, pyrite, matrix and porosity. The analysis was carried out using a Swift automatic point counter and mechanical stage. Three hundred grains were counted per slide for statistically reproducible results and then the results recalculated to 100%. The porosity measurements were estimated by standard modal analysis techniques and the porosity in the Hawaz Formation classified into three types for counting purposes: primary porosity, secondary porosity and micro-porosity.

PETROGRAPHIC ANALYSIS RESULTS AND INTERPRETATION

Compositional Analysis

The model composition of the Hawaz Sandstone provides evidence of the composition of the source and the diagenetic events that affected the post depositional burial history of the sandstone.

The detrital particles in siliciclastic rocks in the Hawaz Sandstone in J4-NC186, have been divided into six categories: (a) rock fragments, (b) quartz, (c) feldspar, (d) micas, (e) heavy minerals and authigenic (f) clay minerals and other constituents.

Quartz: Quartz is the most common mineral in sandstone and the most physically and chemically stable under sedimentary conditions at the earth's surface.

In wells J4-NC186; Al-NC186 and H27-NC115, the Hawaz sandstones are composed mainly of quartz grain (Fig. 2), dominated by monocrystalline grains

Fig. 3. Photomicrograph showing a metamorphic polycrystalline quartz grain. XPL (X20).

considerable compaction during burial. Sutured contacts are also recognized. These varieties of grain contact types can be used as a rough measure of the degree of compaction and packing, and thus the depth of burial of the sandstone.

Quartz overgrowths can be recognized in thin-section either by dust rims between detrital grains and the overgrowth, or by the development of excellent rhombohedral crystal terminations growing into pore space (Fig. 4).
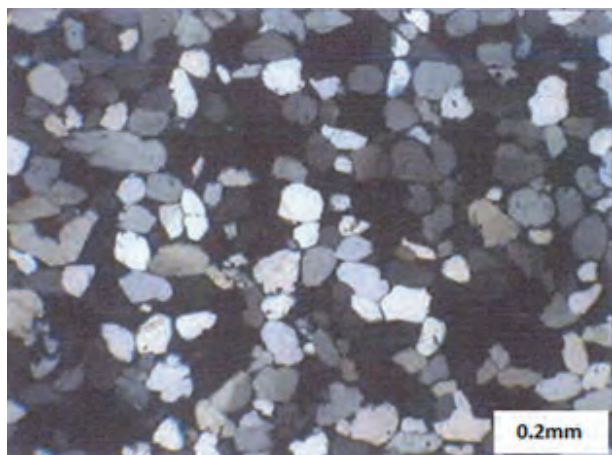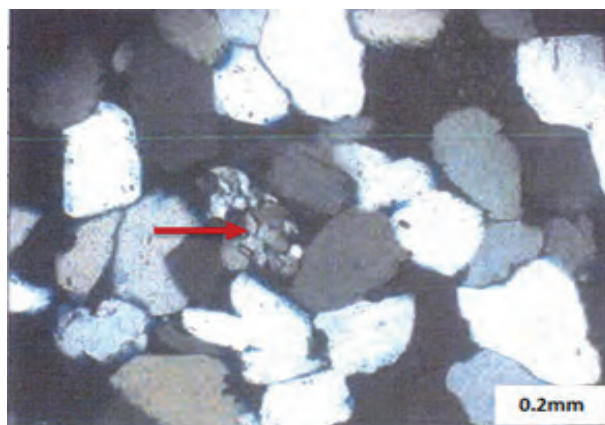

Fig. 2. Photomicrograph of a quartz arenite in the Hawaz Sandstone, which is dominated by monocrystalline quartz. XPL (X4).

(96 to 99%), relative to feldspar and rock fragments with some 2% of polycrystalline grains. Most of the quartz grains in the Hawaz sandstones in these wells show strong undulose extinction, which are more abundant in strained source rocks, especially metamorphic rocks. Also, the polycrystalline quartz grains are characterized by relatively straight boundaries between equant grains, and straight to slightly undulose extinction (Fig. 3).

The grain contact types in the Hawaz sandstones are related to the particle shape and packing. The packing depends on the spatial density of particles in a sediment accumulation. Most monocrystalline quartz grains have concavo-convex contacts, suggesting that these grains have undergone
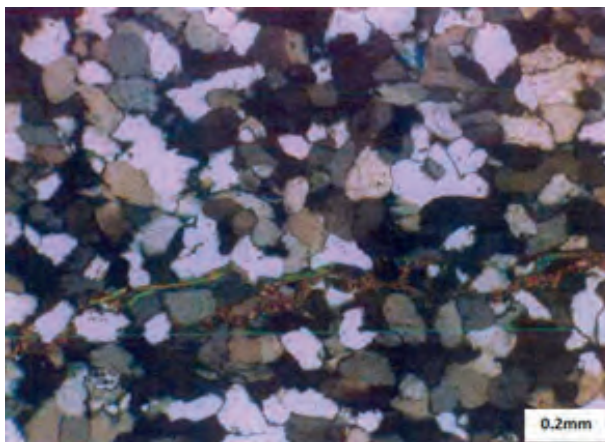

Fig. 4. Photomicrograph of quartz overgrowth, in which the quartz grew into the pore on one side which is not filled by clay minerals at the time, PPL, (Xl0).

Feldspar: The feldspar content in most sandstones averages between 10 and 15%, but in arkoses it may reach 50%. The mechanical stability of feldspar is lower than that of quartz, since feldspars are softer and have a stronger cleavage. This leads to disintegration of feldspar crystals during transportation, particularly in high energy depositional environments, so that on a broad scale, for example, fluviatile sediments contain more feldspar than beach or shallow marine sediments (Tucker, 1981). The alteration of feldspar

has been considered to reflect climatic conditions prevailing at the time at the depositional site. Feldspar occurs nearly in all types of crystalline rocks, so that feldspar grains of sand-size can be derived from granitoid igneous rocks, gneisses and schists in large amounts. The percentage and type of feldspar m sandstone depends on the rate and type of tectonic activity, and climate.

Feldspars are the second most abundant mineral in most sandstones (Boggs, 1995). The complex nature of the feldspar minerals has resulted in their being subdivided into many categories on the basis of their chemical, physical and structural characteristics. The categories of feldspar normally used by sedimentary petrologists are: (i) potassium (orthoclase, microcline and sanidine); (ii) plagioclase (albite through anorthite); and (iii) perthite (an intergrowth of sodium feldspar and potassium feldspar) (Blatt, 1982). The relative proportions of K-feldspar and albitic and anorthic plagioclases may be controlled either by the relative abundance of those feldspars in the igneous and metamorphic source rocks or by differential stability at the earth's surface (Pettijohn *et al*, 1987).

The feldspars are the second most abundant detrital grain types in the Hawaz Sandstone ranging from traces to 9%. The bulk of the feldspar grains are either K-feldspar or microcline, with lesser amounts of plagioclase. The untwined orthoclase is characterized by low relief and cleavage.

Rock Fragments: Pieces of polymineralic source rock form 15-20% of the average sandstone but can supply much more than 15% of the provenance information about the rock (Blatt, 1992). The composition of the rock fragment depends basically on source-rock geology and durability of particles during transportation. In sandstone, the lithic fragments are commonly fine-grained sedimentary and metasedimentary rocks such as mudstones, siliceous sedimentary rocks such as chert, and igneous, volcanic rocks (Tucker, 2001). The coarser-grained source rocks will contribute mostly mineral grains but depending upon the ratio of the grain-size of the source rock to the grain-size of the sandstone, they may also provide rock fragments. Thus, the larger the grain-size of the sandstone, the more likely is the occurrence of rock fragments, and the better the assessment of source terrane lithologies (Pettijohn *et al*, 1987).

Rock fragments in the Hawaz Sandstone are present, but not common, ranging from traces up to 3% in wells J4-NC186; A1-NC186 and H27-NCI15. They consist of metamorphic polycrystalline quartz

rock fragments or chert, with a few clays mineral fragments.

Mica: Sand-size detrital mica, because of its platy mature, would be expected to be the hydraulic equivalent of smaller particles of other minerals. As a result of the transportation and depositional characteristic of mica, its areal distribution in sediments reflects short-term response to environmental energy conditions. The absence of mica in recent sediments should indicate that either no mica is being contributed, or that energy conditions are such that winnowing, and/or by-passing of fines are important processes. The presence of mica flakes, on the other hand, indicates possible deposition, or that winnowing and/or by-passing are not being carried out efficiently (Doyle *et al*, 1957). The mica in the Hawaz Sandstone ranges from traces up to 3%, locally 6%, and it occurs as elongate grains under the SEM (Figs. 5 & 6). Muscovite is easily identified by its platy nature and parallel extinction. It is colorless in plane-polarized light and shows bright second-order colors under-crossed polars. Muscovite is distinguished by its tabular appearance bent through compaction between quartz grains.
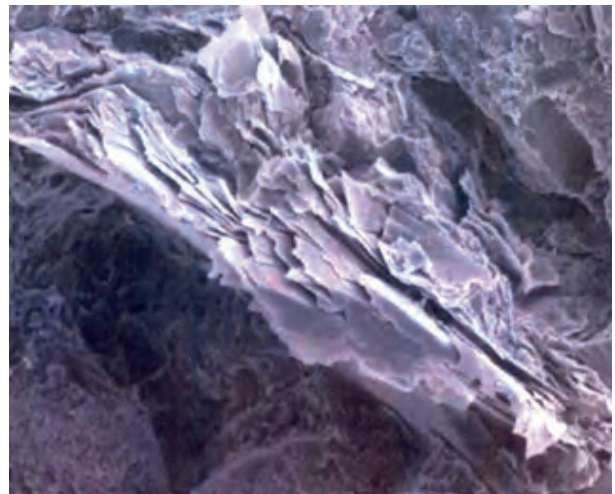

Fig. 5. SEM –photo: shows an elongate mica in the Hawaz Sandstone.

Clay Minerals: Clay minerals are the most common mineral group in sedimentary rocks, totaling about 45% by weight or volume. They are very small particles, commonly less than 1mm in size. The major clay minerals are kaolinite, montmorillonite, and illite. Nearly all clay-bearing sedimentary rocks contain more than one type of clay mineral (Blatt, 1982). The major origin of clay minerals is as subaerial weathering products of silicate minerals. All the chief clay groups are found in weathered residues and
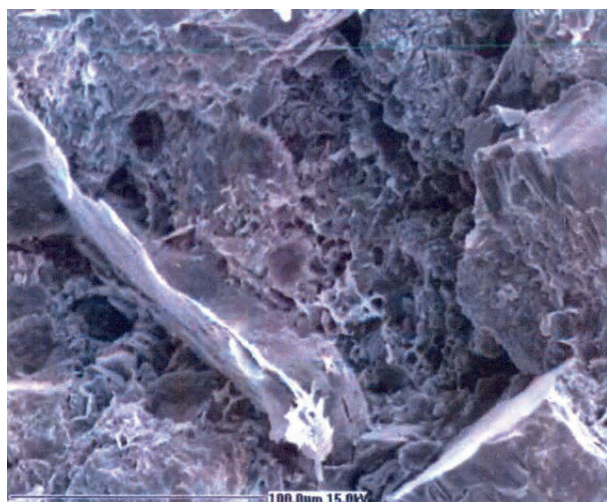
Fig. 6. SEM –photo: showing sheets of mica within the Hawaz Sandstone.

soils. Humid climates and well-drained topographies lead to extensive weathering of feldspars and their silicates to kaolinite. Lower rainfall and poorer drainage may result in the formation of smectite from the same parent materials. Mafic silicates in many climates will go to smectite. Illite products may form in intermediate to humid climates (Pettijohn *et al*, 1987). The clay minerals in the Hawaz sandstones are dominated by kaolinite (Fig. 7), which is colorless in plane-polarized light and grey-dark grey in cross polarized light, with weak birefringence.

Other Constituents
Pyrite: The mineral pyrite is a common and widespread authigenic constituent of sediments and sedimentary rocks where it is almost always found associated with organic matter. FeS_2 forms from
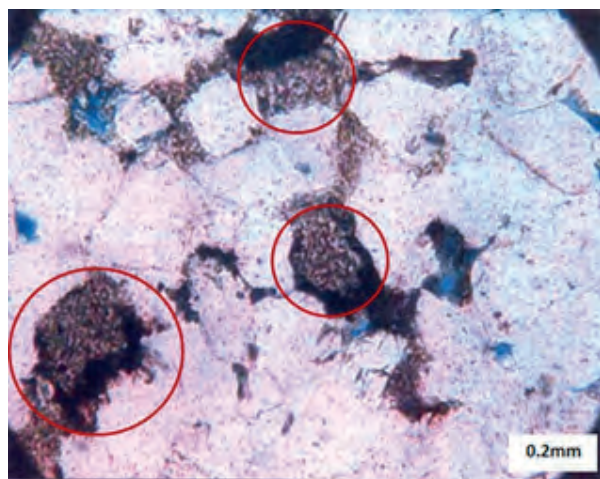

Fig. 7. Photomicrograph showing kaolinite replaced detrital grains and kaolinite fill pores in the Hawaz Sandstone, PPL, X20.

aqueous solution only in the presence of elemental sulphur or substances that produce elemental sulphur during decompaction (Berner, 1970). Several types of pyrite are present, with some having provenance significance whereas, others are post-depositional in origin (Gavinil *et al*, 2002). Pyrite is most common in marine sandstones because of the availability of the sulphate in seawater, but it is only an accessory diagenetic mineral. Pyrite is commonly altered to goethite/limonite on surface weathering (Tucker, 1981). Pyrite crystals in the Hawaz Formation range from traces up to 1%. Although the cubic pyrite grains are authigenic rather than detrital, they show the typical yellow-gold metallic color of pyrite in reflected light.

Sandstone Maturity
A distinction may be drawn between mineralogical maturity, which is strongly influenced by the composition of the source rock area, and textural maturity, which is more related to the history of transport and deposition (Nichols, 1999). Typically, compositionally immature sediments are located close to their source area, or they have been rapidly transported and deposited with little reworking from a source area of limited physical and chemical weathering (Tucker, 2001). It is widely believed that sorting is best when sand is repeatedly exposed to reworking by currents of moderate intensity. Probably the worst sorting occurs in sands subject to one brief episode of mass transport, such as a submarine slide, which is deposited below wave base in deep water (Pettijohn *et al*, 1987). Folk in (1951) described four stages of textural maturity. (1) Immature stage in which the sediment contains considerable clay and fine mica, the non-clay portion is itself poorly sorted, and the grains are angular. (2) Sub-mature stage in which the sediment contains very little or no clay, but the non-clay portion is still itself poorly sorted and the grains are angular. (3) Mature stage in which the sediment contains no clay and is well-sorted, but the grains are still subangular. (4) Super-mature stage. The framework grains in the Hawaz Sandstone are subrounded to subangular well sorted to moderately well sorted and texturally mature (Fig. 8 and Nichols, 1999).

Classification of the Hawaz Sandstone
A full description of sandstones usually includes some information concerning the types of grain present. Informal names such as 'micaceous sandstone' are used when the rock clearly contains a significant amount of a distinctive mineral, in this case mica (Nichols, 1999). There are several
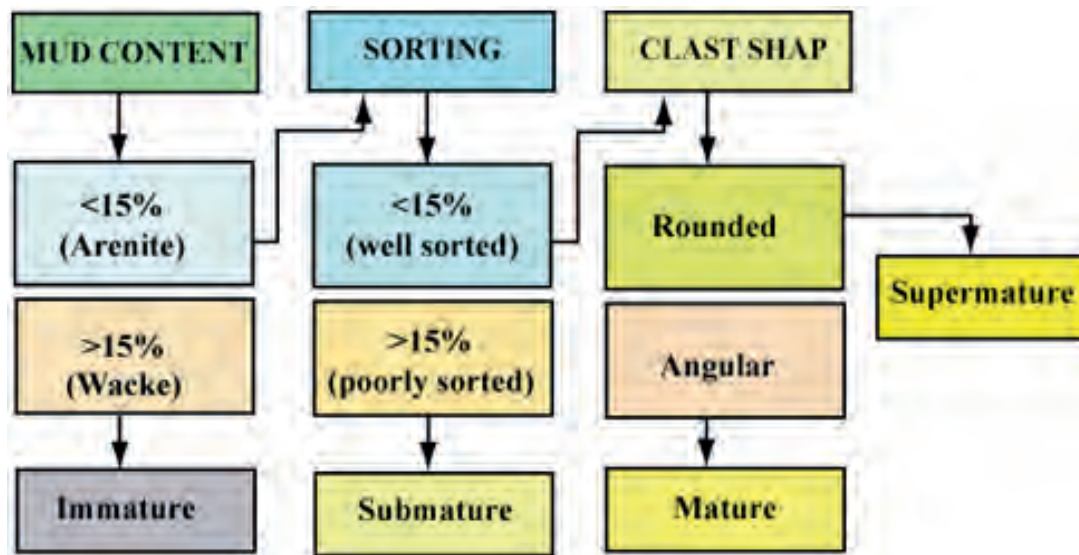
Fig. 8. Flow diagram for the determination of the textural maturity of a terrigenous clastic sediment or sedimentary rock (Nichols, 1999).

classification schemes available and most use a triangular diagram with end members of quartz (Q), feldspar (F) and rock fragments (L). The triangle is divided into various fields, and rocks with an appropriate modal analysis are given a particular name (Tucker, 1981). A widely used simple classification of sandstones is presented by Pettijohn *et al* (1987) based on the origin of the sandstone. The classification distinguishes between the "clean" sands or arenite-sands with less than 15% matrix and the "dirty" sands or wackes with more than 15% matrix (Pettijohn *et al*, 1987). The sandstones of the Hawaz Formation are classified according to that as mainly arenites, quartz-rich but feldspar and rock fragment poor (Fig. 9). The percentage of quartz in the Hawaz sandstones ranges between 96 to 99%, relative to feldspar and rock fragments, and the quartz is dominated by monocrystalline grains with abundant polycrystalline grains.

Many quartz arenites originate as shallow marine (but above storm wave base) sands that accumulated along or near the shoreline as beach, shoreline dune, tidal flat, spit, barrier island, or longshore bar deposits (Prothero and Fred, 1996).

Provenance of the Hawaz Sandstone

The term provenance, derived from the French "provenir", meaning to originate or to come forth, has been used to encompass all the factors relating to the production or "birth" of the sediment (Pettijohn *et al*, 1987). Sand composition, which is initially a function of the breakdown of a particular parent rock type under a given set of climate-

induced weathering conditions, is subject to later modification during transportation, deposition, and diagenesis (Suttner *et al*, 1981).

In many cases quartz arenites are the products of extended periods of sediment reworking, so that almost all grains other than quartz have been broken down by mechanical abrasion. Climate in the source area can also play a major role in producing quartz arenites. A warm humid climate will lead to the removal of many unstable grains, and if this is coupled with low relief and slow sedimentation rates, quartz will dominate the detritus. Many quartz grains in these arenites could be second cycle, derived from preexisting sediments (Tucker, 1981). Ternary diagrams have been used to plot the Hawaz Sandstone composition data for J4-NC186 (Fig. 10). These indicate that they were derived from similar parent rocks, under humid climatic conditions from plutonic and metamorphic rocks. According to Suttner *et al* (1981) humid weathering raises the proportion.

Diagenesis

Diagenesis has been divided into two broad stages: early diagenesis, for processes taking place from deposition and into the shallow-burial realm, and late diagenesis for those processes affecting the sediments at deeper levels, and on uplift. The terms eogenesis, mesogenesis and telogenesis have been used for early and burial diagenesis and diagenesis-on-uplift, respectively (Tucker, 2001).

From the microscope observations various diagenetic features can be recognized in the Hawaz
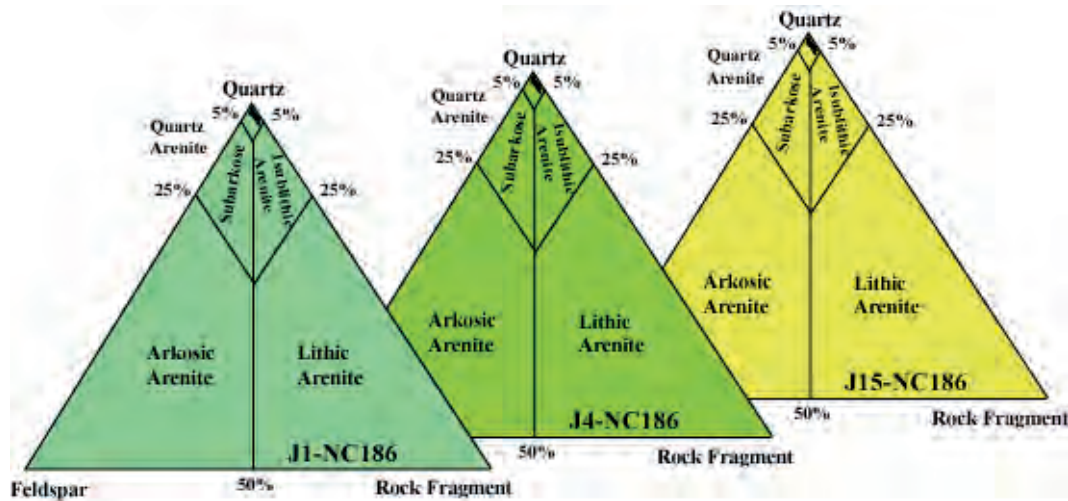
Fig. 9. Detrital composition of the Hawaz sandstones J4-NC186; A1-NC186, and H27-NC115, plotted in on a Pettijohn *et al* (1987) classification diagram.
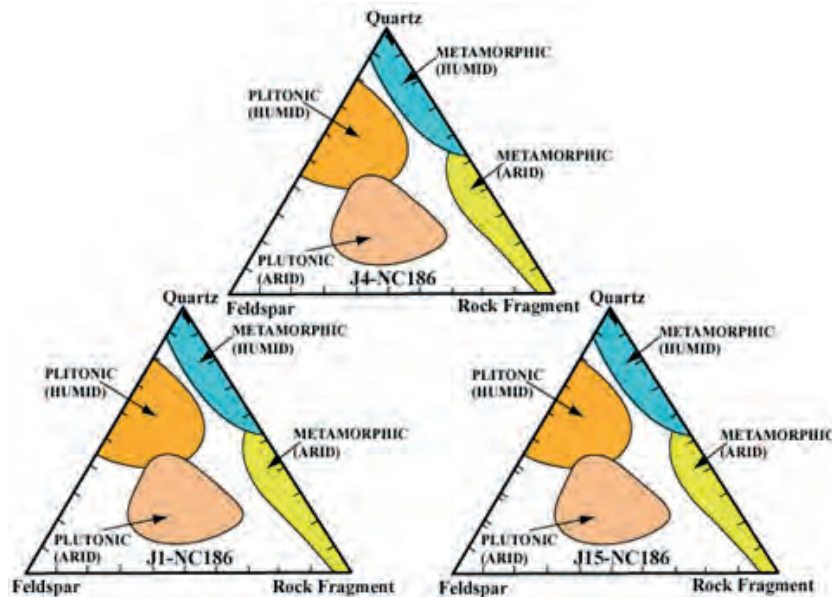

Fig. 10. Ternary QFRF plot showing the average composition of sandstones and source rocks for J4-NC186, which fall within the metamorphic humid climate field, (Suttner *et al*, 1981).

Formation including quartz overgrowth, calcite cement, chemical compaction (including pressure dissolution of minerals) and kaolinite and pyrite cement (Fig. 11).

Quartz Overgrowth: Quartz is the most common silicate mineral that acts as a cement in most sandstones, the quartz cement is chemically attached to the crystal lattice of existing quartz grains, forming rims of cement called overgrowths. Overgrowths can be recognized by a line of impurities or bubbles that mark the surface of the original grain. Quartz overgrowths are particularly common in quartz-rich sandstones (Boggs, 1995).

The quartz overgrowth is the first diagenetic precipitate and characterizes early burial (Siever *et al*, 1962), but it can occur at any time in the diagenetic sequence (Hancock and Taylor, 1978).

From thin sections analysis and SEM studies, it can be demonstrated that the deposition of quartz overgrowths occurred at an early diagenetic stage and continued to grow periodically throughout burial diagenesis, as evidenced by preservation of primary intergranular volume. The early quartz overgrowths can be seen under the microscope by a dust rim but good crystal terminations are scarce or absent (Figs. 12 & 13). The quartz grains are medium to very fine-grained, subrounded to
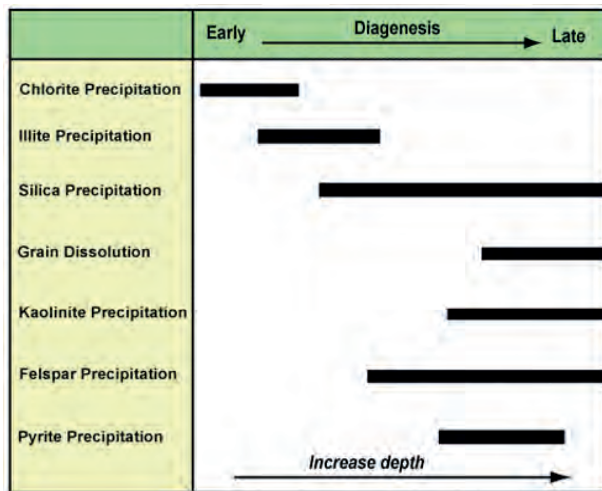
Fig. 11. Paragenetic sequence of diagenetic events in the Hawaz Sandstone, J1-NC186; J4-NCI86 and H15-NC186.

Fig. 13. SEM Photomicrography, showing quartz overgrowth with good crystal face. Note the quartz grain surface shows small features (wisps) which may be an indication that the grains were carried out by floating ice to the place where it was deposited.

subangular, well-sorted to moderately well-sorted, and near symmetrically skewed.

Carbonate Cementation: The most common diagenetic phase in sandstone (up to 30%) is carbonate cements in the form of calcite and dolomite, which rarely coexist in one sample. Dolomite occurs chiefly as a sparry interstitial cement or more rarely as a replacement of detrital plagioclase or as a fracture fill. The bulk of the calcite and dolomite is interpreted to be a relatively early cement, because when abundant within a rock, associated detrital micas are compacted (Boles, 1982).

Calcite is one of the most common cements in sandstones, but other carbonate cements of more local importance are dolomite and
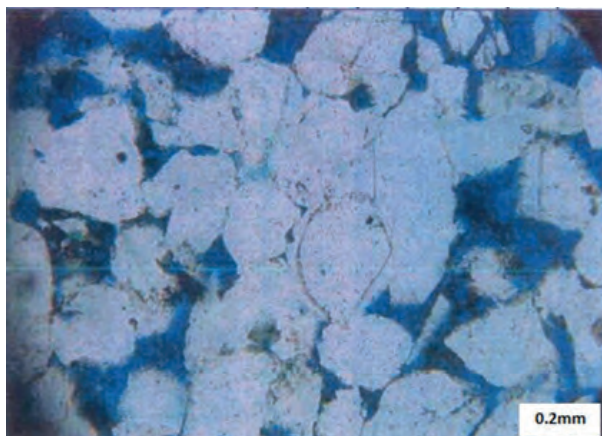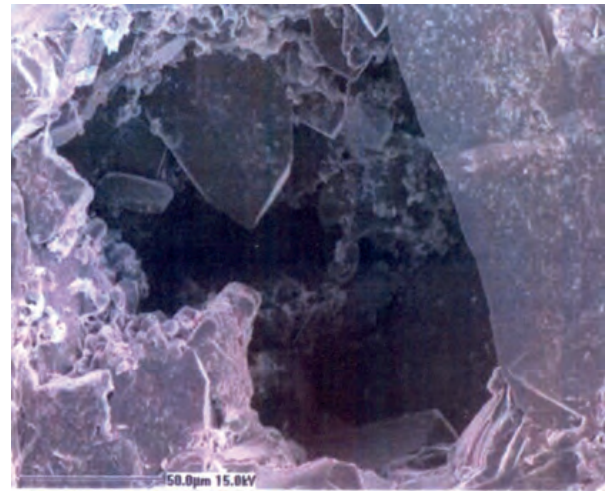
siderite. The cement may vary from a uniform to patchy distribution, to local segregations and concretions. The two main types of calcite cement are poikilotopic crystals and drusy calcite spar (Tucker, 1981). Carbonate cementation is favoured by increasing concentration of calcium carbonate in pore waters and increasing burial temperature (Boggs, 1995). They take several forms. In most cases each individual pore is filled by a single crystal of calcite, whilst in others, the calcite crystallized in large "poikilitic" patches which enclose many sand grains (Pettijon *et al*, 1987). Carbonate cementation in the Hawaz Formation (J4-NC186; A1-NC186 and J15-NC186) is volumetrically minor and dominated by calcite. The calcite occurs

Fig. 12. Photomicrograph showing quartz overgrowths, PPL, (X20), in the studied wells.

Fig. 14. Photomicrograph, showing pore-filling calcite cement within the Hawaz Sandstone, XPL, (Xl0).

both as isolated patches between grains as a grain-support, and as pore-filling (Fig. 14). The calcite causes corrosion of the margins of quartz grains. The calcite can be interpreted as an early cement which has been dissolved and the space probably filled by authigenic and kaolinite.

Dissolution of Unstable Grains: The potassium feldspars show petrographic evidence of alteration (Fig. 15) which can also be recognized under the SEM (Fig. 16). Most K-feldspar grains appear quite fresh or slightly broken whereas, the microcline and plagioclase encountered have been affected by dissolution. The microcline feldspar can be recognized by its grid twining. Late-stage quartz overgrowths can be distinguished by the quartz filling the pore space on one side, destroying the porosity, and being surrounded by crystals on the other sides (Figs. 15 & 16).
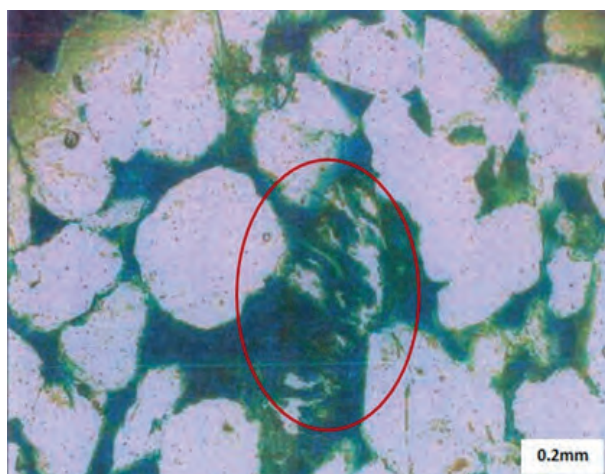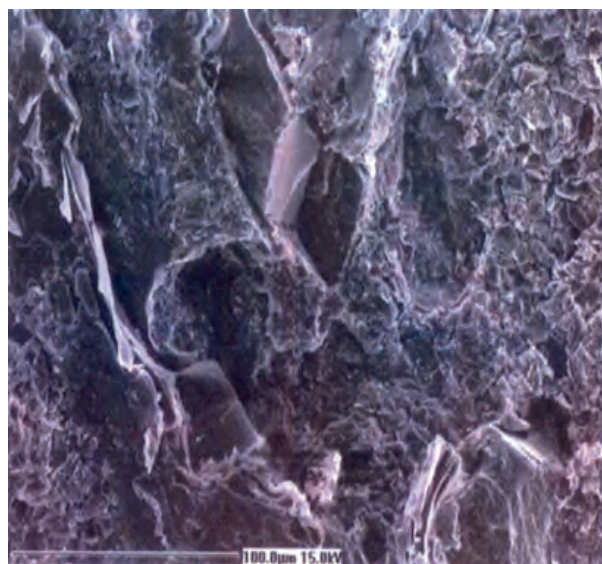

Fig. 16. SEM Photomicrography, shows the dissolution in the feldspars,

were subsequently dissolved, leaving a residue of kaolinite clay (Scholle and Schluger, 1979), showing well developed pseudo-hexagonal basal plates in curved vermicular stacks, (Fig. 17).

Authegenic Illite and Chlorite: Other clay minerals present in the Hawaz Formation sediments are smectite, illite and chlorite, which are present in amounts ranging from traces to up to 1%. The smectite under the SEM (Fig. 18) shows irregular, wavy plates or sheets. Illite forms needle-shaped crystals with strong birefringence, but it has not been recognized in the selected SEM samples. Chlorite is precipitated from pore fluids in rare patches on detrital grains, and from rock weathering and alteration of ferromagnesian minerals, such as biotite.

Fig. 15. Photomicrograph, shows the dissolution of an unstable feldspar grain in the Hawaz Sandstone, PPL, (Xl0).

Authegenic Clay Minerals: Clay minerals in sandstones may be both detrital and authigenic. Detrital clay mineral types cannot be identified with the petrological microscope, but some authigenic clays can. All the chief clay-mineral groups are represented in sandstones: kaolinite, illite, chlorite, smectite and mixed-layer clay. Detrital clays reflect the source-area geology, climate and weathering processes (Tucker, 2001).

Authegenic Kaolinite: The authegenic clay minerals in the Hawaz Sandstone are dominated by kaolinite. It partly fills both primary and secondary porosity. Secondary porosity probably formed from feldspar crystals which
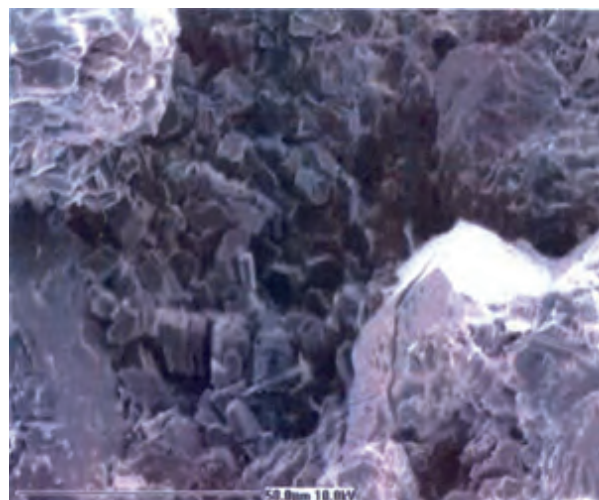

Fig. 17. SEM photomicrography shows pore-filling, book-shape plates of kaolinites.
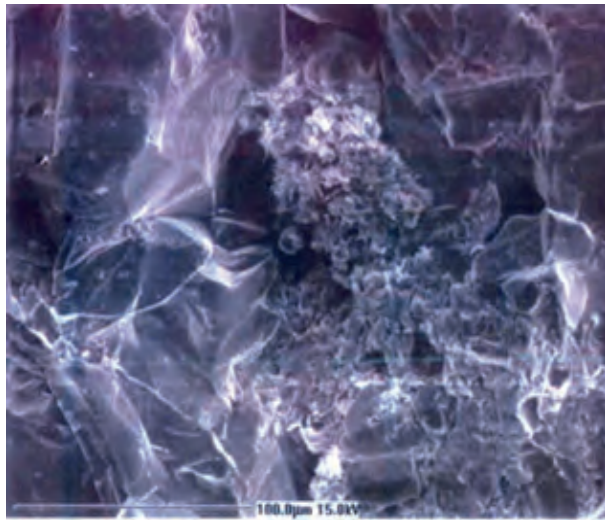
Fig. 18. SEM Photomicrography, showing the smectite within the Hawaz Sandstone.

CONCLUSIONS

This study of the Hawaz Sandstone shows that:
Hawaz Formation consists predominantly of alternating fine to medium-grained, well-sorted to moderately well-sorted sandstone displaying a variable degree of bioturbation.

- The Hawaz Formation was deposited in wave-dominated shoreface and shelf environments. The stratigraphical and sedimentological characteristics of the Hawaz Formation in the study area in the Murzuq Basin are attributed to shoreface and shelf facies associations within which some 9 facies have been distinguished. The lower part of the cored section of the Hawaz Formation is dominated by the outer and inner shelf facies associations.
- The outer shelf association is dominated by mudstone whereas, the inner shelf association is dominated by siltstone/sandstone.
- Petrographic data shows that the Hawaz sandstones can be classified mainly as a quartz arenite, with local subarkoses.
- Diagenetic cement is mainly in the form of quartz overgrowths, and local calcite and clay matrix, all of which have reduced the porosity.

REFERENCES

Bellini, E. and Massa, D. (1980). A Stratigraphic Contribution to the Palaeozoic of the Southern Basins of Libya. In: *Geology of Libya* (Ed. by: M. J. Salem and M. T., Busrewil), 2nd Symp.. Univ. Libya, Fac. Sci., Tripoli, V. *1*: 3-27.

Berner, R. A. (1970). Sedimentary Pyrite formation. *Am. Jour. Science, 268*: 1-23.

Blatt, H. (1982). Sedimentary Petrology. *Freeman and Company*, New York, 514p.

Boles, J. R. (1982). Active Albitization of Plagioclase, Gulf Coast Tertiary. *Am. Jour. Sci, 282*: 165-180.

Boggs, S. JR. (1995). Principles of Sedimentology and Stratigraphy. Merrill, Columbus, Ohio,-Hall, Upper Sander River, New Jersey, *2nd edition*: 774p.

Davidson. L.; Beswetherick. S.; Craig. J.; Eales, M.; Fisher, A. and Himmali, A. (2000). The Structure, Stratigraphy and Petroleum Geology of the Murzuq Basin, Southwest Libya. In: *M. A. Geological exploration in Murzuq Basin*. Elsevier Science, Amsterdam: 295-320.

Doyle, J. L.; Cleary, W. J. and Andpilkey, O. H. (1957). Mica: Its Use in Determining Shelf-Depositional Regimes. *Marine Geology, V. G*: 381-389.

Folk, R. L. (1951). A Comparison Chart for Visual Percentage Estimation. *Jour. Sed. Petrol., V. 21(1)*: 32-33.

Gavinil, E.; Rasmussen, B.; Krapez, B. and Groves, D. I. (2002). Paleo-Environmental Significance of Rounded Pyrite in Siliciclastic Sequences of the Late Archaean Witwatersrand Basin: Oxygen-Deficient Atmosphere or Hydrothermal Alteration? *Sedimentology, V. 49*: 1133-1156.

Hancock, N. J., and Taylor, A. M. (1978). Clay Mineral Diagenesis and Oil Migration in the Middle Jurassic Brent Sand Formation. Geol. Soc., London, *V. 135*: 69-72.

Nichols. G. (1999). *Sedimentology and stratigraphy*. Sedimentology and stratigraphy: Blackwell Science, Oxford, 355pp.

Pettijohn, F. J.; Potter, P. E. and Siever, R. R. (1987). *Sand and sandstone*. Spring-Verlage, New York: 260p.

Prothero, D. R., and Fred, S. (1996). *An introduction sedimentary rocks and stratigraphy*. Publ. W. H. Freeman and Company: 574pp.

Scholle, P. A. and Schluger, P. R. (eds.). (1979). Aspects of diagenesis. Soc. *Econ. Paleont. Miner. Spec. Publ., V. 26*: 443pp.

Siever, R. (1962). Silica Solubility, 0-200C, and the Diagenesis of Siliceous Sediments. *Jour. Geol., V. 70*: 127-150.

Suttner, L. J.; Basu, A. and Mack, G. (1981). Climate and Origin of Quartz Arenites, *Jour. Sediment. Petrol., V. 51*: 1235-1246.

Thomas, D. (1995). Geology, Murzuq Oil Development Could Boost S.W. Libya Prospects. *Oil & Gas Jour. 93(10)*: 41-46.

Tucker, M. E. (1981). *Sedimentary Petrology: An Introduction to the origin of Sedimentary Rocks*. Blackwell Science. Oxford. 252p.

ABOUT THE AUTHOR

Eman A. M. Taktek had finished her BSc at the University of Tripoli, Faculty of Engineering in 2009. She completed her MSc at the Libyan Academy in the field of Earth Science in 2017. Eman is started her professional job with Waha Oil Company, Tripoli, Libya since 2015 and still.

e-mail: eman_tek2012@yahoo.com

GEOCHEMICAL EVALUTION OF THE TANEZZUFT FORMATION IN THE JIFARAH TROUGH, NW LIBYA

Aisha K. Shalghum[1] and Mahmoud T. Elbakai[1]

Abstract: The study area (Jifarah Trough) is bound to the north by a coastal fault system. To the south the Jifarah Trough is bound by the east-west trending Al Aziziyah Fault System and to the southwest by the Telmzane Arch; the Nafusah Uplift defines its eastern limit. The region lies at the intersection of two major structures the NNW trending Tripoli-Tibisti Arch formed in Caledonian times and the E-W trending Jifarah Uplift formed during the Hercynian Orogeny. The best expected hydrocarbon source rock in the area is the lower hot shale member of the Tanezzuft Formation. Several reservoirs can be targeted as hydrocarbon traps such as the Ordovician quartzitic sandstone in Tunisia and the sandstone of the Silurian Acacus Formation in Libya. The objectives of this study are to assess the source rock potential, measure the thermal maturity of the source rock (Silurian Tanezzuft Formation), and to recognize the sources of organic matter and probable depositional conditions for this formation.

A Rock-Eval 6 was used for bulk geochemical screening analysis. The analytical error of the system was assessed using an IFP standard sample. Seventeen samples were analysed by GC and GC/MS. The results gained during this study show that the TOC wt.%, S1 and S2 are high in the lower part of the formation and low in the upper part. Furthermore, all maturity parameters based on Rock-Eval, and biomarker maturity parameters give indicators to vertical variation of thermal maturity from late immature to early mature, although the aromatic hydrocarbons show higher ratios in the lower part than in the upper part of the Tanezzuft Formation. The Tanezzuft Formation is characterized by marine algae organic input with a bacterial contribution and that, dysoxic-anoxic conditions may be the most probable for the depositional environment of the lower Tanezzuft Formation with slightly more oxic conditions associated with some samples of the upper Tanezzuft Formation.

INTRODUCTION

Geographic Location

The Jifarah region is at the eastern end of the South Atlas Lineament or Saharan Flexure which defines the southern margin of the Atlas fold belt (Dewey & Burke, 1973; Biju-Duval *et al.,* 1977). The flexure runs from Morocco ENE to ESE and extends into Tunisia, where it branches to northwest Libya as the Jifarah Axis (Anketell, 1981; Anketell & Ghellali, 1991). This Jifarah Axis forms the southern margin of the Pelagian Platform (Burollet, 1978) and the Jifarah Trough (Fig. 1).

Regional geophysical data suggest that the depth to basement in the trough ranges from 1820 to 6060 metres (Echikh & Suleiman, 1983). The trough is bounded to the north by a coastal fault system which separates it from the related offshore Tarabulus Basin (Swire & Gashgesh, 2000). To the south the Jifarah Trough is bounded by the east-west trending Jifarah Fault System and to the southwest by the Telmzane Arch and Dahar Uplift; the Nafush Uplift defines its eastern limit (Fig. 1). Sedimentary infill of the trough is predominantly of Carboniferous, Permian and Triassic age and its genesis is mainly related to tectonic movements associated with the Hercynian Orogeny. There was also an extensional tectonic phase in the Middle to Late Triassic and some younger tectonic activity which led to rejuvenation of old fault trends, folding and associated volcanic activity.

The structural history of the Jifarah region has been discussed by a number of authors. The region lies at the intersection of two major structures,
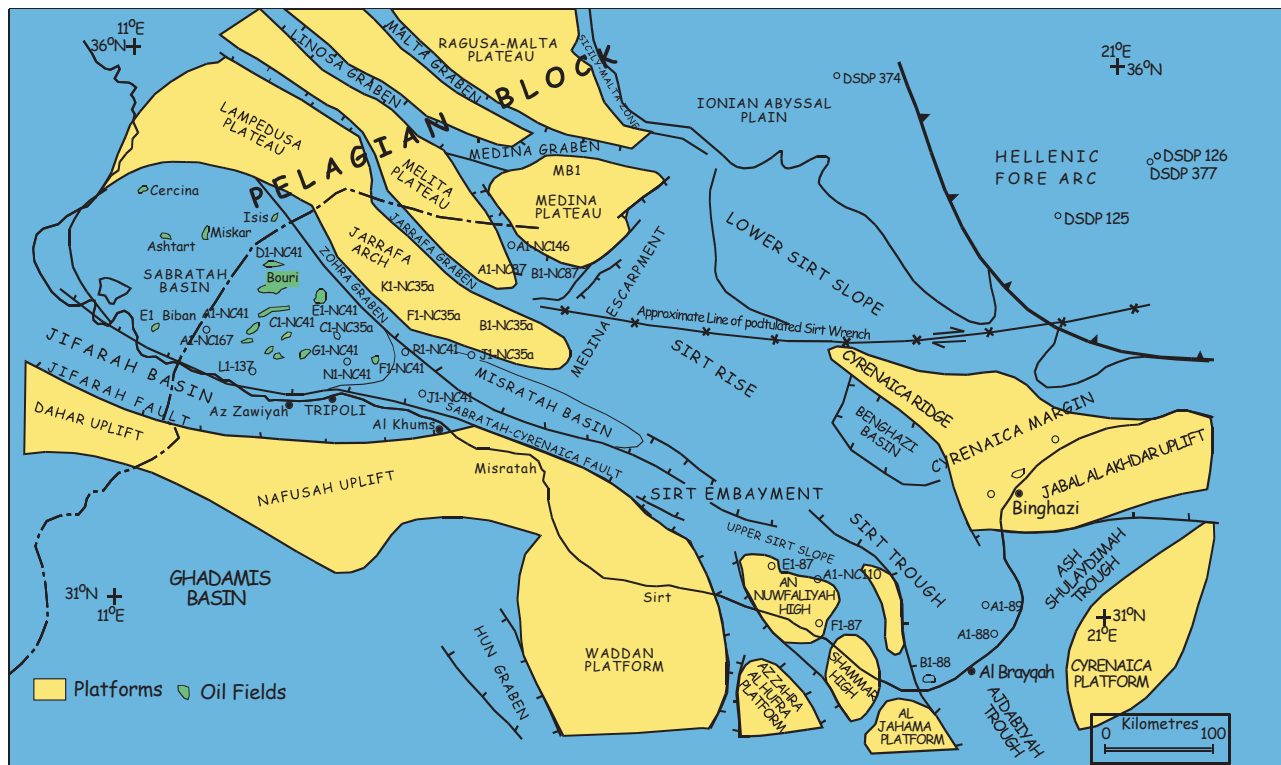
Fig. 1. Location Map of the Jifarah Trough, Libya.

the NNW trending Tripoli-Tibisti Arch formed in Caledonian times and the E-W trending Jifarah Uplift formed during the Hercynian Orogeny (Mikbel, 1977; Goudarzi, 1980).

Busson (1967) suggested that a subsidence zone, the Jifarah Flexure, occurred north of the Saharan Platform where thicker and more marine strata are characteristic.

Structure Components of the Jifarah Area

The Jifarah area can be distinguished by three main geomorphological units (El Hinnawy & Cheshitev, 1975) as follows:
1. The Jifarah Plain: This is nearly flat and is bounded in the north by the Mediterranean Sea and in the south by Jabal Nafusah. It is covered by Quaternary deposits with occasional outcrops of limestone hills belonging to the Al Azizyah Formation.
2. The Jabal: This is one of the dominant morphological features of northwestern Libya and is known as Jabal Nafusah (Jabal Gharyan). The Jabal runs in south-west to north-east direction from Al Khums and westwards to beyond the Libyan-Tunisian border. The Jabal is built by Mesozoic rocks which are made of limestone, sandstone, clay, dolomite, dolomitic limestone and gypsum.

3. The Plateau: This is made mainly of hard and resistant dolomitic limestone of Upper Cretaceous age. In the area southeast of Gharyan it is covered by basalt sheets forming a flat and broad plain.

Regional and Stratigraphic Geology

The stratigraphic sequence of the Jifarah Trough which extends from the basement to Quaternary is illustrated in (Fig. 2).

Basement and the Early History of the Jifarah Trough: The igneous basement was emplaced during the Pan-African Orogeny which took place during the late Precambrian to Middle Cambrian. This was as a result of continental collision and it established many of the fundamental tectonic patterns in North Africa. The only well to have penetrated the basement in the Jifarah Trough is the A1-9 well. Following the Pan African Orogeny there was a period of peneplanation of uplifted areas which led to deposition of siliciclastic sediments in the Late Cambrian and Ordovician periods. In the Jifarah Trough directly overlying the basement, transparent to white fine grained sandstones with thin interbeds of green shale (Hasaouna Formation) were deposited in subtidal to intertidal environment (Albani *et al,* 1991).

Fig. 2. Composite stratigraphical column, Concession 9, Jifarah Trough.

Ordovician System: A thick sequence of Ordovician age siliciclastic sediments was deposited to the south of the Jifarah Trough in the Ghadamis and Murzaq basins. The Ordovician section in the Jifarah Trough has been partly truncated by an unconformity. Erosion was associated with tectonic movements related to the Hercynian event.

Organic-rich black shales of the basal Tanezzuft Formation (Fig. 2) subcrop to the south of the Al Azizyah Fault Zone. The shales represent deposition during what was probably post-glacial flooding across much of the North African and Arabian platforms (Ref.).

The Tanezzuft Formation is a thick sequence of graptolitic, thinly laminated siltstones, shales and fine-grained sandstones. The type section is in the Wadi Tanezzuft near to the town of Ghat in the south west of Libya. The Tanezzuft Formation is of Early Silurian age.

In the Jifarah area of NW Libya the thickness of the Tanezzuft Formation is very variable. A

thick sequence of the Tanezzuft Formation was penetrated by the MER-1 well on the Tunisian side of the Libyan-Tunisian Border (Swire & Gashgesh, 2000). The only well north of the Al Azizyah Fault Zone (and therefore in the Jifarah Trough) that has been recorded as penetrating the Tanezzuft Formation is the Tunisian well LG-1 (Swire & Gashgesh, 2000).

AIM AND OBJECTIVES OF THIS STUDY

In the Jifarah area, important oil shows have been observed in some drilled water and oil wells, but there has been no significant oil discovery in the region. Accordingly, this area is not classified as good for hydrocarbon prospection. Geochemical studies in neighbouring sedimentary basins emphasized that the shales of the Silurian Tanezzuft Formation have a high quantity of organic matter, which could generate significant amounts of hydrocarbons. Regarding previous geochemical correlations between oil samples and the potential source rocks, it is believed that the Tanezzuft Formation is the main source rock in the western part of Libya. The geological studies showed that the Tanezzuft Formation is present in considerable thickness in this region and there are good structures for the migration and accumulation of hydrocarbons.

There are 17 samples from the Tanezzuft Formation of Well (B1-23), comprising ditch cutting and core samples covering the interval from 1291 to 1431m. All samples from this interval are dark greenish to olive grey (95-100%) shale.

Therefore, the aim of this paper is to identify and evaluate the probable source rock (Tanezzuft Formation) of the study area, as well as to gain a better understanding of the petroleum potential of source rock within the Jifarah Trough. The objectives include the following: i) to assess the source rock potential of the Tanezzuft Formation using Rock-Eval 6. ii) to measure the thermal maturity of source rock samples, and any thermal maturity changes exhibited by the Tanezzuft Formation in the Jifarah Trough using biomarker-based maturity parameters as well as Rock-Eval (Tmax). iii) to recognize the sources of organic matter and probable depositional conditions for the source rock samples using biomarker distribution characterization with Gas Chromatography/Mass Spectrometry (GC/MS).

MATERIALS AND METHODS

Cutting and core samples of Tanezzuft Formation from B1-23 well were analyzed using Rock-Eval 6, gas chromatography (GC) and gas chromatography mass spectrometry (GC-MS). Rock-Eval 6 was used for bulk geochemical screening analysis at laboratories of the Libyan Petroleum Institute, Tripoli, Libya. The analytical error of system was assessed using an IFB standard sample. The source rock samples were progressively heated in an inert atomosphere (S1) and were thermally cracked (S2 & S3). Total organic carbon (TOC) was determined by oxidation under air, Tmax, HI, OI, and PI were also obtained.

All aliphatic and aromatic hydrocarbon fractions were analyzed by GC. The fractions were run on an HP5890 gas chromatograph with an auto-sampler and automatic split/splitless injector. Gas chromatography mass spectrometry (GC-MS) analysis of aliphatic and aromatic hydrocarbon fractions were carried out using a Hewlett-Packard 5890 II GC spilt/ spiltless injector (280 °C) linked to a Hewlett-Packard 5972 Mass Selective Detector.

RESULTS

Bulk Geochemistry

Geochemical analyses of rock samples from upper and lower part of the Tanezzuft Formation in well (B1-23) were used to evaluate their hydrocarbon potentials Table 1. The Total Organic Carbon (TOC) and hydrocarbon potential (S2) showed a broad variation with depth through the formation. The lowest value of TOC in the upper Tanezzuft is 0.36% at a depth of 1301m, while the highest value is 1.07% at 1360.93m depth. In the lower Tanezzuft the lowest value of TOC is 1.45% at 1401m deep, while the highest value is 12.35 % at 1431 m. The lowest value of S2 is 0.48mg HC/g rock recorded at a depth of 1301 m and the highest value is 2.37mg HC/g rock at depth 1360.93m in the upper Tanezzuft, while the lowest value of S2 is 3.59mg HC/g rock recorded at depth 1401m and the highest value is 34.90mg HC/g rock at depth 1431m of depth. The Tmax and PI values are very low and range from 433 to 437°C and 0.03 to 0.09 respectively in the upper Tanezzuft, and 426 to 436°C and 0.05 to 0.06 in the lower Tanezzuft. The samples show hydrogen indices (HI) values which

range from 110 to 280mg HC/g TOC through the upper Tanezzuft and 284 to 379mg HC/g TOC through the lower Tanezzuft.

Molecular Geochemistry
Gas Chromatography (GC)

Table 2 provides a summary of the geochemical data for the upper and lower Silurian Tanezzuft Formation. The molecular distribution of saturated hydrocarbons is shown in fig. 3 and 4. The Upper and Lower Silurian Tanezzuft Formation show *n*-alkanes distribution dominated generally by short chain C_{14} to C_{25} and acyclic isoprenoids (pristane and phytane). The Pr/Ph ratios range from 0.81 to 1.48 through the upper part of the Tanezzuft, and 1.26 to 1.48 through the lower part of the Tanezzuft. The Pr/*n*-C_{17} and Ph/*n*-C_{18} ratios<1 through the whole formation which indicates that *n*-alkane (*n*-C_{17} and *n*-C_{18}) is more abundant than Pr & Ph. Generally, the distribution of *n*-alkanes shows no relative dominance of odd carbon numbers (CPI~1).

Gas Chromatography/Mass Spectrometry (GC/MS)
1- *Hopane*: The aliphatic fractions of both parts were analysed by GC-MS to obtain the percentage composition of hopane, sterane and diasterane. The hopane as monitored by the *m/z* 191, two selected samples are shown in Fig. 5 and 6. All Tanezzuft samples show similar distributions with predominance of $C_{30}αβ$ hopane. The doublets of $C_{29}αβ$ hopane and $C_{29}Ts$, series of $C_{31}αβ$ to $C_{35}αβ$ hopanes with two isomers (22S & 22R), $C_{29}βα$, $C_{30}βα$ (diahopane), C_{27} 18α (H) T_s (neohopane), and C_{27} 17 α (H)T_m are all present. The variation of hopanes biomarkers are represented by gradual changes in the relative concentration of some isomers with depth, with consequent effects on molecular parameters Table 3 and Table 5.
2- *Sterane and diasterane*: The selected mass chromatogram *m/z* 217 (steranes) and *m/z* 259 (diasteranes) are shown in Fig. 7, 8, 9 and 10. Generally, the diasteranes and sterane have similar distributions in all Tanezzuft samples, with some gradual changes in the relative abundance of some isomers with the depth. The distribution includes:
i) The C_{27} to $C_{29}βα$ diasterane (20S & 20R).
ii) The C_{27} to $C_{29}ααα$ and αββ steranes with two isomers (20S & 20R).
iii) The $C_{30}ααα$ 20R sterane is present in all lower Tanezzuft Formation samples but low or absent in upper Tanezzuft Formation samples.

Table 1. Rock-Eval Pyrolysis Results for Selected Core and Cutting samples from well B1-23.

Depth (m)	Formation	S1 mg HC/g rock	S2 mg HC/g rock	S3 mg HC/g rock	PI	S2/S3	TOC wt %	Tmaxº C	HI mg HC/g TOC	OI mg CO₂/g TOC
1291	U.Tanezzuft	0.04	0.64	0.47	0.06	1.36	0.48	435	134	91
1301	U.Tanezzuft	0.02	0.48	0.64	0.04	0.75	0.36	434	134	179
1315	U.Tanezzuft	0.03	0.55	0.94	0.05	0.59	0.50	435	110	188
1325	U.Tanezzuft	0.02	0.58	0.83	0.03	0.69	0.48	434	121	174
1335	U.Tanezzuft	0.02	0.68	0.70	0.03	0.97	0.52	434	131	135
1345	U.Tanezzuft	0.03	0.86	0.50	0.03	1.72	0.61	435	140	82
1352.70	U.Tanezzuft	0.18	1.78	0.59	0.09	3.02	0.89	436	201	66
1356.36	U.Tanezzuft	0.17	2.25	0.25	0.07	9.00	0.80	437	280	31
1360.93	U.Tanezzuft	0.08	2.37	0.13	0.03	1.82	1.07	435	222	12
1361	U.Tanezzuft	0.04	0.74	0.77	0.05	0.96	0.61	435	122	127
1371	U.Tanezzuft	0.08	0.98	1.16	0.08	0.84	0.72	433	136	161
1381	U.Tanezzuft	0.07	1.11	1.05	0.06	1.06	0.68	434	162	154
1391	U.Tanezzuft	0.03	0.63	0.44	0.05	1.43	0.45	434	141	99
1401	L.Tanezzuft	0.21	3.59	0.49	0.06	7.33	1.45	436	248	34
1411	L.Tanezzuft	0.55	8.35	0.68	0.06	12.28	2.74	433	305	25
1421	L.Tanezzuft	1.05	15.93	0.81	0.06	19.67	4.20	432	379	19
1431	L.Tanezzuft	1.85	34.90	2.12	0.05	16.46	12.35	426	283	17

Table 2. The Geochemical data (acyclic isoprenoid and *n*-alkanes ratio) in well B1-23.

Depth (m)	Formation	Pr/Ph	CPI	Pr/nC_{17}	Ph/nC_{18}	(Pr+nC_{17})/(Ph+nC_{18})
1291	U.Tanezzuft	0.83	1.09	0.32	0.33	0.85
1301	U.Tanezzuft	0.83	1.09	0.27	0.33	0.97
1315	U.Tanezzuft	0.81	1.09	0.34	0.34	0.81
1325	U.Tanezzuft	0.86	1.09	0.33	0.33	0.86
1335	U.Tanezzuft	1.07	1.09	0.33	0.30	0.99
1345	U.Tanezzuft	1.04	1.12	0.34	0.32	1.00
1352.70	U.Tanezzuft	1.03	1.09	1.14	0.99	0.97
1356.36	U.Tanezzuft	1.48	1.09	0.95	0.74	1.29
1360.93	U.Tanezzuft	1.38	1.00	0.96	0.75	1.20
1361	U.Tanezzuft	0.83	1.07	0.31	0.29	0.79
1371	U.Tanezzuft	1.03	1.09	0.35	0.32	0.96
1381	U.Tanezzuft	1.00	1.10	0.31	0.30	0.97
1391	U.Tanezzuft	1.00	1.08	0.34	0.30	0.90
1401	L.Tanezzuft	1.26	1.08	0.41	0.37	1.18
1411	L.Tanezzuft	1.38	1.03	0.56	0.46	1.20
1421	L.Tanezzuft	1.36	1.00	0.37	0.36	1.34
1431	L.Tanezzuft	1.48	1.10	0.32	0.32	1.48

Some common maturity parameters such % $C_{29}\alpha\alpha\alpha$ (20S/20S+20R), % C_{29} ($\alpha\beta\beta/ \alpha\beta\beta+ \alpha\alpha\alpha$), and % diasteranes/steranes and environment parameters such as $C_{27}\alpha\alpha\alpha/C_{28}\alpha\alpha\alpha$ 20R and $C_{27}\alpha\alpha\alpha/C_{29}\alpha\alpha\alpha$ 20R ratios were calculated using peak area from *m/z* 217 chromatogram, as shown in Table 4 & Table 5 respectively.

3- *Aromatic*: GC/MS was used to analyse the aromatic hydrocarbon fractions for seventeen selected samples. Five ions were detected (*m/z* 142 methylnaphthalenes, *m/z* 156 dimethylnaphthalenes, *m/z* 170 trimethylnaphthalenes, *m/z* 178 phenanthrene and *m/z* 192 methylphenanthrenes) to calculate some aromatic maturity parameters and *m/z* 134 which indicate an environmental condition: examples of these mass chromatograms are shown in Fig. 11, 12, and 13. Table 6 shows calculated aromatic maturity parameters. These ratios were
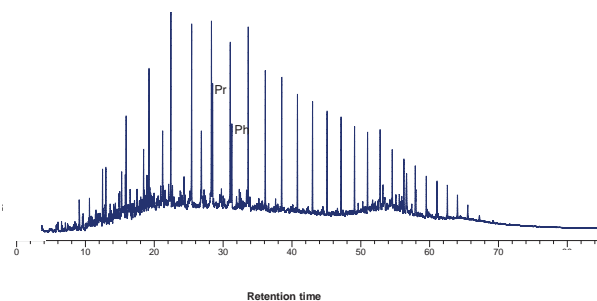
Fig. 3. Gas chromatogram showing the normal alkane distribution for the sample 1356.36m.
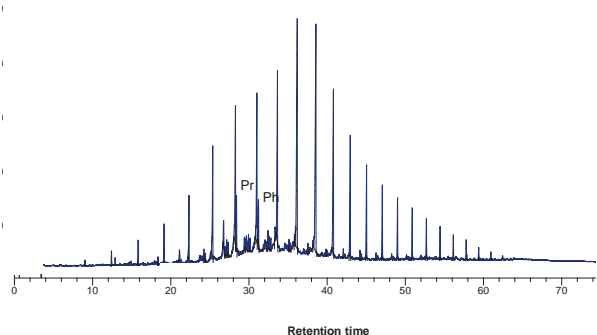

Fig. 7. m/z 217 mass chromatogram showing the sterane and diasterane distributions for the sample 1391m.

Fig. 4. Gas chromatogram showing the normal alkane distribution for the sample 1381m.

Fig. 8. m/z 217 mass chromatogram showing the sterane and diasterane distributions for the sample 1421m.

Fig. 5. m/z 191 mass chromatogram showing the hopane distribution for the sample 1352.70m.

Fig. 9. m/z 259 mass chromatogram showing the diasterane distribution for the sample 1356.36m.
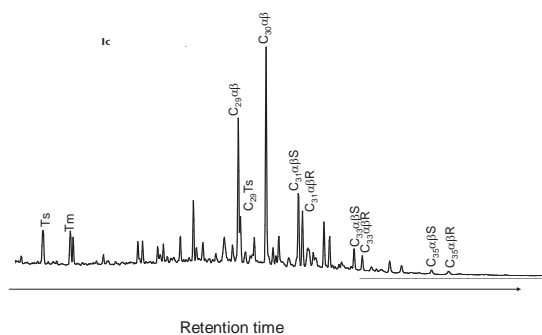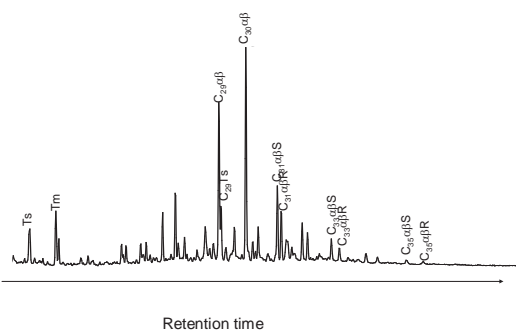

Fig. 6. m/z 191 mass chromatogram showing the hopane distribution for the sample 1361m.

Fig. 10. m/z 259 mass chromatogram showing the diasterane distribution for the sample 1381m.
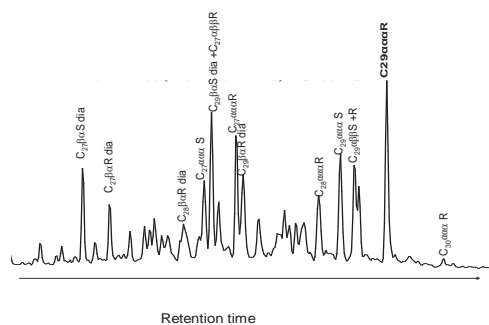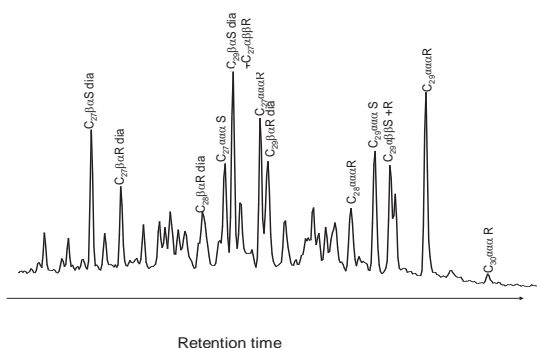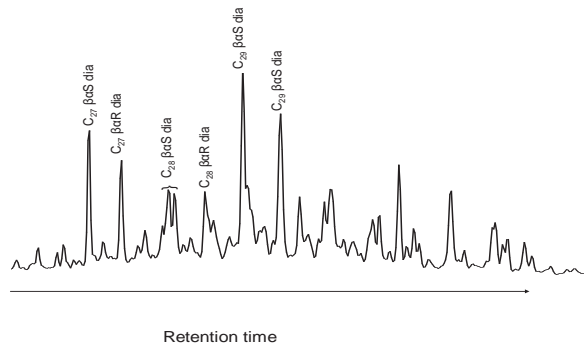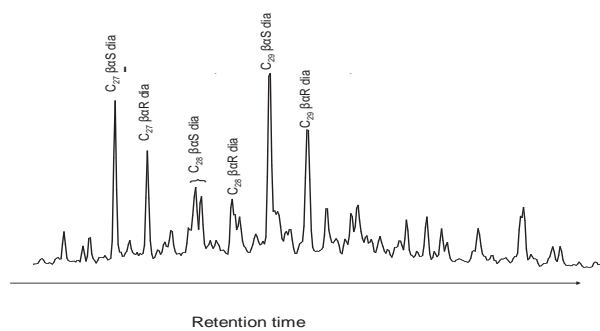
Table 3. Selected maturity parameters using *m/z* 191 hopane biomarker peak areas.

Depth (m)	Formation	$T_s\%$	$\%C_{29}T_s$	$\%C_{31}\alpha\beta22S/(22S+22R)$	$\%C_{30}\beta\alpha/\beta\alpha+\alpha\beta$
1291	U.Tanezzuft	41	17	61	20
1301	U.Tanezzuft	37	20	61	15
1315	U.Tanezzuft	41	15	60	20
1325	U.Tanezzuft	38	20	62	17
1335	U.Tanezzuft	37	23	59	16
1345	U.Tanezzuft	41	24	61	13
1352.70	U.Tanezzuft	55	23	62	11
1356.36	U.Tanezzuft	29	30	58	13
1360.93	U.Tanezzuft	29	30	61	12
1361	U.Tanezzuft	46	22	62	13
1371	U.Tanezzuft	45	25	62	13
1381	U.Tanezzuft	43	32	59	13
1391	U.Tanezzuft	41	32	59	15
1401	L.Tanezzuft	48	32	59	14
1411	L.Tanezzuft	52	29	58	14
1421	L.Tanezzuft	57	28	60	13
1431	L.Tanezzuft	59	22	64	11

Table 4. Selected maturity parameters using *m/z* 217 sterane biomarker peak areas.

Depth (m)	Formation	$\%C_{29}\alpha\alpha\alpha$ 20S	$\%C_{29}\alpha\beta\beta/\alpha\beta\beta+\alpha\alpha\alpha$	%Diasteranes/ steranes
1291	U.Tanezzuft	32	29	35
1301	U.Tanezzuft	32	36	31
1315	U.Tanezzuft	33	31	36
1325	U.Tanezzuft	30	27	41
1335	U.Tanezzuft	30	29	48
1345	U.Tanezzuft	32	30	52
1352.70	U.Tanezzuft	36	35	32
1356.36	U.Tanezzuft	29	27	27
1360.93	U.Tanezzuft	29	27	26
1361	U.Tanezzuft	33	32	33
1371	U.Tanezzuft	32	32	41
1381	U.Tanezzuft	35	33	63
1391	U.Tanezzuft	39	37	47
1401	L.Tanezzuft	38	31	53
1411	L.Tanezzuft	40	33	53
1421	L.Tanezzuft	42	36	58
1431	L.Tanezzuft	45	41	65

calculated by using absolute peak areas of the respective compounds. The MNR parameter in the upper part of the Tanezzuft Formation does not show considerable variation. The values range from 0.90 to 1.50, whereas, in the lower part they range from 1.14 to 1.77, with slight increase with increasing of depth Table 6. DNR1 shows wide variation in both the upper and in the lower parts of the formation. The ratio ranges from 1.64 to 8.23 and from 3.31 to 6.36 in the upper and the lower parts of the Tanezzuft Formation respectively (Table 6).

The rest of maturity parameters (TNR1, MPI-I, MPR and Rc) do not show a great variation in the upper and in the lower parts of the Tanezzuft Formation (Table 6).

INTERPRETATION AND DISCUSSION

Source Rock Potential
Organic Richness
According to bulk geochemistry (Table 1), the Tanezzuft Formation in Jifarah Region is a potential

Table 5. Selected depositional environment parameters calculated using *m/z* 217, 191 peak areas.

| Depth (m)	Formation	$C_{27}\alpha\alpha\alpha(20R)/$ $C_{28}\alpha\alpha\alpha(20R)$	$C_{27}\alpha\alpha\alpha(20R)/$ $C_{29}\alpha\alpha\alpha(20R)$	Homohopane Index
1291	U.Tanezzuft	1.64	0.88	3.10
1301	U.Tanezzuft	1.34	0.74	3.42
1315	U.Tanezzuft	1.66	0.89	3.21
1325	U.Tanezzuft	1.65	0.87	2.47
1335	U.Tanezzuft	1.68	0.88	C_{35} hopanes are absent
1345	U.Tanezzuft	1.52	0.75	2.73
1352.70	U.Tanezzuft	1.22	0.53	4.11
1356.36	U.Tanezzuft	1.26	0.65	3.97
1360.93	U.Tanezzuft	1.23	0.64	3.26
1361	U.Tanezzuft	1.48	0.76	3.87
1371	U.Tanezzuft	1.48	0.70	C_{35} hopanes are absent
1381	U.Tanezzuft	1.37	0.64	3.24
1391	U.Tanezzuft	1.41	0.64	3.14
1401	L.Tanezzuft	1.63	0.67	3.53
1411	L.Tanezzuft	1.65	0.65	3.29
1421	L.Tanezzuft	1.79	0.76	4.06
1431	L.Tanezzuft	1.51	0.71	C_{35} hopanes are absent
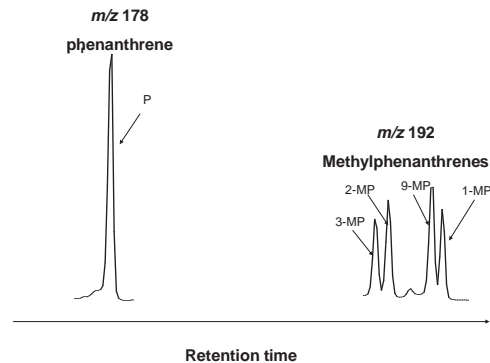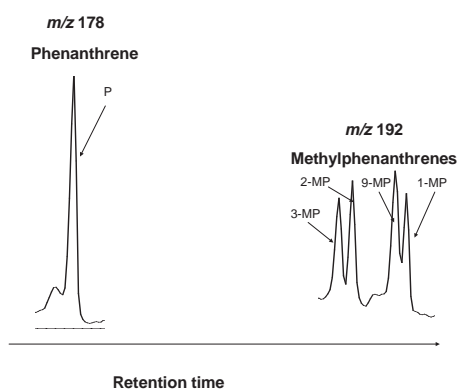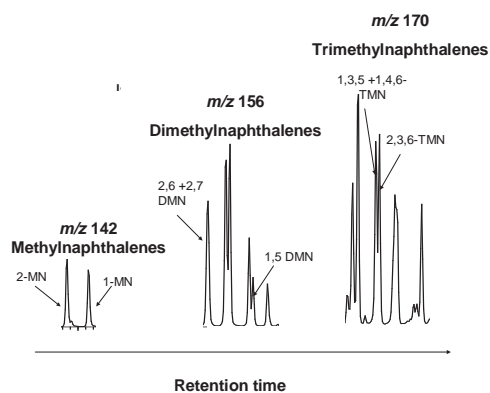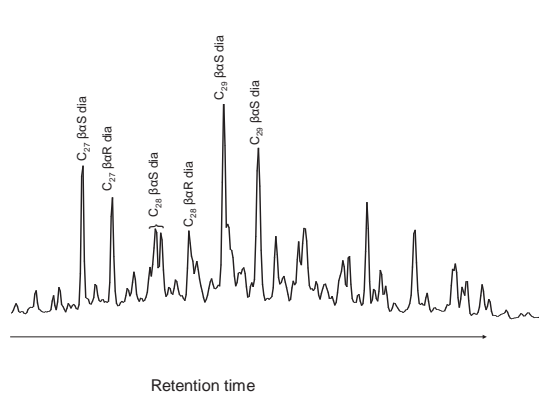
Fig. 11. GC/MS mass chromatograms for the aromatic hydrocarbon in sample 1356.36m.

Fig. 12. GC/MS mass chromatograms for the aromatic hydrocarbon in sample 1401m.
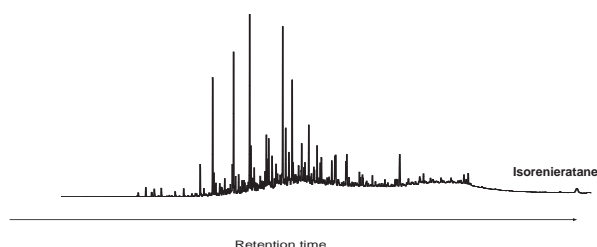
Fig. 13. *m/z* 134 mass chromatogram showing the isorenieratane distribution for the samples 1401m.

source rock in Well B1-23 because the upper part of this formation has a mean TOC value greater than 0.63 wt. %, which indicates good source potential. The mean of residual hydrocarbon (S2) is >1.05 mg/g HC indicating poor residual potential. The lower part of the Tanezzuft Formation has mean TOC values greater than 5 wt %, which indicates very rich source rock, and mean residual hydrocarbon (S2) value of around 15 mg/g HC indicating very good residual potential (Table 7; Peters, 1986). Figure 14 shows the linear relationship between TOC and S2 in the Tanezzuft Formation. This diagram can be used as an indicator of petroleum potential and the type of kerogen by calculating the average HI (Langford & Blanc-Valleron, 1990). The HI calculated from the slope of TOC and S2 is greater than the mean of measured HI by about 100 (Cornford, 1998). The regression slope of lines for upper Tanezzuft samples give an average HI of 301mg HC/g TOC indicating type II oil prone kerogen. The slope for lower Tanezzuft samples represent mean HI value of 277mg HC/g TOC, this line indicates kerogen type II/III (Fig. 14 a). In contrast figure 14b shows that the regression slope of lower part of Tanezzuft Formation indicates a mean HI of 450mg HC/g TOC (one sample with a TOC 12.35% excluded). This suggests that the lower part of Tanezzuft Formation is type II kerogen and good oil prone.

In summary, TOC value and residual hydrocarbon of the upper part of the Tanezzuft Formation indicate poor potential source rock. The same parameters indicate that the lower part of this formation is very rich potential source rock.

Organic Matter Maturity
Bulk geochemical data: The Production Index (PI) together with Tmax values were used to evaluate maturity level. Table 8 shows how to use the production indicators (PI) and Tmax to estimate maturity.

Table 6. Maturity parameters based upon aromatic hydrocarbons.

Depth (m)	Formation	MNR	DNR 1	TNR 1	MPI-1	MPR	Rc
1291	U.Tanezzuft	0.96	2.85	0.97	0.54	1.16	0.73
1301	U.Tanezzuft	1.09	3.45	0.85	0.59	1.33	0.75
1315	U.Tanezzuft	1.45	3.72	0.80	0.56	1.26	0.73
1325	U.Tanezzuft	0.91	1.46	1.00	0.60	1.22	0.76
1335	U.Tanezzuft	1.10	2.98	0.70	0.53	1.25	0.72
13459	U.Tanezzuft	1.14	3.20	0.81	0.52	1.22	0.71
1352.70	U.Tanezzuft	1.29	5.06	0.61	0.64	1.10	0.79
1356.36	U.Tanezzuft	1.50	8.23	0.43	0.77	1.17	0.86
1360.93	U.Tanezzuft	1.42	5.63	0.55	0.74	1.19	0.84
1361	U.Tanezzuft	1.05	3.33	0.82	0.64	1.35	0.79
1371	U.Tanezzuft	0.90	2.78	1.05	0.59	1.26	0.75
1381	U.Tanezzuft	1.22	3.71	0.79	0.63	1.25	0.78
1391	U.Tanezzuft	1.20	3.32	0.78	0.59	1.25	0.75
1401	L.Tanezzuft	1.29	3.36	0.61	0.66	1.25	0.79
1411	L.Tanezzuft	1.77	6.36	0.92	0.64	1.13	0.78
1421	L.Tanezzuft	1.46	5.66	0.69	0.69	1.19	0.81
1431	L.Tanezzuft	1.14	3.31	0.46	0.67	1.15	0.80

Methylnaphthalene Ratio (MNR) = 2-MN/1-MN
Dimethylnaphthalene Ratio (DNR 1) = (2, 6-DMN+2, 7-DMN)/1, 5-D
Trimethylnaphthalene Ratio (TNR 1) = 2, 3, 6-TMN/ (1, 3, 5-TMN+1, 4, 6-TMN)
Methylphenanthrene Index (MPI-1) = 1.5*(3-MP+2-MP)/ (P+9-MP+1-MP)
Methylphenanthrene Ratio (MPR) = 2-MP/1-MP
Vetrinite Reflectance (Rc) = (0.6*MPI 1) + 0.4

Table 7. Geochemical parameters describing source rock generative potential.

Quality	TOC (wt%)	S1 mg HC/g rock	S2 mg HC/g rock
Poor	0-0.5	0-0.5	0-2.5
Fair	0.5-1	0.5-1	2.5-5
Good	1-2	1-2	5-10
Very good	2+	2+	10+

Table 8. Geochemical parameters describing level of thermal maturation (after Peters *et al*, 2005).

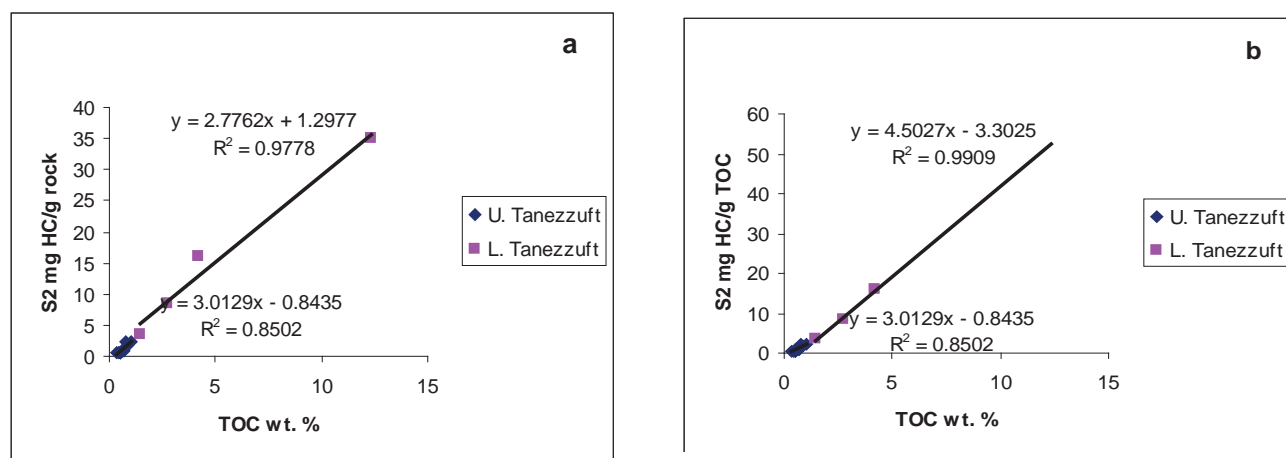| Quality	TOC (wt%)	S1 mg HC/g rock	S2 mg HC/g rock
Poor	0-0.5	0-0.5	0-2.5
Fair	0.5-1	0.5-1	2.5-5
Good	1-2	1-2	5-10
Very good	2+	2+	10+

Fig. 14. Cross plot between TOC & S2 for the Tanezzuft Formation. a: with high TOC value, b: excluding high TOC value.

Tmax ranges in both parts, from 426-437°C, these values are very low which indicates late immature to early mature source rock. Production indices (PI) values throughout this formation are low (0.03-0.09), which correspond with the Tmax values (Fig. 15), and indicate the sediments are late immature to early mature. Figure 16 illustrates a cross plot between Tmax and HI. This diagram showing a vertical variation in HI may indicate kerogen variation. Most of the Tanezzuft samples are late immature (Tmax < 435), and kerogen is type II and II/III.
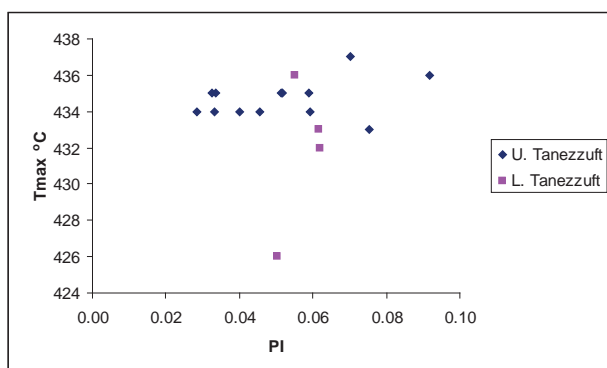

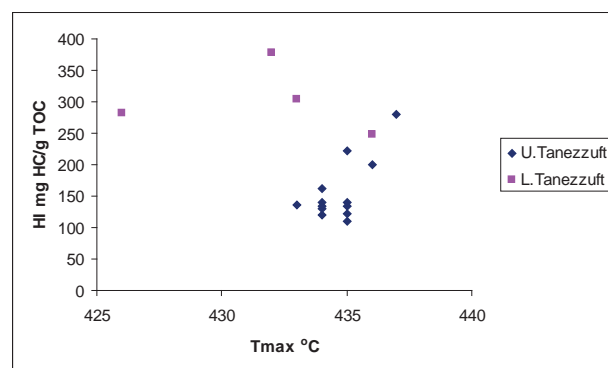Fig. 15. Cross plot between PI and Tmax for Tanezzuft Formation.

Fig. 16. Tmax plotted against HI for the Tanezzuft samples.

*Molecular Maturity Parameters***:** The relative abundance of odd even carbon-numbered n-paraffins can be used to obtain a crude estimate of thermal maturity of petroleum. These measurements include the carbon preference index [(CPI) (Bray & Evans, 1961)]. CPI values significantly above (odd preference) or below (even preference) 1.0 indicate low thermal maturity. Values of 1.0 do not prove that an oil or rock extract is thermally mature (Peters & Moldowan, 1993). Based on this, most Tanezzuft samples showed a CPI value > 1.0 which suggest immature to low mature samples.

Maturity parameters based on hopane and sterane ratios were shown in Table.3 and Table 4 respectively. The $C31\alpha\beta\%22S/22S+22R$ parameter is the most widely applied of the hopane maturity parameters, and records the relative enrichment of the more thermally stable 22S isomer compared to the biologically-derived 22R stereochemistry. The increases in 22S% is initially the result of a greater proportional increases of 22S isomer, followed by the earlier and more rapid decreases in abundance of 22R isomer. Therefore, the main two factors controlling this parameter are the relative rate of generation and thermal degradation (Farrimond *et al*, 1998). Bishop and Abbott (1993) also reported that 22S/22S+22R being to increase as a result of release/generation of 22S which increases more rapidly relative to its initial concentration than 22R. This parameter shows equilibrium values throughout two parts of the Tanezzuft Formation, the upper part ranging from 58 to 62%, whereas, the lower part ranges from 58 to 64% (the equilibrium value of 55-60%; Seifert & Moldowan, 1986). These values of %22S indicate that the Tanezzuft Formation is at early mature level. The T_S/T_S+T_m parameter is commonly used for maturity assessment, although it is known to be very dependent on organic facies (Moldowan *et al*, 1986). This parameter increases with maturity, just before and within the oil window. The T_S parameter increases with maturation when T_m decreases in abundance, and T_S concentration continues to increase; the main increases in this parameter is controlled by earlier and faster thermal degradation of T_m (Farrimond *et al*, 1998). In the present study there is a slightly noticeable variation in this ratio through the upper and lower Tanezzuft Formation, it remains constant due to the early mature level. Furthermore, $\%C_{29}T_S$ parameter behaves in a similar way to $\%T_S$ parameter (Farrimond *et al.*,

1998). The relative loss of 17 β-hopanes occurs in the early stages of thermal maturity (Farrimond *et al*., 1998). The maturity sensitive sterane isomers ratios are based on the percentage of C29ααα 20S/20S+20R. This ratio increases from zero to equilibrium at 50 -55% (Mackenzie *et al*, 1980). It is based on the relative enrichment of 20S isomers compared with 20R isomers. An increases in 20S/20S+20R is concomitant with a loss in concentration of 20S, the rate of loss of which is less than that of 20R, hence 20S continuous to increase relative to 20R (Bishop & Abbott, 1993). Abbott *et al* (1990) noted that release or generation of 20R and 20S from extracted vitrinite kerogen occurred in the laboratory, concluding from this the control on the maturity dependent variations of 20S/(20S+20R), is composite of empire release or generation from components followed by sterane loss. The Tanezzuft Formation has %20S parameter range from 29 to 39% at the upper part of the section which increases to range from 38 to 45% at the lower part, it is considered as late immature to early mature. The $\%C29\alpha\beta\beta$ parameter reaches to equilibrium at 67 to 71% (Seiferd & Moldowan, 1986). This ratio is effective at higher level maturity, due to being slower to reach equilibrium than %20S parameter (Peters & Moldowan, 1993). In the upper part of Tanezzuft Formation the ratio ranges from 27 to 37%, from 31 to 41% in the lower part of Tanezzuft Formation which is considered as an immature formation. Moreover, Figure 17 illustrates the relationship between %C29ααα and C29%αββ which indicates that not all samples have reached their end point values. Figure 18 represents the variation of thermal maturity biomarker parameters of sterane and diasterane with depth. This plot shows that the maturity increases gradually with depth.
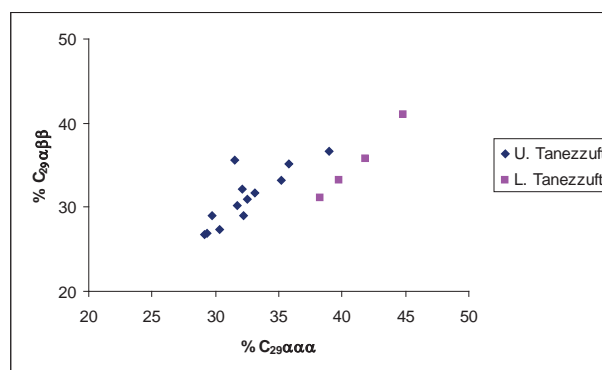

Fig. 17. Cross plot between $\%C_{29}\alpha\alpha\alpha$ and $\%C_{29}\alpha\beta\beta$
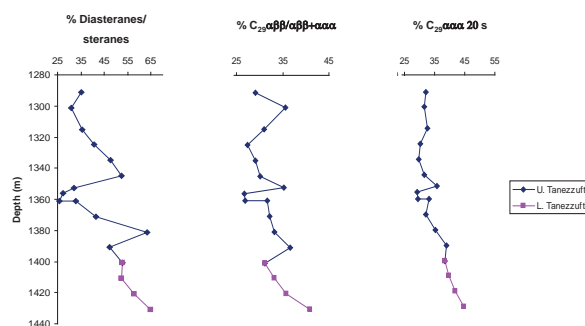
Fig. 18. Displays the variation of sterane and diasterane thermal maturity parameters within the Tanezzuft Formation.

From Tmax, the production indices (PI), and biomarker data it can be seen that the section of the Tanezzuft Formation in the well B1-23 is at late immature to early mature level.

Maturity parameters based on alkylphenanthrene and alkylnaphthalene are displayed in Table 6 and Figure 19. The methylphenanthrene index (MPI-1) appears to be useful as vitrinite reflectance to determine the thermal maturity of source sediments in late oil window and gas prone. It increases with maturity due to the relative thermal stabilities of methylphenanthrene isomers (α & β) and methylation of phenanthrene, which represent stable (β) methylphenanthrene isomers (2-MP & 3-MP) relative to less stable (α) methylphenanthrene isomers (1-MP & 9-MP) and phenanthrene (P).

The MPI-1 parameter within the two parts of the Tanezzuft Formation shows values that range from 0.52 to 0.77, indicating mature formation. Calculated vitrinite reflectance (VRc%) estimates, using the formula proposed by Radke et al (1984), shows values ranging from 0.71 to 0.86 within the whole Tanezzuft section, again considered as a mature section. Methylphenanthrene ratio (MPR)

is also used as a maturity parameter in late oil window and gas zone, and increases with maturity due to the relative stabilities of β & α. MPR ratio within the study section shows a range from 1.10 to 1.35, and this given an indication to mature section. Methylnaphthalene ratio (MNR) is also used as maturity parameter at a higher maturity level than MPI-1; it increases with maturity due to the thermal stabilities of β methyls and α methyls. The MNR within the Tanezzuft section shows a range from 0.90 to 1.77, indicating mature section

Based on aromatic parameters the Tanezzuft sediments seem to be mature. This conclusion is in contradiction with all other parameters (Rock-Eval data, CPI, hopane & sterane ratios), which conclude that the Tanezzuft samples used in this study are late immature to early mature. This contradiction can be explained by that the aromatic ratios e.g. MPI are good parameter within oil window as a hydrocarbon internal maturity parameter (Radke et al, 1981). Moreover, this contradiction also can be related to organic facies; at the maturity stage onset of intense n-alkane generation has been found in coals (Radke et al, 1980) and sediments predominantly terrestrial organic matter (Radke et al, 1981), and the sediments of Tanezzuft Formation found to be kerogen type II amorphous (AOM).

SOURCE OF ORGANIC MATTER AND DEPOSITIONAL CONDITIONS

Source of Organic Matter

Rock-Eval 6 parameters suggest a kerogen type II and II/III. Type II kerogens are mainly dominated by well-preserved amorphous (AOM), but not all type III kerogen is derived from land plants as hydrogen indices of any kind of organic matter can be lowered
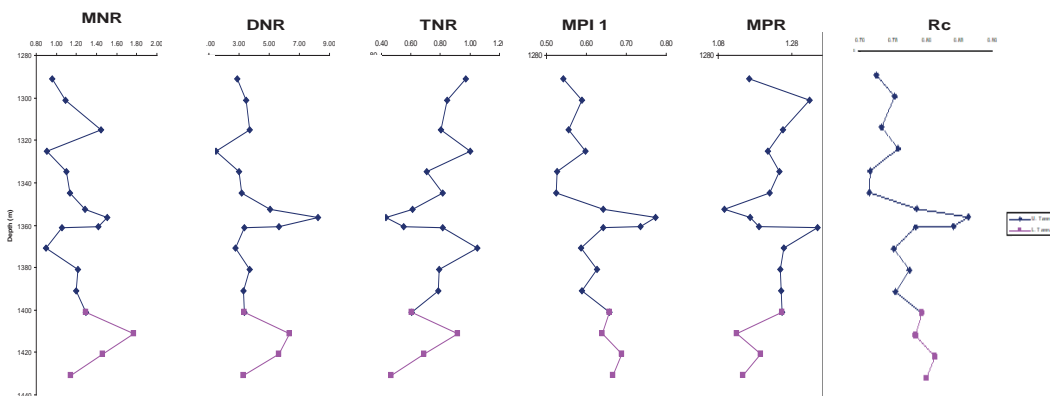

Fig. 19. Display the variation thermal maturity of aromatic parameter within upper and lower Tanezzuft Formation

by aerobic degradation, and thus its kerogen type increased e.g. II to III, III to IV. Original type II AOM partially degraded in depositional environment thus often end up with a type III gas prone composition. According to above type II/III in our samples which belong to Silurian do not mean land plants as to be known the diversity and distribution of terrestrial increased greatly during the Devonian (Killops & Killops, 1993). The source of the organic matter can be described using the Van Kervelen diagram (atomic O/C versus O/C) or a modified Van Kervelen diagram (OI versus HI), but the result should be supported by microscopy, element analysis or both (Peters, 1986). From the Rock-Eval data the observed linear relationship between the S2 and TOC values (Fig. 14) indicates that the organic matter within the Tanezzuft section in well B1-23 has generally the same origin (Espitalié *et al*, 1985) or is at least of the same source Type (II,III) with composition between type II and III. Gas fingerprints are indicative of certain types of source organic matter input (Peters *et al*, 1993). A representative gas chromatogram of saturated hydrocarbon fraction shows the normal alkanes distribution to have an abundance of the short-chain compounds within most of the upper and lower Silurian Tanezzuft samples which indicates an algal phytoplankton and/or bacterial input (Hunt, 1995). Gelpi *et al*, (1970) also reported that the high relative abundance of short-chain *n*-alkane suggested algal contribution. The Pr/*n*-C_{17} and Ph/*n*-C_{18} data points give a result indicating that the source rock samples are type II and III kerogen mixture and algal marine which agree with the Rock-Eval results. The sterane distribution of the whole of the Tanezzuft samples is largely dominated by C_{27} and C_{29} homologs, with the sterane carbon number predominance being $C_{29} > C_{27} > C_{28}$ at the beginning of upper part of the section and $C_{27} \sim C_{29} > C_{28}$ at the end of the Tanezzuft section and a predominance of C_{27} and C_{29} over $C_{28}\alpha\alpha\alpha$ 20R sterane. The relative abundance of $C_{29}\alpha\alpha\alpha R$ steranes in organic matter can often be associated with a predominant input of terrestrial land plants, where, the $C_{27}\alpha\alpha\alpha R$ steranes are often associated with marine organic matter (zooplankton), and $C_{28}\alpha\alpha\alpha R$ represent phytoplankton input (Huang & Meinschein, 1979). Caution needs to be implemented when interpreting the distribution of the relative abundance of C_{27}, C_{28}, and C_{29} steranes, as it has been reported that brown algae and many species of green algae contain predominantly C_{29} sterols (Moldowan *et al.*, 1985). Furthermore,

previous studies showed oil and sediments having a high proportion of C_{29} sterane which is not related to land plants (Mickirdy *et al*, 1986). The concentration of C_{29} $\alpha\alpha\alpha$ steranes observed through the section of the Tanezzuft Formation in most of the samples must be predominantly phytoplankton algal in origin. Figure 20 illustrates the relationship between the C_{27} $\alpha\alpha\alpha 20R/C_{29}$ $\alpha\alpha\alpha 20R$ ratio and the C_{27} $\alpha\alpha\alpha 20R/C_{28}$ $\alpha\alpha\alpha 20R$ ratio as they are not dramatically influenced by maturity (Peters & Moldowan, 1993), and there are small distributions between these ratios in both parts, which indicate that the upper and lower Tanezzuft Formation have relatively the same source (algal input). Significant algal contribution in both parts of the Tanezzuft Formation is also suggested from the relative high abundance of diasteranes (Rubinstein *et al*, 1975), steroidal compounds (Volkman, 1986), and an absence of any obvious higher plant marker compounds (Peters & Moldowan, 1993). Bacterial contribution is clearly recorded in all Tanezzuft samples as evidenced by the high abundance of the hopanes (Ourisson *et al*, 1979). Moreover, homohopanes (C_{31}-C_{35}), which are derived from bacteriohopanetetrol and other polyfunctional C_{35} hopanoids common in prokaryotic microorganisms (Ourisson *et al*, 1984; Rohmer, 1987), are present through the upper and lower parts of the Tanezzuft Formation although these may be either bacterial or algal lipid source indicators.

The Rock-Eval, gas chromatogram, and biomarker results indicate a marine algae organic input, with additional abundance of bacterial contribution.

Depositional Conditions

The following Rock-Eval data point to an environmental condition at Tanezzuft Formation. The relationship between TOC and HI (Fig.21) represents a high variation in TOC and hydrogen
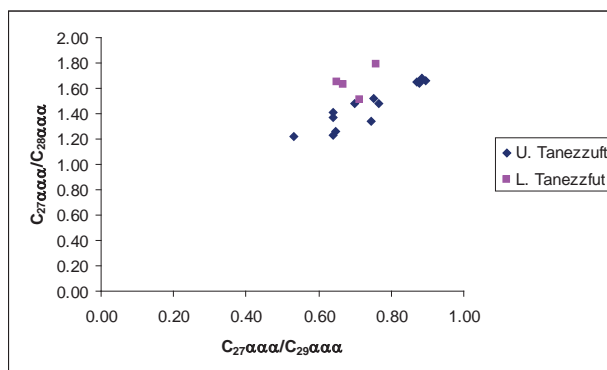

Fig. 20. Cross plot between $C_{27}\alpha\alpha\alpha$ /$C_{29}\alpha$ $\alpha\alpha$ 20R and $C_{27}\alpha\alpha\alpha$ /$C_{28}\alpha\alpha\alpha 20R$
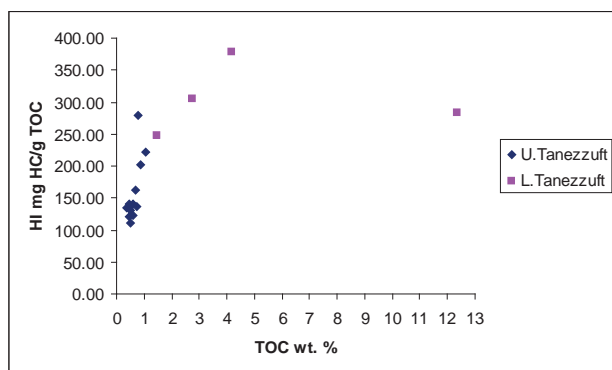
Fig. 21. Cross plot between TOC versus hydrogen indices

indices (HI) which may reflect changes in the degree of preservation through this formation. The TOC plot of HI indicates that the upper Tanezzuft Formation has lower TOC and HI values compared to the lower Tanezzuft Formation, which represent an increase of TOC due to an increase in the preservation of organic matter (HI); this may due to an enhancement of primary production and low dilution. According to the relationship between the TOC and HI, the samples that have high organic carbon content and hydrogen indices may indicate dysoxic-anoxic conditions. However, dysoxic-anoxic conditions 2.0-0.2 ml/l O_2; (Tyson & Pearson, 1991) may be the most probable for the depositional environment of the lower Tanezzuft Formation with slightly more oxic conditions associated with some samples of the upper Tanezzuft Formation that have low HI and TOC %.

Furthermore, Figure 22 shows a cross plot of the TOC and oxygen indices (OI) in both parts of the Tanezzuft Formation. This diagram illustrates an increase in TOC values with decreasing OI values which may also reflect the degree of preservation, and the change in sedimentary facies. The upper
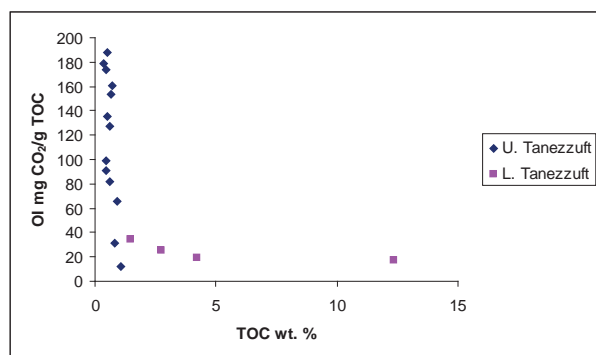

Fig. 22. Cross plot of TOC versus OI

Tanezzuft Formation (TOC≤1.07 and high OI 12-188mg CO_2/g TOC) suggests that organic matter deposited under oxic conditions with a low sedimentation rate. The remaining samples of the Lower Tanezzuft Formation have TOC≥1.45 and low OI 17- 34mg CO_2/g TOC which indicate that sediments were probably deposited in anoxic facies. Therefore, the depositional environment of the Tanezzuft Formation may possibly have ranged from the suboxic to dysoxic-anoxic in some parts of the section.

Geochemical parameters based on *n*-alkane and acyclic isoprenoid alkane distributions are given in Table 2. The pristane/phytane ratios of oils and bitumens are commonly used as indicators of the redox potential of the source sediments. Pr/Ph ratios less than 1 generally indicate anoxic deposition, while Pr/Ph ratios more than 1 often indicate oxic deposition (Didyk *et al*, 1978). Pr/Ph for the Upper Tanezzuft Formation samples varies between 0.81-1.48 suggesting facies differences between samples.

The lower Tanezzuft Formation has a slightly higher Pr/Ph ratio varying between 1.26 to 1.48 suggesting changes in organic facies and depositional conditions. According to Volkman & Maxwell (1981), a Pr/Ph ratio between 0.6 and 2.5 is difficult to use as an indicator of the palaeoenvironment without corroborating data. Despite other evidence for low oxygen conditions, the relatively high Pr/Ph ratio in the Tanezzuft Formation may be due to additional sources of pristane, e.g. algal tocopherol (Goosens *et al*, 1984). Moreover, the relative distribution of C_{35} relative to total C_{31} to C_{35} αβ 22S and 22R hopanes, measured by the homohopane index has been proposed as an indicator of the redox potential during and immediately after deposition of the source sediments (Peters & Moldowan, 1993). In the lower Tanezzuft Formation the homohopane index ratios are 3.29 to 4.09 suggesting reducing condition. In the upper Tanezzuft Formation the homohopane index ratios are 2.47 to 4.06, again suggesting a reducing marine environment with more oxidizing conditions. The relationship between the homohopane index and Pr/Ph ratio (Fig. 23) suggests some variability in oxygen concentration through the section of the Tanezzuft Formation.

A ternary plot of the relative distribution of C_{27}, C_{28} and C_{29} ααα 20S+20R steranes is shown in Figure 24. It is apparent from this figure that both parts of the Silurian Tanezzuft source rock samples have similar carbon number distributions of steranes, and
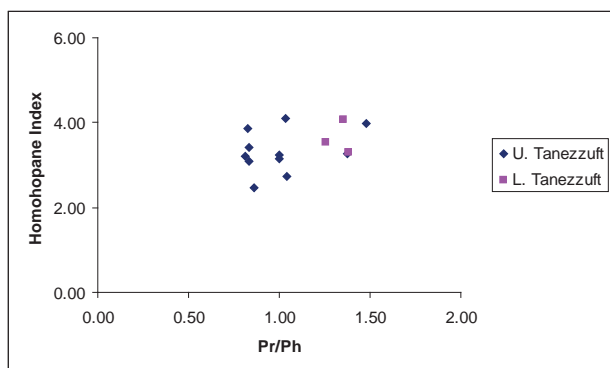
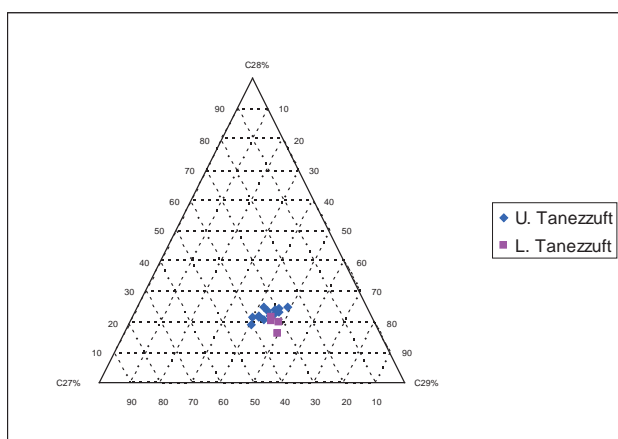Fig. 23. Cross plot between Pr/Ph and Homohopane index.

Fig. 24. Ternary diagram of C_{27}, C_{28}, & C_{29} $\alpha\alpha\alpha$(20S+20R) steranes.

show a higher relative abundance of C_{27} and C_{29} than C_{28}. These mean they were derived from generally the same organic matter assemblages with high algal input. They plot in the area where most marine source rock samples are found to be located (Huang *et al*, 1979).

Moreover, the presence of C_{30} sterane is the most powerful parameter for identifying the input of marine organic matter to source rock (Moldowan *et al*., 1985). The origin of C_{30} steranes suggests they arise from the marine sterols (Djerassi, 1981). The presence of C_{30} steranes within all of the Lower Tanezzuft Formation and most of the samples of the upper Tanezzuft Formation at Well B1-23, is considered as a good indicator for marine depositional setting. Furthermore, biomarker diagnostic for anoxygenic photosynthesis by Chlorobiaceae (green sulfur bacteria) was identified in Tanezzuft sediments. The anoxic conditions are favorable for Chlorobiaceae; these bacteria use a distinct light-harvesting pigment and require sulphide comprising bacteriochlorophylls, carotenoids isorenieratane

and chlorobactene (Grice *et al*, 2005) and (Damsté *et al*, 2001). Isorenieratane is preserved in upper and lower part of Tanezzuft Formation (Fig. 13 & 25), reflecting intense green sulfur bacterial activity and, thus, provides unequivocal evidence for anoxic conditions.

We can conclude that, dysoxic-anoxic conditions may be the most probable for the depositional environment of the lower Tanezzuft Formation with slightly more oxic conditions associated with some samples of the upper Tanezzuft Formation.

CONCLUSION

Rock-Eval data (i.e. S2, TOC, & HI), indicate that the upper part of Tanezzuft retains fair source rock potential and mixed kerogen type II/III. Whereas, the lower part is very good source rock potential and kerogen type II. No commercial hydrocarbon can be expected from the upper part of this formation, but oil could be generated from the lower part.

Rock-Eval analysis (Tmax, PI) and molecular biomarker data (i.e. %20S/20S+20R, %22S/22S+22R), indicate that both parts of the Tanezzuft Formation are late immature to early mature, although the aromatic ratios indicate a mature source rock.

Based on the biomarker parameters, the Tanezzuft source rock in this locality is dominated by marine algae as evidenced by abundant of short
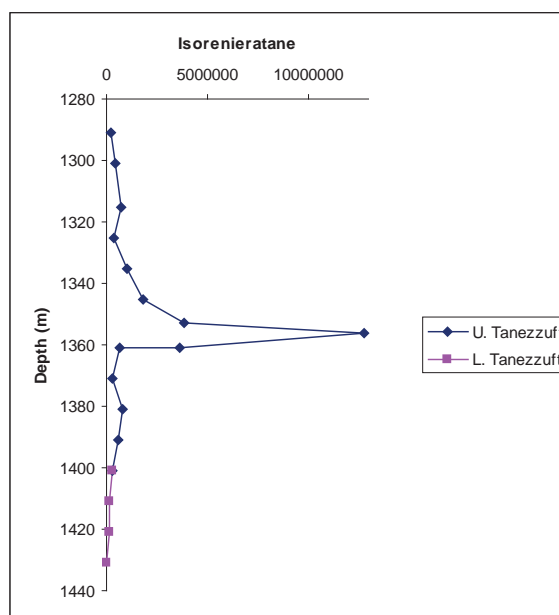

Fig. 25. Display the variation of isorenieratane within upper and lower Tanezzuft Formation.

chain *n*-alkanes with additional bacterial input, suggested from the abundance of hopanes.

Some combination of Rock-Eval, *n*-alkanes and biomarker data (such as the relative abundance of C27ααα , C28 ααα , C29 ααα20R , presence of C30 ααα 20R, and isorenieratane), suggest that both parts of the Tanezzuft succession were deposited in marine conditions, however, the upper part is relatively more oxidized. Furthermore, we can conclude that, dysoxic-anoxic conditions may be the most probable for the depositional environment of the lower Tanezzuft Formation with slightly more oxic conditions associated with some samples of the upper Tanezzuft Formation.

ACKNOWLEDGEMENTS

REFERENCES

Abbott, G. D.; Wang, G. Y.; Eglinton, T. I.; Home, A. K. & Petch, G. S. (1990). The Kinetics of Sterane Biological Marker Release and Degradation Processes During the Hydrous Pyrolysis of Vitrinite Kerogen. *Geochimica et Cosmochimica Acta,.* **54**: 2451-2461.

Albani, R.; Massa, D. & Tongiorgi, M. (1991). Palynostratigraphy (Acritarchs) of Some Cambrian Beds from the Rhadames (Ghadamis) Basin (Western Libya-Southern Tunisia). *Bollet. Della Soc. Pale. Italiana*. **30 (3)**: 255-280.

Anketell,, J. M. (1981). Report on Structural and Sedimentological Trends in the Pelagian Basin and Related Onshore Areas. In: *Continental Shelf (Tunisia/Libyan Arab Jamahiriya). International Court of Justice, III*, Annex, 12A and 12B: 45p.

Anketell, J. M. & Ghellali, S. M. (1991). A Palaeogeographic Map of the Pre-Tertiary Surface in the Region of the Jifarah Plain and its Implication to the Structural History of Northern Libya. *In: The Geology of Libya*, (Edit. by: M. J. Salem, A. M. Sbeta and M. R. Bakbak, Academic Press, London, **VI**; 2381-2406.

Biju--Duval, B.; Dercourt, J. & Le Pichon, X. (1977). From the Tethys Ocean to the Mediterranean Seas: A Plate Tectonic Model of the Evolution of the Western Alpine System. In: *Structural History of the Mediterranean Basins* (Edit. by: B. Biju-Duval and L. Montadert eds),. Paris: 143-164.

Bishop, A. N. & Abbott, G. D. (1993). The Interrelationship of Biological Marker Maturity Parameters and Molecular Yields During Contact Metamorphism. *Geochimica et Cosmochimica Acta.* **57**: 3661-3668.

Boote, D. R. D.; Clark-Lowes, D. D. & Traut, M. W. (1998). Palaeozoic Petroleum Systems of North Africa. In: *Petroleum Geology of North Africa*, (Edit. By: D. S. Maggregor, R. T. J. Moody and D. D. Clark-Lowes),. *Geol. Soc. London, Spec. Pub.*, **132**: 7-68.

Bray, E. E. & Evans, E. D. (1961). Distribution of N-Paraffins as a Clue to Recognition of Source Beds. *Geochimica et Cosmochimica Acta.* **22**: 2-15.

Burollet, P. F. (1978). The Geology of the Pelagian Block: The Margins and Basins off Southern Tunisia and Tripolitania. *In: The Ocean Basins and Margins: The Western Mediterranean, Plenum, New York, 48*: 331-359.

Busson, G. (1967). Le Mesozoique Saharien, pt. 1: L' Extreme-sud Tunisien: France, Cent. Rech. Zones Arides, Ser. Geol., **8**, 194p. Summarized as Mesozoic of Southern Tunisia in Guidebook to the Geology and History of Tunisia, *Petroleum Expl. Libya.* **9**[th] *Ann. Field Conf.*: 131-151.

Cornford, C. (1998). Source Rocks and Hydrocarbons of the North Sea. In *Introduction to the Petroleum Geology of the North Sea,* (Edit. By: K. W. Glennie),. Blackwell, Oxford, **4th edit**.: 376-462.

Damstee, J. S. S.; Schouten, S. & Vanduin, A. C. T. (2001). Isorenieratene Derivatives in Sediments: Possible Controls on their Distribution. *Geochemica et Cosmochimica Acta, 65(10)*: 1557-1571.

Dewey, J. F. & Burke, K. C. A. (1973). Tibetan, Variscan and Precambrian Basement Reactivation: Products of Continental Collision. *J. Geol.*, **81**: 683-692.

Didyk B. M.; Simoneit, B. R. T.; Brassell S. C. & Eglinton S. C. (1978). Organic Geochemical Indicators of Palaeoenvironmental Conditions of Sedimentation. *Nature, 272*: 216-222.

Djerassi, C. (1981). Recent Studies in the Marine Sterol Field. *Pure and Applied Chemistry*, **53**: 873-890.

Echikh, K. (1998). Geology and Hydrocarbon Occurrences in the Ghadamis Basin, Algeria, Tunisia, Libya. In: Petroleum Geology of North Africa (Edit by: D. S. Maggregor, R. T. J. Moody and D. D. Clark-Lowes), *Geol. Soc. London, Spec. Pub.* **132**: 109-129.

Echikh, K. & Suleiman, S. (1983). Geological and Petroleum Evaluation of North-Western Libya

(Nafusa Uplift-Jiffarah Trough, South of Zuara Basin). National Oil Corporation, Libya, *Report*: 1-45.

El Hinnawy, M. & Cheshitev, G. (1975). Geological Map of Libya, Tarabulus (N133-13). *Explanatory Booklet. Ind. Res. Cent.*, Tripoli.

Espitalie, G. ; Deroo, G. & Marquis, F. (1985). La pyrolyse Rock-Eval et ses applications, *premiére partie: Revue de l'Institut Francais du Pétrole*, **40**: 563-57

Etap (1991). Petroleum Potential Evaluation of Tataouine Block in Southern Tunisia. Acres de III Emes. *Jour. De Geolg. Appliq. A la Rech. Des Hydrocarbbures*.

Farrimond, P.; Taylor, A. & Telnaes, N. (1998). Biomarker Maturity Parameters: the Role of Generation and Thermal Degradation. *Organic Geochemistry, 29*: 1181-1197.

Gelpi, E.; Schneider, H.; Mann, J. & Oro, J. (1970). Hydrocarbons of Geochemical Significance in Microscopic Algae. *Phytochemistry*, **9**: 603-612.

Goosens, H. ; De Leeuw, J. W. ; Schenck, P. A. & Brassel, S. C. (1984). Tocopherols as Likely Precursors of Pristane in Acient Sediments and Crude Oils. *Nature, 312*: 440-442.

Goudarzi, G. H. (1980). Structure–Libya. In: *the Geology of Libya*. (Edit. by: M. J. Salem and M. T. Busrewil), Academic Press. London, ***III***: 879-892.

Grice, K.; Cao, C.; Love, G. D.; Bottcher, M. E.; Twitchett, R. J.; Grosjean, E.; Summons, R. E.; Turgeon, S. C.; Dunning, W. & Jin, Y. (2005). Photic Zone Euxinia During the Permian-Triassic Superanoxic Event. *Science*, **307**: 706-709.

Hammuda, O. S. (1980). Geological Factors Controlling Fluid Trapping and Anomalous Freshwater Occurrence in the Tadrart Sandstone, Al Hamada Al Hamra Area, Ghadames Basin. In: *Geology of Libya*) Edit. by: M. J. Salem, & M. T. Busrewil), **2**: 501-507.

Hammuda, O. S.; Sbeta, A. M. & Worsley, D. (2000). Field Guide to the Mesozoic Succession of Jabal Nafusah, NW Libya: 1-50.

Huang, W. Y. & Meinschein, W. G. (1979). Sterols as Ecological Indicators. *Geochimica et Cosmochimica Acta.* **43**: 739-745.

Hunt, J. M. (1995). Petroleum Geochemistry and Geology. ***2nd edition*** Freeman Francisco: 743p.

Killops, S. & Killops, V. (1993). An Introduction to Organic Geochemistry. *Harlow, Essex, England: New York:* Longman Scientific & Technical; Wiley: 265p.

Langford, F. F. & Blanc-Valleron, M. (1990). Interpreting Rock-Eval Pyrolysis Data Using Graphs of Pyrolizable Hydrocarbons vs. Total Organic Carbon. *Am. Assoc.Petrol. Geo. Bulletin, 74*: 799-804.

Mackenzie, A. S.; Patience, R. L.; Maxwell, J. R.; Vandenbroucke, M. and Durand, B. (1980). Molecular Parameters of Maturation in the Toarcian Shales, Paris Basin, France-1. Changes in the Configuration of Acyclic Isoprenoid Alkanes, Steranes, and Triterpanes. *Geochemica et Cosmochimica Acta, 44*: 1709-1721.

Mickirdy, D. M.; Cox, R. E. & Volkman, J. K. (1986). Botrycoccane in a New Class of Australian Non-Marine Crude Oils. *Nature.* **320**: 57-59.

Mikbel, S. R. (1977). Basement Configuration and Structure of West Libya. *Libyan J. Sci.*, **7A**: 19-33.

Moldowan, J. M.; Seifert, W. & Gallegos, E. (1985). Relationship Between Petroleum Composition and Depositional Environment of Petroleum Source Rocks. *Amer. Assoc. petr. Geol. Bulletin.* **69(8)**: 1255-1268.

Moldowan, J. M.; Sundararaman, P. & Schoell, M. (1986). Sensitivity of Biomarker Properties to Depositional Environment and/or Source Input in the Lower Toarcian of SW-Germany. *Organic Geochemistry, 10:* 915-926.

Montgomry, S. (1994). Oil in the Ghadames Basin: A Basic Overview. In: *Petroleum Frontiers* (Edit. by: T. Cheney and D. Cain), ***10, 4.***

Nelson, R. A. & Hsu, M. Y. (1993). Fractures in the Ordovician Sandstones of the Sabria and El Franig Structures, Tunisia. In: *Fractured Reservoir Seminar* (Edit. by: B. Hassine, and M. Borgi), Tunis, 1-4 Sept., Etap, Tunis: 29-39.

Ourisson, G. ; Albrecht, P. & Rohmer, M. (1979). The Hopanoids Palaeochemistry and Biochemistry of a Group of Natural Products. *Pure and Applied chemistry*, **51**: 709-729.

Ourisson, G.; Albrecht, P. & Rohmer, M. (1984). The Microbial Origin of Fossil Fuels, *Scientific American, 251*: 44-51.

Peters, K. E. (1986). Guidelines for Evaluating Petroleum Source Rock Using Programmed Pyrolysis. *Am. Assoc. Petr. Geo.s*, **70(3)**: 318-329.

Peters, K. E. & Moldowan, J. M. (1993). The Biomarker. Interpreting Molecular Fossils in Petroleum and Ancient Sediments. *Prentice Hall, Englewood Cliffs, New Jersey*: 363p.

Peters, K. E.; Walters, C. C. & Moldowan, J. M. (2005). The Biomarker Guide. ***Volume 1*** Biomarker and Isotopes in the Environment and Human History. Cambridge University Press.

Radke, M., Schaefer, R. G., & Leythaeuser, D. (1980). Composition of Soluble Organic Matter in Coals: Relation to Rank and Liptinite Fluorescence. *Geochemica et Cosmochimica Acta, 44*: 1787-1800.

Radke, M., Welte, D. H, & Willsch, H. (1981). Geochemical Study on a Well in the Western Canada Basin: Relation of the Aromatic Distribution Pattern to Maturity of Organic Matter. *Geochemica et Cosmochimica Acta, 46:* 1-10.

Radke, M., Leythaeuser, D., & Teichmuller, M. (1984). Relationship Between Rank and Composition of Aromatic Hydrocarbons for Coals of Different Origins. *Organic GeochemistrY, 6*: 423-430.

Rohmer, M. (1987). The Hapanoids, Prokaryotic Triterpenoids and Sterol Surrogates. In: *Surface structure of microorganisms and their interaction with the Mammalian Host* (Edit. By: Schriner *et al.*). Proceedings of the Eighteenth Workshop Conference, Hocchst, Schloss Ringberg: 227-242.

Rubinstein, I.; Sieskind, O. & Albrecht, P. (1975). Rearranged Sterenes in Shale: Occurrrence and Simulated Formation.. *Jour. Chem. Soc.,* perkin Transaction, *I*: 1833-1836.

Seifert, W. K. & Moldowan, J. M. (1986). Use of Biological Marker in Petroleum Exploration. *Methods in Geochemistry and Geophysics*, *24*: 261-290.

Swire, P. H. & Gashgesh, T. M. (2000). Concession9 and Surround the Bio-Chrono- and Lithostratigraphy and Hydrocarbon Prospectivity of the Northwest Ghadames Basin. *Unpublished Internal LIB* **Report**, Veba Oil Operations: 1-52.

Tyson, R. V. & Pearson, T. H. (1991). Modern an Ancient Continental Shelf Anoxia*, Geological Society, London, Special Publication*, *58*: 1-26.

Volkman, J. K. (1986). A review of Sterol Markers for Marine and Terrigenous Organic Matter, *Organic Geochemistry, 9*: 83-99.

Volkman, J. K., & Maxwell, J. R. (1981). Acyclic Isoprenoids as Biological Markers. *Biological Markers in Sedimentary Record,* Elsevier (1986): 1-42.

ABOUT THE AUTHORS

Aisha K. Shalghum has got Bachelor Degree in the field of geology from the University of Azawia in 1998. She joined Libyan Petroleum Institute in 2000 where she still working. Aisha have completed her MSc at the University of Newcastle, England, UK in the field of organic geochemistry in 2005.

Mahmoud T. Elbakai Has finished his Bachelor Degree in the field of geology in the University of Tripoli in 1980. Mahmoud has joined the Petroleum Research Centre since 1980. He completed his MsC degree at the University of Hull, England in 1990 and PhD degree with Leicester University in 1996 in the field of sedimentology.

DELINEATION OF MINERAL POTENTIAL ZONE USING GIS IN THE SOUTHERN PART OF LIBYA

Dr.Younes Ajal Abulghasem[1], Dr. Ahmed Salem Saheel[2,] and Dr. Tareq Hamed Mezughi[3]

Abstract: The powerful tools of Geographic Information System (GIS) and remote sensing (RS) have significantly contributed to the modern geological mapping and mineral exploration by enhancing, interpretation and integration of various geological datasets. Integration of remote sensing and airborne magnetic data with other geological data sets are the most promising and cost-effective method to add new structural and lithological aspects to the map of the geology in a diverse geological province as in the area of current research. This is due to the fact that all the geosciences information together with pre-processed remotely sensed data can be used as evidence to delineate possible areas for further study and more investigation (Chang-Jo & Fabbri 1993). The study area is a belt of Upper Devonian sedimentary formation including iron ore bearing layers, which extend over about 160km, in ENE-WSW direction, on the northern border of the Murzuq Basin. The study area is located in the western central part of Libya within the bounder's 27º South and 28º North Latitude and 12º to 16º East-longitude covering an area of nearly 40,000km^2. This study examines the integration of aeromagnetic data with remote sensing to discover any probable extensions of iron ore deposits and any associated minerals in the area of study. The study involves analysis of magnetic data to delineate geological, structures, faults and to extract important information about the locations of buried magnetic bearing rocks. Spatial data integration and analysis for the study area and predicting mineral potential were carried out on the available digital remote sensing data (Landsat ETM+). While searching for mineral potential areas, accurate and up-to-date geological maps are essential as it represents the most basic information for directing exploration activities. To this end, the existing geological map of the study area, which was published by Industrial Research Centre (IRC) in 1984, is too old to extract up-to-date information for mineral exploration. The main objective is to integrate these datasets to update the geological map and produce mineral potential map of the study area. In this research, the various datasets (aeromagnetic data, geological, remote sensing) were processed, integrated, and modeled using GIS techniques. The primary field study was conducted in the potential areas of the iron ore deposits. Few samples were collected from the area and subjected to XRF, XRD analyses. The produced Total Magnetic Intensity (TMI) map shows prominent NW-SE and N-NW trends. The Reduction to the Magnetic Pole (RTP) map is characterized by a dominant WNW-ESE trend in the study area. Total horizontal derivative of the pseudogravity map generally reflects fault or compositional changes which can be seen to describe structural trends. The central part of the study area can be divided into five zones where the eastern and northern zones show many short anomalies of NW-SE orientation and the southern zone shows E-W orientation, in the northern zone of the central part shows WNW-ESE orientation trends. Strong magnetic anomaly detected in the south of Idri Town can be interpreted as lenses of magnetite or magnetite-rich sandstone within the sedimentary rock sequence. The selective principal component analysis, band ratio, techniques allowed the discrimination of altered areas and the detection of iron and iron oxide bearing minerals. The most important finding in this study is discovering new potential areas covering about 1000km2 of mineral deposits in the southeast and north-western parts of the area. These results increased the assumption of extending the iron ore belt under the sand dunes in the west and east parts of study area. The mineralogical analysis indicates that the iron ore type is goethite and hematite with percentage between 8 to 46 % Fe2O3 associated with very important minerals such as pyrochlore (Na, Ca, U). Finally, new potential map mineral deposit was produced and classified into four zones which are low, moderate, high, and very high potential zone.

Keywords: Geographic Information System (GIS), Remote Sensing (RS), Wadi Ash Shati, Iron Bearing Layer, Landsat ETM+, Aeromagnetic Survey.

---

[1]*Geologic Department, Faculty of Sciences. Alabel Alghrabi University.*
e-mail: younesajal17@gmail.com
[2]*Exploration Department, Libyan Petroleum Institute (LPI), Tripoli-Libya.*
e-mail: a.saheel@lpilibya.com
[3]*Geography Department, Faculty of Arts, Tripoli University, Tripoli-Libya.*
e-mail: thmezughi@yahoo.com

INTRODUCTION

Now days the interpretation of magnetic data has increased in the form of new models of the

causal body, after the development of computerized multiparameters inversion methods. Many of these permit interpreter interactions by the graphics display system for computer imposing geological allows sensitive that resulted in a significant increases in the use of the magnetic survey for mineral exploration. Over the past 40 years advances in measurement technology and digital recording of data, particularly on the extensive use of the air-magnetometer as a tool for geological mapping (Sharma, 1987). Aeromagnetic anomalies can be used to extract important information about the locations of buried faults and magnetic bearing rocks.

Geographic Information System (GIS) and Remote Sensing (RS) technology (RS) are very important tools in mineral exploration that large areas of land surface can be covered for detailed geological studies. Landsat ETM+ data provides a new digital geological mapping technique which can be used in this study to determine new potential areas for iron deposits. Integrating remote sensing data with geological and aeromagnetic data has the potential of delineating geological structures (e.g., fractures, faults) and ring system of the basement rocks, which possibly control the mineralization in the area.

XRD and XRF are very complementary methods to improve the analysis, the accuracy of phase identification and quantitative analysis. Those two methods increase the number of parameters measured, which means fewer assumptions required for analysis. This tour offers higher accuracy, not only results but also increases the range of measured samples. XRD is the most direct and accurate analysis of the present and the absolute number of mineral species in a sample to be determined. Ambiguous results can be achieved using XRD. In contrast, XRF provides very accurate information regarding the elemental composition of the sample. It has versatility in handling and conducting solids, accuracy and has excellent precision for the majority of the elements with its wide dynamic range from 0ppm to 100% (Bonvin & Yellepeddi 2000).

The Study Area

Wadi Ash Shati deposits are a belt of Upper Devonian sedimentary formation, including iron ore bearing layers, which extends over 160 km^2, in ENE-WSW direction, on the northern border of the Murzuq Basin, in the province of Sabha (Fig. 1). The western and eastern ends of the iron ore bearing layers are covered by more recent formations, which completely cover the ore outcrops (Sterojexport

Fig. 1. location map of the study area

1977). The study area is situated in the province of Sabha, Libya, bounded by latitudes 27° and 28°N, and longitudes 12° and 16°E. The territory covers an area of nearly 40,0000km^2. The area of study lies to the south of the Gargaf Arch, an E-W trending anticline, built up of a Precambrian core and Cambrian to Devonian clastic sediments with Lower Carboniferous rocks at its southern fork, striking about 85° with 1-3° dip towards the south. Paleozoic formations containing iron-bearing oolitic layers are reported to occur in several areas beside the study area. The iron bearing deposit are mostly confined to the Middle and Upper Devonian Awaynat Wanin Formation. In the Shati Valley, the Upper Devonian formation consists of 140m of gray, tan and brown, fine to medium grained, well-rounded, and well-sorted cross bedded sandstone. It is interbedded with thin beds of quartzitic sandstone, varicoloured claystone and siltstone and contains several intra-formational conglomerates.

Aeromagnetic Survey: The aeromagnetic data were provided by the Libyan Petroleum Institute (LPI), Tripoli, Libya, as grid data, with grid cell size of 1000m. The survey of the study area was carried out along a set of parallel flight lines at 2km spacing, while the flight height was 755m a.s.l. The aeromagnetic data were corrected and reduced to their final form. The magnetic intensity map was constructed with the aim of enhancing geological structures and for qualitative interpretation.

Landsat ETM+ Image: Three cloud-free Landsat ETM+ scenes of (186-41) acquired on October 7th, 2000, (187-41) acquired on March 9th, 2001 and

(188-41) acquired on March 9, 2001 provided by Industrial Research Centre (IRC), Tripoli, which covered the investigated area were used in this research. Thematic Mapper Plus (ETM+) instrument onboard this spacecraft is an eight-band multispectral scanning radiometer, capable of providing high-resolution imaging information of the earth's surface. The nominal ground sample resolution or "pixel" sizes are 15 meters in the panchromatic band, 30 meters in the 6 visible, near, and mid-infrared bands, and 60 meters in the thermal infrared band. Geological map of the study area NG33-1, NG33-2, G33.3 Scale 1:250,000 were published by Industrial Research Centre (IRC) Libya in 1984 used as a base map to extract the geological formations that were included in the study area and the previous structures map of lithology, tectonic and geologic setting.

Field Data: Three field visits in exploratory fieldwork are done in the study area to be familiarized with the general conditions of the area. The aims of fieldwork in this research are:

1 The information collected during fieldwork is the spatial distribution of rock units at the surface. This requires determining what rock units are exposed were on the surface, and tying that data to a geographic database, usually a topographic map or satellite image. This also requires determining the general composition of each rock type by visual identification. For most rock types, the minerals can be visually identified and other components using either the naked eye or a hand-held 10x pocket magnifier.

2 The second type of data collected is an actual sample of the different rock units encountered. Samples provide the ability to take the field units back into the laboratory, and to conduct more detailed examinations (XRD, XRF) on the composition and texture of the maps units seen in the field. Rock samples are collected as part of a field mapping exercise which invariably leads to a more complete understanding of the geology of a particular locality. Also, they needed to define the ore deposit types, the chemical composition and identify the percentage of iron.

DATA PROCESSING

The methodologies applied in this study involved several steps. The literature review was the first step in deriving information about the general geology of the study area. This was followed by data preparation and pre-processing of aeromagnetic data remotely sensed images (Landsat ETM+).

Total Magnetic Intensity (TMI)

The African Magnetic Map (AMMP) was a compilation of all available airborne, ground and marine magnetic data for the whole of Africa from (Getech et al, 2000). The used data, covering a variety of resolutions, vintages, and types, were merged into a unified 1km grid at a constant 1km elevation above terrain. International Geomagnetic Reference Field (IGRF) was removed from the original data with the use of computer program supplied by Geosoft package software. The total intensity map (Fig. 2) shows the magnetic field amplitude, which reaches 70nT, where it is relatively high comparing with its spatial distribution of the survey. The map shows an acute variation in the magnetic intensity, indicating variation in either lithology or basement topography. Sedimentary rocks are seen to be high magnetic and usually give only an insignificant contribution to the magnetic anomalies. The main sources of the magnetic anomalies are expected to depend on the basement setting and its magnetic features.

The total magnetic intensity (TMI) map of the south-eastern study area was obtained to delineate the subsurface structure (Fig. 2). The aeromagnetic anomalies range from- -10 to 70nT and are characterized by both low and high frequencies of anomalies. The map reveals that the positive magnetic anomalies have a general E-W, N-S and NE-WS directions respectively. The configuration of positive anomalies could be attributed to relatively deep-seated low relief basement structure. The TMI anomalies could be strongly influenced by the regional tectonic. The negative magnetic anomalies have a generally N-S, E-W and ENE-WSW directions. The negative anomalies are related to shallow thick sediments. At low magnetic latitudes as is the case here, it is not very easy to correlate the observed anomaly maxima. The position of magnetic sources because in the TMI anomaly map, the maxima are not found vertically above magnetic sources, thus making it difficult to link the observed anomalies with the sources. To partially come to this, it is usually necessary the performer a standard phase shift operation known as reduction-to-pole on the observed magnetic field, the operator affects the phase as well as the amplitude.

Reduction-to-the pole (RTP)

Reduction to the pole transformation of an anomaly in the fourier domain was used in Geosoft Package Software. RTP grids were easy to be interpreted because anomalies placed directly above the source of the magnetic field. The RTP transformation applied anomaly map was given in (Fig. 3) The inclination and declination angles of the ambient field were taken as 26.5°N and 14°E, respectively (38.44°N, -9.43°E). The RTP
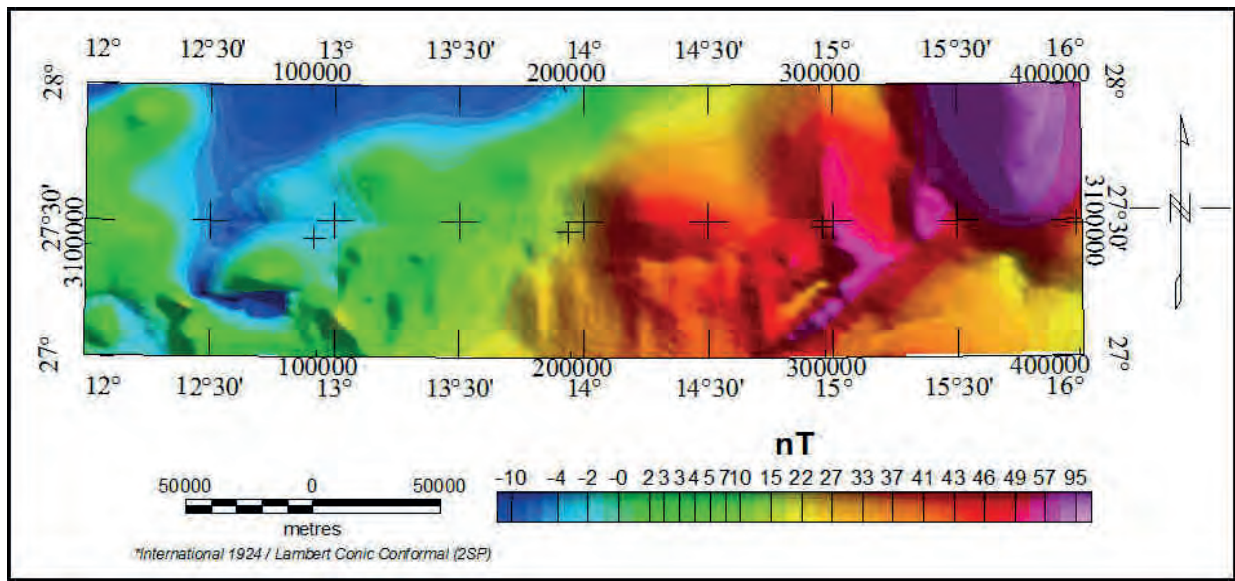
Fig. 2. Total Magnetic Intensity (TMI) map of the study area (Grid cell size 1000m).
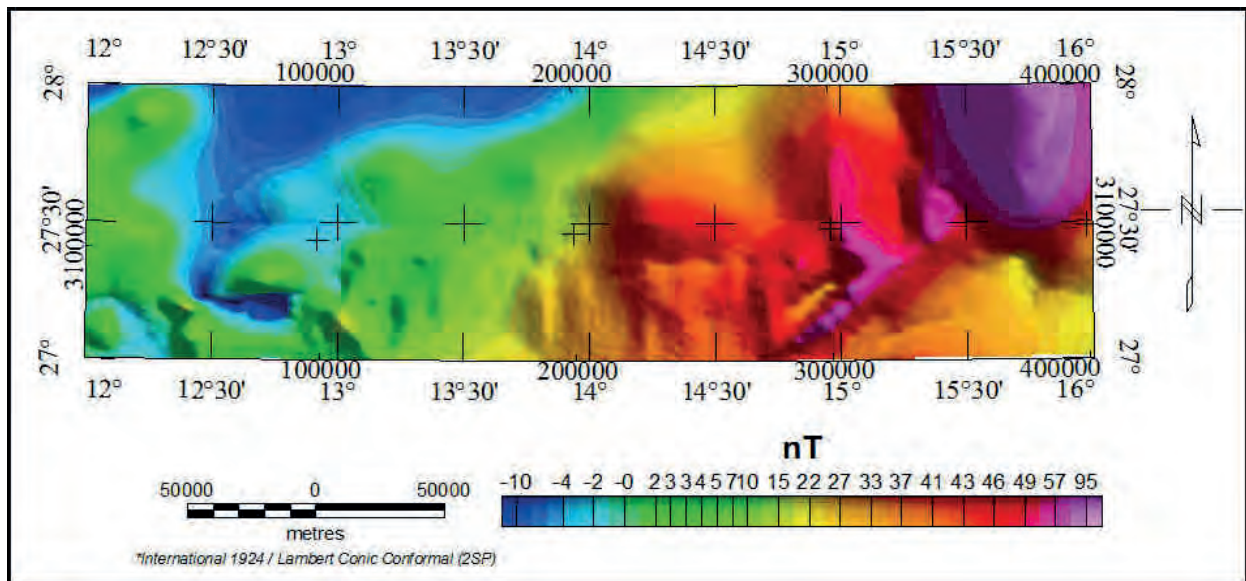

Fig. 3. Reduction to the pole map of the study area

aeromagnetic anomaly map (Figure 3) showed that both low and high frequency anomalies characterized the magnetic field in the study area. The elongated negative magnetic anomaly with values between -4 to -10NT was observed over the locations of the western and eastern part of the study area. The extended negative magnetic anomaly was characterized by high frequency and high amplitude. Such magnetic anomaly is associated with thick sediment which was mainly recognized by high magnetic susceptibilities. This magnetic anomaly was bounded by steep magnetic gradients, which indicated the presence of two faults, trending in the NW-SE direction.

The First Vertical Derivative (FVD)

Derivatives tend to sharpen the edges of anomalies and improve shallow features. The vertical derivative map is much more responsive to local influences than to broad or regional effects and therefore tends to give sharper picture than the map of total field intensity. Thus, the smaller anomalies are more readily apparent in area of strong regional disturbances. In fact, the FVD is used to delineate high frequency features more clearly where they are shadowed by large amplitude, low frequency anomalies. To emphasize the effect of the geological contact, critical for the structural framework of the area, the data processing involved accurate enhancement

of the short-wavelength and linear features. In that regard, the aeromagnetic data were first gridded with a grid-cell spacing of 1000m and were subjected to regional/residual separation to isolate short-wavelength signal which is more suitable for high-resolution mapping of shallow magnetic boundaries (Fig. 4). The regional/residual separation was made by subtraction of the upward-continued grid to 200m from the total magnetic intensity aeromagnetic grid. Upward continuation transformation attenuates high-frequency signal components and tends to emphasize deep, regional-scale magnetic anomalies. Subtraction of the low-frequency upward-continued data from the original grid produces a residual map that is enhanced in short-wavelength signal. The enhancement of magnetic anomalies associated with faults and other structural discontinuities were achieved by the application of FCD to the residual map in (Fig. 4 & Dobrin and Savit 1988; Telford *et al*, 1993). The reprocessed aeromagnetic data set is significantly enhanced in high frequency and is much better suited to detailed regional shallow mapping and analysis of basement magnetic boundaries.

Pseudo-gravity

To locate and outline crustal magnetic sources, transformation techniques must be applied to the data as magnetic anomalies very rarely are centered above their source. The pseudo-gravity transform (Baranov, 1957) is applied to the magnetic data. By using the pseudo gravity transform, the apex of the magnetic anomalies is shifted over the source body and distortion due to the earth's magnetic field can easily be removed. A pseudo-gravity transformation

is useful in interpreting magnetic anomalies, not because a mass distribution actually corresponds to the magnetic distribution beneath the magnetic survey, but because gravity anomalies are in some ways more instructive and easier to interpret and quantify than magnetic anomalies (Blakely, 1995). The pseudo-gravity transform was applied to the total magnetic intensity grid using the FFT (Fast-Fourier-Transform) filter package available in Oasis Montaj by considering the density contrast of $1g/cm^3$ and a magnetization of 0.5 Gauss. The pseudo-gravity field of the study area in magnetic anomaly for induced magnetization of the present-day field (I= 38.44° and D= -9.19°) shows poor correlation with the observed total magnetic intensity anomaly (Fig. 5), suggesting that the causative body has a remnant magnetization. The contribution of the pseudogravity analysis permits us to better constrain the geodynamic of the study area.

Total horizontal derivative technique

The Total Horizontal Derivative method (HD) was used for many years to locate density boundaries from gravity data (Cordell, 1979) and density and susceptibility boundaries from magnetic (as pseudogravity) data (Cordell and Grauch, 1985; Ma *et al*, 2006). These authors discussed a technique to estimate the location of abrupt lateral changes in magnetization or mass density of upper crust at rocks. The method is normally applied to mapped data rather than profiles. Maximum magnitudes of total horizontal gravity gradient normally occur above geological boundaries such as faults or steeply dipping lithological boundaries. Areas of
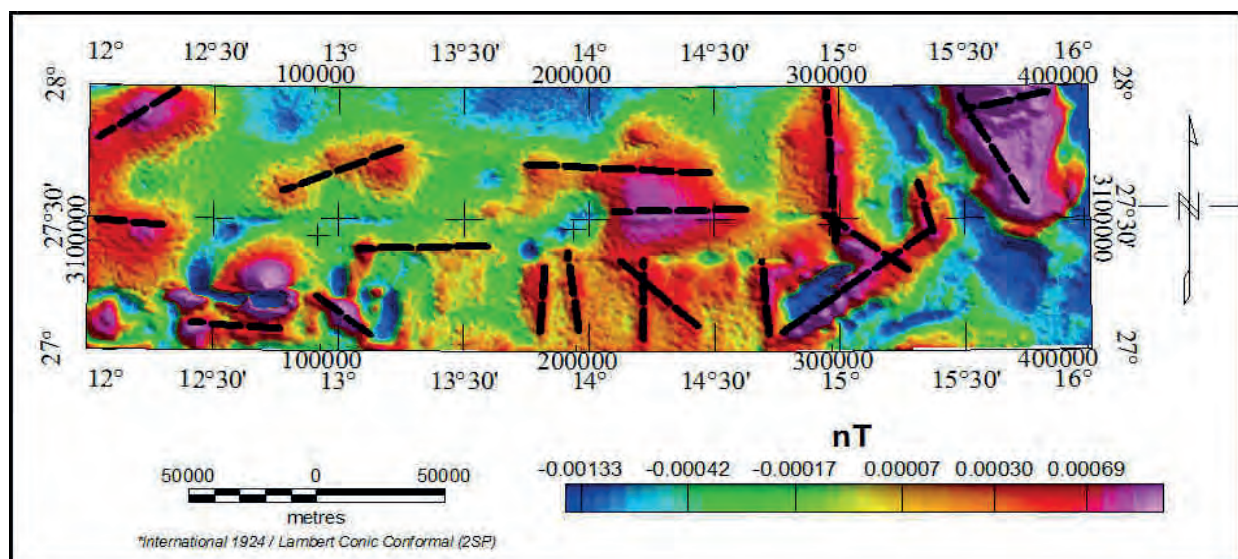

Fig. 4. First vertical derivative (FVD) of upward continuation 200m map of study area.

steep lateral gradients have higher scalar amplitude values of total horizontal gravity gradient (Blakely and Simpson, 1986). In applying this technique to a gridded dataset, the gridded pseudogravity for each grid point (x, y) is determined. Then the pseudogravity gradient function is calculated according to the following equation:

$$f = \sqrt{\left(\frac{\partial g}{\partial x}\right)^2 + \left(\frac{\partial g}{\partial y}\right)^2}$$

Where, f is "total horizontal gradient", $\left(\frac{\delta g}{\delta x}\right)$ is the x derivative and $\left(\frac{\delta g}{\delta y}\right)$ is the y derivative. The technique is influenced by several factors such as dip of discontinuity, data spacing, reliability of data and density contrast. Shallow dipping faults

are shown in a position shifted in a downdip direction (Cordell and Grauch, 1985); Hansen and Pawlowski, 1989). In study area map of total horizontal gradient of pseudo-gravity grid data (Fig. 6), anomalies are observed throughout. The Map shows the present of total horizontal gradient anomalies especially in the eastern, western and central parts of the study area. In the eastern part, the strong anomaly is indicated trending in the NW-SE and NE-WS direction. About two anomalies are detected in the central part of the study area indicated NW-SE trending direction. One anomaly is observed in the western part of study area in the NW-SE direction.
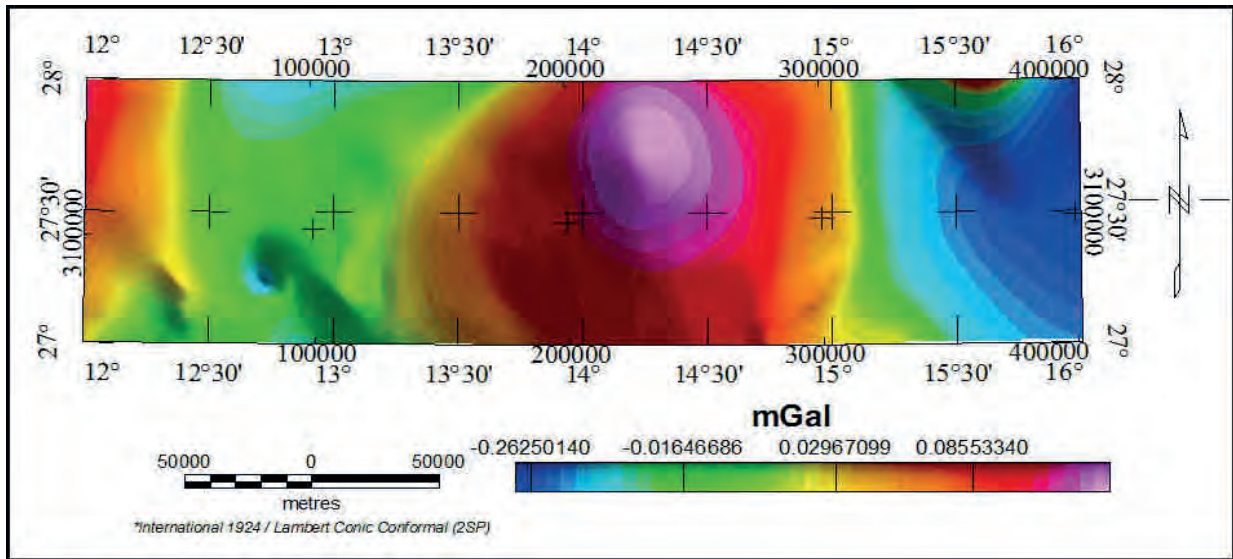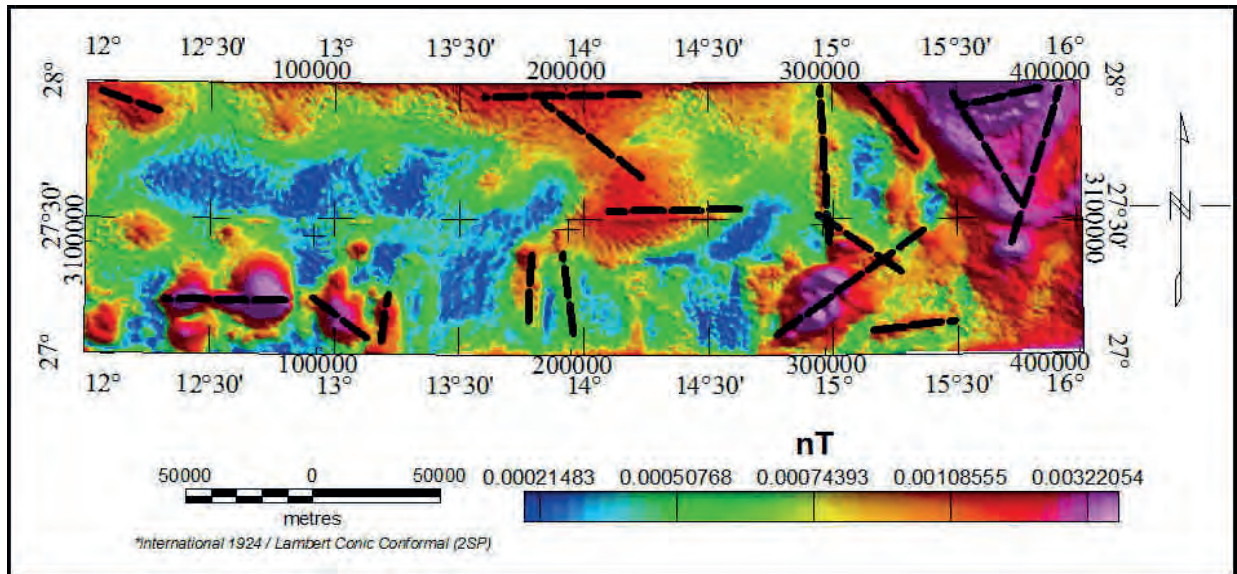

Fig. 5. Pseudogravity map of study area.

Fig. 6. Total horizontal gradient of Pseudogravity map of study area.

Analytic Signal Method

The concept of analytic signal was provided by (Nabighian 1972; 1984) defined as a square root of the sum of the squares of the derivatives of total magnetic field in the x, y and z directions:

$$AS= \sqrt{\left(\frac{dT}{dx}\right)^2 + \left(\frac{dT}{dY}\right)^2} \; \sqrt{\left(\frac{dT}{dx}\right)^2}$$

The analytic signal is useful for locating the edges of magnetic source bodies, especially where remanence and low magnetic latitude complicate interpretation. Analytic signal picks up the highest amplitude anomalies (Fig. 7) and is independent of inclination of the geomagnetic field. The analytic signal signature of the study area was calculated in the frequency domain using the Fast Fourier Transform technique (Geosoft). The most of trending showing from analytic signal in the eastern part of study area direction NW-SE and NE-SW.

Low-Pass and High-Pass Filtering

Filtering magnetic data is an essential process prior to analysis and interpretation. The purpose of the filter is to exceed the data set and make the presentation result in a way that it is easier to interpret the meaning of anomalies in relation to their geological sources. Therefore, the most effective way to filter data is by understanding the geological control and desired outcomes filtered. Multiple filtering techniques can be performed in the frequency domain. However, one of the most traditional filters used in the potential field, is the separation of long (deep) and short (shallow) wavelength anomalies. The success of this technique depends on the correct choice of the cut-off *wavelength of the filter design*: The frequency bands corresponding to these linear segments which were used through the band pass filter technique to produce the low-pass and high-pass magnetic component, maps. The regional (low-pass) magnetic anomaly maps, is characterized by large, homogenous and high-amplitude anomalies, which are caused by deep-seated causatives. The low-pass filter applied on reduced to the pole data to produce regional maps. The cut off wavelengths used were 10 000m, 15 000m, 20,000m, 25,000m, 30,000m, and 40,000m, the best result which presented the clear and smooth magnetic map found in wavelengths 30,000 (Fig. 8). The residual (high-pass) magnetic anomalies' maps were produced by subtracting total magnetic intensity (TMI) from the regional magnetic anomaly map, which was produced by (low pass) filter with cut off wavelengths 30,000m (Fig. 9). The (residual, regional, RTP, analytic signal and pseudo-gravity) maps were all subjected to horizontal derivative filter to delineate the lithological boundaries and faults' directions and to estimate the physical properties of the source structure causing the anomaly.

Remote Sensing Data Processing

Pre-image processing such as radiometric and image enhancement were employed to clearly visualize the image. During the image processing, all images were geo-referenced into one projection system. Images were subseted to the bounding coordinates of the research area. Appropriate band combinations were chosen for and structural lithological interpretations.
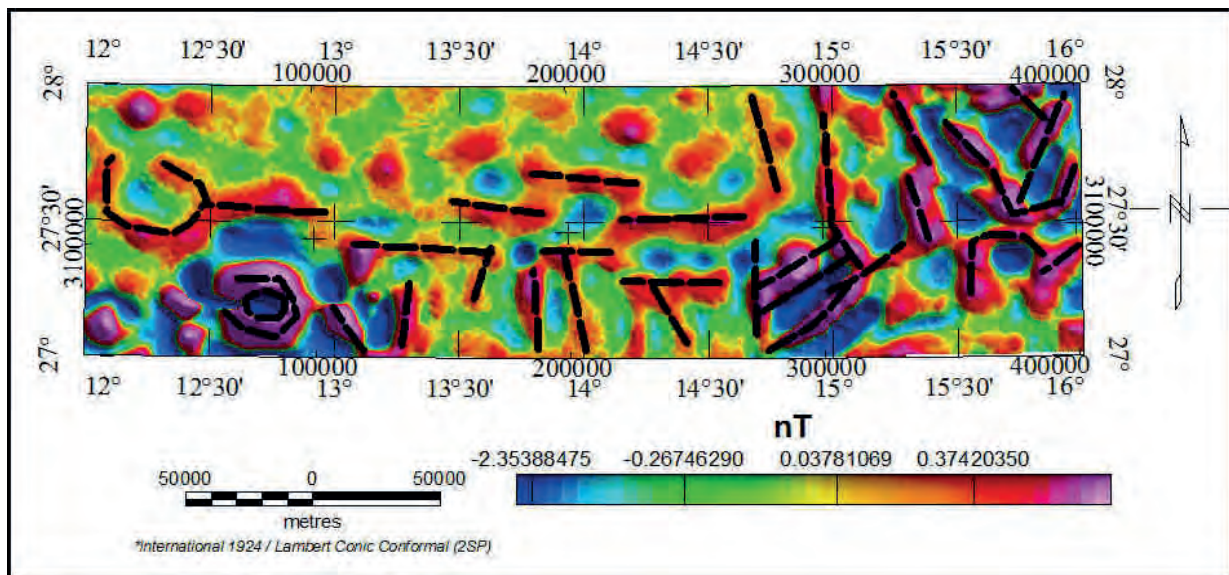

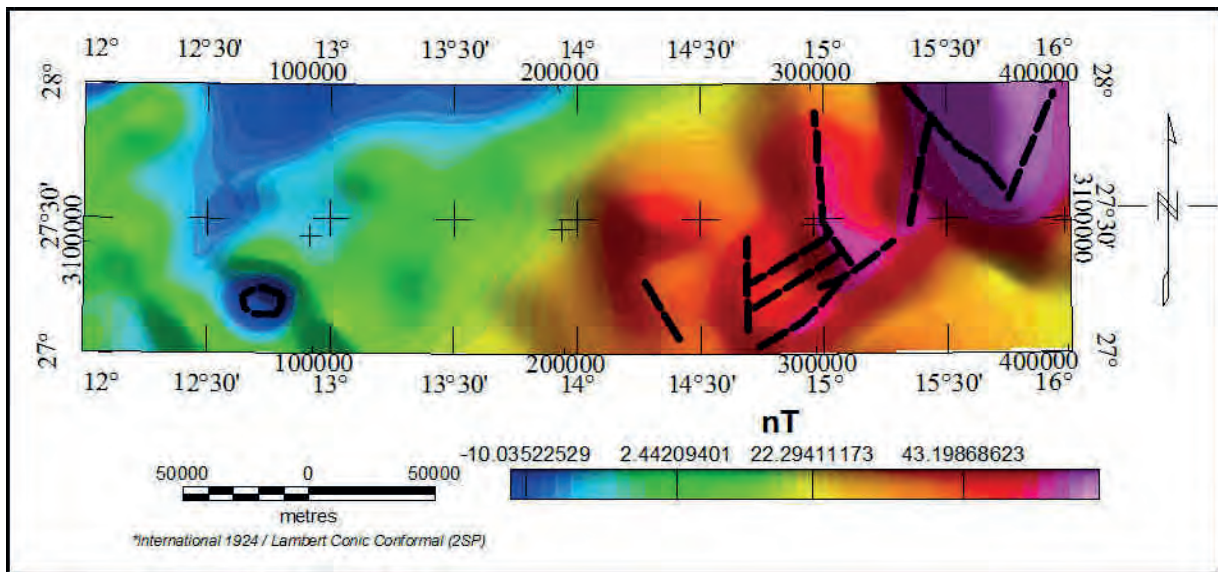Fig. 7. Analytic signal of magnetic data of the study area.

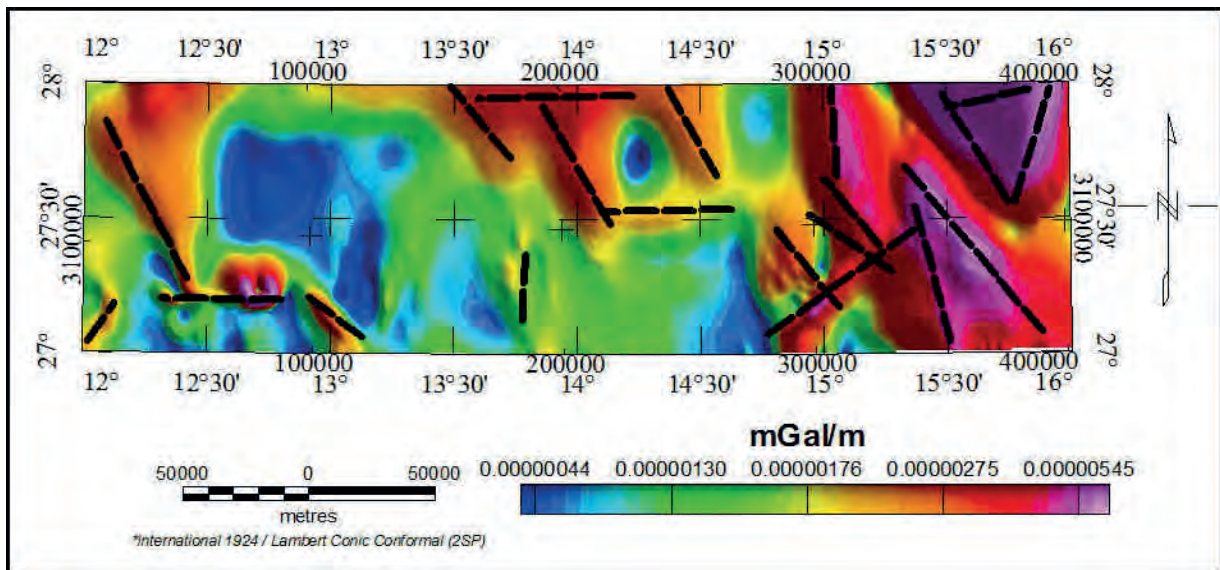Fig. 8. Map showing low-pass filter for total magnetic Intensity data

Fig. 9. Map showing high-pass filter for total magnetic Intensity data

Supervised Classification Techniques: Image classification is a very important method in the interpretation of remote-sensing data. The computer-assisted classification of an image automatically categorizes all pixels of an image into land cover classes (Poovalinga and Rajendram, 2009). The bands (7, 4, and 2) have been used in the image-supervised classification technique namely maximum likelihood classifier (MLC) to classify lithological units. Geologic maps for Idri and Wadi Ash Shati published in 1984 were used as reference ground data.

Principal Component Analysis: Principal component analysis (PCA) has been called one of the most valuable results from applied linear algebra. The "principal component analysis transformation," is a multivariate statistical method used to compress multi spectral dataset into few PC images in which spectral difference between materials become apparent in PC image than individual bands (Gillespie *et al*, 1986; Sabins, 1987). Principal components are commonly calculated using the covariance matrix obtained from the input multi-spectral data whereby the corresponding Eigen matrices is also determined.
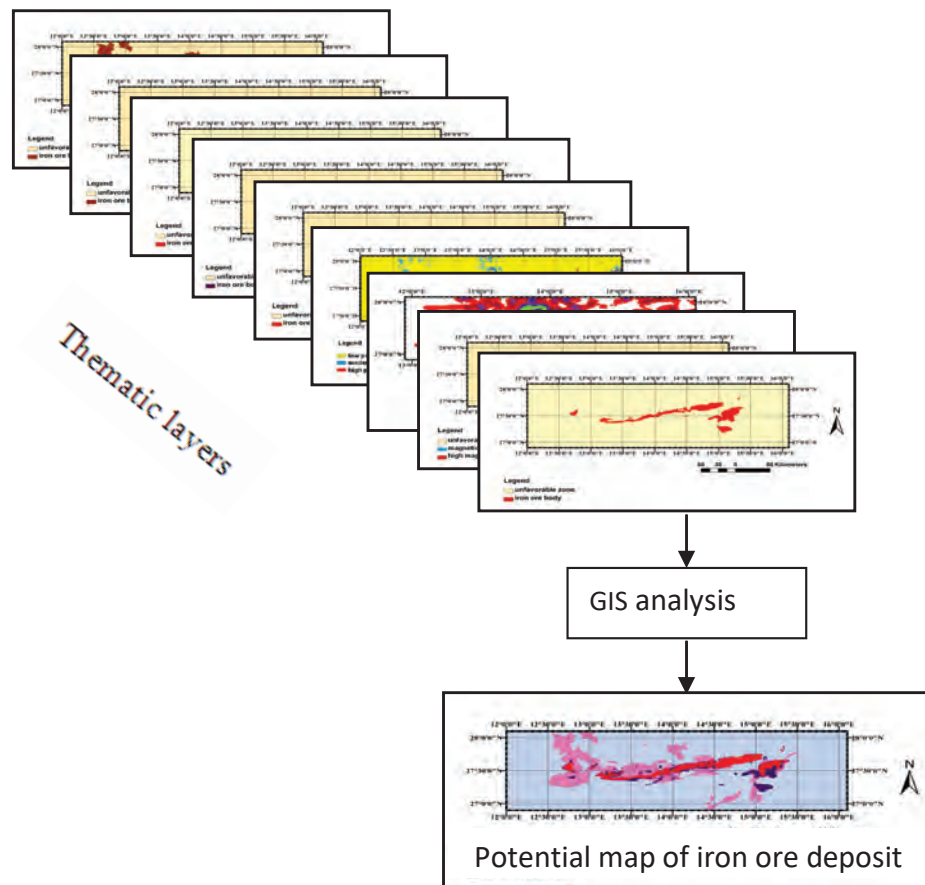
Fig. 10. GIS data analysis

Band Ratio Technique: In this study ratio image is mainly used for mineral alteration mapping, Landsat ETM+ bands selected for the band rationing for mineral alteration mapping is based on alteration minerals reflectance features. It is used here for lithologic investigation and mineral discrimination. The digital numbers were divided in a band by the DNs corresponding to a different tape for each pixel aspect ratio of the resulting value and draw the new values as an image.

Lineament Extraction: Different techniques of digital processing were applied to enhance and correct the acquired images as well as to choose the best band data for later analysis. From visual evaluation, band 7 of Landsat ETM+ image was selected for lineament analysis since it shows a better contrast and displays better visualization of geological features compared to the other band for each satellite. For lineament analyses spatial enhancement were performed using directional filters. Directional filters are quite useful for producing artificial effects, which may

reveal tectonically controlled linear features (Drury, 1987). Filtering technique was used to enhance the structural geological information (lineaments) for each selected band. Lineaments for directions (NS, NE-SW, E-W, NW-SE) are filtered separately, and then the tracings were overlapped to produce final lineaments map for each satellite. Sobel directional filter 3 by 3pixel kernels were applied to extract the lineaments in the area.

GIS Analysis

Thematic Map Preparation: Getting an advantage of the power of GIS is to integrate various digital data set in a single unified database (Fig. 10), the maps which were extracted from, principal component analysis, band ratios, supervised classifications and geophysical data were digitized, analyzed and georeferenced with the same projection (geographic lat/long). The aim for this is to identify the areas of minerals occurrence and then combined in one map, which presents the potential areas of mineral deposit. After all data layers were extracted from remote-sensing data converted to raster format by digitizing

all those layers and save it in the same feature class under one geodatabase. The structure maps of the study area which were extracted from remote sensing and aeromagnetic results were integrated by using GIS system to produce one density structure map of the area. weighted overlay was used to combine all factor layer maps into new information to produce individual value for each pixel and a new map was produced (potential map). The weighting values used in the overlay operations were only performed on raster maps, and weighting value was given based on the influence of every subclass. The heuristic value for each factor and classification were given between 1 to 10, where value of 1 indicates that the influence or result towards is very low, while value 10 is very high. appropriate areas for mineral deposit were determined through six thematic layers: PCA, band-ratio, supervised classification, magnetic anomaly map, structure density map. Weights are assigned based on several experts' knowledge and by comparing each of these thematic layers with the geological map of the study area which are used as reference to define most accurate layers for highest weight and based on the conformation form the field trip and mineralogical analysis (Table 1) presents the weights assigned to every unit.

Table 1. Presents the weights assigned to every unit

Factor	Classes	i (rate)	W (weight)%
PCA 1, 2 & 3	Class 1	2	9
	Class 2	9	
PCA 7, 5 & 4	Class 1	2	7
	Class 2	9	
Band-ratio (5/4)	Class 1	1	9
	Class 2	2	
	Class3	9	
Supervised classification	Class 1	2	8
	Class 2	8	
Magnetic anomaly	Class 1	2	8
	Class 2	8	
	Class 3	9	
Density lineament Map	Class 1	1	3
	Class 2	2	
	Class 3	3	
	Class 4	4	

Calculation of the sum of weights:

PM= (SC *W+ B1*W +B2*W + HIS*W + PC1*W+PC2*W+ Mg*W+D*W)

Where PM = the final potential map of Wadi Ash Shati iron ore deposit and

SC= supervised classification map

B1= Band ratio map of bands 5/7, 5/4, 3/1

B2= Band ratio map of bands 5/4

IHS= Intensity-Hue-Saturation map

PC1= Principal Component map 7, 5 and 4

PC1= Principal Component map 1, 2 and 3

Mg= magnetic anomaly map

D= lineament density map

W= weight of each class

RESULTS AND DISCUSSION

Magnetic Data

The main results obtained in this study bring new elements allowing improvement of our knowledge on the geological structure of the study area spatial analysis, helped detect morphological differences in the lineament patterns. The eastern sector of the map shows a lineament toward WNW-ESE and ENE-WSW trend. The northern and western sectors of the map show of lineament toward NE-WSW. Accordingly, the terrain can be divided into tectonic sector. The comparison of the results with the geoscientific data (structural, lithological) confirms morphological difference. The tectonically subdivision into two tectonic corresponding to the Hercynian Croton in the eastern and western part of study area. Pan-African Croton in the southern east and helped identify the tectonic boundary separating them at depth assigned to the major normal faults in the centre. This geophysical study suggests that the structures of crust modeled are situated on the flank of the major faults in the basements it is a product of an active continental collision. This collision has provoked considerable over thrusting of the Pan-African Rift. The use of high-resolution magnetic data coupled with filter processing has increased the geologic information about the study area. Detailed magnetic interpretation can assist significantly in mapping the geology of the region.

Remote Sensing Data

Supervised Classification Technique: The results of image classification show that the iron ore body (appears in red colour on the map) extends

towards the west and northwest of the known iron ore deposit (Wadi Ash Shati) and new areas of iron ore detected by supervised classification that these areas carrying the same DN value with the existing iron ore body. The results of supervised classification shown in (Fig. 11).

Principal Component Analysis: The PCA images were prepared using three visible (VIS) and three infrared bands of available sub-set of Landsat ETM+ mosaic. The first three PC images contain 98.33% of the information of the six Landsat-ETM+ bands. PC1, PC2, and PC3 display fair lithologic contrast and the rest of the PC (PC4 to PC7) appear to be less informative in terms of lithologic discrimination but the iron ore body still appears very clear. RGB composite of PC1, PC2 and PC3 have better colour contrast. It allowed best lithologic discrimination and the iron ore belt appears very clear in yellow colour on the map (Fig. 11). Landsat ETM+ image can be widely used to generate exploration targets in study area using the wavelengths characterized by iron absorption.

Band ratio: This technique is used to enhance contrasts between selected features and suppresses illumination differences between spectral features attributable to surface, look angle, and topographic effects. In a band ratio image, the black-and-white extremes represent areas with the greatest differences in the spectral reflectance of the two bands. Ratio image was produced using bands (5, 4), band ratio 5/4 has been computed to enhance possible ferrous oxides. The combination of ratio image 5/4 appears with black-and-white colour whereas, ferrous oxides appear with white colour and the rest of land cover appears with black thus this method very effective at detecting the ferrous oxides as shown in (Fig. 12).

Lineament extraction: The lineaments direction is parallel with the major faults reported by previous researchers. It seems that there is a relationship between the length of the lineaments and the orientation in the area, which means the length of the lineaments, plays the important role of certain orientations. The sun azimuth effect was clearly evidence of the appearing of lineaments in the EW & ENE-WSW directions (Figs. 13 & 14). Lineament density and intersection density of lineaments are also useful for characterizing the spatial patterns of lineaments (Figs. 15 & 16).
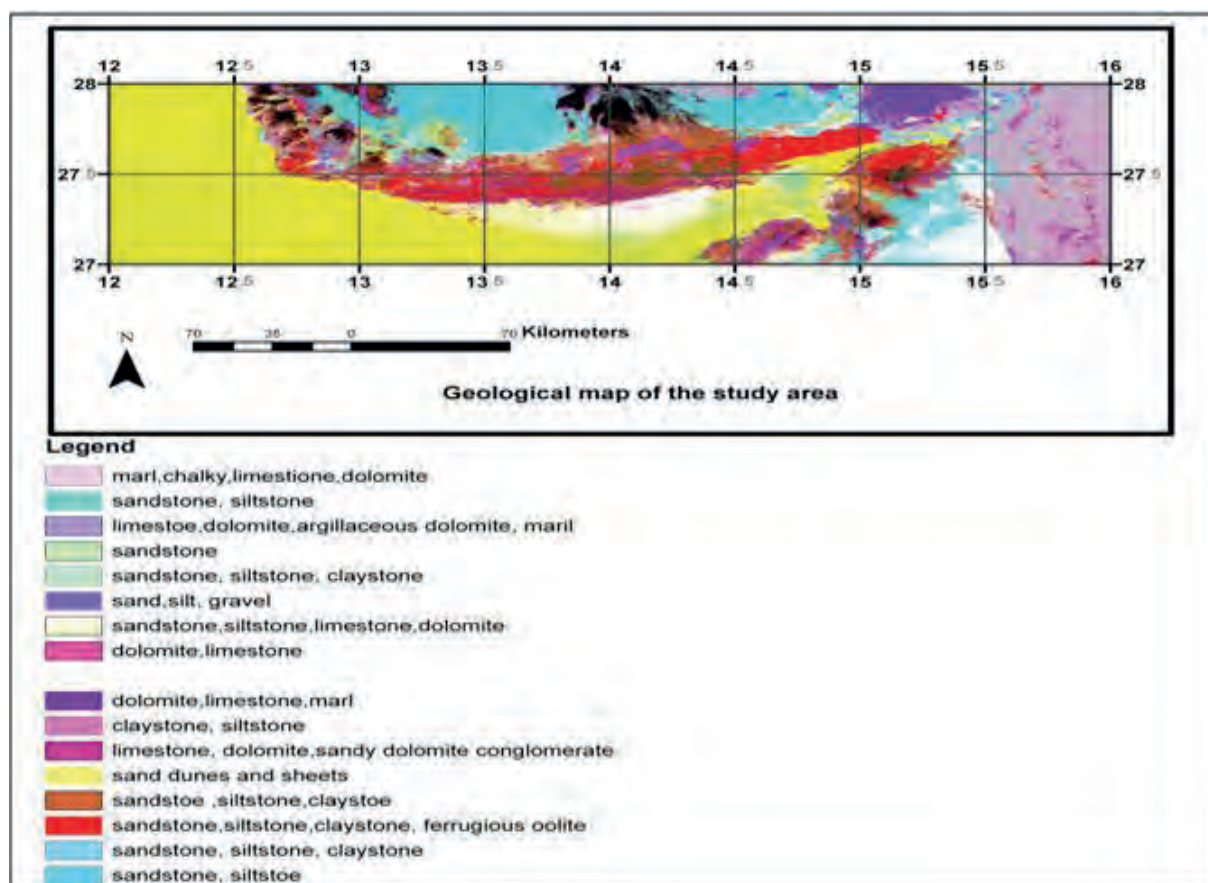

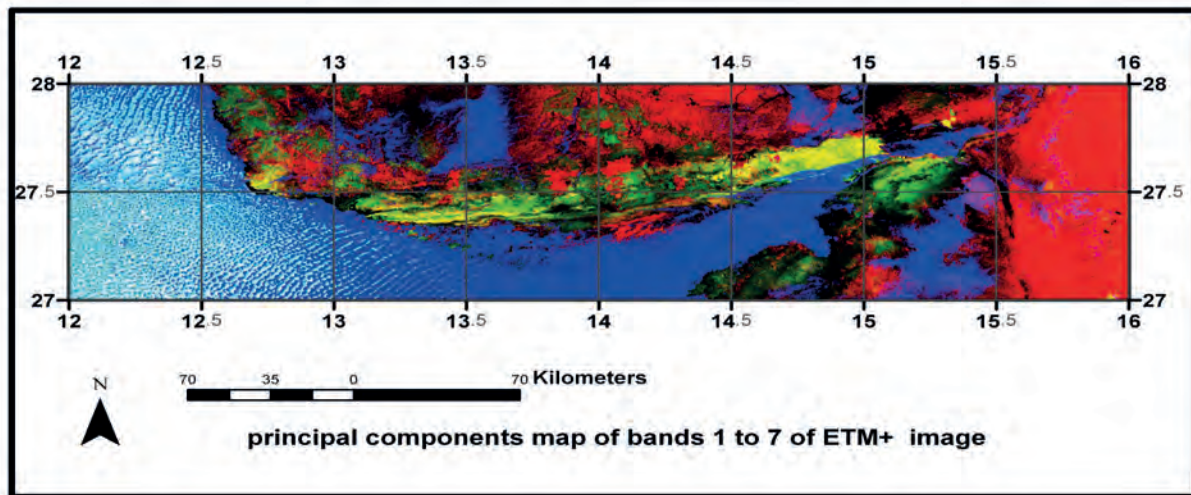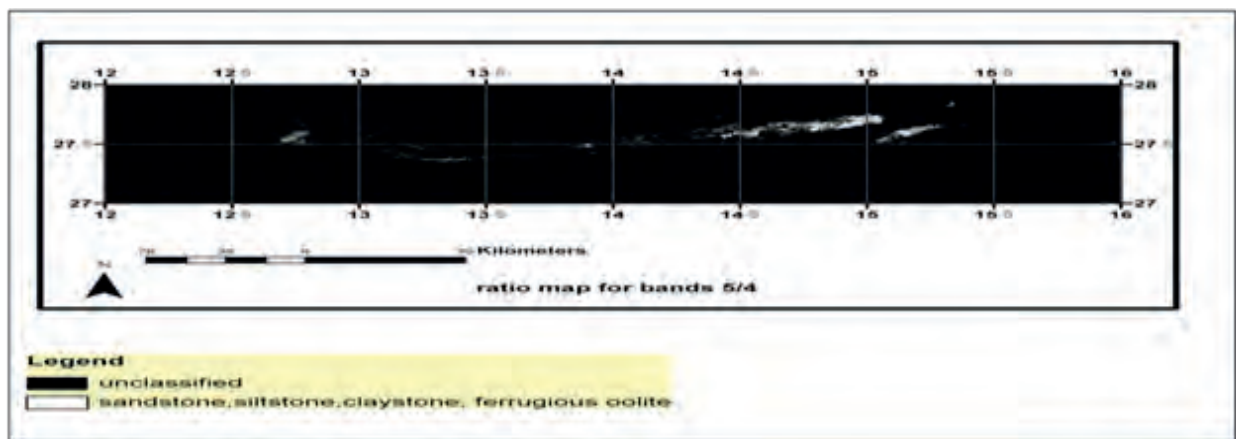Fig. 11. Supervised classification map of the study area

Fig. 12. Principal Analysis Component map of the study area

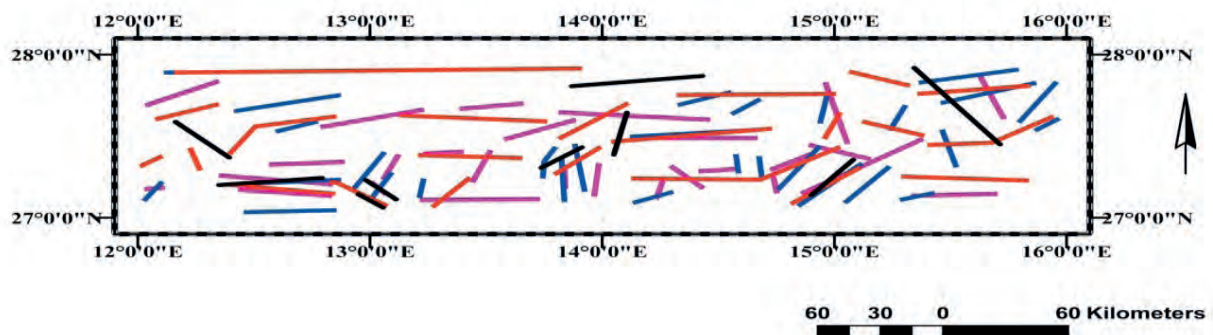Fig. 13. band ratio map of the study area

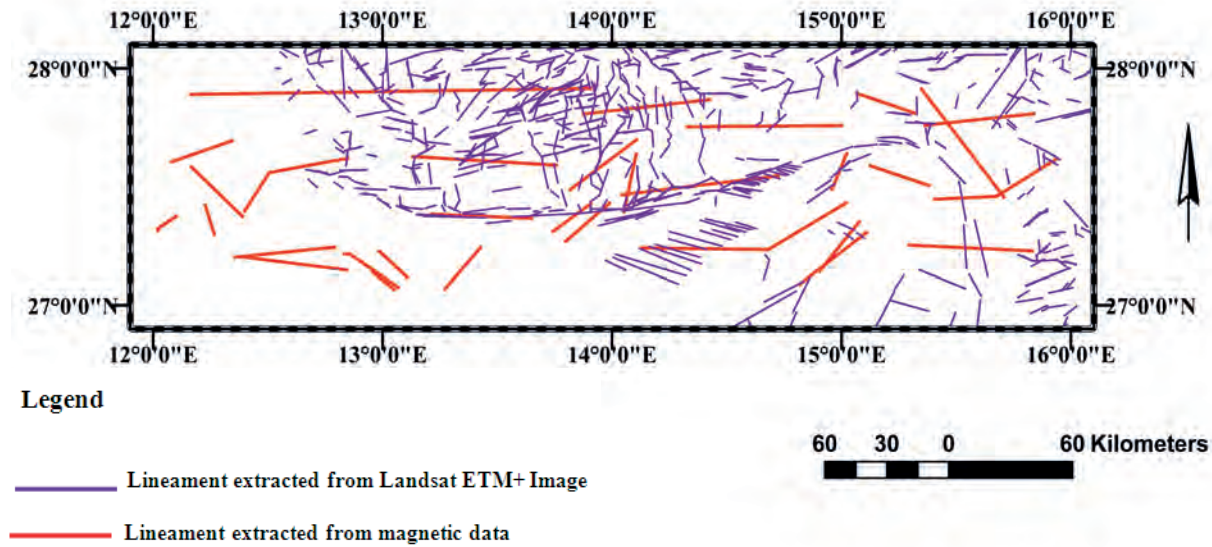Fig. 14. New tectonic map of the study area showing tectonic elements derived from aeromagnetic data
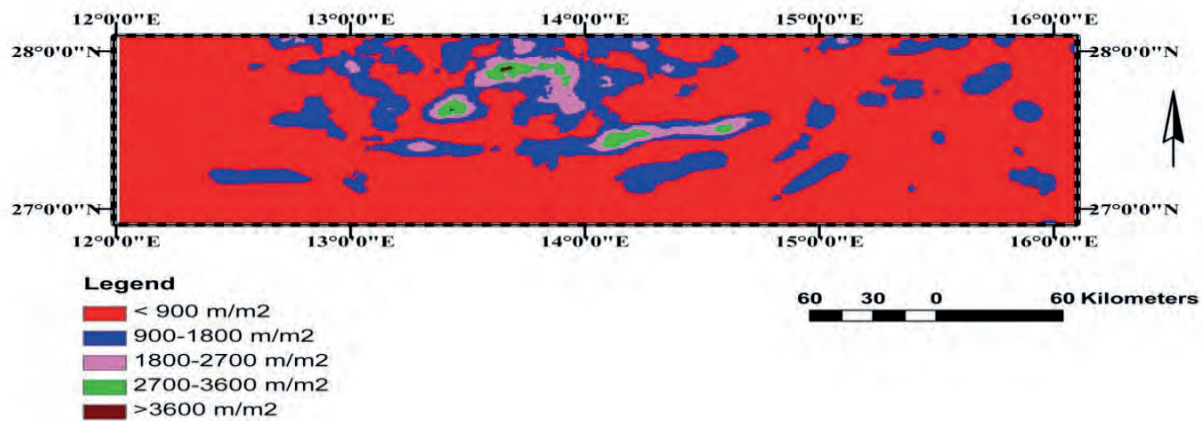
Fig. 15. Lineament map of the study area

Fig. 16. Lineament density map of the study area

Potential Map: The delineation of iron ore deposit potential zones through the integration of different thematic layers obtained from remote sensing, aeromagnetic data interpretation and other secondary data have found to be effective techniques for analyzing the information content of each layer in GIS environment. The analysis would give meaningful results without the need of conducting fieldwork, which are time, effort and cost consuming activities. This technique would give broad ideas about the iron ore potentiality of the areas and then minimize the areas where iron ore deposit can be found and reduce the exploration activities to be carried out for subsurface study through geophysics

and drilling tests. The outcome of the application of remote sensing, aeromagnetic data and GIS on Wadi Ash Shatti area showed reasonable results where there was high potentiality on the areas of Wadi Ash Shatti valley and Idri Town. The Wadi Ash Shatti iron ore is one of the most important of mineral's deposit in Libya. Iron ore potential map generated through this process will help planners and decision makers for devising and feasible mining development plans. However, more field work still needs to be carried out to estimate the depth of the iron body and to estimate the volume of the lenses of the iron ore in the area. The new potential map was further classified into four zones which were low, moderate,

high and very high potential as shown in (Table 2). The moderate, high, and very high-potential zones in classified map were confirmed with evidence of geochemical analysis through the collected samples from the field (Fig. 17). The magnetic anomaly identified more potential zones within the boundaries of magnetic anomaly and new structure in the study area. This was deducted from the interpretation of the magnetic data, whereas the low potential zone still needs more study in terms of field visit and collecting samples for geochemical analysis and mineralogical investigation. However, the estimation of the exact amount of the iron ore is still not accurate and more iron ore is expected to be found in the potential area. Therefore, more boreholes are suggested to be drilled and more samples have to be collected and analysed especially from the classes of high and moderate in the new potential map. Figure (18) and Table (2) showing the area by km. sq. for each zone in the potential area.

CONCLUSIONS

In this research, the various datasets available for the study area (remote sensing and aeromagnetic data) were processed, integrated, and modeled using Geographic Information System (GIS). The objective of this research was to integrate the available geological datasets to update the geological map and to produce an iron potential map in the study area. The magnetic survey data analyzed using the most advanced and suitable techniques. This technique includes pseudo gravity, reduction to the pole filter, low-pass/high-pass filtering, and total horizontal derivative. The magnetic anomalies produced by deep geologic sources were separated from anomalies produced by shallow geologic effects using low-pass/high-pass filtering and depending on the anomalies' wavelength using matched band pass filtering. Tectonically, the magnetic methods were useful for detecting the geometry of the basement rocks, and the structures related to tectonic forces. The results indicate that the principal tectonic trend is oriented in the NE-SW direction (Fig. 14), which is found to be from the same direction of iron ore body in the study area. Magnetic data thus helped for extracting subsurface information to delineate host rocks and structural features which are responsible for mineral distribution in the study area. The magnetic intensity map showed clearly intrusive bodies, and a high magnetic anomaly observed in the southwest part of the study area probably caused by magnetic response of rocks is due to the presence of magnetic minerals such as magnetite, and hematite. This variation of susceptibility exists between different rock types. The basement is usually very vulnerable due to their high content of magnetite (iron), whereas sedimentary rocks have much lower susceptibilities. High-pass and low-pass filter techniques were used to decompose the magnetic

Table 2. Distribution of iron ore zones in the study area

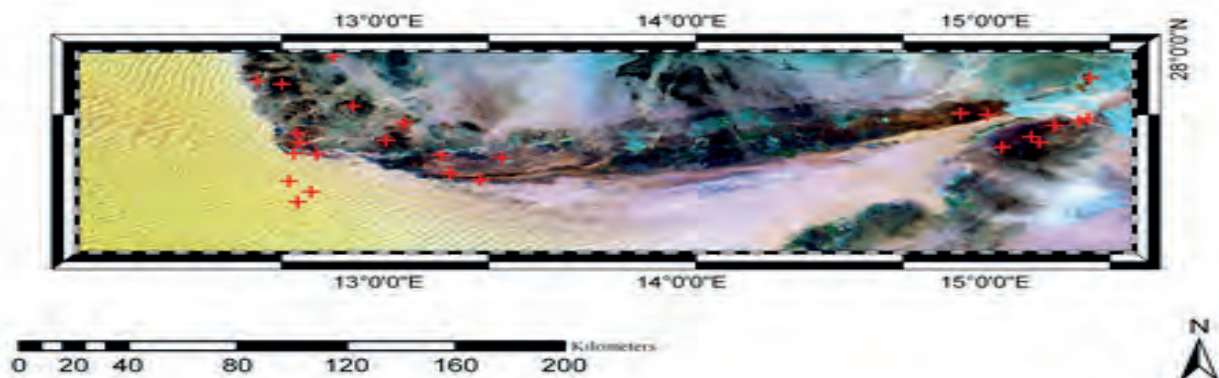| Iron ore potential zone	Number of pixel	Area (Km2)
Very high zone	2480538398	2480
High zone	1124088208	1124
Moderate zone	1633129344	1633
Low zone	5540404361	5540

Fig. 17. Shows locations of collected samples from the study area

intensity map into the components related to shallow depths (residual anomalies) and those from deeper sources (regional anomalies). This study showed that integrating aeromagnetic with remote sensing data are an efficient tool for geological mapping. Different processing techniques were applied to the Landsat ETM+ and to discriminate and delineate the lithological units and regional lineaments. Moreover, remote sensing has proven a valuable aid in exploring mineral resources. New potential map of iron ore deposit in the study area was produced and classified into four zones which were low, moderate, high and very high-potential zone (Fig. 18), based on the weight of each layer and the confirmation with evidence of geochemical analysis (XRD, XRF,) through the collected samples from the field (Table 3). The outcome of the application of remote sensing, aeromagnetic data and GIS in the study area showed reasonable results of high potentiality minerals (iron ore) associated with very important minerals (Pyrochlore) in Wadi Ash Shatti valley and Idri Town (Fig. 19).

Table 3. XRF results showing the percentage (%) composition of the samples

| Element	Samples									
	S-NO-1	S-NO-2	S-NO-3	S-NO-4	S-NO-5	S-NO-6	S-NO-7	S-NO-8	S-NO-9	S-NO-10
SiO2	68.46	70.88	58.42	88.25	33.69	68.69	63.05	82.68	88.19	67.35
Fe2O3	29.37	22.06	32.67	8.51	45.69	29.09	33.6	10.37	9.13	27.11
CaO	0.72	5.28	7.00	0.97	9.4	0.18	0.1	3.34	0.61	1.42
P2O5	0.39	0.27	0.26	0.05	0.72	0.1	0.2	0.91	0.04	0.08
SO3	0.27	0.27	0.15	0.79	2.61	0.27	0.15	0.18	0.80	1.55
Al2O3	0.21	0.59	0.75	0.25	3.61	1.27	1.6	1.60	0.17	0.26
WO3	0.12	0.06	0.05	0.14	0.02	0.1	0.14	0.06	0.12	0.09
As2O3	0.09	0.04	0.00	0.00	0.00	0.00	0.00	29 PPM	0.00	0.00
MgO	0.07	0.23	0.18	0.07	1.26	0.04	0.05	0.40	0.05	1.25
Cl	0.05	0.03	0.01	0.02	0.42	0.02	0.02	0.02	0.01	0.10
Na2O	0.04	0.00	0.00	0.00	0.14	0.00	0.05	0.04	0.00	0.33
BaO	0.03	0.04	0.1	0.67	0.07	0.00	0.02	0.08	0.57	0.00
V2O5	0.03	0.03	0.02	0.00	0.07	0.02	0.01	0.02	0.00	0.00
MnO	0.03	0.05	0.16	0.02	0.77	0.01	0.07	0.06	0.02	0.14
TiO2	0.02	0.04	0.07	0.19	0.48	0.04	0.19	0.05	0.22	0.11
Gd2O3	0.02	0.02	0.02	0.00	0.00	0.02	0	0.00	0.00	0.02
Co2	0.02	0.00	0.02	0.01	0.03	0.00	0.1	0.00	0.00	0.00
K2O	0.01	0.04	0.02	0.02	0.00	0.00	0.65	0.00	0.01	0.06
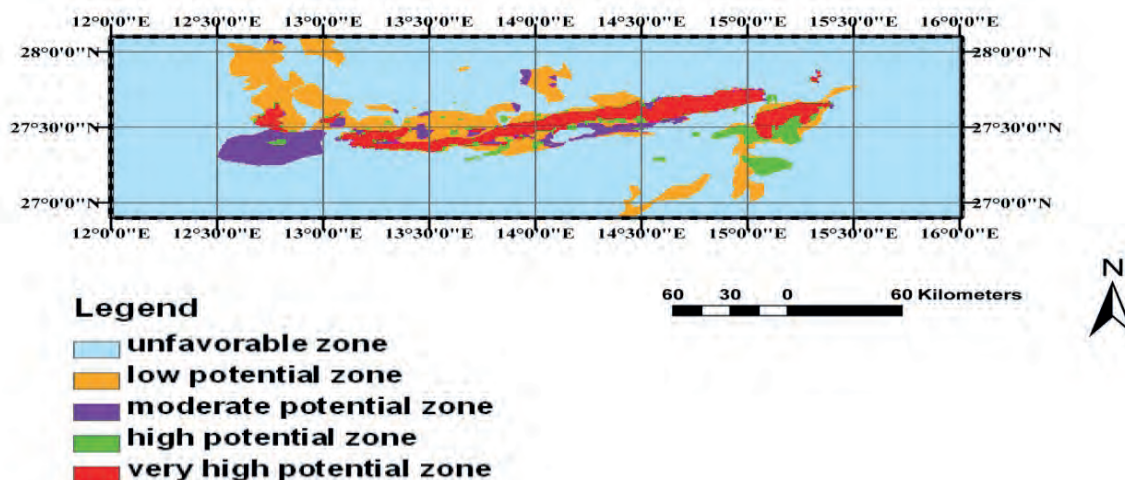
Fig. 18. Potential map of iron ore deposit in the study area include known iron ore deposit
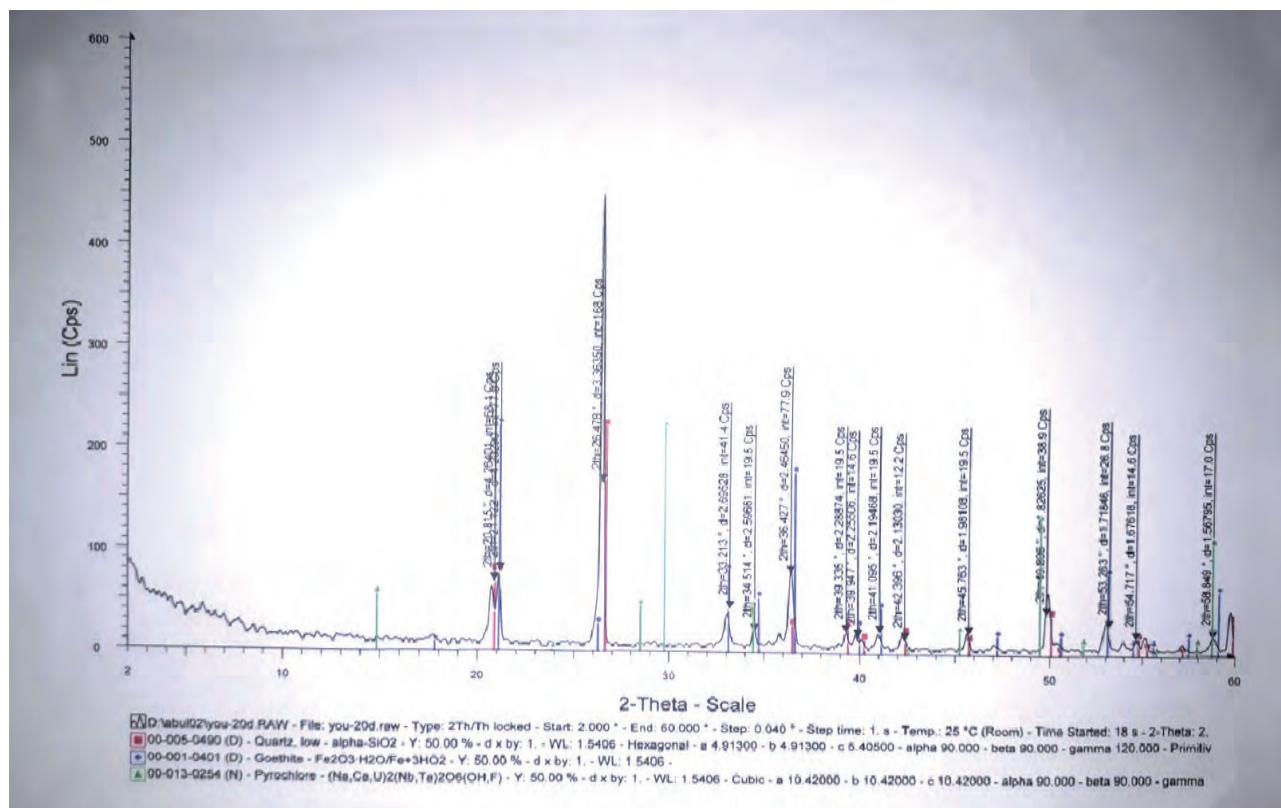
Fig. 19. Diffractograms the sample No (11) from study area shows the most important minerals (Pyrochlore) associated with Goethite and Quartz

ACKNOWLEDGEMENTS

REFERENCES

Baranov, V. (1957). A New Method for Interpretation of Aeromagnetic Maps: Pseudo-Gravimetric Anomalies, Geophysics, V. 22: 359-383.

Blakely, R. J. (1995). Potential Theory in Gravity and Magnetic Application. Cambridge University Press London: 511p.

Bonvin, D. & Yellepeddi, R. (2000). Applications and Perspectives of A New Innovative XRF-XRD Spectrometer In Industrial Process ControL. Paper Read at Advances in X-ray Analysis: 126-136.

Blakely, R. J. & Simpson, R. W. (1986). Locating Edges of Source Bodies from Magnetic Andgravity Anomalies. Geophysics, V.51(7):1494-1498.

Chang-Jo, F. C., & Fabbri, A. G. (1993). Representation of Geoscience Information for Data Integration. Nonrenewable Resources:122-139.

Cordell, L. (1979). Gravimetric Expression on Graben Faulting in Santa Fe Country and the Espanola Basin, New Mexico, Guidebo., 30th Filed Conf., Santa Fe Country, N.Mex. Geol. Soc.: 59-64.

Cordell, L. and Grauch, V. J. S. (1985). Mapping Basement Magnetization Zones from Aeromagnetic Data in the San Juan Basin, New Mexico. The Utility of Regional Gravity and Magnetic Anomaly Maps, Soc. Expl. Geoph.: 181-197.

Dobrin, M. B. and Savit, C. H. (1988). Introduction to Geophysical Prospecting. McGraw-Hill, New York: 867p.

Drury, S. (1987). Image Interpretation in Geology, 3d ed. Allen and Unwin. V. 1: 48p.

Geosoft, Reference Manual (2009). Software for Earth Sciences Geosoft INC., Toronto, Canada.

Getech and Saad. Z J. (2000). Libya A Tectonic and Depth-to-Basement Study Using Well, Gravity and Magnetic Data, Unpublished report, No G0030.

Gillespie, A. R.; Kahle, A. B. & Walker, R. E. (1986). Color Enhancement of Highly Correlated Images Decorrelation and HSI Contrast Stretches. In Remote Sens. Envir. New York, NY: 209-235.

Hansen, R. O and Pawlowski R. S. (1989): Reduction to Pole at Low Latitudes by Weiner Filtering. Geophysics, V.54: 1607-1613.

Ma, Z. J.; Gao, X. L. & Song, Z. F. (2006). Analysis and Tectonic Interpretation to the Horizontal-Gradient Map Calculated from Bouguer Gravity Data in the China Mainland. Chinese Jour. Geophysics (Acta Geophysica Sinica), V.49(1): 106-114.

Nabighian, M. N. (1972). The Analytic Signal of Two-Dimensional Magnetic Bodies With Polygonal Cross-Section: Its Properties and Use for Automated Anomaly Interpretation. Geophysics, V. 37: 507-517.

Nabighian, M. N. (1984). Toward the Three Dimensional Automatic Interpretation of Potential Field Data Via Generalized Hilbert Transforms: Fundamental Relations. Geophysics, V.53: 957-966.

Poovalinga, B. Rajendran, S. A. (2009). Visualizing Uncertainty-How Fuzzy Logic Approach Can Help to Explore Iron ore Deposits. Indian Soc.Remote Sens. V. 37: 1-8.

Sterojexport. (1977). Clays Investigation of Wadi Ash Shat. Tripoli Industrial Research Center.

Sabins, P. V. (1987). Magnetic Method Applied to Mineral Exploration, Ore Geology Reviews. In; P.V. Sharma (Ed.), V. 2(4): 323-357.

Sharma, P. V. (1987). Magnetic Method Applied to Mineral Exploration, Ore Geology Reviews. In; P.V. Sharma (Ed.), V. 2(4): 323-357.

Industrial Research Centre (1984). Geological Map of Libya: Sheet Sabha- NG 33-1,33-2, 33-3, With Explantory Book.

Telford, M. W.; Geldart, P. L. & Sheriff, E. R. (1993). Applied Geophysics, 2d Edition. Cambridge University Press: 769p.

ABOUT THE AUTHORS

Dr.Younes Ajal Abulghasem qualification is as following:
PhD (Geology / Remote Sensing), University Kebangsaan Malaysia (UKM), 2014
MSc (Remote Sensing and GIS) University Putra Malaysia (UPM), 2005
MSc Information technology (IT) Golden State University, 2004.
B.Sc (Geology) Tripoli university , 1992.
Dr Younes is working with the Geologic Department, Faculty of Sciences. Aljabel Alghrabi University.
e-mail: younesajal17@gmail.com

Tareq Hamed Mezughi is a Lecturer at University of Tripoli, Department of Geography and GIS. Dr Tareq has got his B.Sc in the field of Geology in 1988 from Tripoli University , Libya. He did his M.Sc in Remote Sensing, Image Processing and Application at the University of Dundee,UK in 1997.
e-mail: thmezughi@yahoo.com

Dr. Ahmed Salem Saheel has got his B.SC. from the Faculty of Petroleum & Mining Engineering, Geophysics Department, Tripoli University, Libya. He finished MPhil at the Earth Science Department, Leeds University, UK in 1995. Dr Saheel got Ph.D. from the Faculty of Science and Technology, Universiti Kebangsaan Malaysia, Malaysia in 2014. He is working with the Libyan Petroleum Institute, Exploration Department, Tripoli, Libya.
e-mail: a.saheel@lpilibya.com

GEOLOGICAL EXPLORATION AND PRODUCTION OF THE BERENICE MARBLE FROM DARNAH FORMATION (BARTONIAN TO PRIABONIAN), AL JABAL AL AKHDAR, NE LIBYA

Saad El Ebaidi[1]

Abstract: The title Berenice (the historical name for Benghazi city) marble is coined by the project's owner, who has the right to exploit the quarry. The excavation of stone blocks from the Darnah Formation's crystalline and durable limestones is one of the most important operations in this paperwork. The study's objectives are to focus on various parts of geology and their importance in enhancing national economic development. Also, pay attention to the rocks' geological properties in order to determine their suitability for marble production and future potential as building stones. The geology of the research area is dominated by Tertiary system successions, which include three major carbonate sedimentary rock formations. Darnah (Middle to Upper Eocene), Al Bayda (Lower Oligocene), and Wadi Al Qattarah (Upper Miocene) of the Ar Rajmah Group. The Darnah Middle Eocene Gizehensis bed contains potentially massive marble productive formation for building stone as in-situ accumulations of large benthic foraminifers of nummulites (Nummulitic bank), which are considered to be good indicators of shallow marine carbonate environments in fossil series. Where the strong and durable stone has been carefully selected, the Darnah Formation is reduced to size and used as slabs, blocks, and columns. Even if output is doubled, this quarry's stockpile is sufficient to last hundreds of years.

Keywords: Darnah Formation, Benghazi, durable limestones, Eocene, Gizehensis.

INTRODUCTION

Al Jabal Al Akhdar has produced a one rock types for building stone that include limestone, which is can be product of more than 10 types of limestone, marble, travertine (travertine is deposited from the water of mineral springs and it is usually used in the form of tiles for wall cladding and flooring) and other decorative stones with different textures, colors and patterns. The Darnah Formation has a wide range of applications in the construction due to their durability and the fact that they can be easily polished. Large benthonic foraminifera *Gizehensis*rich accumulations very common in this formation and can be easily observed in polished sections. In industrial raw materials, the limestone is classified as a low-value commodity because it's wide availability. In general, we do important discussing with the owner to know what type of marble is required and then we start making our geological study to choose the most appropriate places in terms of quality and quantity as well as the closest to its factory taken into account the factor of transportation. This area of study has been explored, selected very carefully and opened as a marble quarry because of its specifications are very close to the marble required and also it has a lateral and vertical extent. Berenice is the ancient name of Benghazi city, NE Libya; the term is defined by the Italian colonization (1911-1942) in World War II.

Location of the quarry

The study area is located in the northwestern part of Al Jabal Al Akhdar (Fig. 1), about 45 km NE of Benghazi city. Bounded by the latitudes of (32° 23'6'' to 32° 25' 30'' N) and longitudes of (20° 31' 30'', 20° 37' 60'' E).

Objectives

The importance of geologists in contributing to the development of the national economy. And to

[1]*Department of Earth Sciences, Faculty of Science, University of Benghazi, Benghazi-Libya, saad.elebaidi@uob.edu.ly*
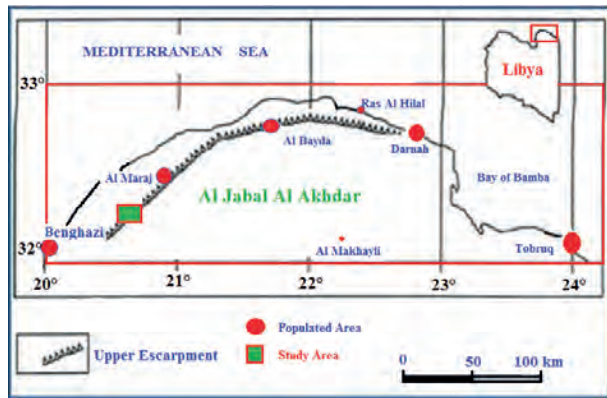
Fig. 1. A map showing the location of the study area.

find out alternative sources of the imported marble from abroad. This kind of limestone raw material of sedimentary rocks of the Darnah Formation is classified as low commodity value (because of its wide availability and cheap). Transport costs are a significant and dominant component of the price paid by customers.

MATERIALS AND METHODS

Perforator Drilling Machine: A perforator drilling machine is used for prepare the vertical and horizontal drillholes the diameter of 76mm (Fig. 2). The vertical and horizontal drill holes must have the same direction to allow easy connection of thediamond wire saw. The diamonds wires saws machines which in use are: Telediam type 45-55S from the Pellegrinicompany, Marini mini fill, Diamond board and Alfa 840 from Benetti machines company (Italy).

Diamond Wire Saw Machine: The use of a diamond wire saw cutting machines in extraction, exploitation of the commercial blocks (dimension stone) in very specific operations (Fig. 3).

Stratigraphy

Al Jabal Al Akhdar anticlinorium lies in the northeast of Libya, in a province known as Cyrenaica. It was developed at the southern margin of the Mediterranean geosyncline of the Tethys, on an attenuated continental crust of the north passive margin of the Afro-Arabian shield (El Hawat*et al*, 2004; El Hawat and Shelmani, 1993). The rocks of Al Jabal Al Akhdar are mainly of marine carbonate sedimentary units ranging in age from Late Cretaceous to Late Miocene (Fig. 4). The geology of the area is mainly represented by successions carbonate sedimentary rocks of Paleogene-

Neogene formations ranging in age from Middle to Upper Eocene to Upper Miocene. The stratigraphic sequences comprise of three formations from oldest to youngest; Darnah Formation which consists of nummulitic limestones; Lower Oligocene; Shahhat Marl and algal limestone members of Al Bayda Formation (Fig. 5); and Middle Miocene Wadi Al Qattarah Formation composed of oolitic limestone of the ArRajmah Group. The total thickness of the exposed section is about 100 meters. Wadi Al Qattarah Formation is observed

Fig. 2. The perforator drilling machine type for preparing drill holes for cutting the rock into commercial blocks using diamond wire.

Fig. 3. Lateral cutting of a primary block with a diamond wire, a Libyan diamond wire saw machine. A) shows the beginning of cutting of the commercial block; B) the final stage of block separation.
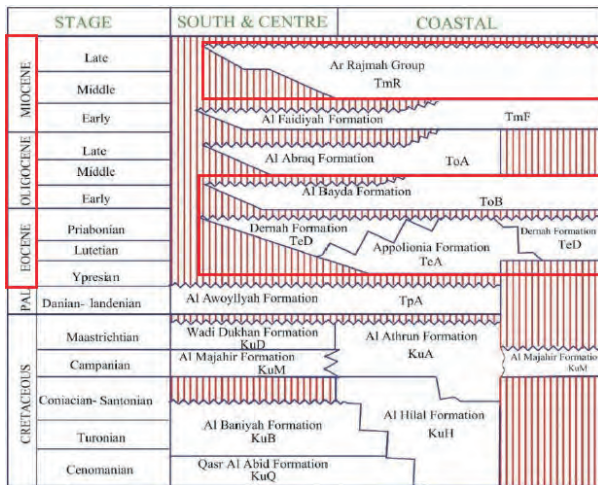
Fig. 4. Stratigraphical chart of northern Cyrenaica (Modified after El Hawat *et al*, 2004; El Hawat and Shelmani, 1993; also see Muftah *et al*, 2017 and Sheltami *et al*, 2018).

Fig. 5. Showing two different formations are well exposed in the first escarpment.

at a higher elevation and not clearly noticed in the first escarpment. These formations are separated by erosional or non-depositional surfaces.

Darnah Formation (Middle-Upper Eocene)

The term Derna (Darnah) was introduced by Gregory (1911) and showed the Apollonia Limestone to be overlain by the Derna. The carbonate sequence conformable overlying the Apollonia and disconformably underlying the Al Bayda Formation represents the Darnah Formation (Klen, 1974; Zert, 1974). Toward the south, the Darnah Formation decreases in thickness gradually and completely wedges out on the Southern part

of Al Jabal Al Akhdar (Rohlich, 1974). In general, Darnah Formation represents the high-energy rim-margin facies, with reefal limestones, corals, nummulites, and algae, and was defined near Darnah where 330 ft (100.584m) are exposed. The age ranges from Bartonian to Priabonian so it is a partial age equivalent of the Apollonia Formation (Hallett and Clark-Lowes, 2016; Hallett, 2002; Sheltami, *et al*, 2018). These rock units of Darnah Formation in the study area are well defined with exposed thickness reaches (60m) and the productive beds with a total thickness of 25m as illustrated at benches 1, 2 & 3 (Fig. 6). The in situ carbonate production of *Nummulites Gizehensis* very thick bed of Middle Eocene Darnah Formation in particularly at the area is recorded and considered to be good indicators of shallow marine carbonate environments in fossil series (Figs. 7A & 7B). The highly porous Nummulitic banks (bench 2; increased in B-Form, Fig. 8), brown in color and acted as an effective barrier and the microstructure in nummulites grains is clearly observed it may due to the highly action current of the storm wave base (El Hawat*et al*, 2007), invasion by carbonate mud took place later and completely filled these fractures (Fig. 9), producing back-bank (bench 3), dark brown, grainstone, crystallized with less porous of calcitic dolomite-rich in *Nummulites Gizehensis* and fore-bank (bench 1), white to yellowish in color, wackestone with less nummulites contents.

In general, the Nummulitic bank of the Eocene sedimentary rocks have attracted the attention of many workers such as: El Hawat*et al*, 2007; Muftah *et al*, 2017, Aly et al., 2001, Abu El Ghar and Hussein, 2005, Papazzoni, 2008, Tawfik *et al*, 2016, Rafi *et al*, 2012,Al-Bloushi and Tanoli, 2018, Sallam*et al*, 2014, Schaub, 1981, Racey, 1995, Imam, 1999, and Megrisi and Mamgain, 1980.

Darnah Formation with Building Stone Potential

The depositional environment, mineralogy and cementing material are all helpful to determine the suitability of Darnah Formation for use in building stone where the strong and durable stone has been correctly selected. That's why is typically quarried at a different level in rectangular commercial blocks then sawed and finished to specified sizes. The blocks in Darnah Formation yield three types of commercial blocks are represented in benches (benches in the open pit are 4-6m high), whereas,

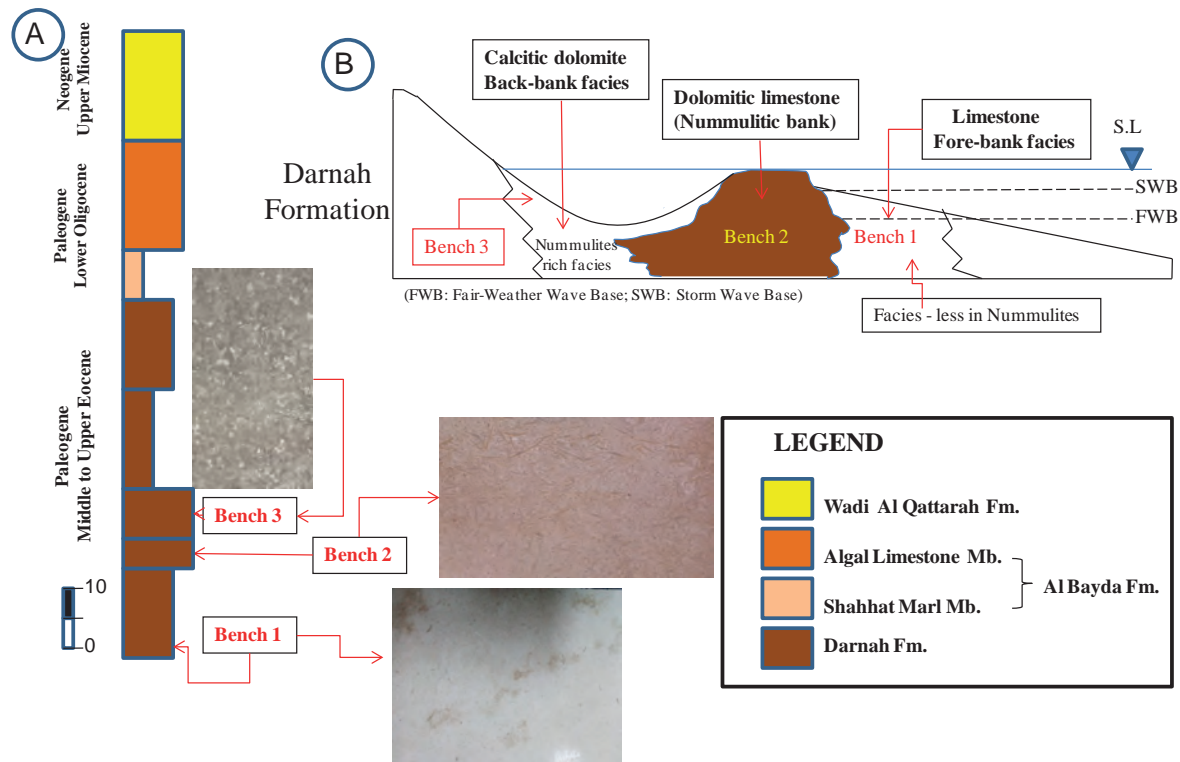Fig. 6. Showing cut benches of Darnah Formation (looking, NE).

Fig. 7. A) successions carbonate sedimentary rocks of Paleogene-Neogene formations and the productive beds of Darnah Formation as illustrated at benches 1, 2 & 3; B) simple scheme of the depositional environment.

bench 4 is a durable conglomerate of Quaternary deposits constitute alluvial terraces and cover the wadi floor (Fig. 10).

The blocks are cut into two sizes with total weigh are ranging from 4 to 6 tones; small one of about 1m x 2m x 2.5m in size and the large block with 2m x 3m x 2m in size and the blocks weigh of up to 4-6 tones can be obtained.That can be produced from a cleaned benches which contain a volume of full annual production of 2000m³ of marble blocks and the number can be increased and that depends on the number of machines and labor availabilities. The marble will be mined by isolating from the main rock mass and then cutting it into blocks with an arm sawing machine and

diamond wire saws to minimize the possibility of the propagation of cracks formed by blasting into the marble. Natural fractures and joints can be a negative factor influence the design of the extraction area and limit the block size that can be produced (Fig. 11). When quarrying stone for building purposes, it is always preferable to extract the largest blocks because larger blocks allow for greater variety in usage. Larger blocks are more difficult to obtain because of the jointing and bedding plane directions and impurities that could cause the rock to crack in undesired places. However, joints at regular intervals can be also a positive factor for building stones because they can aid in extraction and give regular stone

Fig. 8. Nummulitic bank of Darnah Formation (bench 2).

Fig. 9. A polished limestone of the uppermost the productive beds of bench (1) Nummulites shells are clearly affected by storm wave base (SWB) action.

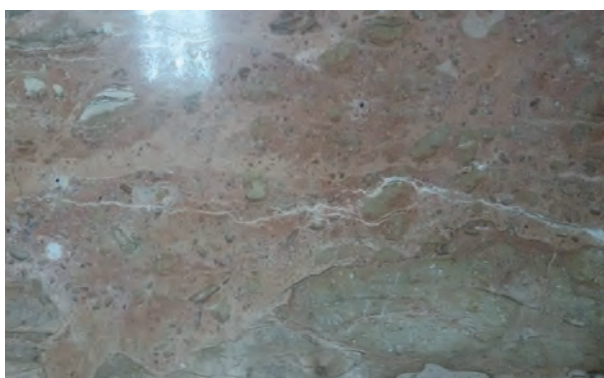Fig. 10. A polished conglomerate of Quaternary deposits (bench 4).

Fig. 11. Natural fractures and joints in the productive units of Darnah Formation.

thicknesses. Some of these joints are completely filled with 3 stages of calcite overgrowth and banded colors due to contamination (Fig. 12). The inclusions resulting of usually a chalky limestone that has been incorporated in the rock of Darnah Formation during deposition affect the quality of the finished surface of the stone and therefore, it is undesired to the buyer in the architecture or landscaping market. The commercial blocks are extracted and moved by fork loaders on the trucks and loaded into the main factory (Fig. 13). The waste is dumped into the landfill close to the open pit. Generally, the price of the larger blocks is proportionately higher, since it is difficult to obtain them intact. After the cutting process, the smaller pieces can be obtained, which are treated and sold for different uses.

The blocks obtained at the quarry blocks are sent to factories for the manufacturing of the finished products that are used in building sites. The block is delivered at the factory and cut into thin layers called slabs or boards. These are typically 2-3cm thick, but any thickness is possible. Treatment is applied with fine grain grinds and subsequent polishing with alumina powder, or other similar products which continuously appear on the market (Fig. 14).

The boards of finished products are further divided into smaller pieces, usually on request. The most common examples are plates for cladding and paving tiles.

Applications and uses of the natural stone

Limestone and other carbonate rocks are extremely valuable raw materials are widely used throughout industry, although the construction (The primary use of carbonate rocks in construction as aggregates) and cement manufacturing industries are generally the principal consumers. Darnah Formation can be used as blocks for walls, sills for windows or archways for doors. It can also be used for decorative purposes and dimension stone. Also is covering a wide range of commercial products, which include paving tiles, flooring e.g marble staircase, veneering for cladding, masonry, slate roofs and individual cut stones. The final product is obtained by cutting up the slabs with different measures, according to demand (Fig. 15). Although the main technological function of claddings is for insulation, day by day innovations in this field appear, creating shapes from different claddings as those of the image with limestone cladding (Fig. 16).

Fig. 12. Joints are parallel to the bedding plane with banded colors of calcite overgrowth (vein-like).

Fig. 13. The commercial blocks are loaded on the trucks to the main factory

Fig. 14. The block is delivered to the factory and cut into thin layers called slabs or boards (typically 2-3 cm thick).

The significances of this paper

It helps in the elimination of unemployment and provides job opportunities for young people, the people who have trucks and loaders in the area where the quarry is located. Educate them to learn the drilling operation techniques and the use of rock cutting machines. The owner of the land is got an attractive price from renting the land annually. An annual rent is also paid to the Ministry of Industry for extraction per cubic meter and the prices are depending on the type of raw materials. Drilling water well at the site as well as benefiting from the land after completion, cleaning, and exploitation by the landowner to use for any other purposes. Economic development and increases the income of citizens through the discovery of many quarries. However, several other quarries have been discovered and selected for other limestone sedimentary rock types (Upper Cretaceous and M. Miocene in age), have very high quantity and quality compared to the Spanish, Italian and Turkish marbles and are currently under construction, where the manufacturer is currently completing administrative issues before starting in extraction processing. Parts of these blocks are

Fig. 15. Cutting up the slabs with different measures, according to demand.

Fig. 16. Shows multiple photos of marble of Darnah limestone used in buildings.

exported to Tripoli with very reasonable prices of about 20 L.D without cutting those blocks into slices. The exploitation of other marble factories where there is no continuous work for the purpose of cutting the rocks in sizes 2 and 3cm, and thus also is a benefit for the owners of these factories and help to increase their income. This type of marble was imported from abroad and in hard currency and sold to the consumers at very high prices. But after the discovery of this national marble, the prices became lower and sold of one-third of the total amount. The reserve of this

quarry is enough for hundreds of years even if the production is doubled for this quarry.

CONCLUSIONS

Limestone and other carbonate rocks are extremely valuable raw materials are widely used throughout industry, although the construction. This kind of research paper is new in Libya because most of the exploitation of carbonate raw materials are concentrated only on the aggregates and its uses in road constructions, concretes, dimension stones and

cement manufacturing industries are generally the principal consumers. Darnah Formation is mainly hard limestone (sedimentary rocks), abundant and low-cost commodity.It was used only in crushed stone prepared for road construction projects. It's used now as a marble for the first time. The limestone is widely used in hallways, guest rooms, washrooms and stairs, solid slab decorations, building stones, flooring tiles, paving stones, curbing and in other decorative purposes. The hard limestone of this formation has been sold to end users as marble in terms of strength, durability, workability, abundance, appearance, abrasion resistance and weathering. Most building-stone quarries occur where the stone outcrops in a valley, escarpment or anywhere that there is minimal overburden. This place of mine has been explored, selected very carefully and opened as a marble quarry because of; 1) very close to the factory of the owner; 2) Gizehensis rich accumulations where the nummulites grains are well distributed and gives a very nice mosaic and add value to the marble slabs; 3) the absence of chert nodules or bed; 4) minimal overburden; and 5) it have lateral and vertical extents. The marble units of economic interest have been identified as a white to cream and light brown marble which is overlain by a dark brown calcitic dolomite-rich in nummulites. The mine comprises of three major benches dimension stone and the commercial blocks differ in sizes; small one about 1m x 2m x 2.5m and the largest block with dimension of 2m x 3m x 2m in size and the blocks weigh up to 4-6 tones is obtained, the full annual production of 2000m^3. In general, Al Jabal Al Akhdar has produced a one rock types for building stone that include limestone, which is can be the product of more than 10 of limestone types, marble, travertine and other decorative stones with different colors and patterns. These visual differences in colors, grain sizes, textures, and patterns can influence the buyer in the architecture or landscaping market. The limestone is mainly obtained from the middle of Darnah Formation. It is called "Berenice" the old name of Benghazi city and is characterized by its patterns and colors.

ACKNOWLEDGEMENTS

REFERENCES

Abu El Ghar, M. S. and Hussein, A.W. (2005). Post-Depositional Changes of the Lower-Middle Eocene Limestones of the Area Between Assiut and Minia, West of the Nile Valley, Egypt. *1STFirst Intern. Conf. Geol. Tethys*, Cairo University: 1-20.

Al-Bloushi, A. J. and Tanoli, S. K. (2018). Facies and Depositional Environments of the Lower to Middle Eocene Dammam Formation in Kuwait. *AAPG Data pages/Search and Discovery Article #90319 ©2018 GEO 2018, 13th Middle East Geosciences Conference and Exhibition*, Manama, Bahrain (Abstract).

Aly, M. F.; Zico, A. and El-Sayed, M. I. (2001). Facies Analysis and Sedimentary History of the Middle Eocene Sequence of Jabal Hafit, Al Ain Area. UAE, JKAU: *Earth Sci., V. 13*: 55-87.

El Hawat, A. S.;Barhathi, H. and Obeidi, A. (2004). Cyrenaica-Transect VII. In: *The TRANSMED Atlas: the Mediterranean Region from Crust to Mantel* (Ed. by: W. Cavazza; W. Roure; F. Spakman; W. Stampfli; G. Ziegler.Springer-Verlag. Web site:*http://www2.unibas.it/transmed/index.htm.*

El Hawat, A. S.;Jorry, S.;Hammuda, O.; Obeidi, A.;Barhathi, H.; Caline, B. and Davaud, E. (2007). The Eocene Ramp Complex of Al Jabal al Akhdar, Cyrenaica, NE Libya: A Surface Analogue for Nummulite Reservoirs. *Proc. EAGE Meeting*, Tripoli.

El Hawat, A. S. and Shelmani, M. A. (1993). Short Notes and Guide-Book on the Geology of Al Jabal al Akhdar, Cyrenaica, NE Libya: 70p.

Gregory, J. W. (1911)**.** Contributions to the Geology of Cyrenaica.*Quart.J. Geol. Soc. London, V67*: 572-615.

Hallett,D. and Clark-Lowes D. (2016).Petroleum Geology of Libya. Elsevier: 392p.

Hallett, D. (2002).Petroleum Geology of Libya. New York, Elsevier: 503p.

Imam, M. M. (1999). Lithostratigraphy and Planktonic Foraminiferal Biostratigraphy of the Late Eocene-Middle Eocene Sequence in the Area Between Wadi Al Zeitun and Wadi Al Rahib, Al BardiaArea, Northeast Libya. *Jour. African Earth Sci., 28(2)*: 619-639.

Klen, I. (1974). Geological Map of Libya 1:250 000. Sheet. NI 34-14, Benghazi. Explanatory Booklet. *Indust. Resear. Cent*. Tripoli: 49p.

Megerisi, M. andMamgain, V. (1980). Al Khowaymat Formation- an Enigma in the Stratigraphy of Northeast Libya. In: *The Geology of Libya* (Ed. by: M. J. Salem and M. T. Busrewil), Academic press, London, *V1*: 73-88.

Muftah, A. M.; El Ebaidi, S. K.; Al Mahmoudi, A.; Faraj, H. F. and Belkasim. K. (2017). New Insights on the Stratigraphy of Tobruq-BurdiArea-Marmarica, NE Libya. *Libyan Jour. Sci.& Tech.*, University of Benghazi, Faculty of Science, Department of Earth Sciences, Benghazi-Libya: *www.sc.uob.edu.ly/pages/page/77*, *6(1)*: 30-38.

Papazzoni, C. A. (2008). Preliminary PalaeontologicalObservations on Some Examples of "Nummulite Banks": Sedimentary or Biological origin? *Rend. Online SGI, 2*: Note Brevi, *www. socgeol.it*: 135-138.

Rafi, S.; Khursheed, S. H. and Mohsin, S. I. (2012). Microfaunal Assemblage of the Sui Main Limestone from Sui Gas Field, Pakistan. *Jou. Basic & Appl. Sci., 8*: 85-90.

Racey,A.(1995).LithostratigraphyandLargerForaminiferal (Nummulitid) Biostratigraphy of the Tertiary of Northern Oman. *Micropaleontology,41*:1-123.

Rohlich, P. (1974).Geological Map of Libya, 1:250,000, Al BaydaSheet NI34-15.Explanatory Booklet; *Indust. Resear. Cent*., Tripoli, Libya: 70p.

Sallam, E.;Issawi, B. and Osman, R. (2014).Stratigraphy, Facies, and Depositional Environments of the Paleogene Sediments in Cairo–Suez District, Egypt. *Arab Jour.Geosci, DOI* 10.1007/s12517-014-1360-8.

Schaub, H. (1981). Nummulites et Assilines de la TéthysPaléogene. Taxinomie, Phylogenèse et Biostratigraphie. *SchweizerischePaläontologischeAbhandlungen*: 104-106.

Sheltami, O. R.; Fares, F. F.; El Oshebi, F. M.;Errishi, H. and Bustany, I. (2018).Strontium Isotopes as Paleo-Indicators of Unconformities: A Case of the Late Cretaceous-Paleocene Deposits in the Al Jabal Al Akhdar, NE Libya. *ICSRI 1.0 2018*: 12-22.

Tawfik, M. M.; El-Sorogy, A. and Moussa, M. (2016). Metre-Scale Cyclicity in Middle Eocene Platform Carbonates in Northern Egypt: Implications for Facies Development and Sequence stratigraphy. *Jour. African Earth Sci., V. 119*: 238-255.

Zert, B. (1974). Geologic Map of Libya. 1:250,000 DernahSheet NI 34-16.Explanatory Booklet. *Inds. Resear. Cent*., Tripoli: 49p.

ABOUT THE AUTHOR

Dr. Saad El Ebaidi

Prof. El Ebaidi is working at the Earth Science Department of the University of Benghazi since 2007. He finished his bachelor's degree from Geololgy Department, University of Benghazi in 1985. Dr El Ebaidi has completed his Doctor of Philosophy at the university of Manchester, England in 2000.
e-mail: saad.elebaidi@uob.edu.ly

UNDERSTANDING THE DISTRIBUTION OF SATURATION EXPONENT IN THE NUBIAN SANDSTONE FORMATION, SIRT BASIN LIBYA USING GLOBAL HYDRAULIC ELEMENT APPROACH

Noreddin Issa A. Mousa[1] and Patrick Corbett[2]

Abstract: The estimation of hydrocarbon reserve is strongly dependent of electric logs data and the saturation exponent has either assumed or used on average value of the whole of reservoir. The reason of this that the petrophysist dos not usually has a more detailed description of reservoir. The main objective of this study is to use the Global Hydraulic Elements approach to estimating the distribution of saturation exponent in the Lower Cretaceous of Nubian Sandstone Formation Sirt Basin, Libya. Amaefule *et al* (1993) introduced the first rock typing approach which was strongly dependent on core plug data sets and was successful in determining different systems in a single dataset. But this method has a major limitation when applied many data sets. This limitation has been overcome by the new concept of 'Petrotyping' (using Global Hydraulic Elements) which was developed by Corbett *et al*, 2003; Kooistra, (2004). In this study two wells are selected from Sirt Basin to evaluate reservoir description of Nubian Sandstone Formation using Global Hydraulic Elements. Six samples plugs have been selected from different Global Hydraulic Elements to determine saturation exponent using porous plate method and to distinguish the saturation exponent between the Global Hydraulic Elements in the Lower Cretaceous of Nubian Sandstone Formation, Sirt Basin Libya.

INTRODUCTION

The most important and emerging challenge for geoscientist and engineering's is to improve the reservoir description programs, which though detailed, have not always included description at the pore throat scale (Amaefule *et al,* 1993). In this study the controls on porosity and permeability in the Lower Cretaceous, Nubian Sandstones Formation Sirt Basin, are considered with respect to their texture and cementation, their petrophysical classification and the effect of subdivision of the petrophysical rock types. The main controls on hydraulic properties and hence the fluid in the porous reservoir media is of major importance for reservoir description. The porosity and permeability of Nubian sandstone Formation which are determined from the laboratory are highly variable across the whole volume of the reservoir being moderate to good in some intervals and poor in

other intervals. For this reason the Global Hydraulic Elements, an adaptation of traditional rock typing method, have been used in this study to improve the description of Nubian Sandstone Formation. Using this breakdown of petrophysical data-and we show that other rock typing approaches produce similar results-is a process of petrotyping (Corbett and Potter, 2004). This is different from more conventional petrophysical rock typing approach (Amaefule *et al,* 1993) because the boundaries of the petrophysical elements are predetermined prior to collecting any plug data. This allows for a rapid and more systematic approach for varying data sets in various wells. The estimation of hydrocarbon reserve is strongly dependent on electric log data and the saturation exponent has either been assumed or an average value for the whole of reservoir has been used. The reason for that is the petrophysist does not usually have a more detailed description of reservoir. Therefore, the main objective of this study is to use this approach to estimate the distribution of the saturation exponent in the Nubian Sandstone Formation, Lower Cretaceous in Sirt Basin, Libya.

_____
[1] *(LPI) Libyan Petroleum Institute.*
[2] *(IPE) Institute of Petroleum Engineering at Heriot-Watt University.*

PETROTYPE METHODOLOGY

Historical Development of Global Hydraulic Element Approach

Reservoir description has many applications in the geology, petrophysics, reservoir engineering and production. Reservoir description is very important to understanding of the reservoir and it is generally hoped that more consideration of reservoir description may lead to less time spent history matching in reservoir modelling. Petrophysists have long tried to define a hydrocarbon-bearing reservoir as a limited set of elements number with unique characteristics of each one. To address this, Amaefule *et al* (1993) introduced the first approach of the Hydraulic Flow Units (HFU) concept. This concept was successful in determining different systems in a single dataset, such as a cored well, but this method has one major limitation, that different HFU's were found in each well. This limitation is of "overcome by the new concept petrotyping" using (Global Hydraulic Elements) which was developed in a series of studies Corbett *et al* (2003); Corbett and Potter, (2004); Svrisky *et al* (2004) Kooistra, (2004). The GHE approach also based on FZI values from the same underlying theory as Hydraulic Units (HU). However, the selecting of a systematic series of FZI values allows to determination of Hydraulic Units (HU) boundaries to define ten Global Hydraulic Elements (Table 1) that can be applied to any reservoir formation (Fig.1). The defineition of these boundaries is arbitrarily chosen in order to split a wide range of possible combinations of porosity and permeability in to a manageable number of Global Hydraulic Elements (Corbett *et al*, 2003; Corbett and Potter, 2004). Corbett and Potter (2004) have pointed

out that the plotting of plug data on the Global Hydraulic Elements "base map" allows trends to be easily determined. This mapping approach allows for the ready comparison between reservoirs, wells, fields, core data and simulation data, and it can be recognized and exploited for permeability prediction. The consistent colour palette of Global Hydraulic Element (GHE) approach (Fig. 1) can also be applied to core data for identification of significant ordered trends in wide range of cross plots of different parameters (Corbett and Potter, 2004). Previous petrotyping studies in the Ordovician in Libya had produced encouraging results (Khalifa, 2006). In this paper, petrotyping has been applied in the Lower Cretaceous, Nubian Sandstone Formation Sirt Basin, Libya (Mousa and Corbett, 2009) and the usefulness of petrotyping as a screening approach to SCAL sample selection is emphasised in this technical note.

Petrotyping (Global Hydraulic Elements) in the study area

The Global Hydraulic Element (GHE) approach has been applied for the study area Southeast Sirt Basin, Libya, to improve the reservoir description and identify petrophysical rock types for this reservoir formation (Two wells are selected A and B). The Global Hydraulic Elements base map was used to identify significant (or lack of) trends of Nubian Sandstone Formation (Figs. 2 and 3). Six (or possibly seven) Global Hydraulic Elements are identified for well A and four for well B (as shown in a Figs. 2 & 3). Photomicrographs (Figs. 4 & 5) show the textural differences between the extreme units.

Definition of Storage and Flow Dominated GHE

The transmissivity (flow) capacity and storability (storage) capacity can be estimated for the Global

Table 1. Shows Boundaries of Global Hydraulic Elements defined by FZI values (Corbett and Potter, 2004).

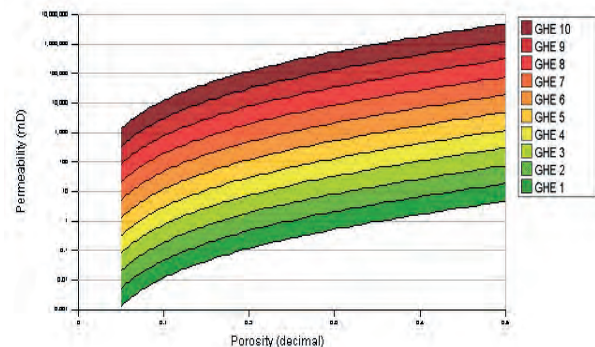| FZI	GHE
0.0938	1
0.1875	2
0.375	3
0.75	4
1.5	5
3	6
6	7
12	8
24	9
48	10

Fig.1. Global Hydraulic Elements Base map template showing GHE at the base GHE-1 at the base and GHE-10 at the top (Corbett and Potter, 2004)
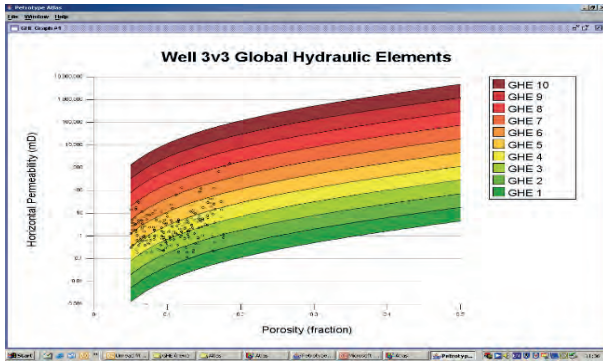
Fig. 2. Shows the GHE trends in well A GHE-1 is the lowest class and GHE-10 the uppermost
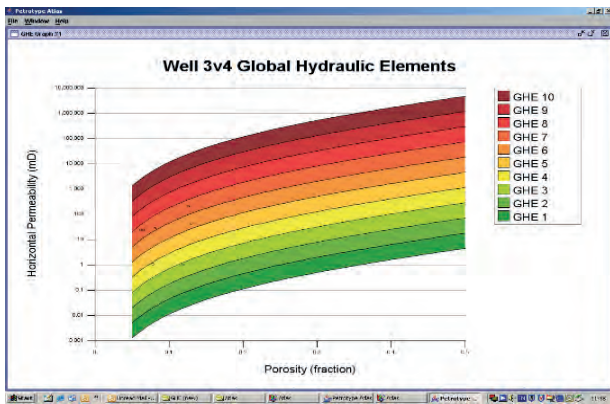

Fig. 3. Shows the GHE trends in well B GHE-1 is lowest class and GHE-10 the uppermost. This well has very few data points but these can be seen to be related to the GHE data in Well A (Fig. 2.).

Hydraulic Elements (GHE) by using a Lorenz Plot. It is useful to identify the storage capacity and flow capacity of the reservoir formation and to use this information in a petrography to see what the difference between the GHEs is dominating storage capacity and GHEs which are dominating flow capacity. The properties transmissivity and storativity are important in well test analysis and the identification of flow intervals, they will affect the thickness assigned in the determination of predominant flow interval indicated. (Zheng *et al*, 2000). The Lorenz Plot displays the petrophysical data in a useful way for reservoir engineering. The Lorenz Plot is the general static measurement of variability and to compute this, first arrange the permeability values in decreasing order of K/Φ and then calculate the partial sums (Jensen *et al*, 2000):

$$F_j = \sum_{j=1}^{j} K_j h_j \bigg/ \sum_{i=1}^{i} K_i h$$

$$C_j = \sum_{j=1}^{j} \Phi_j h_j \bigg/ \sum_{i=1}^{i} \Phi_i h_i$$
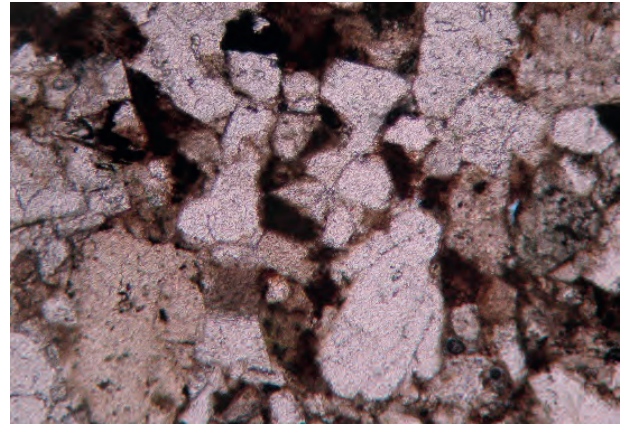

Fig. 4. Nubian Sandstone GHE 2–the worst reservoir quality found in this study–showing very little porosity
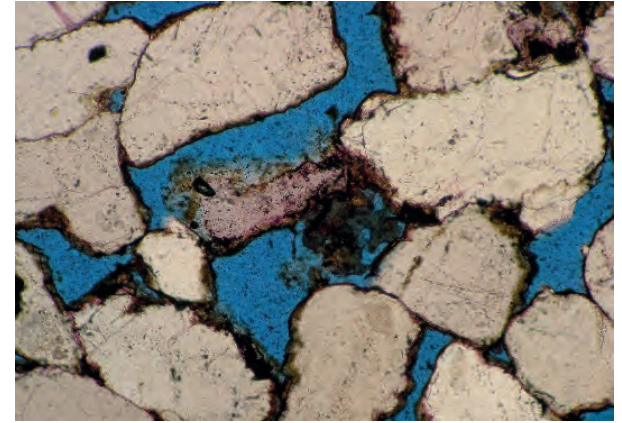
Fig. 5. Nubian Sandstone GHE 7–the best reservoir quality in this study showing well connected porosity.

Where:
F_j = Fraction of total flow capacity (permeability * thickness).
C_j = Fraction of total storage capacity (porosity * thickness).
K = Permeability (mD).
Φ = Porosity (fraction).
h = Thickness (ft).

In the well A, the Lorenz Plot shows that the approximately 83% of the total flow is coming from GHE's 8 and 7 which provide only 8% of the storage. Only 17 % of the total flow is coming from the GHE's 3, 4, 5 and 6, which provide 92% of the storage capacity of these Global Hydraulic Elements. The core data porosity and permeability in Well B is actually not sufficient to make analysis but from the

Lorenz Plot we can recognise that the 60% of the flow is coming from GHE-7. We recognize from the Lorenz Plot that the permeability distribution are very heterogeneous with the flow capacity (TGHE) and storage capacity (SGHE) elements for both wells (A and B) being very unevenly distributed (Figs. 6 and 7).

EXPERIMENTAL MEASUREMENTS

Seven core plugs samples from well A were selected following the petrotype screening process described above and have been examined in details (Table 2). These samples are representative of the GHE found in the two wells (Tables 3 and 4). These core plugs show a distinct trend in texture contrast where the finer grained and poorly sorted sands are associated with GHE-2 which has the worst reservoir rock quality (Figs. 4) while the coarse grained and well sorted sands are associated
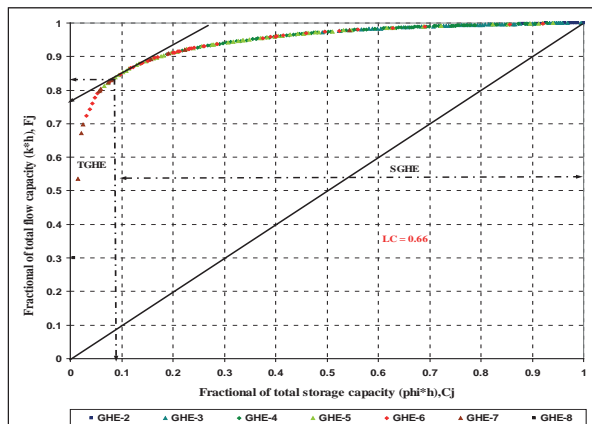

Fig. 6. Well A GHE-coded Lorenz Plot shows the transmissive – dominated GHE,s (TGHE) and storage dominated GHE's (SGHE) defined by tangent to the curve (Mousa, 2008).
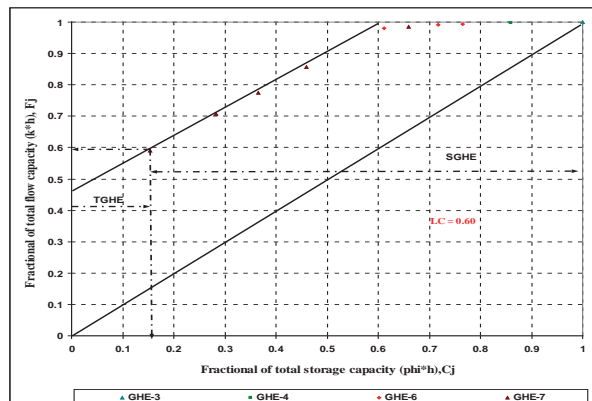

Fig.7. well B GHE-coded Lorenz plot shows the transmissive-dominated GHE's (TGHE) and storage-dominated GHE's (SGHE) defined by a tangent to the curve.

with GHE-7 and GHE-8 with the best reservoir rock quality (Fig.5). Primary depositional texture (grain size), quartz overgrowth and clay minerals appear to drive the variation in the permeability and porosity relationship in the Lower Cretaceous Nubian Sandstone Formation.

CAPILLARY PRESSURE

The Mercury Injection Capillary Pressure technique was used in this study to investigate the pore throat properties of the GHE's in the Lower Cretaceous of the study area to confirm the rock type selection and to predict the variation in the hydrocarbon saturation in the Nubian Sandstone reservoir. The reservoir capillary pressure/water saturation relationship in the Lower Cretaceous here is dependent on rock type (Fig. 8) and related to grain size and cementation. This would suggest that rock type distribution within oil-column height could have a large impact on oil in- place determination as oil-water contact (Khalifa, 2006).

POROUS PLATE METHOD

The porous plate method is used in this study to derive the saturation exponent in the laboratory. Six samples plugs have been selected from different Global Hydraulic Elements for the NSF to determine water saturation, cementation exponent and saturation exponent. The samples were cleaned in hot solvents, dried and then mounted in to the core holder. All the samples were saturated with the brine (110,000ppm) which represents the salinity of the NSF. Clay powder was used between the samples and the porous plate to maintain hydraulic contact during the test. A fi ne metal coated sponge was placed at the inlet end of the plug to ensure good electrical contact. The resistivity of saturated samples (*Ro)* and brine resistivity (*Row)* were measured on consecutive days until the results were stabilized. The resistivity index measurements were carried out using the porous plate method. In this method, the resistivity measurements and de-saturation process takes place separately. The samples were de-saturated simultaneously. By placing them on a porous place in a pressure cell, and gas pressure was applied. The gas (nitrogen) enters the samples from all direction except from the end face. The gas pressure was maintained until no more brine was produced. After capillary equilibrium was reached, the gas was then released and the samples removed from the pressure

Table 2. Showing the selection GHE core samples for detail study

Well A	Plug No.	Porosity %	Permeability mD	FZI	Grain Size	Sorting	GHE
A	240	11.6	0.2	0.316	fine	Poor	2
A	138	15.9	1.12	0.443	fine	Moderately-Poor	3
A	87	15.8	7.2	1.207	fine-medium	Moderatly-Poor	4
A	216	13.4	24.7	2.74	fine-medium	Moderately	5
A	76	16.6	96	3.82	fine-medium	Moderately	6
A	69	18.3	1104	10.9	medium-coarrse	Well Sorted	7
A	66	18.6	1535	12.6	medium-coarrse	Well Sorted	8

Table 3. Showing the Nubian Sandstone Well A Global hydraulic Elements Statistical Summary

GHE	Number of samples	Average FZI	Average permeability (mD)	Average Porosity %
2	11	0.298	0.53	14.6
3	45	0.601	1.07	12.1
4	85	1.093	2.8	11.1
5	58	2.031	7.7	9.3
6	41	4.174	15.5	15.5
7	13	8.911	155	7.1
8	1	12.58	1536	18.5

Table 4. Showing the Nubian Sandstone Well B Global Hydraulic Elements Statistical Summary

GHE	Number of samples	Average FZI	Average permeability (mD)	Average Porosity %
3	1	0.681	1.014	12
4	1	1.379	1.068	7.8
6	3	4.03	15.5	7.3
7	5	7.773	56.4	7.4

cell and weight measurements were taken as well as resistivity reading. The procedure was repeated for several pressures in the range of 1-120psi. The de-saturated process for each sample typically took 2-3 days to complete. Finally, the saturation exponent (n) was calculated (Table 5 & Al-Mahtot *et al*, 1998).

DISCUSSION OF SATURATION EXPONENT RESULTS

The laboratory measured saturation exponent (n) showed some variation. An exact value of saturation exponent is necessary for a good log interpretation analysis aiming to a precise water saturation determination. There are concerns with any laboratory method but here we wish to illustrate that the samples produce a trend. There are many factors affecting saturation exponent such as rock wettability, grain pattern, presence of certain authigenic clays, particularly chamosite, which may promote oil wet characteristics and history of fluid displacement. However, it is found that the rock wettability is the main factor affecting the saturation

exponent (Hamada et al, 2002). The saturation exponent value is a function of both pore system geometry and formation wettability. The saturation exponent value is therefore, of essential importance for the calculation of true initial water saturation from logs. Saturation exponent is normally determined experimentally in the laboratory on core samples of the actual formation under consideration. To obtain a more realistic evaluation of the (n) value because the saturation exponent value varies with both lithology and wettability a suite of saturation exponent value measurement is often conducted on samples from range of porosity and permeability and lithology which may be present in the formation (Bennion et al, 1996). The saturation exponent is related to the texture and affected by wettability and clay minerals, the wettability of those Global Hydraulic Elements are water-wet because the range of saturation exponent is from 1-2. Figure 9 shows that there is a good relation between the Global Hydraulic Elements and saturation exponent. For this study the saturation exponent decreases from GHE-2 which is the poorest reservoir quality and

Table 5. Showing the saturation exponent (n) of Global Hydraulic Elements

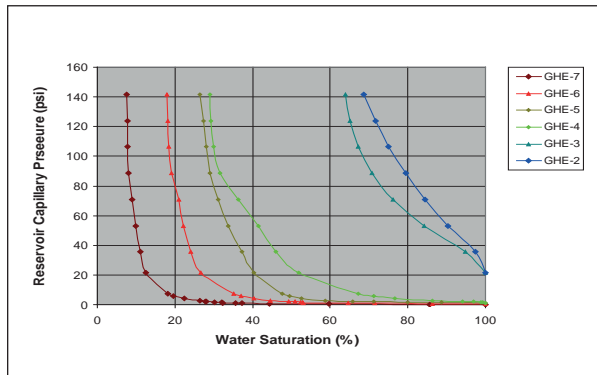| Sample No.	Porosity %	Porosity (fraction)	Permeability (mD)	Swi	Saturation Exponent (n)
GHE-2	11.77	0.1177	0.1	0.71	-2.7
GHE-3	15.85	0.1585	1.12	0.7	-1.99
GHE-4	14.35	0.1435	7.19	0.6	-1.91
GHE-5	13.23	0.1323	24.7	0.17	-1.98
GHE-6	16.55	0.1655	96.4	0.27	-1.75
GHE-7	18.27	0.1827	1104	0.11	-1.54

Fig. 8. Shows the relationship between reservoir capillary pressure, water saturation and systematic trend according to the GHEs in the study area
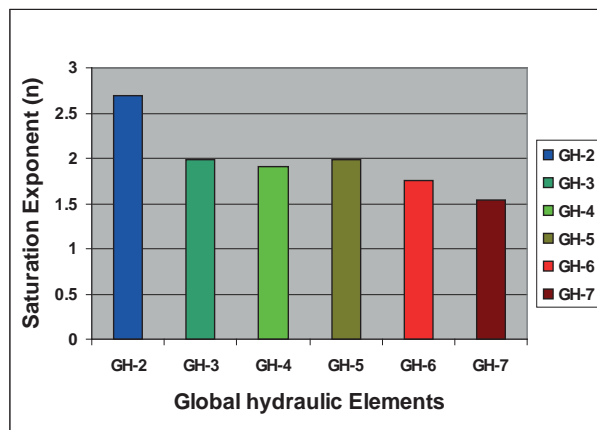

Fig. 9. Showing the distribution of saturation exponent for Global Hydraulic Elements which derived from laboratory study.

tends to be oil-wet to GHE-7 which is the best reservoir quality and is water-wet.

DISCUSSION OF PETROTYPE SAMPLING APPROACH

A single core plug is selected from each petrotype class. Clearly using this very limited dataset to draw conclusions about this field is perhaps stretching the data. In that context this study might be considered a screening study. Additionally, the Generalized Hydraulic Unit (Shenawi *et al*, 2009) approach might also supply

an alternative set of equations that could be used for petrotyping. The rationale for having a limited number of possible rock type elements in a reservoir takes in to account the following: sedimentologists use a limited number of grain size classes to describe texture and rock types in clastics are predominantly texturally controlled (Brayshaw *et al*, 1996). The variation-for a given porosity within a GHE-is within one order of magnitude and therefore is essentially homogeneous (Corbett and Jensen, 1992). Simulation studies suggest that capturing the variability between rock types is more important that the variability within rock type classes/elements when sampling issues are concerned (Mohammed and Corbett, 2003). Modelling the correlation lengths of many rock type elements (lithofacies) within a pixel (sequential indicator simulation) or object modelling workflow is most effective with a limited number of rock types. Using an industry-wide, standard, set of petrophysical elements for all reservoirs can also provide benefits. Identifying porosity and permeability properties within a limited and standard element framework allows for the consistent mapping of these properties within and across wells provides a basis for database construction at the rock typing level (rather than lithology, age, environment or any other criteria) and this has been found useful in petrophysical database studies (Kooistra, 2004). The petrotyping approach, therefore, provides a consistent approach for the petrophysical requirements for reservoir modelling where lithofacies-guided rock typing approaches are the vehicle to enable the 3D distribution of reservoir properties.

CONCLUSIONS

- Seven Global Hydraulic Elements (GHE's 2, 3, 4, 5, 6, 7 and 8) have been identified in Well A and four Global Hydraulic Elements (based on a more limited data set) have been identified in well B (GHE 3, 4, 6, and 7). Because the approach taken, the GHE's are consistent between the wells.

- The core data porosity and permeability for both wells A and B have been plotted on Global Hydraulic Elements Base map to identify the GHE trends.
- Seven representative core plug samples have been selected for the Global Hydraulic Elements in study wells for more detailed study.
- The Lorenz Plot shows that the flow capacity (TGHE) and the storage capacity (SGHE) of the study wells are unevenly distributed. Most of the flow in the wells comes from a few thin zones.
- The textural characteristics of Global Hydraulic Elements are variable. The grain size of GHE-2 is fi ne grained with poor sorting which is the poorest reservoir quality while in GHE-8 is coarse grained and well sorted which is the best reservoir quality. The primary depositional texture has a major role on controlling reservoir properties in the Lower Cretaceous sandstones.
- The petrotyping approach gives a clear trend idented able in the capillary pressure, despite the small sample size.
- The relationship between water saturation and height shows that the water saturation is 18.18% at 51.04ft for GHE-7 which is the best reservoir quality whereas, is 90.23% at 400ft for GHE-2 which is the poorest reservoir quality.
- There is a good relationship between water saturation and reservoir capillary pressure for Global Hydraulic Elements of study wells.
- The relationship between reservoir capillary pressure and water saturation is dependent on grain size, sorting and cementation which control the porosity and permeability.
- The saturation exponent in the reservoir volume is not uniform and the Global Hydraulic Elements approach provides a method for mapping saturation exponent which is a variable in the NSF.
- The petrotype (Global Hydraulic Elements) approach is useful for understanding variation in petrophysical properties which are extreme in the Nubian Sandstone Formation. The range of Global Hydraulic Elements in the reservoir volume can have a significant control on saturation exponent, the distribution of saturation (OIP) on GHE's.
- Following such a screening study, a more comprehensive programme across the range of rock types and porosities is recommended.

NOMENCLATURE

FZI Flow Zone Indicator
GHE Global Hydraulic Element
HFU Hydraulic Flow Units
NSF Nubian Sandstone Formation
SCAL Special Core Analysis

REFERENCES

Al-Mahtot, B. O.; Mason, E. W. and Nasar, M. (1998). Effect of Porosity Type Upon Archie's Parameters of Carbonate Reservoir. *Petr. Res. J., V. 10*: 13-15.

Amaefule, J. O.; Altunbay, M.; Tiab, D.; Kersey, D. G. and Keelan, D. K. (1993). Enhanced Reservoir Description: Using Core and Log Data to Identify Hydraulic (Flow) Units and Predict Permeability in Uncored Intervals/Wells. *Paper SPE 26436 presented at the SPE Annual Technical Conference and Exhibition*, Houston, Texas: 3-6 October.

Bennion, D. B.; Thomas, F. B. and Bietz, R. F. (1996). Determination of Initial Fluid Saturations Using Traced Drilling Media. *Jour, Canadian Petr. Tech., V. 40(1)*: 1-11.

Brayshaw; A. C., Davies, G. W., and Corbett, P. W. M. (1996). Depositional Controls on Primary Permeability and Porosity at the Bedform Scale. In: *Fluvial Reservoir Sandstones. Advances in Fluvial Dynamics and Stratigraphy* (Ed. by: P. A. Carling and M. Dawson). Chichester: John Wiley and Sons, p. 373-394.

Corbett; P. W. M. and Potter, D. K. (2004). Petrotyping-A Basemap and Atlas for Navigating Through Permeability and Porosity Data for Reservoir Comparison and Permeability Prediction. *Paper SCA 2004-30 presented at the International Symposium of the Society of Core Analysts*, Abu Dhabi, United Arab Emirates, 5-9 October.

Corbett; P. W. M., and Jensen, J. L. (1992). Estimating the Mean Permeability: How Many Measurements Do You Need? *First Break, V. 10*: 89-94.

Corbett; P. W. M.; Ellabad, Y. R.; Mohammed, K. R., and Posysov, A. (2003). Global Hydraulic Elements: Elementary Petrophysics for Reduced Reservoir Modelling. Paper presented at the *EAGE Annual Technical Meeting, Stavanger*, Norway, 2-5 June.

Hamada; G. M.; Al-Awad, J. N. M. and Alsughayer, A. A, (2002). Water Saturation Computation from Laboratory, 3-D Regression. *Paper SPE 78575* presented at the Abu Dhabi International Petroleum Exhibition and Conference, 3-16 October.

Jensen; J. L.; Lake, L. W.; Corbett, P. W. M. and Goggin, D. J., (2000): Statistical for Petroleum Engineers and Geoscientists. *2ⁿᵈ Edition*, Elsevier: 338p.

Khalifa, S. A. (2006): Identification of Global Hydraulic Elements in the Ordovician of H-Field, Libya and Implication for Oil in Place. H-Field, Murzuq Basin NC 115. *Unpublished MPhil Thesis,* Heriot Watt University-Edinburgh: 126p.

Kooistra, J. (2004). Links Between Global Hydraulic Elements and Facies, Grain Size and Sorting. *MSc Thesis*, Heriot-Watt University-Edinburgh: 28p.

Mohammed, K. and Corbett, P. W. M. (2003). How Many Relative Permeability Samples Do You Need? A Case Study from a North African Reservoir. *Petrophysics, V. 44(4):* 262-270.

Mousa; N. I. A. and Corbett, P. W. M. (2009). The Distribution of Saturation Exponent and Cementation Factor in the Nubian Sandstone Formation, Sirt Basin, Libya Using Global Hydraulic Element Approach. Presented at the *EAGE North African/Mediterranean Petroleum and Geosciences Conference & Exhibition*, Tunis, Tunisia, 2-4 March.

Shenawi, S.; Al-Mohammadi, H. and Faqehy, M. (2009). Development of Generalized Porosity-Permeability Transforms by Hydraulic Units for Carbonate Oil Reservoirs in Saudi Arabia. *Paper SPE 126073 presented at the SPE Saudi Arabia Technical Symposium and Exhibition*, Saudi Arabia, 9-11 May.

Svirsky, D; Ryazanov, A.; Pankov, M.; Corbett, P. W. M. and Posysoev, A. (2004). Hydraulic Flow Units Resolve Reservoir Description Challenges in a Siberian Oil Field. *Paper SPE 87056 presented at the SPE Asia Pacific Conference on Integrated Modelling for Asset Management*, Kuala Lumpur, Malaysia, 29-30 March.

Zheng, S.; Corbett, P. W. M.; Ryseth, A. and Stewart, G. (2000). Uncertainty in Well Test and Core Permeability Analysis: A Case Study in Fluvial Channel Reservoir, Northern North Sea, Norway, *AAPG, Bull. V. 84(12)*: 1929-1954.

ABOUT THE AUTHORS

Noreddin Issa A. Mousa working in Libyan Petroleum Institute he is received his Bsc. in Geological Engineering from faculty of Petroleum and Mining Engineering Tripoli University Libya in 1985 and Master of Philosophy (Mphil) in Petroleum Engineering from Heriot- watt University, Edinburg UK in 2008. Noreddin has 33 years' experience covered data interpretation including reservoir characterization, rock properties, well logging, several joint venture studies and university teaching.

Patrick Corbett is Total Professor of Petroleum geoengineering in the Institute of Petroleum Engineering at Heriot-Watt University. He has researched the integration of geoscience and engineering through petrophysical methods for the last 30 years. Prior to that worked for Unocal for 10 years in UK, Netherland and Indonesia. He is a member of SPWLA, EAGE, SPE, SEG and AAPG.

MODELING STUDY OF CARBONATION MECHANISMS OF
CO$_2$−CaO AND CO$_2$−NaOH REACTIONS

Mustafa Abunowara[1] and Mohamed Elgarni[1]

Abstract: Calcium oxide (CaO) and sodium hydroxide (NaOH) have been used among various solid sorbents for CO$_2$ capture. Therefore, it is necessary to study the major controlling steps between the reactions of CO$_2$ and solid sorbents. The CO$_2$ uptake and the rate constant of the CO$_2$-CaO and CO$_2$-NaOH reactions were investigated using atmosphere thermogravimetric analyzer (ATGA) to understand its reaction mechanisms and speed span. A shrinking core model was utilized to determine the rate controlling steps, mass transfer coefficient, diffusion coefficient, and the time for complete conversion of a particle at ash diffusion controls regime. The results have been shown that the time for complete conversion of CaO and NaOH particles is chemical reaction controls regime for carbonation cycle. The chemical reaction was found to be the major controlling step reaction at initial minutes. After that the product layer diffusion became gradually more dominant controlling step in CO$_2$-CaO and CO$_2$-NaOH reactions. Therefore, the results been shown that diffusion mechanism is the main dominant regime for the remaining reaction cycle. These outcomes contribute to the understanding of how CO$_2$ reacts with CaO and NaOH solid sorbents at various temperature ranges.

Keywords: CO$_2$ sorption; CaO carbonation; NaOH; Shrinking core model; Thermogravimetric analyzer.

INTRODUCTION

Carbon dioxide (CO$_2$) emissions have been increased into atmosphere due to the combustion of fossil fuels, resulting in adverse impacts on the earth environment such as global warming, increasing sea level and climate change (Lin *et al,* 2021). According to the Intergovernmental Panel on Climate (IPCC), carbon emissions will raise without any intervention from 36Gt/yr to between 48 and 55Gt/yr by 2050 with the continuous increase of energy demand (Pachauri *et al*, 2014). The CO$_2$ concentration for 2100 on current trend will reach 530-980 ppm, possibly doubling the present level of ~410ppm and much higher than the preindustrial level of 280ppm. To avoid the apparent mean temperature rise caused by the rapid accumulation of CO$_2$, active removal of CO$_2$ is highly demanded (Hu *et al*, 2021). Extensive research has been dedicated recently to CO$_2$ capture technologies due to growing

concerns with respect to greenhouse gases emissions (Breidenich *et al*, 1998; Huaman *et al*, 2014; Aydin *et al*, 2010; Abunowara *et al*, 2020 and Suleman *et al*, 2020). CO$_2$ capture efficiency is the main challenge, where the core technology involves the usage of adsorption materials. Such as porous polymer-based solid amine adsorbents, fiber-based solid amine adsorbents, and thermo-responsive adsorbents have been developed for CO$_2$ capture. CO$_2$ adsorbents such as porous carbons and metal−organic frameworks particularly involve physical adsorption as the main CO$_2$ adsorption mechanism, where the adsorption characteristics specifically depend on the pore volume (Lin *et al,* 2021). However, non-catalytic fluid solid reactions are common occurrence in chemical and metallurgical industries, pollution abatement (Bhattacharya and Purohit, 2004). Calcium based materials have attracted particular attention as potential sorbents for cyclic CO$_2$ capture processes. Among the possible applications of calcium based sorbents for CO$_2$ removal are steam reformers, gasifies of fossil fuels to enhance water-gas-shift reaction giving high hydrogen yields, and fluidized bed

[1] *Libyan Petroleum Institute (LPI) Tripoli, Libya.*
E-mail address: abunowara1980@gmail.com,
mohamed.elgarni@cnrl.com

combustors with *in situ* CO_2 capture. These applications all involve sorbent cycling between calcination and carbonation (Sun *et al*, 2008a). The CO_2–CaO and CO_2-NaOH reactions are growing interest because of their potential usefulness and high affinity in CO_2 capture in such industrial systems as steam reformers, gasifies and fluidized bed combustors (Sun *et al*, 2008b).

As a typical gas–solid reaction producing a solid product, carbonation is initially fast, followed by a much slower stage (Barker, 1973; Bhatia & Perlmutter, 1983; Abanades & Alvarez, 2003 and Alvarez & Abanades, 2005). An intrinsic kinetic study for the CaO-CO_2 reaction with a wide range of CO_2 partial pressure was tested using both atmosphere thermogravimetric analyzer (ATGA) and pressurized thermogravimetric analyzer (PTGA). It has been found that the intrinsic rate have a variable order with respect to CO_2 partial pressure. It was initially first–order reaction changing to zero–order and dependence when the CO_2 partial pressure exceeded ~10kPa (Sun *et al*, 2008a & b).

Non catalytic reaction of particles with surrounding fluid, there are several models in which two of them which are characterized as simple idealized models namely, progressive-conversion and shrinking unreacted-core models which are considered for studying the carbonation cycles. For instance, progressive-conversion model (PCM) the reactant gas enters and reacts throughout the particle at all times, most likely at various rates and at various locations within the particle. Solid reactant is converted continuously and progressively throughout the particle. While, in the shrinking–core model (SCM), the reaction occurs first at the outer layer of the particle and the zone of reaction then moves into the solid matrix. As result, leaving behind completely converted material and inert solid and this considered as "ash". At any time there exists an unreacted core of material which shrinks in size during reaction (Levenspiel, 1999).

In this study, thermogravimetric analyzer (TGA) has been utilized to measure CO_2 sorption on CaO and NaOH solid sorbents at various temperature ranges. The results of CO_2 sorption on CaO and NaOH solid sorbents have been investigated using shrinking core model to understand how CO_2 molecules interact with the sorbent matrix. The kinetic model has been utilized to determine the rate controlling steps,

mass transfer coefficient, diffusion coefficient, and the time for complete conversion of a particle at ash diffusion controls regime. Therefore, this paper focuses on studying rate controlling steps for the CaO-CO_2 and CO_2 NaOH reactions at various temperature ranges.

EXPERIMENTAL PROCEDURE

The *Labsys* TG SETARAM instrument has been used in thermal analysis and calorimetry for gas solid reactions and in thermal degradation process. Thermal gravimetric analyzer (TGA) instrument has been utilized in this study to record the mass uptake of the samples when exposed to carbon dioxide atmosphere. A schematic diagram of TGA apparatus is shown in (Fig. 1). The reactivity testing of calcium oxide (CaO) and caustic soda (NaOH) sorbents for carbonation processes has been carried out separately in the TGA apparatus. A small sample of the sorbent (65mg) was placed in a platinum crucible and the weight of the sample was recorded progressively at every second. The scanning rate was maintained at 10°C/min. First precursor was calcium carbonate; the furnace temperature raised from 30°C to 1000°C then started the decarbonation cycle for $CaCO_3$ to assure that the material (calcium carbonate) fully decomposed to CaO. After that the instrument started cooling down until it reaches the required temperature and after that the isotherm cycle directly started for one hour, hence finishing the decarbonation and isotherm cycles under nitrogen gas (N_2) then switch to carbon dioxide gas to begin the carbonation cycle for three hours and the temperature ranges were used in study between (550-750°C). The second material was caustic soda (NaOH). The furnace temperature was raised from 30°C to the required temperature ranges between (75-225°C) then the furnace started automatically heating under the isotherm cycle for half hour. The heating and isotherm cycles performed under nitrogen gas (N_2) then directly switch to carbon dioxide gas (CO_2) to begin the carbonation cycle for one hour.

Modelling of Carbonation Reactions
Shrinking-Core Model
This model was first developed by (Yagi and Kunii, 1955 & 1961) who visualized five steps occurring in succession during reaction:
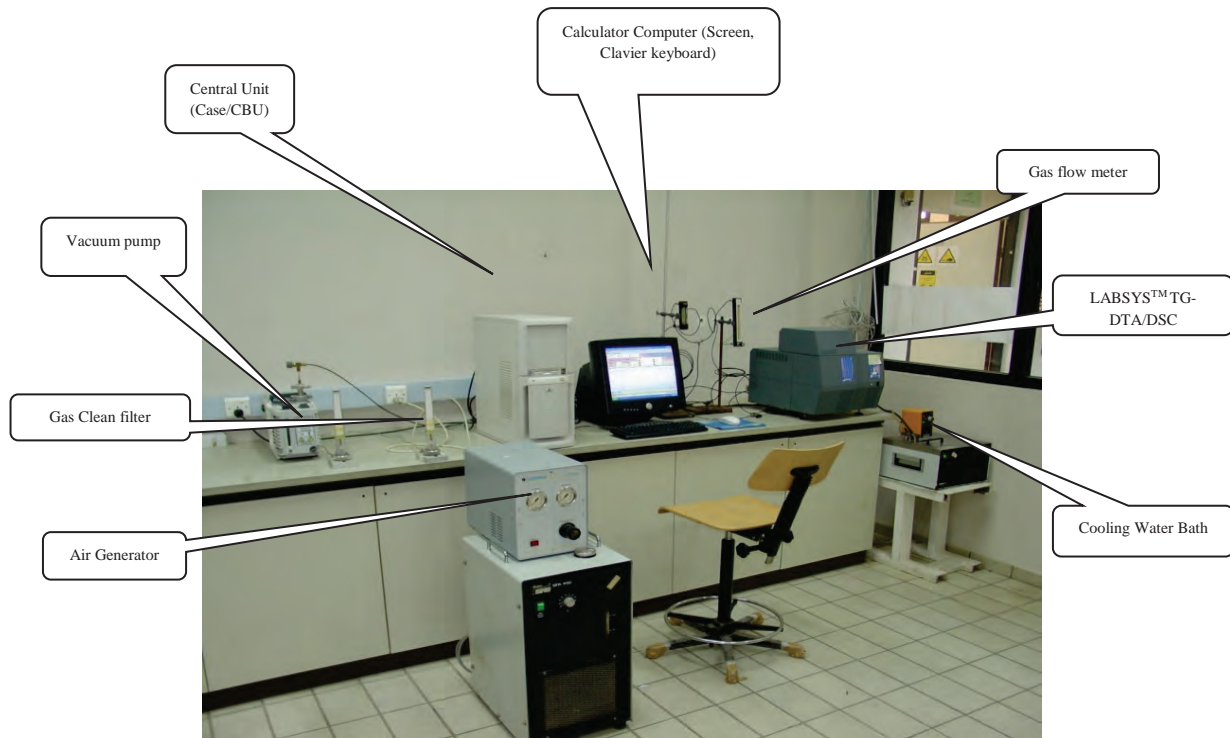1. Diffusion of gaseous reactant (A) through the film surrounding the particle to the surface of the solid.

Fig. 1. Schematic of TGA apparatus

2. Penetration and diffusion of (A) through the blanket of ash to the surface of the unreacted core.
3. Reaction of gaseous (A) with solid at this reaction surface.
4. Diffusion of gaseous products through the ash back to the exterior surface of the solid.
5. Diffusion of gaseous products through the gas film back into the main body of fluid.

Diffusion through Gas Film Controls

In this regime the resistance of the gas film controls, indicates that no gaseous reactant is present at the particle surface and the concentration driving force, C_{Ag}–C_{As} becomes C_{Ag} and is constant at all times during reaction of the particle. Hence, the time for complete conversion of a particle will be:

$$\mathcal{T} = \frac{\rho_B R}{3bk_{Ag}C_{Ag}} \tag{1}$$

And the conversion X_A is defined as:

$$t/\mathcal{T} = X_A \tag{2}$$

The carbonation reaction is:

$$CaO + CO_2 \leftrightarrow CaCO_3 \tag{3}$$

$$2NaOH + CO_2 \rightarrow Na_2CO_3 + H_2O \tag{4}$$

With the assumption of ideal gas phase, where

$$PV = nRT \tag{5}$$

Film resistance at the surface of a particle is dependent on numerous factors, such as the relative velocity between particle and fluid, size of particle, and fluid properties. These factors have been correlated for various ways of contacting fluid with solid, such as packed beds, fluidized beds. Froessling (1938) gave, an example, for mass transfer of a component of mole fraction (y) in a fluid to free-falling solid. Theoretical maximum weight gain (%) of CaO =78 mg of CO_2/mg of CaO and theoretical maximum weight gain % of NaOH =37 mg of CO_2/100 mg of NaOH:

$$Sh = 2+0.6(Sc)^{1/3}(Re)^{1/2} \tag{6}$$

$$\frac{k_{Ag}h\,d_p\,y}{\mathcal{D}} = 2+0.6(Sc)^{1/3}(Re)^{1/2} = 2+0.6\left(\frac{\mu}{\rho\mathcal{D}}\right)^{1/3}\left(\frac{dp\,u\rho}{\mu}\right)^{1/2} \tag{7}$$

In order to estimate time required for complete conversion in a gas film controls regime, the following procedure has been used: Chapman

and Enskog equation (Poling *et al*, 2001) for describing self diffusivity coefficient for gas (self diffusion of CO_2):

$$\mathcal{D}_{(CO2\text{-}CO2)} = (0.00266 T^{3/2})/(PM^{1/2}\sigma^2 \Omega_D) \qquad (8)$$

$$\sigma_{AA} = (\sigma_A + \sigma_A)/2 \qquad (9)$$

$$\Omega_D = A/(T^*)^B + C/\exp(DT^*) + E/\exp(FT^*) + G/\exp(HT^*) \qquad (10)$$

$$(\mathcal{D}_{T1}/\mathcal{D}_{T2}) = (T_1/T_2)^{3/2} \qquad (11)$$

Where:
$T^* = kT/\varepsilon_{AA}$, $A = 1.06036$, $B = 0.15610$, $C = 0.19300$, $D = 0.47635$, $E = 1.03587$, $F = 1.52996$, $G = 1.76474$, $H = 3.89411$, $\sigma_{CO2} = 3.941$ Å, $\varepsilon_{(CO2)}/k = 195.2$K, and. $\Omega_D = 0.87486$.

Diffusion through Ash Layer Controls

In this regime the resistance to diffusion through the ash controls the rate of reaction so that both reactant (A) and the boundary of the unreacted core move inward toward the center of the particle. Where the time ($\mathcal{T}$) required for complete conversion is:

$$\mathcal{T} = \frac{\rho_B R^2}{6b\mathcal{D}_e C_{Ag}} \qquad (12)$$

$$t/\mathcal{T} = 1 - 3(1-X_A)^{2/3} + 2(1-X_A) \qquad (13)$$

Chemical Reaction Controls

The progress of the reaction is unaffected by the presence of any ash layer, the rate is proportional to the available surface of unreacted core. Where the time ($\mathcal{T}$) required for complete conversion is

$$\mathcal{T} = \frac{\rho_B R}{bk''C_{Ag}} \qquad (14)$$

$$t/\mathcal{T} = 1 - (1-X_A)^{1/3} \qquad (15)$$

RESULTS AND DISCUSSION

Carbonation of Calcium Oxide

The reaction of CO_2-CaO proceeds through two rate−controlling regimes. The first regime involves a rapid, heterogeneous chemical reaction. In the second regime, the reaction slows down due to the formation of an impervious layer of $CaCO_3$. This product layer prevents the exposure of unreacted CaO in the particle core to CO_2 for further carbonation. The kinetics of the second regime is governed by the diffusion of gaseous species through the $CaCO_3$ product layer. However, the relative importance of the gas film, ash layer, and reaction steps will vary as particle conversion progresses. For example, for a constant size particle the gas film resistance remains unchanged, the resistance to reaction increase as the surface of unreacted core decreased, while the ash layer resistance was nonexistent at the start because no ash is present, but became progressively more and more crucial as the product layers build up.

Scanning electron microscope (SEM) images for pure CaO, CaO and CO_2 reactant samples at various temperatures have shown in (Fig. 2). Figure 3 represents the film diffusion controls, ash diffusion controls and reaction controls for CO_2-CaO system which changes with time and affected significantly by high temperature ranges (> 550ºC). Table 1 gives the molecular diffusion coefficient ($\mathcal{D}$) from Chapman and Enskog equation (8), mass transfer coefficient (k_{Ag}) which has been calculated from Froessling equation (7), and the time for complete conversion of a CaO particle with gas film controls ($\mathcal{T}_{film}$) using equation (1). Time required to complete conversion for gas film control regime within the temperature range from 550ºC to 750ºC indicated that this control regime is not rate limiting mechanism. The time required for achieving high conversions exceeding times longer than 50 seconds as shown in (Figs. 4-8).

The initial linear stage identifies the kinetic control regime with the slope of this stage giving the intrinsic surface reaction rate. Furthermore, the starting points of the linear stage, featuring the maximum slope, usually reside at low conversions, i.e. 5% to 7%. As carbonation proceeds product layer diffusion becomes more crucial, resulting in much slower carbonation rate. The shrinking core model which has been applied for CO_2-CaO system when chemical kinetics control the overall reaction (Equations 13 & 14) that is also equivalent to grain model that has been described by Szekely *et al* (1976).

Table 2 illustrates the effect of temperature on chemical reaction rate constant (k'') between gas (CO_2) and particles (CaO) calculated from equation (14). Even though there is scattered in surface reaction rate constants given in Table 2 which could be due to non uniform solid sample and its transformation as a result of thermal stresses, causing surface area to vary as a function of temperature. Activation energy obtained from this data gave of 12kJ/mole as shown in (Fig. 9).
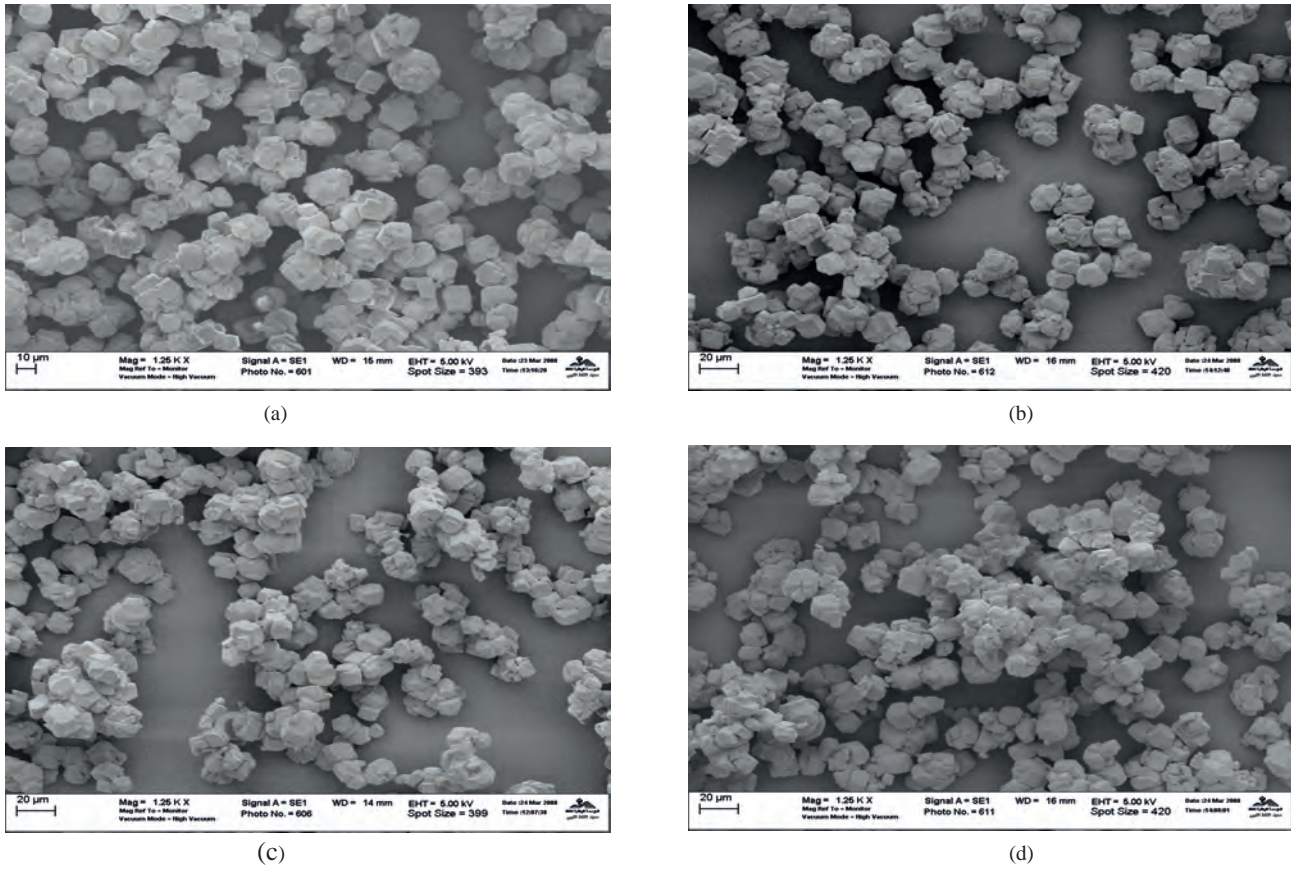
(a)

(b)

(c)

(d)

Fig. 2. SEM images (1250X) of pure calcium carbonate (CaCO$_3$) (a), calcined calcium carbonate (CaCO$_3$) at 1000ºC (b), CaO-CO$_2$ reaction sample at 550ºC (c) and CaO-CO$_2$ reaction sample at 700ºC (d)

Table 1. Estimated molecular diffusion coefficient ($\mathcal{D}$), mass transfer coefficient (k_{Ag}) and time for complete conversion ($\mathcal{T}'_{film}$) assuming gas film regime controls for the CaO-CO$_2$ system

Temperature (ºC)	ρ_{CO2} (kg/m^3)	μ_{CO2} (kg/sec*m)	$C_{Ag(CO2)}$ (mol/m^3)	$\mathcal{D}$ (m^2/sec)	k_{Ag} (m/sec)	$\mathcal{T}_{film}$ (sec)
550	0. 6516	0.3962	14.8	0.00006969	2.8616	0.01151
600	0. 6143	0.4131	13.95	0.000076135	3.1254	0.01118
650	0. 581	0.4296	13.2	0.000082767	3.3968	0.010875
700	0. 5511	0.4460	12.5	0.000089582	3.6757	0.010613
750	0. 5242	0.4623	11.91	0.000096574	3.9618	0.010334

This activation energy is lower than values which have been reported by Sun *et al* (2008a & b) which found activation energy of 29±4 kJ/mole for CaO obtained from natural limestone which indicates that this reaction is faster than that reported by Sun *et al* (2008a & b). However, Sun *et al* (2008a & b) who studied the kinetics of this system (CO$_2$-CaO) using various models suggested activation energies near zero, which is an average value between present activation energy and those reported in (Sun *et al* 2008a & b). The effective diffusion coefficient ($\mathcal{D}_e$) of gaseous reactant in the ash layer calculated from equation (12) and the

time ($\mathcal{T}$) required for complete conversion in both chemical reaction and ash diffusion regimes from (Figs. 4-8). Times for complete conversion for ash diffusion controls regime within the temperature ranges of 550ºC to 750ºC as shown in Table 2 indicating that this control regime is the major rate controlling step. Effective diffusion coefficients reported in the Table 2 are much smaller than molecular diffusion coefficients given in (Table 2) indicating that either Knudsen and/or surface diffusion mechanisms are operating within the pores of calcium carbonate. Actually, effective diffusion coefficients are of combined Knudsen/
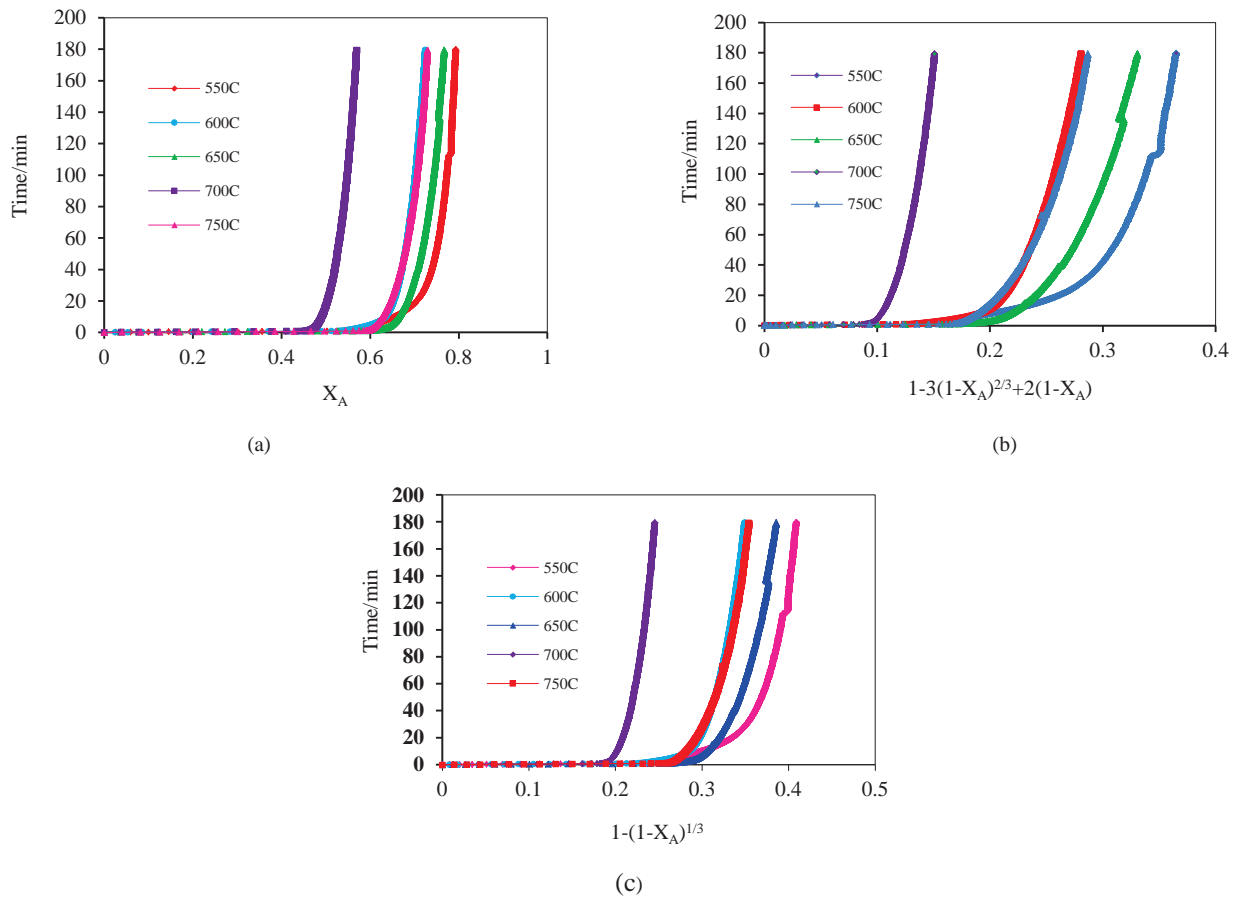
(a)

(b)

(c)

Fig. 3. Conversion vs time for (a) gas film controls, (b) chemical reaction controls and **(c)** ash diffusion controls carbonatonation cycle for CO_2-CaO system
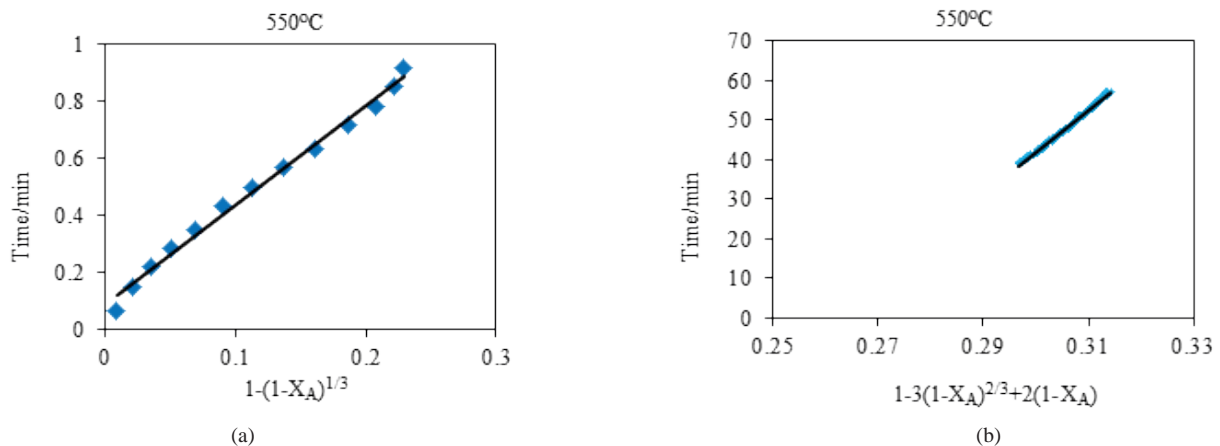

(a)

(b)

Fig. 4. Slope of reaction of CaO-CO_2 with the aid of Shrinking Core model during early stage (a) of carbonation and diffusion product layer of CaO-CO_2 during final stage (b) of calcium oxide at 550 °C

Surface diffusion types because their values are of the order of 10^{-12} m²/sec but with restricted activation giving activation energy in the order of 20kJ/mol. Knudsen diffusion has temperature dependency of 0.5 whereas, surface diffusion usually shows a temperature variation of greater than 15. Present data temperature dependency is of the order of 3. Shrinking unreacted core model without structural variation has a limitation in completely describing quantitively in this reaction system. Shrinking core model gave reasonable representation and at rest semi-quantitive for
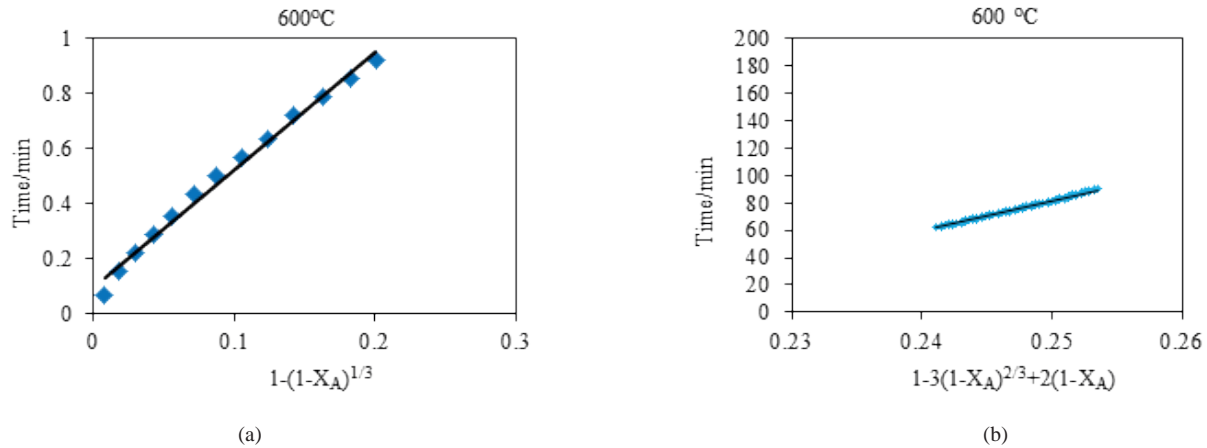
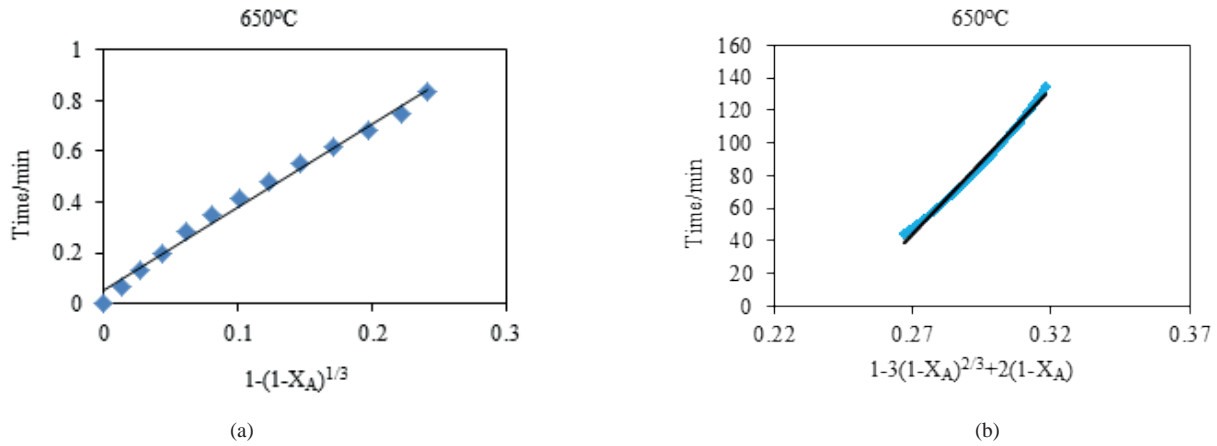(a)   (b)

Fig. 5. Slope of reaction of CaO-CO_2 with the aid of Shrinking Core model during early stage (a) of carbonation and diffusion product layer of CaO-CO_2 during final stage (b) of calcium oxide at 600°C

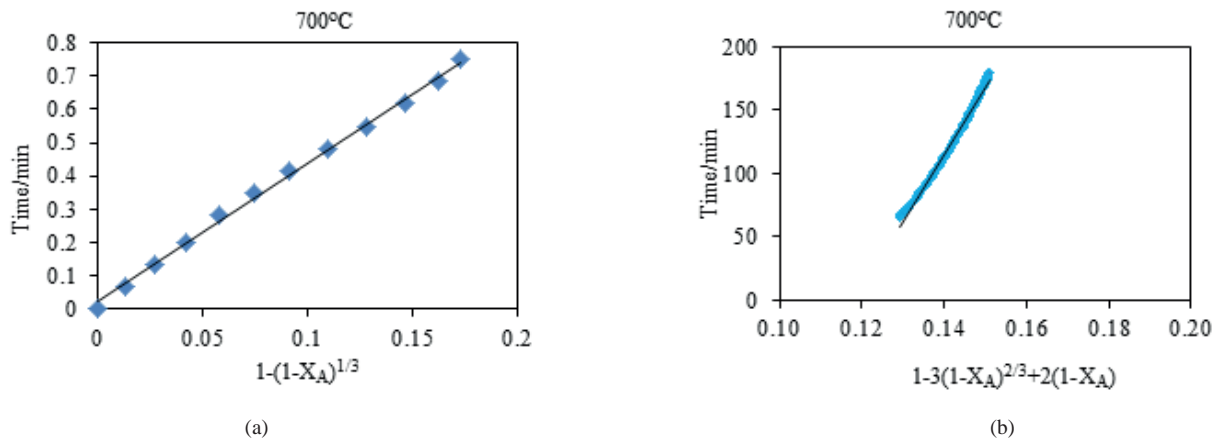(a)   (b)

Fig. 6. Slope of reaction of CaO-CO_2 with the aid of Shrinking Core model during early stage (a) of carbonation and diffusion product layer of CaO-CO_2 during final stage (b) of calcium oxide at 650 °C

(a)   (b)

Fig. 7. Slope of reaction of CaO-CO_2 with the aid of Shrinking Core model during early stage (a) of carbonation and diffusion product layer of CaO-CO_2 during final stage (b) of calcium oxide at 700°C

CO_2-CaO reaction system. Modeling approach employing a variable diffusivity shrinking core model (Szekely *et al*, 1976) or a variable pore size distribution model (Levenspiel *et al*, 1999) would provide a better gas−solid reaction model.

After times exceeding roughly 50 seconds, rate of reaction slows down due to the resistance to diffusion generated from the formation of $CaCO_3$ layer (ash) as described above. The shrinking core model under ash diffusion controls has short

(a)   (b)
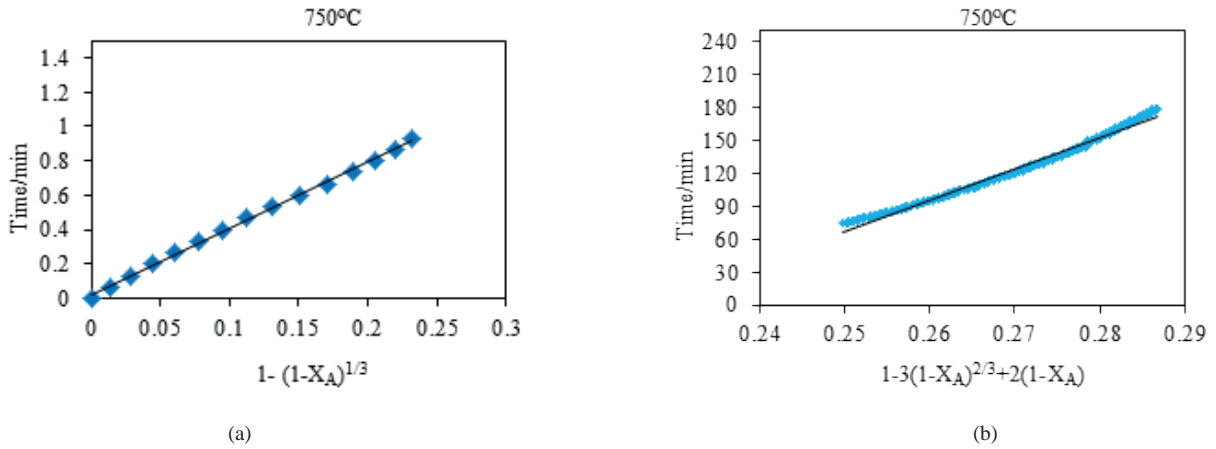
Fig. 8. Slope of reaction of CaO-CO$_2$ with the aid of Shrinking Core model during early stage (a) of carbonation and diffusion product layer of CaO-CO$_2$ during final stage (b) of calcium oxide at 750°C

Table 2. Chemical reaction rate constant ($k°$) between gas (CO$_2$) and particles (CaO) and effective diffusion coefficient ($\mathcal{D}_e$) of gaseous reactant in the ash layer and the time ($\mathcal{T}_{reaction}$) & ($\mathcal{T}_{diffusion}$) required for complete conversion for both chemical reaction and ash diffusion regimes

Temperature/°C	$\mathcal{T}_{diffusion}$/sec	$\mathcal{D}_e$(m^2/sec)	$\mathcal{T}_{reaction}$/sec	$k°$(m/sec)
550	137520	2.93418E-12	209.43	0.00047184
600	134460	3.18324E-12	256.2	0.00040914
650	106620	4.24431E-12	197.94	0.00055988
700	314880	1.51498E-12	250.08	0.00046715
750	171720	2.92073E-12	231.48	0.00053062

coming in totally describing this behavior as shown in (Figs. 4 to 8). According to equation (13) plots must pass the origin so, estimated diffusion coefficients are only approximate values, because it is suspected that CaCO$_3$ solid layer is not completely impervious or nonporous for which shrinking core model with diffusion control has been originally proposed. This data could be empirically modified to estimate the time for complete conversion of a particle at ash diffusion controls regime using a power and exponential relations:

$$t = (a_o)e^{a_1} (X_A) \tag{16}$$

$$t = b_o (X_A)^{b_1} \tag{17}$$

Figure 10 presents the fit of the experimental data with exponential and power correlations for ash diffusion controls regime and (Table 3) gives the parameters of those correlations which

indicated that the CO$_2$-CaO system data can be fitted with exponential and power correlations.

Carbonation of Caustic Soda

Scanning electron microscope (SEM) images for pure NaOH, CO$_2$ and NaOH reactant samples at various temperatures have shown in (Fig. 11). The film diffusion controls, the ash diffusion controls and chemical reaction controls for CO$_2$-NaOH system which changed with the time and affected by various temperature ranges have been shown in (Fig. 12). Table 4 gives the molecular diffusion coefficient ($\mathcal{D}$) from Chapman and Enskog equation (8), mass transfer coefficient (kAg) which has been calculated from Froessling equation (7), and the time for complete conversion of a particle within the gas film (Tfilm) using equation (1).Time for complete conversion for gas film controls regime within temperature range 75°C to 225°C around 11 sec indicating that this control regime is not rate limiting
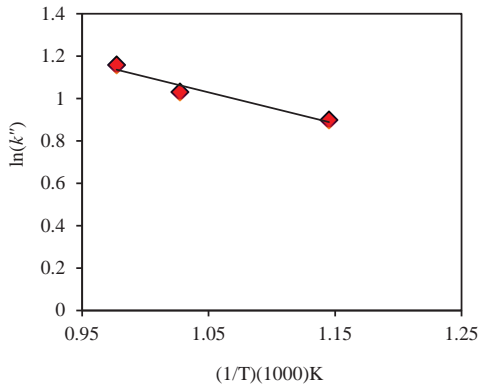
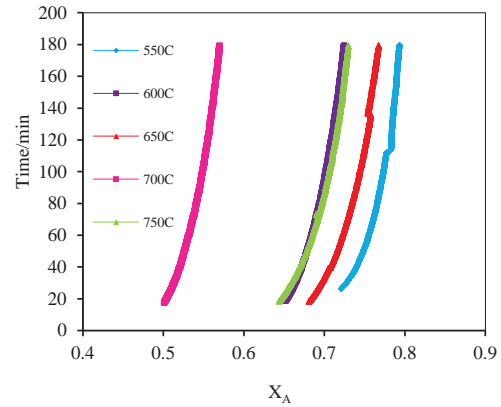Fig. 9. Arrhenius plot for chemical reaction rate constant (k'') at high temperature range

Fig. 10. Correlating high conversion range with empirical power and exponential equations for CaO-CO₂ reaction system

Table 3. Empirical power and exponential equations for fitting high conversion range with power and exponential equations for CaO-CO₂ reaction system

Temperature/°C	Exponential Equation: $t = (a_o)e^{a_1(X_A)}$			Power Equation: $t = b_o^{(X_A)b_1}$		
	a_0	a_1	R^2	b_o	b_1	R^2
550°C	9E-08	26.87	0.995	19232	20.49	0.994
600°C	8E-08	29.81	0.994	14375	20.58	0.996
650°C	6E-07	25.48	0.997	25020	18.63	0.998
700°C	3E-06	31.71	0.992	3E+06	17.11	0.995
750°C	2E-06	25.28	0.998	43810	17.49	0.999

mechanism compared with experimental time for achieving more than 60% conversion exceeding 3600sec as shown in (Fig. 12). This clearly indicates that gas film controls is not dominant control mechanism. Gas film resistance may only influence the reaction during few seconds at the beginning, where the reaction rate is fast within the period which commonly known as the starvation period. The kinetic control regime and ash diffusion controls regime were based on the shrinking core model as shown in (Figs. 13-19) and calculated from equations (12 & 13) and (14 & 15). The initial linear stage identifies the kinetic control region with the slope of this stage giving the intrinsic surface reaction rate. The starting points of the linear stage, featuring the maximum slope, usually reside at low conversions, i.e. 6%. As carbonation proceeds further, product-layer diffusion became more significant, resulting in much slower carbonation rate due to the formation of sodium carbonate. This has been clearly seen from SEM micrographs given in (Fig. 11) which provide the effect of temperature on chemical reaction rate constant (k'') between fluid (CO₂) and NaOH particles and the effective diffusion coefficient ($\mathcal{D}e$) of gaseous reactant in the ash layer (Na₂CO₃ layer) as shown in (Table 5). Activation energy obtained from (k'') data is estimated to be 13kJ/mol and the results are shown in (Fig. 20). Time for complete conversion for ash diffusion controls regime within temperature range of 75°C to 225°C indicates that the ash diffusion control regime is the major rate controlling step compared with experimental time for achieving high conversion 27mg of CO₂ per 100mg of NaOH after 2760sec at 225°C. The effective diffusion coefficients which reported in Table 5 are much smaller than the molecular diffusion gas coefficients as shown in (Table 4). This could be due to the formation of Na₂CO₃ with a low diffusion coefficient into its structure. According to the equation (13) plots must pass

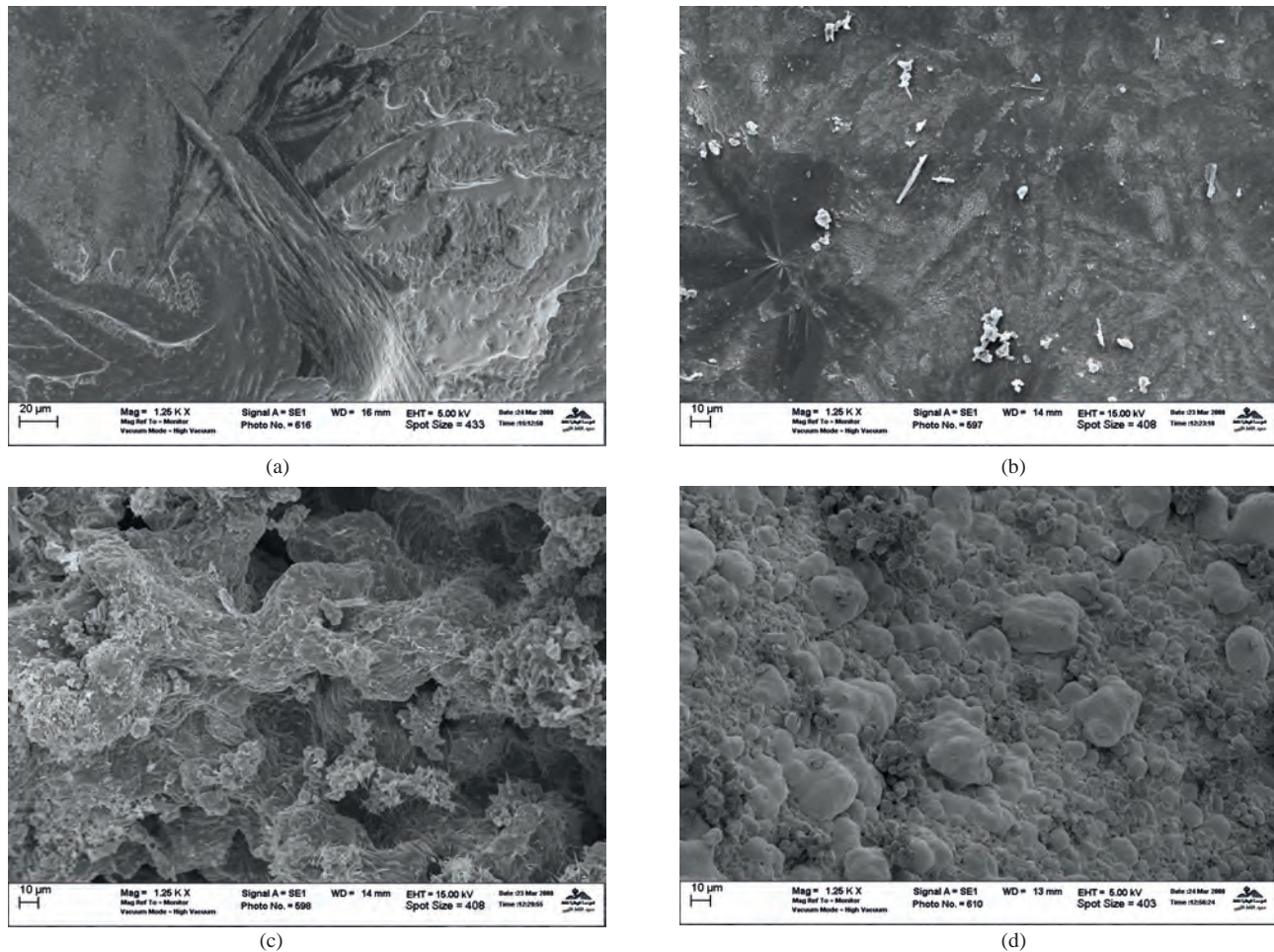Fig. 11. SEM image (1250X) of calcined caustic soda (NaOH) sample (a), NaOH-CO_2 reaction sample at 150°C (b) NaOH-CO_2 reaction sample at 200°C (c) and NaOH-CO_2 reaction sample at 225°C (d)

the origin so, estimated diffusion coefficients are only approximate values as shown in (Fig. 21). Empirical equations (16) and (17) could be used to estimate the time for complete conversion of a particle for ash diffusion controls regime as shown in (Table 6).

CONCLUSIONS

The shrinking unreacted core model for gas solid non-catalytic reactions has been utilized to describe CO_2-CaO and CO_2–NaOH reaction systems. This model has been found to semi quantitatively in describing these reactions. In CaO and NaOH systems, gas film resistance has been ruled out as rate controlling step since complete conversion times were much smaller (0.015 and 12 seconds) than actual times (137 minutes for CaO and 60 minutes for NaOH)

required to achieve high conversions above 70% for CaO and above 60% for NaOH. Reaction rate was established as rate controlling step for both CaO and NaOH systems within earlier times. Activation energies were estimated about 12 kJ/mol and 13 kJ/mol respectively. These energies have been found to agree with those obtained from initial rates analysis. CO_2-CaO and CO_2–NaOH reactions after initial times were larger than 1.5 minutes. Reactions become dominated by diffusion of CO_2 reactant with $CaCO_3$ and Na_2CO_3 solid product layers. Estimated effective diffusion coefficients of the order of 10^{-12} and 10^{-10} m^2/sec for CaO and NaOH systems respectively were below those for molecular diffusion with values of the order of 10^{-4} and 3×10^{-5} m^2/sec for the same systems. These effective diffusion coefficients are within diffusion transport *via* Knudsen and/or surface flows.
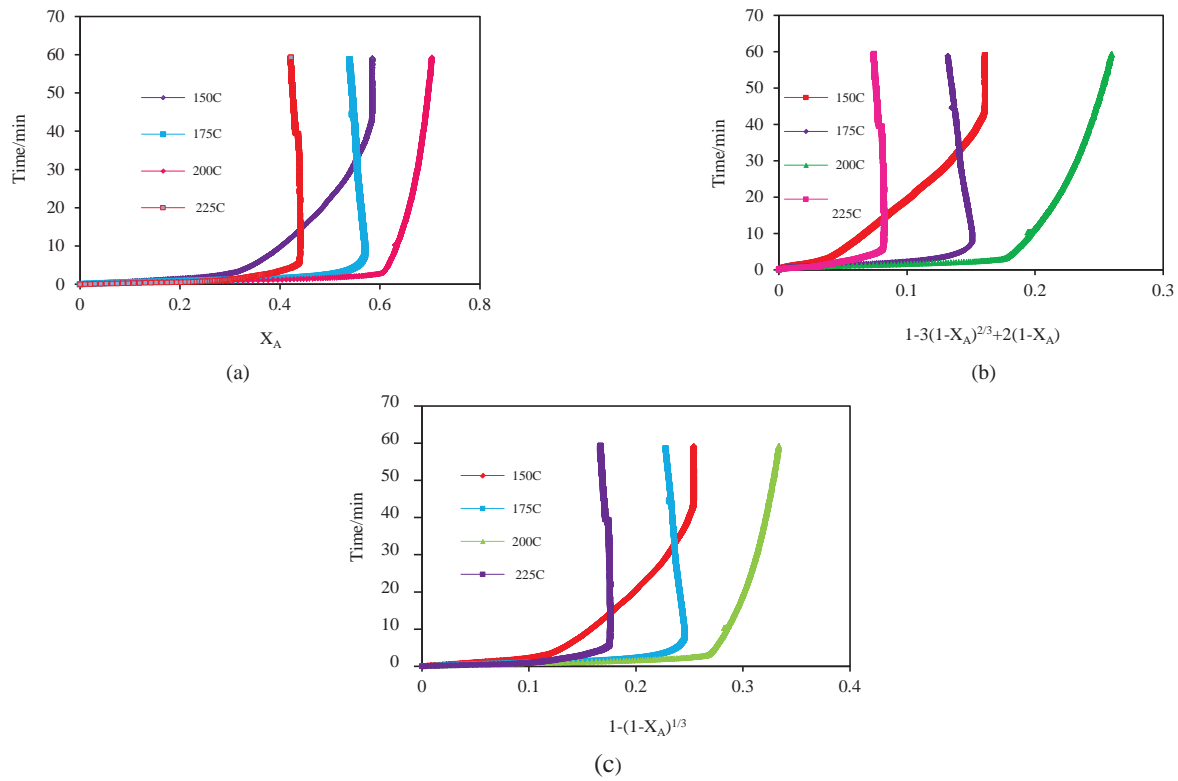
Fig. 12. Conversion vs time for (a) gas film controls, (b) chemical reaction controls and (c) ash diffusion controls at the carbonatonation cycle for CO_2-NaOH system

Table 4. Estimated molecular diffusion coefficient ($\mathcal{D}$), mass transfer coefficient (k_{Ag}) and time for complete conversion ($\mathcal{T}_{film}$) assuming gas film regime controls for the NaOH-CO_2 system

Temperature (ºC)	ρ_{CO2} (kg/m³)	μ_{CO2} (kg/sec.m)	$C_{Ag(CO2)}$ (mol/m³)	$\mathcal{D}$ (m²/sec)	k_{Ag} (m/sec)	$\mathcal{T}_{film}$ (sec)
75	1.546	0.1738	0.00350	0.000019169	0.0206706	12.0967
100	1.442	0.1879	0.00326	0.000021272	0.022844	11.7523
125	1.35	0.2020	0.00306	0.000023358	0.0249920	11.444
150	1.27	0.2162	0.00288	0.000025592	0.0272917	11.135
175	1.199	0.2303	0.00272	0.0000278937	0.0293837	10.9506
200	1.135	0.2443	0.002575	0.000030260	0.0320834	10.5939
225	1.078	0.2581	0.002446	0.0000326897	0.0345801	10.3474

Table 5. Chemical reaction rate constant (k^s) between gas (CO_2) and particles (NaOH) and effective diffusion coefficient ($\mathcal{D}_e$) of gaseous reactant in the ash layer and the time ($\mathcal{T}_{reaction}$) & ($\mathcal{T}_{diffusion}$) required for complete conversion for both chemical reaction and ash diffusion regimes

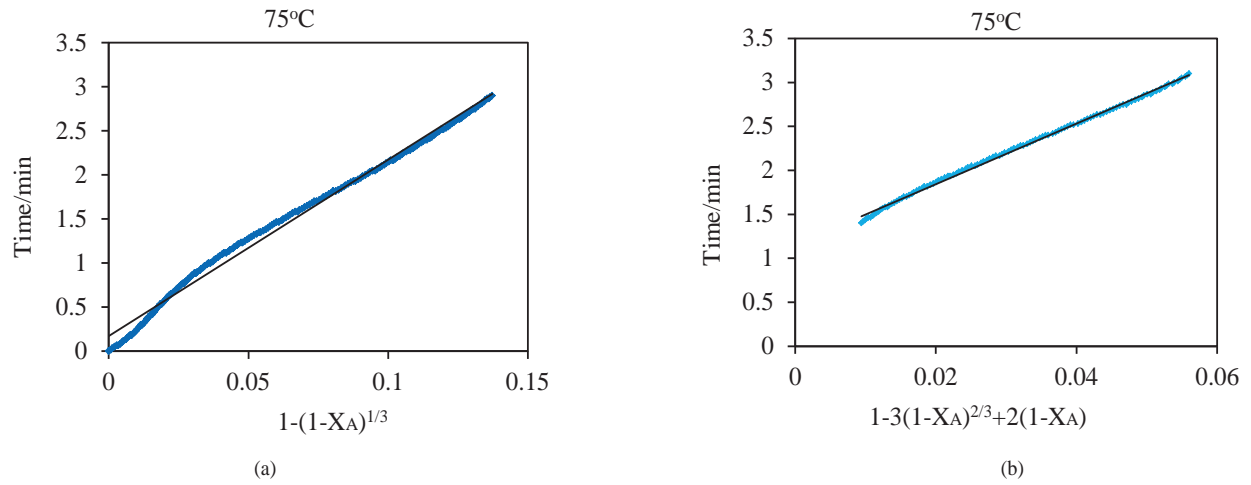| Temperature/ºC	$\mathcal{T}_{diffusion}$/sec	$\mathcal{D}_e$(m²/sec)	$\mathcal{T}_{reaction}$/sec	k^s(m /sec)
75	22066.4	6.05E-08	1200.6	0.000928
100	41442	3.23E-09	482.16	0.002476
125	3176.4	4.50E-08	653.4	0.001949
150	36504	4.16E-09	1245.6	0.001087
175	20406	7.88E-09	568.44	0.002522
200	58200	2.92E-09	425.58	0.003557
225	351840	5.08E-10	452.28	0.003524

Fig. 13. Slopes of reaction of NaOH-CO_2 with the aid of the Shrinking Core model at 75°C during early stage (a) and diffusion product layer of NaOH-CO_2 with the aid of the model during final stage (b) of carbonation for NaOH.
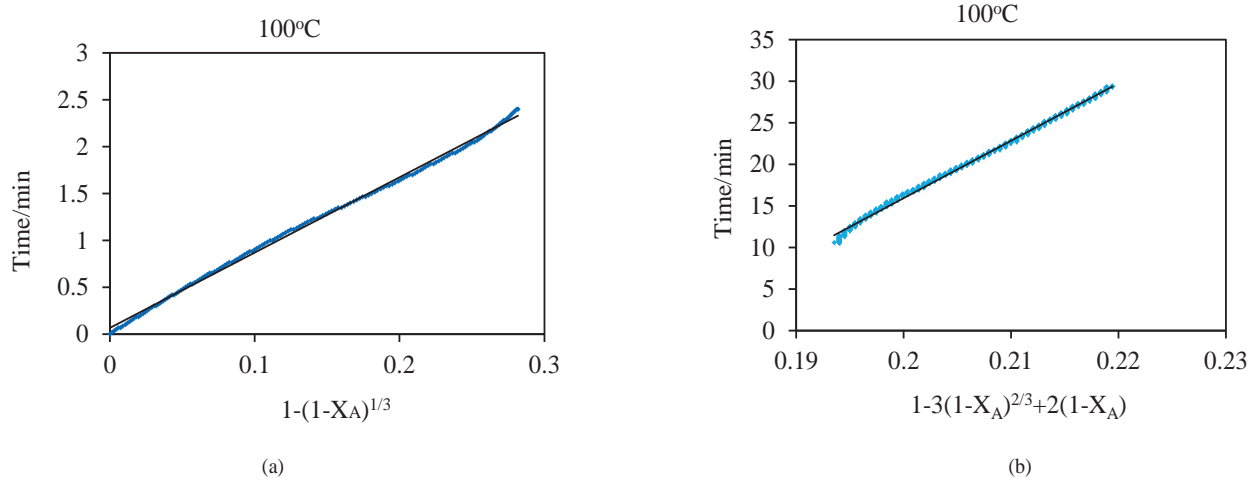

Fig. 14. Slopes of reaction of NaOH-CO_2 with the aid of the Shrinking Core model at 100°C during early stage (a) and diffusion product layer of NaOH-CO_2 with the aid of the model during final stage (b) of carbonation for NaOH.
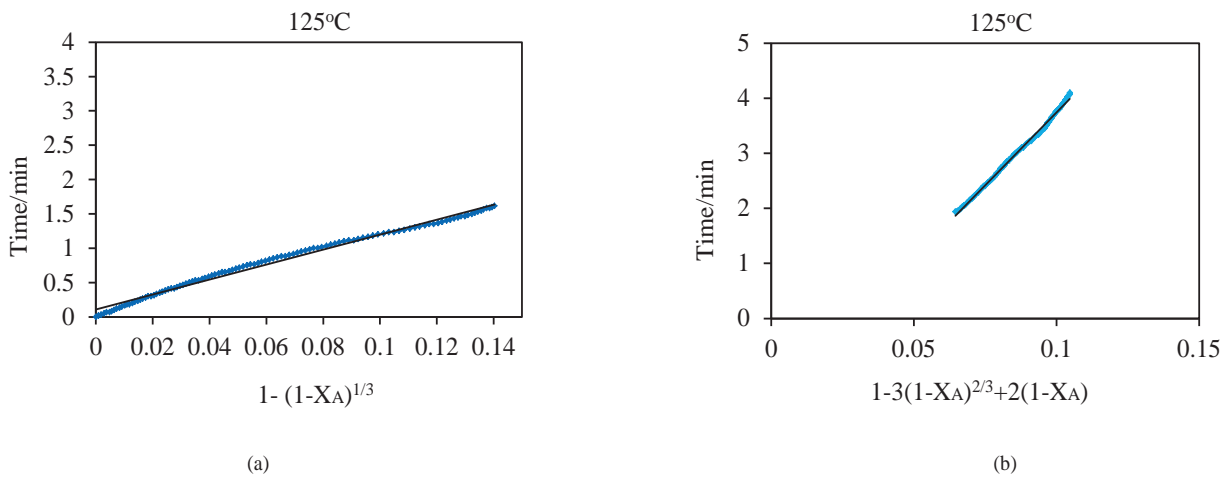

Fig. 15. Slopes of reaction of NaOH-CO_2 with the aid of the Shrinking Core model at 125°C during early stage (a) and diffusion product layer of NaOH-CO_2 with the aid of the model during final stage (b) of carbonation for NaOH.

(a)   (b)

Fig. 16. Slopes of reaction of NaOH-CO$_2$ with the aid of the Shrinking Core model at 150ºC during early stage (a) and diffusion product layer of NaOH-CO$_2$ with the aid of the model during final stage (b) of carbonation for NaOH.

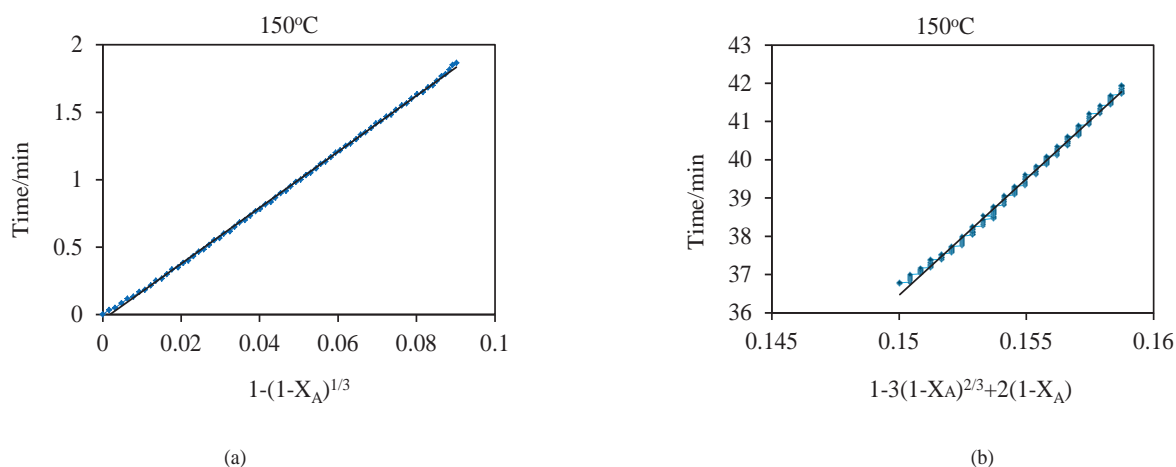(a)   (b)
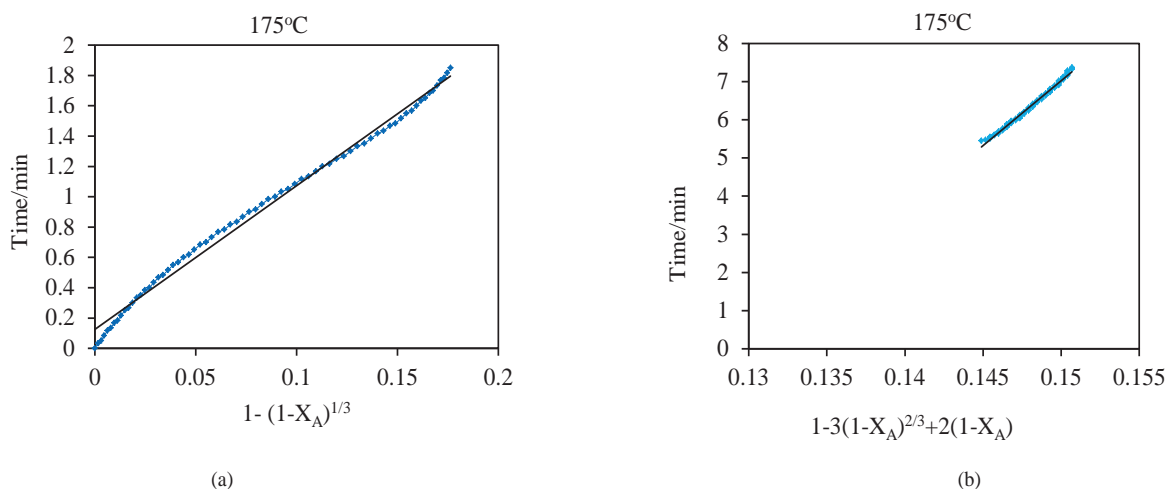
Fig. 17. Slopes of reaction of NaOH-CO$_2$ with the aid of the Shrinking Core model during early stage (a) and diffusion product layer of NaOH-CO$_2$ with the aid of the model during final stage (b) of carbonation for NaOH at 175ºC

(a)   (b)

Fig. 18. Slopes of reaction of NaOH-CO$_2$ with the aid of the Shrinking Core model during early stage (a) and diffusion product layer of NaOH-CO$_2$ with the aid of the model during final stage (b) of carbonation for NaOH at 200ºC

(a)

(b)

Fig. 19. Slopes of reaction of NaOH-CO$_2$ with the aid of the Shrinking Core model at 225°C during early stage (a) and diffusion product layer of NaOH-CO$_2$ with the aid of the model during final stage (b) of carbonation for NaOH.
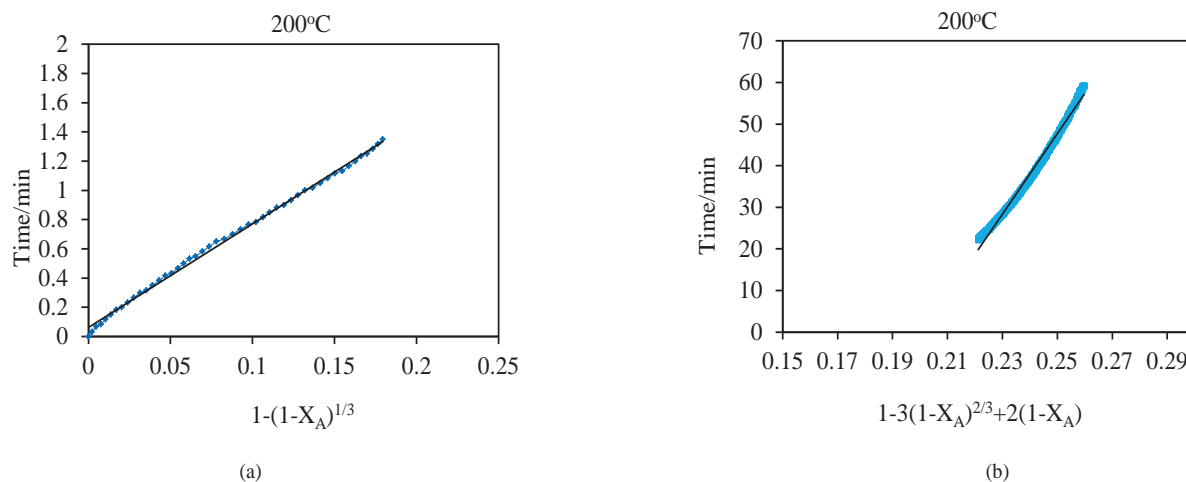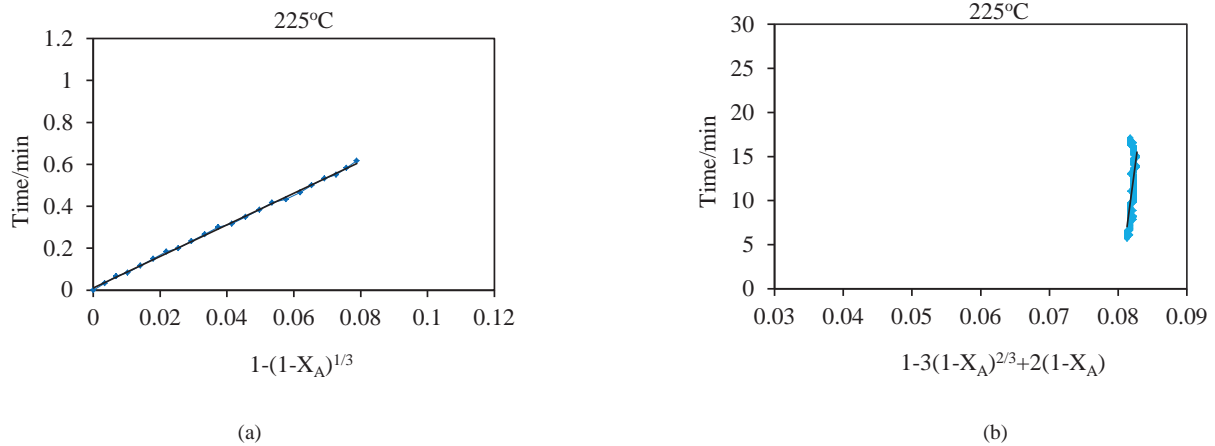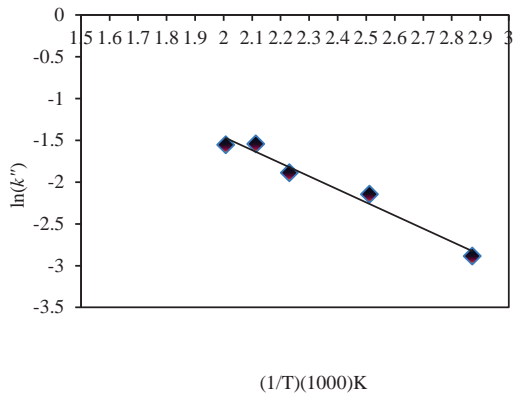

(1/T)(1000)K

Fig. 20. Arrhenius plot for chemical reaction rate constant (k") at low temperature range
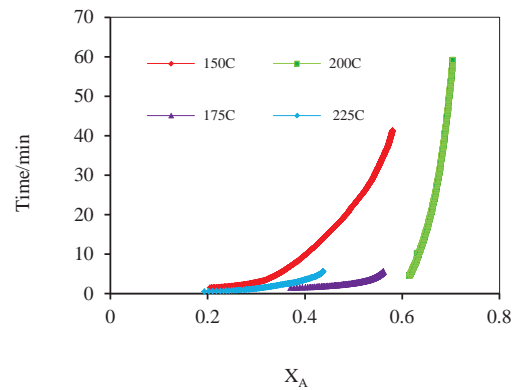

X$_A$

Fig. 21. Correlating high conversion range with empirical power and exponential equations for NaOH-CO$_2$ reaction system

Table 6. Empirical power and exponential equations for fitting high conversion range with power and exponential equations for NaOH-CO$_2$ reaction system

Temperature/°C	Exponential Equation: $t = (a_o)e^{a_1(X_A)}$			Power Equation: $t = b_o{}^{(X_A)^{b_1}}$		
	a_0	a_1	R^2	b_o	b_1	R^2
150°C	0.249	8.9	0.985	313.1	3.811	0.993
175°C	0.061	7.689	0.93	37	3.642	0.902
200°C	6E-07	26.22	0.992	27796	17.43	0.994
225°C	0.062	10	0.996	75.5	3.332	0.620

NOMENCLATURE

X$_A$ (weight gain % mg of CO$_2$/mg sorbent)/(theoretical maximum weight gain % of sorbent)

$\mathcal{T}$ Time for complete conversion a particle (CaO & NaOH) (sec) at gas film controls

t Time experiment for the reaction of CO$_2$ with solid sorbents (CaO/NaOH) (sec)

ρ_B Molar density of solid sorbents (ρ_{CaO} =0.05971 mol/cm^3 & ρ_{NaOH} =0.052513 mol/cm^3)

b Stoichiometry coefficient of solid sorbents (1 for CaO & 2 for NaOH)

k_{Ag} Mass transfer coefficient between fluid (CO$_2$) and particle (CaO/NaOH) (m/min)

C_{Ag} Concentration of gaseous reactant (CO$_2$) (mol/cm^3)

P   Atmospheric pressure (1atm)

R	Ideal gas constant (82.056 cm^3 atm/mol K)
T	Temperature (K)
Sc	Schmidt number
Re	Reynolds number
Sh	Sherwood number
k_{Ag}	Mass transfer coefficient between fluid (CO_2) and particles (CaO/NaOH) (m/sec)
d_p	Diameter of solid sorbent particles (0.0049cm for CaO & 0.2 cm for NaOH)
y	Mole fraction of the fluid (CO_2)
$\mathcal{D}$	Molecular diffusion coefficient (m²/sec)
μ	Kinematic viscosity of fluid (CO_2) (cp)
ρ	Mass density of the fluid (CO_2)
u	Gas (CO_2) velocity = 1.179cm/sec
$\mathcal{D}_{(CO_2)}$	Self-diffusion coefficient (m²/sec)
σ_{AA}	Characteristic length (Å)
Ω_D	Diffusion collision integral, dimensionless
M_{CO_2}	44 g/mol
R	Diameter of solid sorbents particles (R_{CaO} =0.00245cm & R_{NaOH}=0.1cm)
$\mathcal{D}_e$	Effective diffusion coefficient (m²/sec)
$k^{"}$	Chemical reaction rate constant (m/sec)

REFERENCES

Abanades, J. C. and Alvarez, D. (2003). Conversion Limits in the Reaction of CO_2 with Lime. *Energy and Fuels, 17*: 308-315.

Abunowara, M.; Bustam, M. A.; Sufian, S.; Babar, M.; Eldemerdash, U.; Suleman, H.; Bencini, R. and Ullah, S. (2020). Experimental Measurements of Carbon Dioxide, Methane and Nitrogen High-Pressure Adsorption Properties onto Malaysian Coals under Various Conditions. *Energy 210*: 118575.

Alvarez, D. and Abanades, J. C. (2005). Determination of the Critical Product Layer Thickness in the Reaction of CaO with CO_2. *Industrial & Engineering Chemistry Research, 44*: 5608-5615.

Aydin, G.; Karakurt, I. and Aydiner, K. (2010) Evaluation of Geologic Storage Options of CO_2: Applicability, Cost, Storage Capacity and Safety. *Energy Policy, V. 38*: 5072-5080.

Barker, R. (1973). The Reversibility of the Reaction $CaCO_3 = CaO + CO_2$. *Jour. App. Chem. Biotech., 23*: 733-742.

Bhatia, S. K. and Perlmutter, D. D. (1983). Effect of the Product Layer on Kinetics of the CO_2 Lime Reaction. *A. I. Ch. E. Jour., 29*: 79-86.

Bhattacharya, A. and Purohit, P. (2004). Predicting Reaction Rates for Non-Catalytic Fluid-Solid Reactions in Presence of Structural Changes in the Solid Phase. *Chem. Eng. J., 102*: 141-149.

Breidenich, C.; Magraw, D.; Rowley, A. and Rubin, J. W. (1998). The Kyoto Protocol to the United Nations Framework Convention on Climate Change. *The American Journal of International Law, V. 92*: 315-331.

Froessling, N. (1938). Uber die verdunstung fallernder tropfen. *Gerland Beittr Geophys, 52*: 170p.

Hu, Y.; Lu, H. and Li, H. (2021). Li_4SiO_4 Pellets Templated by Rice husk for Cyclic CO_2 Capture: Insight into the Modification Mechanism. *Ceramics International 47.22*: 32060-32067.

Huaman R. N. E. and Jun, T. X. (2014). Energy Related CO_2 Emissions and the Progress on CCS Projects: A Review. *Renewable and Sustainable Energy Reviews, V. 31*: 368-385.

Levenspiel, O. (1999). Chemical Reaction Engineering. *3rd*: 704.

Lin, J.; Lu, W.; Shi, X.; Lu, Q.; Wang, L. and He. H. (2021). Design of an Intelligent Nanofiber-Based Solid Amine Adsorbent with High CO_2 Capture Capacity and an Ultralow Regeneration Temperature. *ACS Sustainable Chem. Eng., 9*: 10184-10195.

Pachauri, R. K.; Allen, M. R.; Barros, V. R.; Broome, J.; Cramer, W.; Christ, R.; Church, J. A.; Clarke, L.; Dahe, Q.; Dasgupta, P. (2014). Climate Change: Synthesis Report. *Contribution of Working Groups I, II and III to the Fifth Assessment Report of the Intergovernmental Panel on Climate Change, IPCC*.

Poling, E. B., Prausnitz, J. M. and Connell, J. P. O. (2001). The Properties of Gases and Liquids: *5rd*: 803.

Suleman, H.; Maulud, A. S.; Fosbøl, P. L.; Nasir, Q.; Nasir, R.; Shahid, M. Z.; Nawaz, M. and Abunowara, M. (2020). A Review of Semi-Empirical Equilibrium Models for CO_2-Alkanolamine-H_2O Solutions and their Mixtures at High Pressure. *Jour. Envir. Chem. Eng., 9*: 104713.

Sun, P.; Grace, J. R.; Jim Lim, C. and Anthony, E. J. (2008a) Determination of Intrinsic Rate Constants of the CaO–CO_2 Reaction. *Chem. Eng. Scie., 63*: 47-56.

Sun, P.; Grace, J. R.; Jim Lim, C. and Anthony, E. J. (2008b). A Discrete-pore Size Distribution-Based Gas Solid Model and its Application to the CaO with CO_2 Reaction. *Chem. Eng. Scie., 63*: 57–70.

Szekely, J.; Evans, J. W. and Sohn, H. Y. (1976). Gas Solid Reactions. *Academic Press, London*: 612.

Yagi, S. and Kunii, D. (1955). Studies on Combustion of Carbon Particles in Flames and Fluidized Beds. In: *5th International Symposium on Combustion*, Reinhold New York, USA: 231.

Yagi, S., Kunii, D. (1961). Chem. *Chem Engi. Japan V. 19*: 500p.

ABOUT THE AUTHORS

Mustafa A. Abunowara had a PhD., MSc, BSc in Chemical Engineering. He was working for Libyan Petroleum Institute from 2004 to 2012.
e-mail: abunowara1980@gmail.com

Mohamed Elgarni is a senior process engineer working in Canadian Natural Resources Limited (CNRL). He holds a PH.D. in Chemical Engineering from University of Wales. He has wealth of knowledge and experience in both field work and process modeling, simulation and troubleshooting of hydrotreaters and hydrogen plants. He has been actively involved in the development of multiple studies & projects related to upgrading of oil streams and utilities including GHG mitigation. Dr. Elgarni has in-depth experience in process design and operation in pilot and fully commercialized scale. He has worked for over 30 years in the oil & gas industry in plant operation, and research & development in the refining and oil production.
e-mail: mohamed.elgarni@cnrl.com

EFFECTIVNESS OF DEMLUSIFIERS IN BREAKING OFF EMULSION IN CRUDE OIL PRODUCTION

Mhamed Kahrwad[1] and Fathi Rezg[2]

Abstract: This work is aimed to evaluate four chemical demulsifiers (DE1, DE2, DE3, and XY) to break-off emulsion formed in oil wellA54. The active ingredient of demulsifiers (DE1, DE2, and DE3) is alkoxylated resins and high molecular weight polyols in an aromatic solvent. Static jar test is carried out at ambient and production separator temperatures (25°C and 85°C). Emulsion is prepared at mixing ratio of oil (70%) and produced water (30%).

The salinity of produced water is changing considerably; chemical demulsifiers are evaluated at low and high salinities. Results showed that temperature plays a significant role in breaking off emulsion. As temperature increases, the rate of oil/water separation rate increases. DE2 showed an optimum effectiveness in breaking off emulsion at 200mg/L. At high saline water (188,727mg/L), emulsion showed less stability comparing with low saline water (33,088mg/L).

Keywords: Demulsifiers, Emulsion, Xylene, alkoxylated resins, polyols

---

INTRODUCTION

Stable water-in-oil emulsions can occur at many stages during the production and processing of crude oils. The formation of these emulsions is generally caused by the presence of resins and asphaltenes which play the role of "natural emulsifiers", and by wax and solids. All these components can organize and form rigid films at the oil/water interface. Effective separation of oil and water is essential in ensuring the crude oil quality and low cost of the oil production. (Dalmazzone & Noik, 2001). Methods currently employed in demusification of crude oil are: heat, electrical, chemical and polymer methods. Emulsion breaking or de-emusification is separation of a dispersed liquid from the liquid in which it is suspended. The objective of demusifiction is to destroy the interface and drive the surfactant to either the oil side or the water side, allowing the oil particles and sediments to coalesce and rise to the surface as in creaming. Decreasing water phase viscosity or increasing the diameter of oil droplets and lowering the density of oil to water also works. There are several strategies for counteracting emulsion:

(i) Decompose the emulsion, modifying or using dissolved air floatation, oxidation or other oxidation process.

(ii) Chemically react the emulsion, modifying the surfactants change so that it no longer acts as an emulsifier. Ionic surfactant neutralization is often the simplest method using an acid base or ionizer if calcium or magnesium salt, such as $CaCl_2$ or $MgSO_4$ is added to emulsion stability by sodium soap, which is less soluble in water because the interfacial film has changed.

(iii) Increase the solubility of the surfactant in either bulk phase. Alcohol or other polar solvents such as acetone can be used to increase solubility in the water phase and pull the emulsifier out of the oil phase. If the aqueous phase is brine, dilution with water may be all that is needed to achieve separation.

(iv) Disrupt the oriented structure of emulsifier interfacial phase with de-emulsifier. Because these materials are not very soluble in either phase they concentrate at the interface (Hajivand and Vaziri, 2015).

THEORY

An emulsion is a dispersion of droplets of one liquid (water) in another liquid (oil) with which it is incompletely immiscible. Emulsion normally does not exist in the producing formation but are formed when oil and water are produced together with a great amount of agitation when water and oil in a reservoir enter the well bore, a comparatively large

---

[1]*Libyan Petroleum Institute (LPI), Gargarish Road, 7Km, P.O.Box:6431, Tripoli, Libya, m.kahrwad@lpilibya.com*
[2]*Libyan Petroleum Institute (LPI), Gargarish Road, 7Km, P.O.Box:6431, Tripoli, Libya, f.rezg@lpilibya.com*

pressure differences are created which violently mix the produced oil and water together so that emulsion forms.

Emulsion consists of three phases: The internal or discontinuous phase of finely divided droplets; The external or continuous phase (i.e. oil) is the matrix that keeps droplets in suspension; The inter-phase consists of an emulsifier or stabilizer, which keeps the emulsion stable, binding the internal and external phases together and preventing droplets form approaching each other and coalescing. Usually, emulsifiers are surfactants and soaps present either by themselves or as part of the makeup of a detergent formation. An emulsifier consists of a molecule with hydrophilic and hydrophobic ends. In the presence of immiscible liquids, the emulsifier migrates to the interface of the internal and external phases, forming a protective sheath round droplets of dispersed phase. While the hydrophobic ends of the molecule migrates or partitions into droplets, the hydrophilic ends stays in the water (Hajivand and Vaziri, 2015).

EXPERIMENTAL METHOD

Materials
Crude oil: Crude oil sample (Image 1) from oil well A54, was used in this study (Table 1).
Brine: Synthetic brine was used with different salinities (188,727mg/L and 33,088mg/L). The status of oil well before and after stimulation is described in (Table 2).

Method
Water in oil emulsion is prepared by mixing crude oil and water (7:3 V/V) to obtain 30% (V/V) water content. All tests were performed at (25°C and 85°C) as follows (Udonne, 2012):
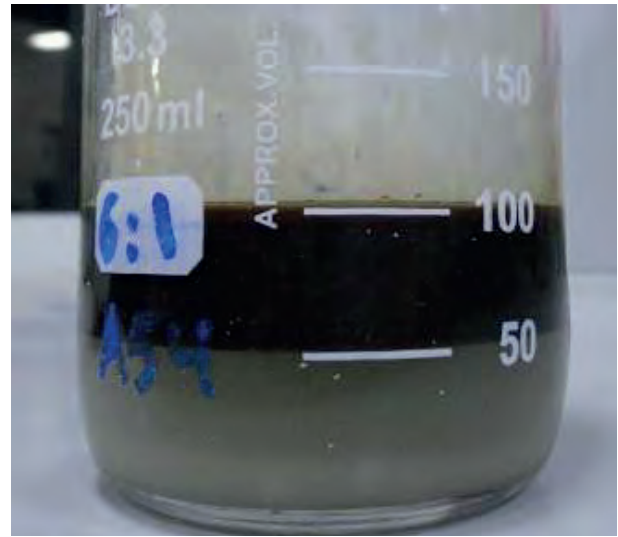

Image 1. Crude oil sample

(i)   Precise volume of the quantity of emulsion poured in graduated test tube.
(ii) Injection of the desired quantity of demulsifier (100, 200, and 400mg/L with pipette).
(iii) First mixing by vigorous hand-shaking.
(iv) Vibration mixer for 10 minutes to ensure homogenous distribution of demulsifier.
(v)   Reading the quantity and clarity of separated water after 30 minutes of rest. The residual interface was noticed for stability.

$$\left(\% \frac{V}{V}\right) = \frac{V_1}{V_2} \times 100$$

Where,
V_1: is the separated water
V_2: is the original volume of water contained

Table 1. Crude oil (well A54), characteristics.

Technical Specification	Value	
Specific Gravity	0.8232	
API	40.4	
Water Cut	Max. 30%	
Salinity	237.91 g/l	
Viscosity	5.62	75
	1.80	175°F

Table 2. Oil well A54 status before and after stimulation

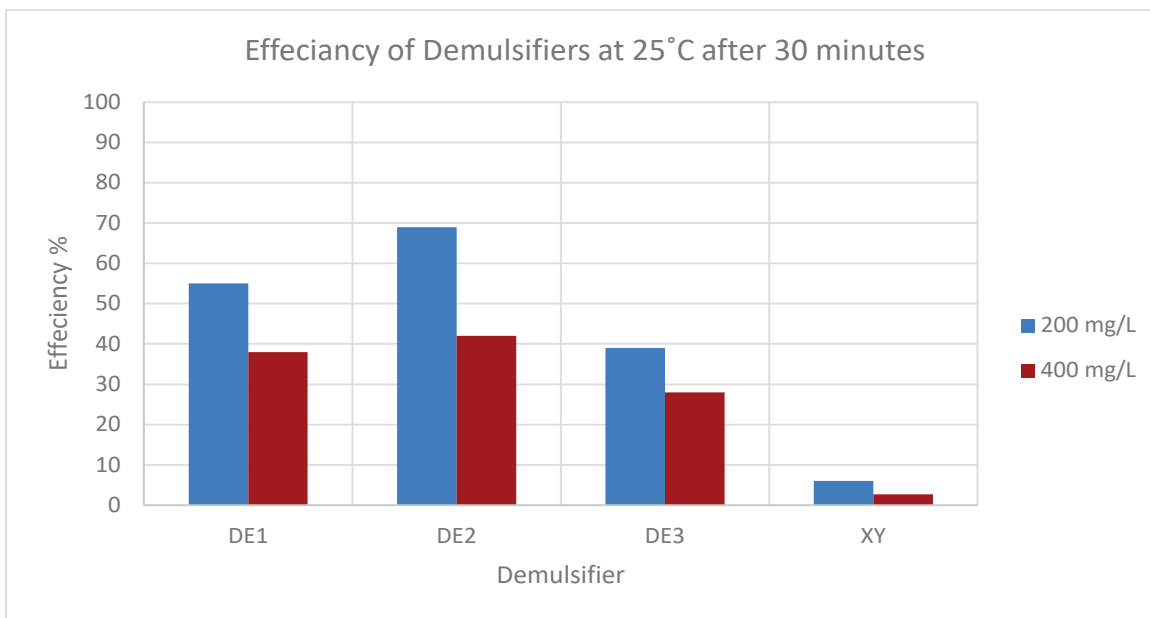| OIL WELL	Before Stimulation	After Stimulation and/or lifting			
	Well Status	Well Status	Choke Size (1/64")	FWHP (Psig)	Oil Rate (BOPD)
A54	SHUT-Due to Low WHP	PTN	64	159	1154

Fig. 1. Efficiency of demulsifiers at 25°C and 30 minutes

Table 3. Results of Static efficiency test for demulsifiers at 25 °C and 200 mg/L

Chemical	Concentration (mg/L)	Time (minutes)	separated Water (ml)
DE 1	400	30	5.5
		60	11.5
DE 2	400	30	6.6
		60	13
DE 3	400	30	4
		60	13
XY	400	30	0.4
		60	1

Table 4. Results of Static efficiency test for demulsifiers at 25 °C and 400 mg/L

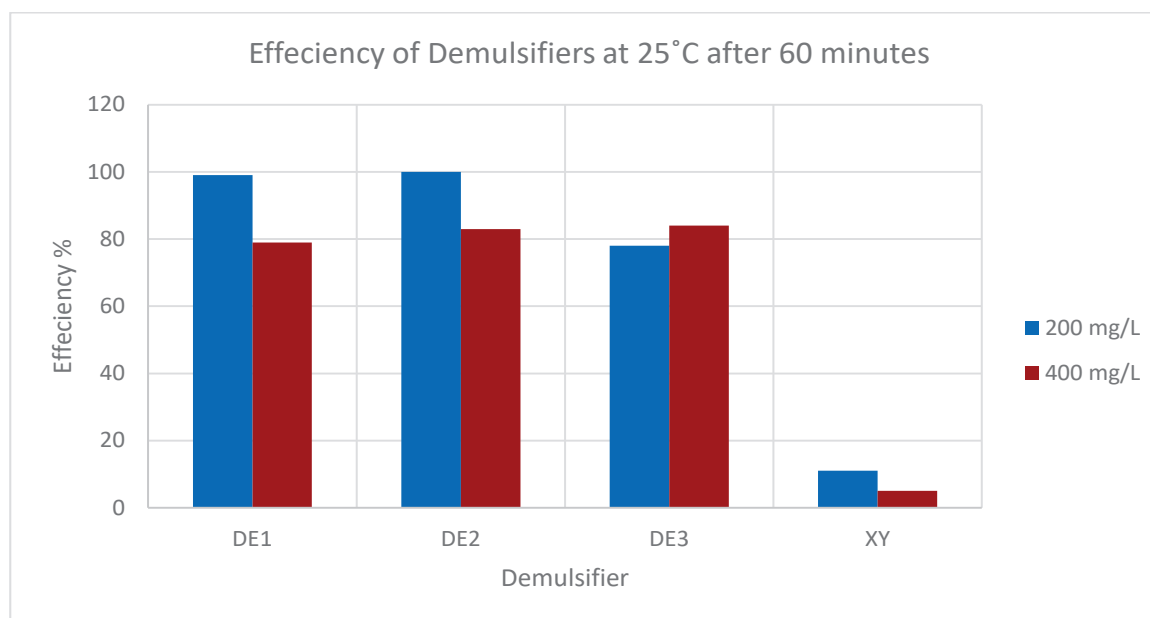| Chemical	Concentration (mg/L)	Time (minutes)	Separated Water (ml)
DE 1	200	30	8
		60	14.8
DE 2	200	30	10.5
		60	14.9
DE 3	200	30	5.7
		60	11.2
XY	200	30	0.4
		60	1

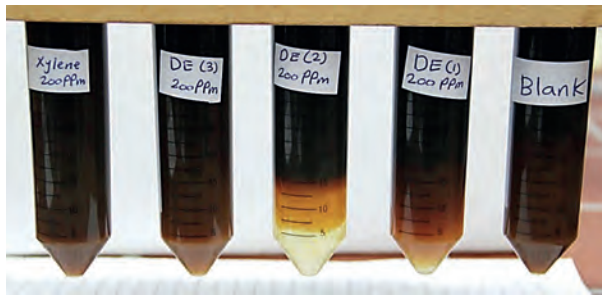Fig. 2. Efficiency of demulsifiers at 25°C and 60 minutes

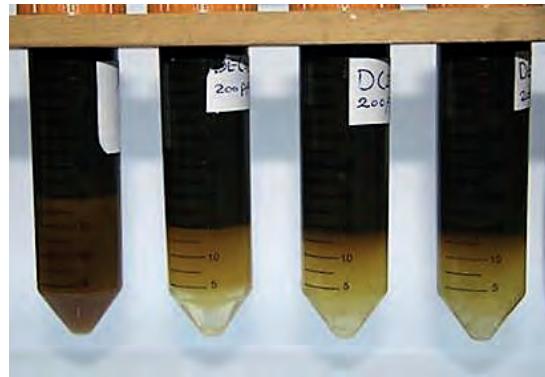Image 2. Static efficiency test for demulsifiers at 200mg/L and 25˚C

Image 3. Static efficiency test for demulsifiers at 200mg/L and 25˚C

Image 4. Static efficiency test for demulsifiers at 200mg/L and 25˚C
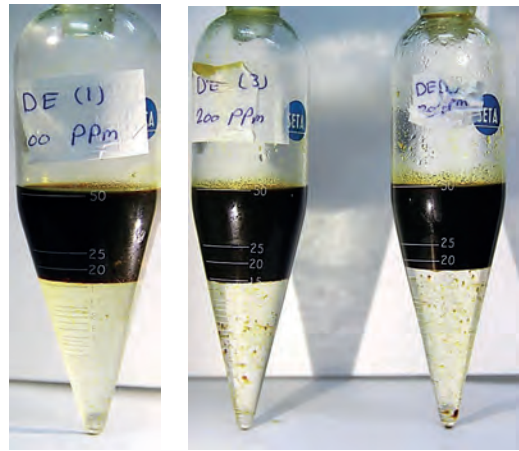

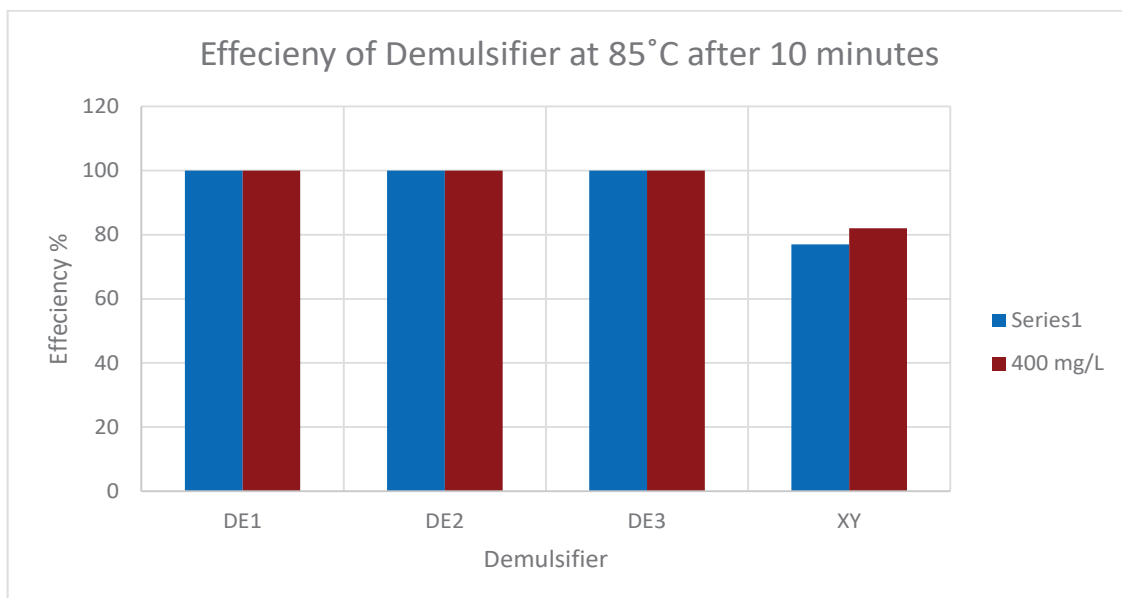Image 5. Static efficiency test for demulsifiers at 200mg/L and 85˚C

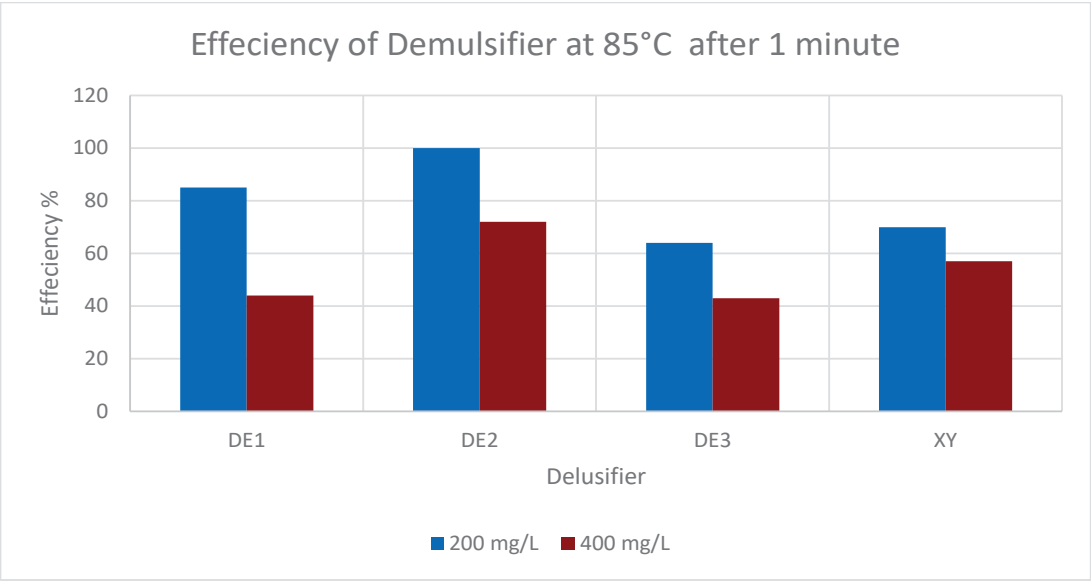Fig. 3. Efficiency of demulsifiers at 85°C and one minute

Fig. 4. Efficiency of demulsifiers at 85°C and 10 minutes
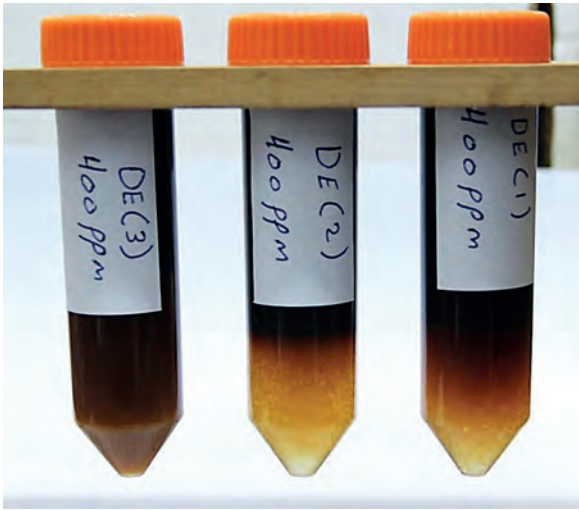
Image 6. Static efficiency test for demulsifiers at 400mg/L and 25˚C (low saline water)
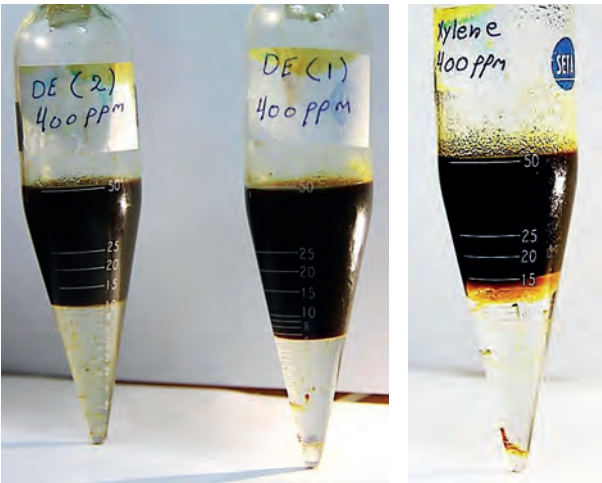
Image 7. Static efficiency test for demulsifiers at 400mg/L and 85˚C

Table 5. Results of Static efficiency test for demulsifiers at 85 °C and 200 mg/L

Chemical	Concentration (mg/L)	Time (minutes)	separated Water (ml)
DE 1	200	1	13
		10	15
DE 2	200	1	15
		10	15
DE 3	200	1	10
		10	15
XY	200	1	11
		10	12.5

Table 6. Results of Static efficiency test for demulsifiers at 85 °C and 400 mg/L

Chemical	Concentration (mg/L)	Time (minutes)	separated Water (ml)
DE 1	400	1	7
		10	15
DE 2	400	1	11
		10	15
DE 3	400	1	7
		10	15
XY	400	1	8
		10	11

RESULTS AND DISCUSSION

Demulsifier are evaluated at different concentration to find out the optimum effective concentration. A low concentration (50 and 100mg/L) the amount and rate of separation of water is low. This screening test reduced the range of demulsifiers concentration for evaluation at operational temperature.

After 30 minutes, and at 25°C, the maximum efficiency was 69% for DE2 (Fig. 1). At 25°C the separated water from static test was measured after 30 and 60 minutes (Tables 3 and 4). Also, results at 25°C indicate that DE1 and DE2 show the maximum separation of water (99.9% V/V) was achieved after 60 minutes (Fig. 2), while DE3 and xylene showed 75% V/V and 7%V/V of separated water respectively.

Image 2 showed a comparison between DE1, DE2, DE3 and XY with blank sample after 5 minutes and at 25°C. After 10 minutes DE2 showed a clear solution in the bottom of test tube, Image 3. After 15 minutes, about 50% of total water was separated, (Image 3). All demulsifiers used in this work showed low separation of water at concentration of 400mg/L comparing with concentration at 200mg/L at the same temperature (Table 5, Images 4 and 5).

Figure 3 shows that at 85°C, DE2 achieved maximum effectiveness in one minute. The temperature 85°C has improved the rate of breaking off emulsion within one minute. Demulsifiers DE 1, 2, and 3, have achieved the maximum efficiency at 85°C after 10 minutes (Fig. 4).

The effect of water salinity on emulsion stability can be clearly observed from results (Table 4), images 6 and 7 (Table 6). Low saline water, the emulsion is more stable. This indicates that a reduction in the effectiveness of the performance of demulsifier in breaking off emulsion in short time.

CONCLUSION

Experimental study was conducted to evaluate the effectiveness of four demulsifiers (DE1, DE2, DE3 and XY) for breaking off emulsion at different temperatures (25°C and 85°C). Temperature plays a significant role in improving the performance of demulsifiers (DE1, 2, and 3) in breaking of formed emulsion. Also, salinity of produced water plays a role in emulsion stability. DE2 showed the maximum efficiency at 200mg/L concentration.

REFERENCES

Dalmazzone, C. and Noik, C. (2001). Development of New Green Demulsifiers for Oil Production. *Soc. Petrol.Eng., SPE 65041*.

Hajivand, P. and Vaziri, A. (2015). Optimization of Demulsifier Formulation for Separation of Water From Crude Oil Emulsions. *Brazilian J.Chem. Eng., V. 32*: 107-118.

Udonne, J. D. (2012). Chemical Treatment of Emulsion Problem in Crude Oil Production. *J. Petrol. Gas Eng., V.3 (7)*: 135-141.

ABOUT THE AUTHORS

Mhamed Kahrwad is Head of Scale & Corrosion Division with Libyan Petroleum Institute (LPI). He holds BSc. in chemical engineering from AL-Mergab University, Al Khums, Libya (2002), and master's degree in petroleum engineering from Herriot-Watt University, Edinburgh, UK, in 2008. Kahrwad has experience in mitigation of scale problems in surface oil facilities, reservoir and well tubular. Kahrwad has published one SPE paper (114108) and several technical papers in local conferences.

Fathi Rezg is graduated from faculty of science of Tripoli University with a bachelor's degree in chemistry in 1998. He has been working for LPI since 2004 in scale Laboratory as a supervisor. Curuntly he is working on MSc research.

OFF ROAD AND MARINE DIESEL FROM LIGHT GAS OIL, VACUM GAS OIL AND KEROSENE BLEND

Yousef A. Al Mestiri[1], Muhammad Alkhufefi, Salah Aldawi[2] and Ali Enan[3]

Abstract: Vacuum gas oil (VGO) produced by Benghazi Asphalt Factory and light gas oil (LGO) used in north Benghazi power plant were mixed in different volume ratio to produce a fuel blend. Kerosene was added in a small different volume ratio to reduce viscosity and improve cold flow LGO/VGO fuel blend property. LGO/VGO fuel blend pour point, flash point, volatility, copper corrosion properties, heat of combustion, water content, ignition quality and ash content are within the range of diesel fuel and light gas oil specifications. Viscosity and sulfur content of fuels A and C are within the range of diesel fuel classified A_2 and marine diesel specifications whilst, carbon residue is slightly higher than that of diesel fuel classified A_2 and No. 2-D specifications.

INTRODUCTION

Vacuum gas oil (VGO) is produced by vacuum distillation of atmospheric residue whilst kerosene and light gas oil (LGO) are both a middle distillate produced by atmospheric petroleum distillation (Hobson, 1992). Kerosene is a fuel for aeroplanes and domestic application and the mean use of LGO is a fuel for diesel engines and heating oil for power plants. The viscous and high sulfur content VGO is a feedstock for hydro and catalytic cracking plants (Hobson, 1992) and heating oil to minor industrial operations as in Benghazi Asphalts Factory. The aim of this research is to prepare marine and off road diesel by mixing LGO and the available cheap VGO produced by Benghazi Asphalt Factory and kerosene in different blending volume ratio. Both fuel blends LGO/VGO and LGO/VGO/kerosene have never been mentioned in literatures.

EXPERIMENTAL

Three fuel blend samples were prepared from light gas oil, vacuum gas oil and kerosene. LGO, VGO and kerosene specifications are shown in (Table 1). The specifications were obtained from Benghazi Asphalt Factory and north Benghazi Power Plant. The first LGO/VGO fuel blend was prepared by blending in a 1L measuring cylinder a 1:0.25 volume ratio LGO and VGO. The LGO/VGO fuel blend was shaken for several minutes then left stand unshaken for several minutes, this fuel blend assigned Fuel B and C were prepared by blending LGO, VGO and kerosene in the following volume ratio 1:0.5:0.1 for fuel B, and 1:0.25:0.05 for fuel C.

Fuel A, B and C physical specifications were obtained following ASTM standard methods at Benghazi Asphalt Factory laboratory (American Society for Testing and Materials, ASTM Test Method, petroleum products, lubricants and fossil fuels analysis 1993, and American Society for Testing and Materials, Standard Specifications for Marine Fuels D 2069-1991, for Fuel Oils, D 396-1997, for Diesel Fuel Oils D 975-1997 and for Aviation Turbine Fuels D1655-1998). Total sulfur carbon residue and ash content were obtained by calculation method. LGO, VGO and kerosene samples used as received.

---
[1]*Ras Lanuf Oil and Gas Co.*
[2]*Benghazi Asphalt Factory.*
[3]*North Benghazi Power Plant.*

Table 1. LGO, VGO and Jet kerosene specifications.

Test & Unit	Method	Result		
		LGO	VGO	Jet kerosene
Specific gravity @ 15.6 °C	ASTM-D 1289	0.8555	0.9389	-
API gravity	ASTM-D 1289	33.90	19.21	-
Density @ 15 °C kg/l	ASTM-D 1289	0.8851	0.9383	0.7902
Distillation:	ASTM-D 86			
Initial boiling point. °C		-	215	147.6
Recovered@280 °C. mL		-	3.5	-
Temperature @ 65% recovery °C		324.3	-	-
Temperature @ 95% recovery °C		369.1	-	-
Final boiling point		-	555	275.4
Flash point °C	ASTM-D 93	62	106	39.5
Pour point °C	ASTM-D 97	-12	+18	-
Cetane index	ASTM-D976	48.7	37	-
Heat of combustion (net) MJ/kg	ASTM-D 4868	46.38	45.71	43.32
Copper corrosion 3 hrs @ 100 °C	ASTM-D130	-	1a	-
Copper corrosion 2 hrs @ 100 °C	ASTM-D130	-	-	1a
Copper corrosion 3 hrs @ 50 °C	ASTM-D130	1a	-	-
Water by distillation V%	ASTM-D 95	-	0.05	-
Total sulfur wt%	ASTM-D 4294	0.10	1.863	0.035
Conradson carbon residue. Wt%	ASTM-D 189	<0.10	1.39	-
Viscosity @ 40 °C. cSt	ASTM-D 445	3.478	21.53*	-
Viscosity @ -20 °C. cSt	ASTM-D 445	-	-	3.24
Ash content Wt%	ASTM-D 482	<0.001	0.0088	-
Freezing point °C	ASTM-D 2386	-	-	-49.5
Total acidity mg KOH/g	ASTM-D 3242	-	-	0.009
Total aromatic V%	ASTM-D 6379	-	-	19.9
Water and sediment	ASTM-D-96	<0.01	-	-

*viscosity at 50°C

RESULTS AND DISCUSSION

The three prepared fuel blends Fuel A, B and C specifications are tabularized in (Table 2). Flammability or flash point which is an indication of fuel handling and storage safety requirements, flash point test result demonstrated the safety handling and storage safety of the three prepared fuel blends A, B and C. Pour point a cold flow property of the three prepared fuels are low and below zero degree celsius appropriating Libyan climate even in winter season. Volatility test or distillation and recovery @ 280°C tests results. This property is related to the objectives of controlling start ability, evaporative emissions, and cold start/warm-up performance emissions. Cetane index which is a measure of the ignition quality of diesel fuel, net heat of combustion, water content, ash content and copper strip corrosion test results. Values of the three fuel blends A, B and C are within the range of diesel fuel and LGO specifications (Hobson, 1992). Viscosity and sulfur content of both fuel A and C are within the range of marine diesel and diesel

Table 2. Fuel A, B and C specifications.

Test & Unit	Method	Result		
		A	B	C
Specific gravity @ 15.6 ˚C	ASTM-D 1289	0.8734	0.8800	0.8715
API gravity	ASTM-D 1289	30.5	29	31
Density @ 15 ˚C kg/l	ASTM-D 1289	0.8729	0.8795	0.8710
Distillation:	ASTM-D 86			
Initial boiling point ˚C		234	172	183
Recovered@280˚C mL		30	32	34
Flash point ˚C	ASTM-D 93	70	68	64
Pour point ˚C	ASTM-D 97	-3	-6	-9
Cetane index	ASTM-D 976	46	44	47
Heat of combustion (net) MJ/kg	ASTM-D 4868	46.22	46.14	46.23
Copper corrosion 3 hrs @ 100 ˚C	ASTM-D 130	1a	1a	1a
Ash content Wt%		0.0027	0.0035	0.0026
Water by distillation V%	ASTM-D 95	traces	Traces	traces
Total sulfur wt%		0.480	0.680	0.462
Conradson carbon residue Wt%		0.380	0.525	0.364
Viscosity @ 40 ˚C cSt	ASTM-D 445	5.6	6.60	5.3

fuel classified A$_2$ and No. 4-D specifications for off-road automotive engines and stationary engine application (Hobson, 1992; Technical Review diesel fuels Chevron Products Company, 2011). Fuel A and C conradson carbon residue test results are a rather higher than that of both on-road diesel fuel classified ultra low sulfur No. 2-D and off-road diesel fuel classified A$_2$ specifications (Hobson 1992 and Technical Review diesel fuels Chevron Products Company 2011). The results are within the range of burner fuels classified E to H of BS 2869 specifications which may be used for medium and low speed large diesel engines as used in power generating installation and within the range of marine diesel fuel specifications (Hobson 1992 and Technical Review diesel fuels Chevron Products Company, 2011). Whilst fuel B viscosity which affects fuel spray atomization and fuel system lubrication, conradson carbon residue that shows only long term effect by coking tendency formation of fuel and may relate to engine deposits. Sulfur content which shows an immediate effect and long term effects by increasing particulate emissions, cylinder wear and deposits these three specifications are all within the range of off-road

diesel fuel classified No. 4-D and marine diesel specifications (Hobson, 1992; Technical Review diesel fuels Chevron Products Company, 2011). During preparation, handling and laboratory testing of the three prepared fuel blends no precipitated sediment was observed or occurred.

CONCLUSION

From the physical specifications as well the calculated chemical properties of fuel A and C (Table 2); these two fuel blends can be used safely to increase power plants LGO storage feedstock for electrical energy generation. The three prepared fuel blends A, B and C are classified as ultra high quality off-road and marine diesel fuels and can handled and storage safely.

ACKNOWLEDGEMENT

REFERENCES

American Society for Testing and Materials (1993). ASTM Test Method, Petroleum Products, lubricants and fossil fuels analysis, *Philadelphia*, *Vols.: 05.01-05.05*.

American Society for Testing and Materials (1991). Standard Specification for Marine Fuels, **D 2069-91**; Standard Specification for Fuel Oils, **D 396-97**; Standard Specification for Diesel Fuel Oils **D 975-97;** Standard Specification for Aviation Turbine Fuels, **D 1655-98**.

Hobson, G. D. (1992). Modern Petroleum Technology. *Part 1 and II, 5th edition*. John Wiley and Sons, IP London: 423, 444, 445, 562, 564, 619, 621, 824-837 and 905-931.

Technical Review Diesel Fuels Chevron Products Company (2011). [WWW Document]. Chevron Fuels Technical Service *fueltek@chevron.com*, *www.chevron.com/products/prodserv/dieselfuel*.